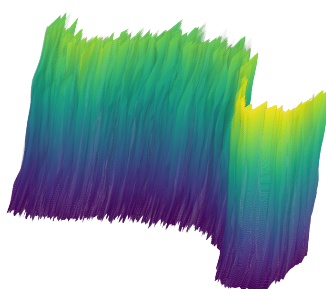


**UNIVERSIDADE DE LISBOA
INSTITUTO SUPERIOR TÉCNICO**

**GHENT UNIVERSITY
FACULTY OF ENGINEERING AND ARCHITECTURE**



Implementation of a X-mode multichannel edge density profile reflectometer for the new ICRH antenna on ASDEX Upgrade

Diogo Elói Trindade de Aguiam

Supervisor: Doctor António Guilherme Pereira Ehrhardt Gonçalves Silva

Co-Supervisors: Doctor Bruno Miguel Soares Gonçalves

Doctor Jean-Marie Noterdaeme

Thesis approved in public session to obtain the PhD Degree in
Technological Physics Engineering (Universidade de Lisboa)
Engineering Physics (Ghent University)

Jury final classification: Pass with Distinction

2018

UNIVERSIDADE DE LISBOA
INSTITUTO SUPERIOR TÉCNICO

GHENT UNIVERSITY
FACULTY OF ENGINEERING AND ARCHITECTURE

**Implementation of a X-mode multichannel edge density
profile reflectometer for the new ICRH antenna on
ASDEX Upgrade**

Diogo Elói Trindade de Aguiam

Supervisor: Doctor António Guilherme Pereira Ehrhardt Gonçalves Silva

Co-Supervisors: Doctor Bruno Miguel Soares Gonçalves

Doctor Jean-Marie Noterdaeme

Thesis approved in public session to obtain the PhD Degree in
Technological Physics Engineering (Universidade de Lisboa)
Engineering Physics (Ghent University)

Jury final classification: Pass with Distinction

Chairperson: Doctor Luís Paulo da Mota Capitão Lemos Alves
Instituto Superior Técnico, Universidade de Lisboa, Portugal

Members of the committee:

Doctor Sam Agneessens

Faculty of Engineering and Architecture, Ghent University, Belgium

Doctor Artur Jorge Louzeiro Malaquias

Instituto Superior Técnico, Universidade de Lisboa, Portugal

Doctor Garrard David Conway

Max-Planck-Institut für Plasmaphysik, Germany

Doctor Onofrio Tudisco

ENEA, Italian National Agency for New Technologies,

Energy and Sustainable Economic Development, Italy

Funding Institutions

Fundação para a Ciência e a Tecnologia, EUROfusion and FUSION-DC

2018

Abstract

Ion cyclotron resonance heating (ICRH) is one of the main heating mechanisms for nuclear fusion plasmas. However, studying the effects of ICRH operation, such as power coupling efficiency and convective transport, requires the measurement of the local edge plasma density profiles. Two new three-strap antennas were designed to reduce tungsten impurity release during operation, and installed on ASDEX Upgrade. One of these ICRH antennas embedded ten pairs of small microwave pyramidal horn antennas. In this thesis, a new multichannel X-mode microwave reflectometry diagnostic was developed to use these embedded antennas to simultaneously measure the edge electron density profiles in front of the bottom, middle and top regions of the radiating surface of the ICRH antenna. Microwave reflectometry is a radar technique that measures the round trip delay of probing waves that are reflected at specific cutoff layers, depending on the probing wave frequency, plasma density and local magnetic field. This diagnostic uses a coherent heterodyne quadrature detection architecture and probes the plasma in the range 40-68 GHz to measure plasma edge electron densities up to $2 \times 10^{19} \text{ m}^{-3}$, with magnetic fields between 1.85 T and 2.7 T, and a repetition interval as low as 25 μs . This work details the implementation and commissioning of the diagnostic, including the calibration of the microwave hardware and the analysis of the raw reflectometry measurements. We study the automatic initialization of the X-mode upper cutoff measurement, which is the main source of error in X-mode density profile reconstruction. Two first fringe estimation algorithms were developed: one based on amplitude and spectral information and another using a neural network model to recognize the first fringe location from spectrogram data. Kalman filters are used to improve radial measurement uncertainty to less than 1 cm. To validate the diagnostic, we compared the density profile measurements with other electron density diagnostics on ASDEX Upgrade, and observed typical plasma phenomena like the L-H transition and ELM activity. The experimental density profile results were used to corroborate ICRH power coupling simulations under different gas puffing conditions and to observe poloidal convective transport during ICRH operation.

Keywords: reflectometry, density profiles, nuclear fusion, diagnostics, plasma

Resumo

O aquecimento por ressonância ciclotrônica de íons (ICRH) é um dos principais mecanismos de aquecimento para plasmas de fusão nuclear. No entanto, estudar os efeitos de operação do ICRH, tal como a eficiência do acoplamento de potência ou transporte convectivo, requer a medida local dos perfis de densidade no limite do plasma. Duas novas antenas com três cintas foram desenhadas para reduzir a libertação de impurezas de tungsténio durante a sua operação, e instaladas no ASDEX Upgrade. Uma destas antenas de ICRH contém dez pares de antenas de microondas de cornetas piramidais. Nesta tese, um diagnóstico multicanal de reflectometria de modo X foi desenvolvido para medir simultaneamente os perfis de densidade electrónica em frente das regiões inferiores, centro e superiores da superfície radiante da antena de ICRH. A reflectometria de microondas é uma técnica de radar que mede o tempo de ida e volta de ondas de sonda que são reflectidas em camadas específicas de corte, que dependem da frequência da onda de sonda, da densidade do plasma e do campo magnético local. Este diagnóstico tem uma arquitetura com detecção heteródina coerente em quadratura e sonda o plasma na banda de frequência 40-68 GHz para medir os perfis de densidade electrónica até $2 \times 10^{19} \text{ m}^{-3}$, com campos magnéticos entre 1,85 T e 2,7 T, em intervalos tão baixos quanto 25 μs . Este trabalho detalha a implementação e o comissionamento do diagnóstico, incluindo a calibração do hardware de microondas e a análise da medida não tratada de reflectometria. Estudamos a inicialização automática da medida do corte superior do modo X, que é a principal fonte de erro de reconstrução de perfis de densidade em modo X. Dois algoritmos de estimativa da primeira franja foram desenvolvidos: um baseado em informação de amplitude e espectral do sinal e outro utilizando um modelo de redes neurais para reconhecer a localização da primeira franja a partir dos dados de espectrograma. Filtros Kalman são utilizados para minimizar a incerteza da medida radial para menos de 1 cm. Para validar o diagnóstico, comparámos os perfis de densidade medidos com outros diagnósticos de perfis de densidade do ASDEX Upgrade, e observámos fenómenos típicos de plasmas, tal como a transição L-H e atividade ELM. Os resultados experimentais de perfis de densidade foram usados para corroborar simulações de acoplamento de potência ICRH sob diferentes condições de abastecimento de gás, e para observar o transporte convectivo poloidal durante a operação de ICRH.

Palavras-chave: reflectometria, perfis densidade, fusão nuclear, diagnósticos, plasma

Abstract

Verhitting met vermogen in het bereik van de ion-cyclotronresonantiefrequentie (ICRF) is een van de belangrijkste verwarmingsmechanismen voor kernfusieplasma's. Om de effecten van de ICRF verhitting te bestuderen, zoals de efficiëntie van de vermogenskoppeling en convectief transport, moeten echter de lokale plasmadichtheidsprofielen worden gemeten. Twee nieuwe antennes met 3 geleiders werden ontworpen om de productie van verontreiniging door wolfram door de ICRF verhitting te reduceren en werden geïnstalleerd op ASDEX-upgrade. Een van deze ICRF antennes bevat tien paar kleine microgolf hoornantennes met een piramidale vorm. In dit proefschrift werd een nieuwe meerkanaals X-mode microgolfreflectometrie diagnostiek ontwikkeld om deze ingebedde antennes te gebruiken en simultaan de elektronendichtheidsprofielen aan de rand te meten voor de onderste, middelste en bovenste regio's van het stralende oppervlak van de ICRF-antenne. Magnetronreflectometrie is een radartechniek die de round-tripvertraging van sonderingsgolven meet die worden teruggekaatst op specifieke cut-off lagen, afhankelijk van de sonderingsgolffrequentie, de plasmadichtheid en het lokale magnetische veld. Deze diagnose maakt gebruik van een coherente heterodyne kwadratuurdetectiearchitectuur en tast het plasma af in het bereik van 40-68 GHz om plasma-rand elektronendichtheden tot $2 \times 10^{19} \text{ m}^{-3}$ te meten, met magnetische velden tussen 1,85 T en 2,7 T, en een herhalingsinterval met een minimum van 25 μs . Dit werk beschrijft de implementatie en ingebruikname van de diagnostiek, inclusief de kalibratie van de microgolfhardware en de analyse van de reflectometriemetingen. We bestuderen de automatische initialisatie van de bovenste cut-off meting in de X-modus, de belangrijkste bron van fouten bij de reconstructie van het dichtheidsprofiel in de X-modus. Twee eerste benaderendingsalgoritmen voor de franjes werden ontwikkeld: één op basis van amplitude- en spectrale informatie en een andere met behulp van een neurale netwerkmodel om de eerste randlocatie te herkennen uit de gegevens van de spectrogram. Kalman-filters worden gebruikt om de radiale meetonzekerheid tot minder dan 1 cm te verbeteren. Om de diagnostiek te valideren, vergeleken we de dichtheidsprofielmetingen met andere elektronendichtheidsdiagnostieken op ASDEX Upgrade en observeerden typische plasmaverschijnselen zoals de L-H-overgang en ELM-activiteit. De resultaten van het experimentele dichtheidsprofiel werden gebruikt om simulaties van de inkoppeling van ICRF vermogen bij verschillende scenario's met gas puff te bevestigen en om het poloidaal convectief transport tijdens ICRF-operatie te observeren.

Sleutelwoorden: reflectometrie, dichtheidsprofielen, nucleaire fusie, diagnostiek, plasma

Extended summary

As world energy consumption continues to increase, new sustainable clean sources of energy must be researched. Thermonuclear fusion is a reaction where two light atoms fuse together, releasing energy, which can be applied to electric power plants, hopefully within the 21st century. One of the main heating mechanisms to reach the thermal conditions for a sustained fusion reaction to occur in a tokamak is Ion Cyclotron Resonance Heating (ICRH), which directly heats the bulk plasma ions using high power radiofrequency waves. Power coupling efficiency depends on the correct matching of the ICRH antenna impedance to the plasma load, which is influenced by the shape and density of the plasma edge. To optimize this power coupling, the local plasma density profile in the small region in front of the launching antennas must be measured. ICRH operation is typically associated with wall impurity release, due to increased plasma surface interactions. A new three-strap ICRH antenna design, aiming to reduce tungsten impurity release during operation, was installed on ASDEX Upgrade as part of an international collaboration between IPP, Germany, ENEA, Italy, ASIPP, China, and IST, Portugal. The new design embedded ten pairs of small microwave pyramidal horn antennas. In this work, we describe the development of a new multichannel X mode reflectometry diagnostic to use the embedded antennas to measure the local plasma edge electron density profiles from different poloidal and toroidal locations in front of the ICRH antenna. The main objectives of the work consisted in the implementation and commissioning of the reflectometry diagnostic on ASDEX Upgrade, the development and validation of the X mode density profile reconstruction codes, and to contribute to ICRH operation studies. The reflectometry measurement in plasmas is a radar technique and depends on the propagation of an electromagnetic wave through the plasma, up to a cut off layer where the index of refraction goes to zero and the wave is reflected. Waves polarized in X mode, where the wave's electric field is perpendicular to the magnetic field, have two cut off regions, which depend on the wave frequency, the local magnetic field and the local plasma electron density. The frequency and the round trip delay of this wave contain information about the distance of the reflection and the dielectric plasma medium. By sweeping the frequency of a probing wave and measuring the reflection delay, an electron density profile of the plasma can be reconstructed. The implemented reflectometer probes the plasma in the range 40-68 GHz and is capable of measuring the edge plasma densities up to $2 \times 10^{19} \text{ m}^{-3}$, with magnetic fields between 1.85 T and 2.7 T, using the X mode upper cut off. Three of the ten available channels are used to probe the plasma from the bottom, middle and top regions of the radiating surface of the ICRH antenna. The diagnostic has an heterodyne quadrature detection architecture, using a single microwave oscillator to maintain coherency between the probing and reference signals. The dynamic tuning response of this voltage controlled oscillator was calibrated to provide a linear frequency sweep in 15 μs , with a minimum repetition interval of 25 μs . The reflectometry delay measurement is proportional to the phase difference between the reference and plasma reflection signals. Delay lines are used to compensate the long waveguides of each channel, connecting the reflectometer hardware to the in-vessel embedded antennas. Additionally, the non-linear waveguide dispersion was measured using a metallic mirror and used to calibrate the acquired raw quadrature interference signals. The reflectometry diagnostic

setup consists of a host computer and a high performance acquisition system, both installed inside the torus hall, and the microwave reflectometer hardware, whose front ends are attached to the waveguides close to the ASDEX Upgrade vessel. To mitigate the effects of the high magnetic fields that arise near the vessel during a discharge, the reflectometer power supplies were encased in a magnetic shielding structure. The main difficulty in X mode density profile reflectometry is automatically determining the start of the upper cut off reflection, called the first fringe frequency, for the over 89 thousand measurements acquired during a discharge. This first fringe indicates the reflection at the lowest residual density layer and may occur anywhere within the probing band, depending on the magnetic field profile and the location of the plasma. Low signal to noise ratio, plasma turbulence, X mode lower cut off reflection and spurious signals all increase the difficulty in determining the first fringe frequency. Wrong initializations of the upper cut off introduce both density and radial errors that are integrated along the density profile reconstruction. Two automatic first fringe estimation algorithms were developed in this work. The first developed algorithm, called *ampfilt*, uses both amplitude and spectral information of the raw signal to determine the start of the upper cut off region between the wall and the separatrix position, even in the presence of lower cut off reflection. The second algorithm is based on a neural network model that was trained with a comprehensive dataset to mimic human pattern recognition to determine the first fringe location from spectrogram data. The error analysis of both algorithms against a known validation dataset showed that the neural network model improved estimation precision by a factor of three. A Kalman filter is applied, assuming small variation of the plasma position between sweeps, to improve the precision of the first fringe estimation and reduce radial measurement uncertainty to less than 1 cm. The automatic density profile reconstruction procedure includes a final data validation step that discards impossible reconstructions and improves the overall quality of the diagnostic output. The edge density profiles measured with the new reflectometry diagnostic were compared with other standard density profile diagnostics on ASDEX Upgrade: Lithium-beam and broadband O-mode reflectometer. There is a good overlap of the different density profiles, mapped to poloidal flux coordinates, in both L mode and H mode plasmas with no ICRH or ELM activity. The radial and poloidal sensitivity of the three reflectometry channels was demonstrated by tracking the density profile evolution during the vertical scan of a circular plasma. The measurements were able to observe the plasma edge moving away from the bottom and middle reflectometry antennas and coming closer to the top antenna, as the plasma moved upwards. In low density and low magnetic field discharges, the reflectometer was able to measure density profiles up to the core region of the plasma and observe the effect of gas puffing in the density profiles. The diagnostic was also used to visualize typical plasma phenomena. The steepening of the individual edge density profiles was observed during the L-H transition. The outwards density profile relaxation during an ELM event was also observed. The high temporal resolution of the diagnostic, down to 25 μ s, allows the analysis of the fine density profile structure during fast events such as ELMs or the L-H transition. The new density profile reflectometer was able to contribute to ICRH operation studies by providing multiple and simultaneous localized measurements in front of the ICRH antenna. 3D simulations have showed that the edge plasma density can be tailored with localized gas puffing to increase ICRH power coupling. The new reflectometer corroborated these simulations by providing the experimental edge

density profile measurements under different gas puffing conditions. Simulations also predicted the formation of convective $E \times B$ transport in front of the ICRH antennas during operation, which may generate hot spots and reduce heating efficiency. These convective cells were observed experimentally using the multiple poloidal measurements. This work consisted in the successful implementation, commissioning and validation of the new X-mode density profile reflectometer. While the diagnostic was originally designed to aid in ICRH operation studies, its poloidal multichannel topology and high temporal resolution may provide useful measurements for other experiments. Future work may include upgrading the reflectometer hardware with additional channels and adapt the microwave generation and acquisition system for filamentary and edge fluctuation measurements.

Resumo alargado

Devido ao contínuo aumento do consumo energético a nível mundial, novas fontes de energias devem ser investigadas. Fusão termonuclear é uma reação onde dois átomos leves fundem-se, libertando energia que pode ser aplicada para alimentar centrais eléctricas, possivelmente durante o século XXI. Um dos principais mecanismos para alcançar as condições necessárias para uma reação de fusão sustentada num tokamak é o aquecimento por ressonância ciclotrónica de iões (ICRH), que aquece os iões do centro do plasma utilizando ondas de radiofrequência de alta potência. A eficiência do acoplamento de potência depende da adaptação correta entre a impedância da antena ICRH e a carga de plasma, que é influenciada pela forma e densidade na fronteira do plasma. Para otimizar este acoplamento de potência, o perfil local de densidade na pequena região em frente das antenas ICRH tem de ser medido. A operação de ICRH é tipicamente associada à libertação de impurezas da parede, devido ao aumento das interações entre a plasma e a superfície. Uma nova antena de ICRH com três straps foi desenhado com o objectivo de reduzir a libertação de impurezas de tungsténio durante a operação, e instalada no ASDEX Upgrade, fazendo parte duma colaboração internacional entre o IPP, Alemanha, ENEA, Itália, ASIIPP, China e IST, Portugal. O novo design contém dez pares de pequenas antenas de microondas de cornetas piramidais. Neste trabalho, descrevemos o desenvolvimento de um diagnóstico de reflectometria multicanal de modo X que utiliza as antenas embutidas para medir o perfil de densidade electrónica na fronteira do plasma a partir de diferentes posições poloidais e toroidais em frente da antena ICRH. Os principais objectivos deste trabalho consistiram na implementação e comissionamento do diagnóstico de reflectometria no ASDEX Upgrade, o desenvolvimento e validação dos códigos de reconstrução de perfis de densidade em modo X, e a contribuição para os estudos de operação do ICRH. A medida de reflectometria em plasmas é uma técnica de radar que depende da propagação de ondas electromagnéticas, através do plasma, até uma camada de corte onde o índice de refração tende para zero e a onda é reflectida. Ondas polarizadas em modo X, onde o campo eléctrico da onda é perpendicular ao campo magnético imposto, tem duas regiões de corte, que dependem da frequência da onda, do campo magnético local, e a densidade electrónica local do plasma. A frequência e o atraso do tempo de voo desta onda contém informação sobre a distância da reflexão e o meio dieléctrico do plasma. Ao varrer a frequência da onda de sondagem e medindo o atraso da reflexão, um perfil de densidade electrónica do plasma pode ser reconstruído. O reflectómetro implementado sonda o plasma na banda 40-68 GHz e é capaz de medir densidades de plasma na fronteira até $2 \times 10^{19} \text{ m}^{-3}$, com campos magnéticos entre 1.85 T e 2.7 T, usando a região superior de corte de modo X. Três dos dez canais disponíveis são usados para sondar o plasma a partir das regiões inferior, centro e superior da superfície radiante da antena ICRH. O diagnóstico tem uma arquitetura com detecção heteródina em quadratura e utiliza um único oscilador de microondas para manter a coerência entre os sinais de sonda e de referência. A resposta dinâmica do ajuste deste oscilador controlado por tensão foi calibrada para fornecer um varrimento de frequência linear em 15 μs , com uma repetição mínima de 25 μs . A medida de reflectometria do atraso é proporcional à diferença de fase entre os sinais de referência e de reflexão do plasma. Linhas de atraso são utilizadas para compensar o longo comprimento dos guias de onda de cada canal,

que ligam o hardware do reflectómetro e as antenas embutidas dentro do tokamak. Consecutivamente, a dispersão não linear dos guias de onda foi medida utilizando espelhos metálicos e usada para calibrar os sinais brutos em quadratura da inferência. O diagnóstico de reflectometria consiste num computador principal e um sistema de aquisição de alta performance, ambos instalados dentro da sala do torus, e o hardware de reflectometria de microondas, cujos front ends estão ligados aos guias de onda junto do vessel do ASDEX Upgrade. Para mitigar os efeitos dos elevados campos magnéticos que surgem perto do vessel durante uma descarga, as fontes de alimentação são envoltas por uma estrutura de blindagem magnética. A principal dificuldade em reflectometria de perfis de densidade de modo X é a determinação automática do início da região de corte superior, chamada frequência da primeira franja, para as mais de 89 mil medidas adquiridas durante uma descarga. Esta primeira franja indica a reflexão da camada de densidade residual mais baixa e pode ocorrer em qualquer lugar dentro da banda de sondagem, dependendo do campo magnético e a localização do plasma. Uma relação sinal-ruído baixa, turbulência de plasma, reflexões devido à região de corte inferior do modo X e sinais espúrios, todos dificultam a determinação da primeira franja. Inicializações erradas da região de corte superior introduzem erros de densidade e radiais que são integrados ao longo da reconstrução do perfil de densidade. Dois algoritmos automáticos de estimativa da primeira franja foram desenvolvidos neste trabalho. O primeiro algoritmo desenvolvido, chamado *ampfilt*, utiliza informação de amplitude e espectral do sinal bruto para determinar a primeira reflexão entre a parede e a posição da separatrix. O segundo algoritmo é baseado num modelo de redes neuronais e foi treinado com um conjunto de dados abrangente para imitar o reconhecimento de padrões de humanos para determinar a localização da primeira franja a partir de espectrogramas. A análise do erro de ambos os algoritmos utilizando um conjunto de dados conhecidos demonstrou que a rede neural melhora a precisão da estimação por um factor de três. Um filtro Kalman é aplicado, assumindo uma pequena variação da posição de plasma entre varrimentos, para melhorar a precisão da estimativa da primeira franja e reduzir a incerteza da medida radial para menos de 1 cm. O processo de reconstrução automática de perfis de densidade inclui um passo final de validação de dados que descarta reconstruções impossíveis e melhorando a qualidade geral dos resultados do diagnóstico. Os perfis de densidade na fronteira medidos com o novo diagnóstico de reflectometria foram comparados com outros diagnósticos típicos do ASDEX Upgrade: Lithium-beam e reflectómetro de modo O de banda larga. Existe uma boa sobreposição dos perfis de densidade, mapeados para coordenadas poloidais de fluxo, em plasmas com confinamento de modo L e modo H, sem ICRH ou atividade de ELM. A sensibilidade radial e poloidal dos três canais de reflectometria foi demonstrada pelo rastreamento da evolução do perfil de densidade durante um varrimento vertical de um plasma circular. As medidas permitiram observar a fronteira do plasma a afastar-se das antenas de reflectometria inferior e central, e aproximando-se da antena superior, enquanto o plasma se movia verticalmente. Em plasma com baixa densidade e campo magnético, o reflectómetro foi capaz de medir perfis de densidade até à região central do plasma e observar os efeitos do abastecimento de gás nos perfis de densidade. O diagnóstico também foi utilizado para visualizar fenómenos típicos de plasma. O acentuar do gradiente dos perfis de densidade individuais na fronteira foi observado durante a transição L-H. O relaxamento dos perfis de densidade também foi observado durante eventos de ELM. A alta

resolução temporal do diagnóstico, até 25 μ s, permite a análise da estrutura fina dos perfis durante eventos rápidos como ELMs ou a transição L-H. O novo reflectómetro de perfis de densidade contribuiu para os estudos de operação de ICRH ao fornecer múltiplas medidas localizadas e simultâneas em frente da antena ICRH. Simulações 3D demonstraram que os perfis de densidade na fronteira podem ser adaptados para melhorar o acoplamento da potência ICRH, abastecendo localmente com gás. O novo reflectómetro corroborou estas simulações com medidas experimentais dos perfis de densidade na fronteira, sob diferentes condições de abastecimento de gás. Simulações também previram a formação de células de transporte convectivo $E \times B$ em frente das antenas ICRH, durante operação, que podem gerar pontos quentes e reduzir eficiência do aquecimento. Estas células convectivas foram observadas experimentalmente usando as várias medidas poloidais do diagnóstico. Este trabalho consistiu na implementação, comissionamento e validação com sucesso do novo reflectómetro de modo X de perfis de densidade. Enquanto este diagnóstico foi originalmente desenhado para ajudar em estudos de operação ICRH, a sua topologia multicanal poloidal e alta resolução temporal pode providenciar medidas úteis para outras experiências. O trabalho futuro pode incluir a atualização do hardware do reflectómetro com canais adicionais e adaptar a geração de microondas e sistema de aquisição para medidas de filamentos e de flutuações na fronteira do plasma.

Uitgebreide samenvatting

Het energieverbruik in de wereld blijft stijgen, nieuwe duurzame schone energiebronnen moeten dus worden onderzocht. Thermonucleaire fusie is een reactie waarbij twee lichte atomen samensmelten en energie vrijgeven. Deze methode kan, hopelijk in de 21e eeuw, worden toegepast om elektrische centrales aan te drijven. Een van de belangrijkste verhittingsmechanismen om de voorwaarden voor de temperatuur te bereiken voor een aanhoudende fusiereactie die in een tokamak kan optreden, is Ion Cyclotron Resonantie Verwarming (ICRH), die direct de bulk plasma-ionen verwarmt met behulp van hoogvermogen radiofrequentiegolven. De efficiëntie van de vermogenskoppeling hangt af van de juiste aanpassing van de impedantie van de ICRH-antenne aan de load als gevolg van het plasma. Deze wordt beïnvloed door de vorm en dichtheid van de plasmarand. Om deze vermogenskoppeling te optimaliseren, moet het lokale plasmadichtheidsprofiel in een klein gebied vóór de antennes worden gemeten.

ICRH-werking is typisch geassocieerd met het vrijstellen van wandvervuiling als gevolg van verhoogde interacties tussen plasma en wand oppervlakken. Een nieuw driedig ICRH-antenneontwerp, bedoeld om de uitstoot van wolframvervuiling tijdens bedrijf te verminderen, werd geïnstalleerd op ASDEX Upgrade als onderdeel van een internationale samenwerking tussen IPP, Duitsland, ENEA, Italië, ASIPP, China en IST, Portugal. Het nieuwe ontwerp bevat tien paar kleine microgolf piramidale hoornantennes. In dit werk beschrijven we de ontwikkeling van een nieuwe meerkanaals X-modus reflectometrie diagnostiek om de ingebedde antennes te gebruiken om de lokale plasma-rand elektronendichtheidsprofielen van verschillende poloïdale en toroïdale locaties voor de ICRH-antenne te meten. De belangrijkste doelstellingen van het werk waren de implementatie en inbedrijfstelling van de reflectometrie diagnostiek op ASDEX Upgrade, de ontwikkeling en validatie van de X-mode dichtheidsprofiel reconstructiecodes, en een bijdrage te leveren aan ICRH-operatiestudies. De reflectometrie-meting in plasma's is een radartechniek en hangt af van de propagatie van een elektromagnetische golf door het plasma, tot een cut-off laag waar de brekingsindex naar nul gaat en de golf wordt gereflecteerd. Golven gepolariseerd in X-modus, waar het elektrische veld van de golf loodrecht staat op het magnetische veld, hebben twee cut-off gebieden, die afhankelijk zijn van de golfrequentie, het lokale magnetische veld en de lokale plasma-elektronendichtheid. De frequentie en de round-tripvertraging van deze golf bevatten informatie over de afstand van de reflectie en het diëlektrische plasmamedium. Door de frequentie van een sonderingsgolf te meten en de reflectievertraging te meten, kan een elektronendichtheidsprofiel van het plasma worden gereconstrueerd. De geïmplementeerde reflectometer tast het plasma af in het bereik van 40-68 GHz en is in staat om de rand-plasmadichtheden tot $2 \times 10^{19} \text{ m}^{-3}$ te meten, met magnetische velden tussen 1,85 T en 2,7 T, gebruikmakend van de bovenste grenswaarde in de X-modus. Drie van de tien beschikbare kanalen worden gebruikt om het plasma te onderzoeken in de onderste, middelste en bovenste regionen van het stralingsoppervlak van de ICRH-antenne. De diagnose heeft een heterodyne kwadratuurdetectiearchitectuur, waarbij een enkele microgolfoscillator wordt gebruikt om de coherentie tussen de sonderings- en referentiesignalen te handhaven. De dynamische afstemmingsrespons van deze spanningsgestuurde oscillator werd gekalibreerd om een lineaire fre-

quentiescan te verschaffen in 15 μs , met een minimum herhalingsinterval van 25 μs . De reflectometrie-vertragsmeting is evenredig met het faseverschil tussen de referentie- en plasma-reflectiesignalen. Vertragslijnen worden gebruikt om de lange golfgeleiders van elk kanaal te compenseren, waarbij de reflectometerhardware wordt verbonden met de ingebouwde antennes. Bovendien werd de niet-lineaire golfgeleider-dispersie gemeten met behulp van een metalen spiegel en gebruikt voor het kalibreren van de verkregen ruwe kwadratuur stoorsignalen. De diagnostische set-up van de reflectometrie bestaat uit een computer en een hoogwaardig acquisitiesysteem, beide geïnstalleerd in de toruszaal, en de microgolf reflectometerhardware, waarvan de vooreinden zijn bevestigd aan de golfgeleiders dichtbij de ASDEX Upgrade tokamak. Om de effecten van de hoge magnetische velden die zich voordoen in de buurt van het vat tijdens een ontlading te verminderen, werden de voedingen van de reflectometer omgeven door een magnetische afschermingsstructuur.

De grootste moeilijkheid in de reflectometrie meting van het dichtheitsprofiel in de X-modus bestaat erin automatisch de start van de bovenste afsnijreflectie te bepalen, deze wordt de eerste franjefrequentie (fringe frequency) genoemd, voor de meer dan 89 duizend metingen die verkregen worden tijdens een ontlading. Deze eerste franje geeft de reflectie aan bij de laag met de laagste resterende dichtheid en kan overal in de meetband voorkomen, afhankelijk van het profiel van het magnetische veld en de locatie van het plasma. Lage signaal / ruis-verhouding, plasma-turbulentie, X-mode lagere afsnijreflectie en stoorsignalen, alle verhogen de moeilijkheid bij het bepalen van de eerste franjefrequentie. Een verkeerde initialisatie van de bovenste afsnijding introduceert zowel dichtheids- als geometrische (radiale) fouten die langs de dichtheidsprofielreconstructie worden geïntegreerd. In dit werk zijn twee automatische eerste schattingsalgoritmen voor de franje ontwikkeld. Het eerste ontwikkelde algoritme, genaamd amfilit, gebruikt zowel amplitude- als spectrale informatie van het onbewerkte signaal om het begin van het bovenste afsnijgebied tussen de wand en de separatrixpositie te bepalen, zelfs in de aanwezigheid van lagere afsnijreflectie. Het tweede algoritme is gebaseerd op een neurale netwerkmodel dat is getraind met een uitgebreide gegevensreeks om menselijke patroonherkenning na te bootsen en de eerste franjelocatie te bepalen op basis van spectrogramgegevens. De foutanalyse van beide algoritmen tegen een bekende validatie-dataset toonde aan dat het neurale netwerkmodel de schattingsprecisie met een factor drie verbeterde. Een Kalman-filter wordt toegepast, uitgaande van een kleine variatie van de plasmapositie tussen de frequentie scans, om de precisie van de eerste schatting van de franjes te verbeteren en de radiale meetonzekerheid tot minder dan 1 cm te verminderen. De reconstructieprocedure voor automatische dichtheidsprofielen bevat een laatste gegevensvalidatiestap die onmogelijke reconstructies verworpt en de algehele kwaliteit van de diagnostische uitvoer verbetert. De randdichtheidsprofielen gemeten met de nieuwe reflectometrie diagnostiek werden vergeleken met andere standaarddensiteitsprofiel diagnostiek op ASDEX Upgrade: Lithiumstraal en breedband O-modus reflectometer. Er is een goede overeenstemming van de verschillende dichtheitsprofielen, uitgezet ten opzichte van poloïdale fluxcoördinaten, zowel in L-modus als in H-modus plasma's zonder ICRH- of ELM-activiteit. De radiale en poloïdale gevoeligheid van de drie reflectometerkanalen werd aangetoond door de evolutie van het dichtheidsprofiel tijdens de verticale scan van een circulair plasma te volgen. De metingen waren in staat te observeren hoe de plasmarand zich van de onderste en middelste

reflectometrie-antennes weg bewoog en dichter bij de bovenste antenne kwam, terwijl het plasma naar boven bewoog. Bij lage dichtheid en lage magneetveldontladingen kon de reflectometer dichtheitsprofielen meten tot aan het kerngebied van het plasma en het effect van gaspuffing in de dichtheitsprofielen observeren. De diagnose werd ook gebruikt om typische plasmaverschijnselen te visualiseren. Het steiler worden van de individuele randdichtheitsprofielen tijdens de L-H-overgang werd waargenomen. De relaxatie naar buiten van het dichtheitsprofiel tijdens een ELM-gebeurtenis werd ook waargenomen. De hoge tijdelijke resolutie van de diagnostiek, tot maximaal 25 μ s, maakt de analyse mogelijk van de fijne structuur van het dichtheitsprofiel tijdens snelle gebeurtenissen zoals ELM's of de L-H-overgang. De nieuwe randdichte reflectometer kon bijdragen tot studies van het bedrijven van ICRH door meerdere en simultane gelokaliseerde metingen aan te bieden vóór de ICRH-antenne. 3D-simulaties hebben aangetoond dat de rand-plasmadichtheid kan worden aangepast met gelokaliseerde gaspuffing om de ICRH-vermogenskoppeling te verhogen. De nieuwe reflectometer bevestigde deze simulaties door de experimentele randdichtheitsprofielmetingen onder verschillende omstandigheden van gas puff te leveren. Simulaties voorspelden ook de vorming van convectieve $E \times B$ -transport vóór de ICRH-antennes tijdens de werking, wat hot spots kan genereren en de efficiëntie van de verhitte kan verminderen. Deze convectieve cellen werden experimenteel waargenomen met behulp van de metingen op verschillende poloïdale plaatsen. Dit werk bestond uit de succesvolle implementatie, inbedrijfstelling en validatie van de nieuwe X-modus dichtheitsprofiel reflectometer. Hoewel de diagnose oorspronkelijk was bedoeld om te helpen bij ICRH-operatiestudies, kunnen de poloïdale meerkanaals topologie en hoge temporele resolutie nuttige metingen ook voor andere experimenten opleveren. Toekomstig werk kan het upgraden van de reflectometerhardware met extra kanalen omvatten en het microgolfgeneratie- en acquisitiesysteem aanpassen voor de meting van filamenten en randfluctuaties.

To Ju

Acknowledgments

A thesis, or any long term project, is never possible without the help and support of many people. Foremost, I would like to sincerely thank my supervisor Dr. António Silva for the opportunity to work with him in this project. Our many technical discussions and friendly conversations gave me the tools and the encouragement required to finish this project. I would also like to thank my co-supervisors and sponsors Professor Bruno Gonçalves and Professor Jean-Marie Noterdaeme for their unending support.

I thank Fundação da Ciência e Tecnologia, for funding my scholarship under the Advanced Program in Plasma Science and Engineering doctoral programme, Fusion-DC, for promoting education in fusion, and the EUROfusion consortium, for funding so many research projects, including this work, to make fusion a reality.

From Instituto de Plasmas e Fusão Nuclear, I would like to thank my colleagues and friends: Carmo Nunes and Catarina Figueiredo, who always guided me through the bureaucracy; Jorge Santos, whose deep critiques led to important breakthroughs; Pedro Carvalho; Filipe da Silva; Valentina Nikolaeva; José Vicente; and my colleagues from APPLAuSE: Ana Dias, Jayanath Koliyadu, João Loureiro, Norberto Catarino, Susana Espinho, Syed Shah, Egor Seliunin and Luís Gil.

I also thank the Max-Planck-Institut für Plasmaphysik in Garching, Germany, where most of this work took place, and the people that made my secondment there great: Dmitrii Prisiazhniuk, Alexandra Kulyk, Mustafa Gaja, Branka Vanovac, Serhiy Mochalsky, Jeppe Olsen, Vladimir Bobkov, Helmut Fünfgelder, Garrard Conway, Anna Medvedeva, Wei Zhang, and all others I failed to mention here.

My sincere thank you to Luís Guimarães for the so many ways you've helped me these past years. It would not have been possible without your incredible support and enthusiasm for fusion and science, and for encouraging through the most difficult times.

I would like to thank my family for their support and specially both my parents, who provided the confidence to reach higher and farther in life.

And my deepest gratitude to my fiancé Joana Santos for her unwavering support through thick and thin, every day of our lives.

Muito obrigado,
Diogo Aguiam

2018

Contents

Abstract	vii
Resumo	ix
Abstract	xi
Extended summary	xiii
Resumo alargado	xvii
Uitgebreide samenvatting	xxi
Acknowledgments	xxvii
List of Tables	xxxiii
List of Figures	xxxv
Nomenclature	xli
Glossary	1
1 Introduction	1
1.1 Thermonuclear fusion for energy production	1
1.2 Tokamak experimental devices	3
1.2.1 Heating the plasma	4
1.3 The ASDEX Upgrade experimental tokamak	5
1.4 Ion cyclotron resonance heating	6
1.4.1 ICRH operation principle	7
1.4.2 ICRF heating system on ASDEX Upgrade	9
1.4.3 The need for a new ICRF antenna	10
1.5 Objectives of this work	12
1.6 This thesis	13
2 Microwave reflectometry	15
2.1 Propagation of waves in plasmas	15
2.1.1 Electromagnetic waves in unmagnetized plasmas	17
2.1.2 Propagation modes of electromagnetic waves in magnetized plasmas	18
2.1.3 Electromagnetic wave cutoffs in fusion plasma	21
2.2 Microwave reflectometry diagnostics for fusion plasmas	23
2.2.1 Measurement principle	23

2.2.2	Swept reflectometry for density profile measurements	25
2.2.3	Other reflectometry techniques for density profile measurements	28
2.3	Microwave reflectometry architectures	29
2.3.1	Homodyne detection	29
2.3.2	Heterodyne detection	30
2.3.3	Extracting the group delay measurement	32
2.3.4	Uncertainty of the reflectometry measurement	33
2.4	Summary	34
3	Implementation of the new reflectometry diagnostic	37
3.1	Specifications for reflectometry diagnostic operation	38
3.1.1	Microwave band and probing frequencies	38
3.1.2	Reflectometry antenna locations and lines of sight	40
3.2	Experimental setup of the diagnostic	43
3.3	Microwave reflectometry system design	47
3.3.1	Reflectometry architecture	47
3.3.2	Microwave generation	48
3.3.3	Generation of coherent references	53
3.3.4	Transmitter and receiver front ends	54
3.3.5	Amplification and quadrature detection	57
3.3.6	Reflectometer bandwidth	58
3.4	Diagnostic support systems	61
3.5	Summary	62
4	Commissioning of the reflectometry diagnostic	65
4.1	Analysis of the raw reflectometry measurement	65
4.2	Calibration of the waveguide dispersion	67
4.2.1	Calibration setup	68
4.2.2	Group delay measurements for multiple distances	69
4.2.3	Fitting the calibration measurements	72
4.2.4	Calibrating raw signal by removing waveguide dispersion	73
4.3	Analysis of the X-mode reflectometry signal	74
4.3.1	Appearance of lower cutoff reflection	75
4.3.2	Evolution of the reflectometry signal during a discharge	76
4.4	First fringe reflection estimation	78
4.4.1	Influence first fringe estimation errors on density profile reconstruction	78
4.4.2	Amplitude based first fringe estimation algorithms	78
4.4.3	The <i>ampfilt</i> first fringe estimation algorithm	80
4.4.4	Improving vacuum distance measurements with Kalman filtering	84
4.4.5	Developing a first fringe estimation algorithm based on Neural Networks	86

4.4.6	Reconstructed density profiles using both first fringe algorithms	93
4.4.7	Conclusions of the first fringe estimation algorithms	96
4.5	Processing the group delay measurement	97
4.5.1	Extracting reflectometry group delay measurement	97
4.5.2	Improving group delay spectrogram	98
4.5.3	Estimation of the residual density at the first reflection	102
4.6	Density profile reconstruction	105
4.6.1	Validation of the reconstruction data	105
4.6.2	Processing the density profiles	108
4.7	Summary	109
5	Experimental results	111
5.1	Validation of diagnostic commissioning	111
5.1.1	Comparison electron density profiles with other diagnostics	111
5.1.2	Radial and poloidal sensitivity to plasma displacement	114
5.1.3	Measuring density profiles deep into the plasma	118
5.2	Observing typical plasma phenomena	119
5.2.1	L-H transition	119
5.2.2	Edge localized modes	120
5.3	ICRF operation studies	123
5.3.1	ICRF power coupling to the plasma	123
5.3.2	Poloidal convective cells induced by ICRF heating	125
5.4	Summary	127
6	Conclusions	129
7	Scientific Contributions	133
	Bibliography	137
A	Quadrature phase uncertainty	151

List of Tables

3.1	ASDEX Upgrade main parameters [20].	38
3.2	Measured lengths, delays and attenuations of each delay line segment.	60
4.1	Variability of dataset	88
4.2	Estimation errors of first fringe estimation algorithms.	93

List of Figures

1.1	Essential components of a tokamak device.	3
1.2	Main components of the ASDEX Upgrade tokamak at the Max-Planck-Institut für Plasma-physik in Garching, Germany	6
1.3	Plasma density profile regions for ICRF power coupling and absorption.	7
1.4	Plasma surface interactions due to ICRF operation on ASDEX Upgrade.	8
1.5	Toroidal location of ICRH antennas on ASDEX Upgrade.	9
1.6	Evolution of the ICRF antenna designs on ASDEX upgrade and ICRF. The ICRF antenna is typically surrounded by the limiter structures, which prevent the rotating plasma from going into the antenna, and the oblique metal rods, in front of antenna straps, are the grounded Faraday protection straps. Vertical arrows indicate possible phasing of the individual antenna straps.	11
1.7	Part of the team involved in the design and installation of the new three-strap ICRF antenna and embedded reflectometer (April 2015).	12
2.1	Electromagnetic waves propagating in a fusion plasma slab model with a magnetic field gradient.	16
2.2	Ordinary and extraordinary modes of propagation in magnetized plasmas.	19
2.3	Dispersion diagrams for X-mode and O-mode.	21
2.4	Nomenclature of fusion plasma regions.	21
2.5	cutoff frequencies for a typical ASDEX Upgrade plasma with 2 T magnetic field and $7 \times 10^{19} \text{ m}^{-3}$ electron density.	22
2.6	Phase shift of probing waves with different frequencies.	24
2.7	Phase measurement of a reflectometry interference signal with constant frequency in a turbulent plasma.	24
2.8	Expected group delay measurement of a reflectometry signal with swept probing frequency, in O-mode or X-mode lower cutoff.	25
2.9	Generic architecture of a reflectometer with homodyne detection.	30
2.10	Heterodyne reflectometry architecture with bistatic antenna configuration and phase locked local reference generator.	31
2.11	Reflectometry architecture with quadrature heterodyne detection.	32

3.1	Probed electron densities for different cutoff frequencies under the typical core magnetic field range on ASDEX Upgrade.	39
3.2	Operational range of the extended U-band X-mode edge density profile reflectometer. . .	40
3.3	Location and details of the reflectometry antenna pairs embedded along the radiating surface of ICRF antenna 4 in sector 12 of ASDEX Upgrade.	41
3.4	a) Poloidal and b) toroidal cross section views of the ASDEX Upgrade tokamak and lines of sight of the installed reflectometry channels 1, 4 and 8.	42
3.5	Main components of the reflectometry diagnostic system.	43
3.6	Placement of the reflectometry diagnostic system cabinets installed inside the ASDEX Upgrade torus hall.	44
3.7	Cabinet containing the diagnostic support hardware: host computer, acquisition system, trigger controller and network interfaces; placed away from the vessel.	44
3.8	Cabinet containing the microwave reflectometry hardware: shielded power supplies, reflectometry signal generation and conditioning hardware, and front ends attached to waveguides; close to the vessel.	45
3.9	Vacuum flange with 14 WR19 pass through windows (left). CAD setup of the in-vessel waveguide routing along the back side of the ICRF antenna (right).	46
3.10	Reflectometer power supply with magnetic shielding and theoretical diagram of operation.	46
3.11	Heterodyne quadrature detection topology implemented in this microwave reflectometry system.	47
3.12	Complete architecture of the microwave reflectometry diagnostic system.	48
3.13	Coarse calibration of the VCO tuning lookup table for output frequency of the reflectometer.	50
3.14	Dynamic frequency calibration setup. The resulting beat signal frequency is proportional to the sweep rate and the delay between the LO and RF signals.	51
3.15	Sweep rate variation (left) of the VCO response using a static calibration and resulting frequency ramp (right). The maximum frequency non-linearity is 113 MHz.	51
3.16	Sweep rate variation (left) of the VCO response using after 27 iterations of the dynamic calibration algorithm and resulting frequency ramp (right). The maximum frequency non-linearity is 38 MHz.	52
3.17	Beat frequency uncertainty due to reflection delay.	52
3.18	Diagram of the frequency translator module that introduces a +50 MHz shift to the input signal.	53
3.19	Diagram of the 400 MHz reference generation.	54
3.20	Diagram of the microwave reflectometry front ends, protection filters and connecting waveguides.	55
3.21	Output powers of the $\times 4$ active multipliers used for probing the plasma (RF) and driving the receiver mixer (LO). The dashed lines represent the output power of each device, while the solid lines represent the average output power for the RF and LO drivers.	56

3.22 Conversion losses of the front end mixers for different LO driving powers and a -5 dBm RF signal with a +400 MHz frequency difference from the LO. For each LO driving power, the dashed lines represent the individual conversion losses of the three detection mixers, while the solid lines represent the respective averaged conversion losses.	56
3.23 Losses of the microwave components and coupling of the bistatic horn and WR42 antennas.	57
3.24 Power output and expected measurement signal power of horn and WR42 antennas.	58
3.25 Intermediate signal conditioning diagram and quadrature detection.	58
3.26 Non-linear propagation delay of a 10 m long WR19 waveguide as a function of wave frequency.	59
3.27 Diagram of the coarse and fine delay lines.	60
3.28 Distribution of the beat signal frequency as a function of the sweep rate and total delay of the received reflectometry signal.	61
4.1 Reflectometry group delay reflection signals measured at the beginning (70 ms) of discharge #33490 with $B_0 = -2.6$ T. The reflection signatures of the edge plasma, the back wall and the Faraday screen can be seen.	66
4.2 Non-linear wave propagation delays inside WR19 waveguides of different lengths.	68
4.3 In-vessel calibration setup to measure waveguide dispersion of reflectometry channel 1.	69
4.4 Raw beat signal and group delay spectrogram measurements for multiple metallic mirror distances using reflectometry channel 1.	70
4.5 Combined spectrogram of normalized calibration waveguide delay measurements of channel 1.	71
4.6 Calibration results and fitting parameters for each reflectometry channel.	72
4.7 Comparison of a plasma reflection signal before (left) and after (right) calibration by removing the respective waveguide dispersion. H-mode He discharge #32774 at 1.5 s with -2.1 T using reflectometry channel 1.	73
4.8 Raw signal of discharges with low and high magnetic fields measured using channel 1. The bandwidth of the plasma reflection decreases with the magnetic field strength.	75
4.9 Raw signal of discharges with high core plasma electron density and low and high magnetic fields, showing both X-mode upper and lower cutoff reflections measured using channel 1.	76
4.10 Simulated probed plasma regions (solid lines) using the X-mode reflectometry diagnostic for plasmas with low and high density profiles.	77
4.11 Amplitude evolution of the reflectometry measurement on channel 1 during ASDEX Upgrade discharge #33291	77
4.12 Influence of small FF estimation shifts in resulting density profile reconstruction of reflectometry channel 1 measurement at 2.452 s of #33291.	79
4.13 Smoothed raw signal amplitude in different magnetic field conditions.	80

4.14	FF estimation steps using the <i>ampfilt</i> algorithm of the reflectometry raw signal at 2.45 s of #33291 with only X-mode upper cutoff reflection.	81
4.15	FF estimation steps using the <i>ampfilt</i> algorithm in the UC+LC regime for a reflectometry raw signal of a high core density plasma, at 3.4 s of #33291.	83
4.16	First fringe estimation along two discharges with low and high core magnetic fields and with UC+LC regimes.	84
4.17	Improved precision of the Kalman filtered first fringe and vacuum distance estimations along two discharges with antenna 1.	85
4.18	Distribution of the plasma discharges depending on their magnetic field and core electron density acquired during the 2016 ASDEX Upgrade campaign.	87
4.19	Raw spectrogram data and ROI limits.	89
4.20	Preprocessed 2D spectrogram matrix used as input image for the neural network; x and y axis correspond to the grid points of the image.	89
4.21	First fringe frequency distributions of the sparse dataset and corresponding prediction error.	91
4.22	First fringe frequency distributions of the extended dataset and corresponding prediction errors.	92
4.23	First fringe error distribution of the <i>ampfilt</i> algorithm using the known sparse dataset.	92
4.24	Estimated first fringe frequencies and Kalman filtered vacuum distances during discharge #33841 using the <i>ampfilt</i> and neural network algorithms.	94
4.25	a) Estimated vacuum distances and moving 5 ms average distance during discharge #33841 using the <i>ampfilt</i> and neural network algorithms; b) Imprecision of the algorithms' measurements; c) Imprecision of the Kalman filtered measurements.	95
4.26	Reconstructed density profiles for discharge #33841 using the vacuum distances estimated by the <i>ampfilt</i> and neural network algorithms.	96
4.27	Reconstructed density profiles using group delays calculated from raw phase and spectrogram peaks using channel 1 at 1.5 s of #32774.	98
4.28	Effect of different window and padding parameters on group delay spectrogram.	99
4.29	Spectrogram evolution with increasing persistence window using mean and median averaging using channel 1 at 1.500-1.501 s of #32774.	100
4.30	Analysis of the deviation of group delay gradients with increasing persistence using mean and median spectrogram averaging.	101
4.31	Comparing the group delays of mean and median persistences and corresponding reconstructed density profiles.	102
4.32	Reconstructed density profiles with different residual density n_{e0} initializations and compared with Lithium beam density profile at 1.6 s of #32774	103
4.33	Comparison of the radial mismatch (σ_E) between the reconstructed density profiles using reflectometry channel 1 and the Lithium beam density profiles (orange), for multiple values of n_{e0} , in UC and UC+LC regimes of discharge #33291.	104
4.34	Validation test of first plasma position estimation.	106

4.35	Validation test of positive plasma propagation delay.	107
4.36	Validation test of reconstructed density profile location compared with the round trip delay assuming propagation in vacuum.	108
5.1	Poloidal lines of sight of the different density profile diagnostics on ASDEX Upgrade. . . .	112
5.2	Comparing X-mode reflectometry density profiles with Li-beam and O-mode reflectometry in L-mode discharge #33523 with $B_T = -1.9$ T.	112
5.3	Comparing measured density profiles with Li-beam and O-mode reflectometry in H-mode discharge #33490 with $B_T = -2.5$ T.	113
5.4	Vertical displacement of a circular plasma in discharge #33830.	114
5.5	Probed plasma regions of the vessel for each plasma shape (left) and group delay mea- surements (right) of #34830 at each antenna.	115
5.6	Probed regions in the cross section and measured density profile evolution during dis- charge #34830 (right).	116
5.7	Three dimensional view of the reconstructed density profiles of channels 1, 4 and 8 for a vertical scan of a circular plasma in discharge #33830.	117
5.8	Density profile measurements in a discharge with low density and low magnetic field. The effects of gas puffing on the density profiles can be observed.	118
5.9	3D reconstruction of density profiles plasma measured with antenna 4 in a discharge with low magnetic field and low core density.	119
5.10	Density profile evolution during L-H transition of discharge #33232 measured using the three reflectometry channels and compared with the Lithium-beam density profiles. . . .	120
5.11	Effect of ELM events on the density profiles.	121
5.12	3D visualization of density profile evolution observed in the three reflectometry anten- nas during an ELM in discharge (divertor shunt current indicated by the solid black line) #33214 with 100 μ s time resolution.	122
5.13	a) Cross section view of the top, middle and lower divertor gas valve locations and embed- ded reflectometry channels. b) Simulated density profiles (dashed lines) at the mid height plane of the ICRF antenna #4 in sector 12 and experimental density profiles (solid lines) measured with channel 4 of embedded reflectometer, for different gas puffing locations. .	124
5.14	Poloidal convective cells associated with ICRF operation. The size of the convective cells is exaggerated.	125
5.15	Simulation of plasma density profiles during ohmic heating (OH, left) and ICRF operation (RF, middle) on ASDEX Upgrade. The density differences between OH and RF phases shows the resulting convective transport (right). Figures reproduced with permission from [30].	126
5.16	ICRF induced convective cells affecting localized density profile measurements during discharge #33520 with non-optimized power ratio between antenna straps.	127
A.1	Diagram of phase measurement in a quadrature detection system.	152

Nomenclature

ADC	Analog to digital converter
AM	Amplitude modulation
AUG	ASDEX Upgrade
BW	Bandwidth
CAD	Computer Aided Design
D-T	Deuterium-Tritium nuclear reaction
DAC	Digital to analog converter
DC	Direct Current
DEMO	DEMONstration Power Station
DL	Delay line
ECRF	Electron cyclotron range of frequencies
ECRH	Electron cyclotron resonance heating
FC	Fully connected layer in neural networks
FDTD	Finite difference time domain
FF	First fringe frequency
FFT	Fast Fourier Transform
FMCW	Frequency-Modulated Continuous Wave
FSR	Full scale range of an analog to digital converter
FT	Frequency translator
H-mode	High confinement mode
HFS	High magnetic field side
ICRF	Ion cyclotron range of frequencies

ICRH Ion cyclotron resonance heating

IF Intermediate frequency

IQ In-phase and quadrature components

ITER International Thermonuclear Experimental Reactor

JET Joint European Torus

L-mode Low confinement mode

LC X-mode lower cutoff

LFS Low magnetic field side

LHCD Lower Hybrid Current Drive

LO Local oscillator

LOS Line of sight

LSB Value of the least significant bit

MHD Magnetohydrodynamics

NBI Neutral beam injection heating

OH Ohmic Heating

PFC Plasma facing components

PLDRO Phase Locked Dielectric Resonant Oscillators

PLL Phase locked loop

PWM Pulse width modulation

RADAR Radio Detection And Ranging

ReLu Rectified Linear Unit activation

RF Radio frequency

RX Receiver

SNR Signal to noise ratio

SOL Scrape off layer

SSB Single side band

Tokamak Toroidal Kamera and Magnitaya Katushka

TX Transmitter or emitter

UC	X-mode upper cutoff
VNA	Vector Network Analyzer
WKB	Wentzel-Kramers-Brillouin

Chapter 1

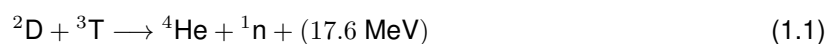
Introduction

World energy consumption will continue to increase in the next few decades. Today, the majority of the energy consumption still comes from unsustainable sources, resulting in the quick depletion of natural energy resources. To delay the upcoming energy crisis, large investments are being made in making the current production processes more efficient, and in expanding renewable energy production, such as solar, wind and hydro, and its storage [1]. This investment is apparently paying off since, despite energy consumption growing 1% in 2016, CO₂ emissions, the main contributor to the greenhouse effect, were only increased by 0.1% during the same period [2]. Developing and exploring new sources of clean energy is one of the main quests for the 21st century.

1.1 Thermonuclear fusion for energy production

Thermonuclear fusion is a reaction where two light atoms are fused together to form a heavier atom. This process releases energy, as the resulting mass is less than the original reactant's total mass. The released energy accelerates other atoms in the medium and contributes to a self-sustained nuclear fusion reaction, provided there is a source of light atom fuel. The excess thermal power produced by a well controlled nuclear fusion reaction may be harnessed to generate electricity, much in a similar way to existing nuclear and fossil fuel power plant systems.

From the known fusion reactions, the one between deuterium and tritium (D-T) in equation (1.1) is one of the easiest to obtain in laboratory conditions due to its higher reaction probability at a lower temperature. The result of this reaction is an ionized Helium atom, or α -particle, a neutron and energy release, which contribute to heating the remaining D-T fuel.



Deuterium is a stable hydrogen isotope that accounts for 0.015% of the natural hydrogen in our oceans. The abundance of this fuel source makes nuclear fusion power plants very attractive. Tritium, on the other hand, is a trace radioisotope with a half-life of approximately 12.3 years [3]. Nuclear fusion operation using D-T fuels does result in small radioactive waste, mainly due to the contamination

of reactor components with T and activation of the alloy materials. However, the reduced half-life of these contaminants makes nuclear fusion waste more manageable than the radioactive waste of nuclear fission reactors, which has half-lives of over a thousand years [4].

For a fusion reaction to occur, two ionized hydrogen isotopes must be accelerated to overcome their Coulomb barrier, the electrostatic repulsive force between both positively charged particles. However, simply accelerating beams of charged particles is not a reliable mechanism, since most of particles are scattered before undergoing fusion reaction. To make a sustained fusion reaction feasible, the probability of interaction must be increased by using a denser plasma medium and heating it to millions of degrees Kelvin [5].

Plasma is a quasi-neutral medium of positive and negative particles that exhibit a collective behaviour. In a plasma, the electric and magnetic fields generated by the movement of a particle interacts with those generated by the remaining particles inside the medium. Plasmas are ubiquitous in nature and exist in low temperature and density conditions, such as in interstellar space, and up to very hot and dense conditions, such as in the centre of stars. The high energy conditions in the cores of stars enables the nuclear fusion reaction of lighter elements, such as Hydrogen and Helium, to occur naturally.

In stars, the outwards thermal pressure resulting from their internal fusion reactions is balanced by their gravity force, in what is called gravity confinement. The size of stars is actually dependent on the output power of the reactions. However, confining a star in a laboratory setting on Earth is not feasible. The energetic particle release can easily damage or destroy the wall material of any container. Two major approaches for controlled nuclear fusion confinement are under research: inertial and magnetic confinement.

In inertial confinement, small dense D-T pellets are heated by laser beams. The laser energy explodes the outer shell, producing shock waves that compress the inner D-T target. Fusion ignition is reached by the fast compression of the nuclear fuel, contained only by its own inertia. A power plant using inertial confinement would adopt a pulsed operation, where the cyclic thermal power release would be harnessed by the reactor to produce electricity [6].

The second approach uses magnetic confinement to contain the fusion plasma. Magnetic fields can be used to confine the charged particles of the plasma and prevent them from running against the walls of the reactor vessel. Magnetic confinement devices may operate in a steady state regime. A simple device consists of a long solenoid structure which imposes an axial magnetic field. The magnetic field forces the charged particles to move in a circular motion around the field lines, restricting their radial movement. A magnetic mirror configuration is capable of trapping most of the charged particles at either end of the solenoids [5]. By reshaping the solenoid structure into a torus, the magnetic field lines are closed into each other, forcing the plasma into a toroidal shape.

The two most developed toroidal magnetic confinement devices are the Tokamak (*Toroidal Kamera and Magnitaya Katushka*) and the Stellarator. Several experimental tokamak and stellarator reactors are currently used for nuclear fusion research. At this time, the largest tokamak device is the Joint European Torus (JET) [7] in Oxfordshire, United Kingdom, and the largest stellarator is the Wendelstein 7-X [7] in Greifswald, Germany.

Despite over 50 years of research, we are yet to reach the break even point, where more energy is produced by the fusion reaction than what is used to heat the plasma. Overcoming the break even point and produce ten times the invested energy is the purpose of the ITER project. The ITER project is an international collaboration currently building the world's largest tokamak in Saint Paul-lez-Durance, southern France [8, 9]. The first plasma of ITER is expected to occur in 2025 and the first D-T reaction after 2030. A working electricity-producing fusion power plant prototype will be demonstrated with DEMO [10], which is predicted to start operation in the 2040s [11].

1.2 Tokamak experimental devices

The tokamak was first developed in the Soviet Union in the 1960s, as a way to magnetically confine the plasma, and is currently the most promising device for controlled nuclear fusion. The simple toroidal structure of the tokamak is illustrated in Figure 1.1. This toroidal vessel, with a shape similar to a donut, contains the hot plasma in a vacuum chamber. The vessel is surrounded by several D-shaped coils that generate the toroidal magnetic field B_ϕ used to confine the plasma column inside the chamber, preventing contact with the outer walls.

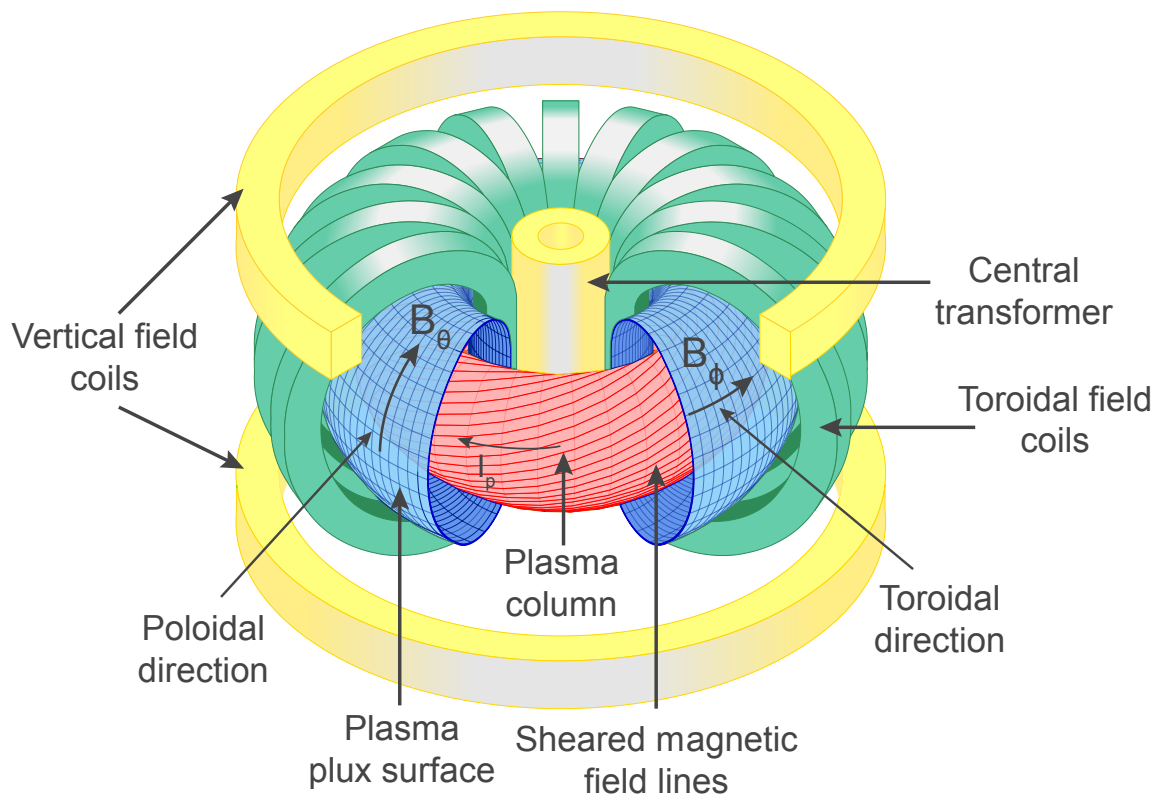


Figure 1.1: Essential components of a tokamak device.

The traditional operation of a tokamak works in a similar way to a transformer. To start the plasma, fuel gas, such as deuterium, is injected into the vacuum chamber and is partially ionized. An increasing current flows through the central transformer solenoid, acting as the primary of a transformer, while the

plasma column acts as the secondary. The toroidal electric field induced inside the chamber forces the plasma current I_p to flow around the torus.

Current flowing through the toroidal field coils generate the toroidal magnetic fields B_ϕ that confine the plasma column within the vessel. The plasma current, at the same time, induces a poloidal magnetic field B_θ . The combination of both the toroidal and poloidal fields result in sheared magnetic field lines with a certain pitch angle. Plasma ions and electrons are trapped to this field, orbiting along the helical field lines.

1.2.1 Heating the plasma

In a nuclear fusion reactor, part of the generated power is used to heat freshly introduced fuel. Using excess generated power to also generate electricity is the basic principle of future fusion power plants. However, the plasma must be heated by external methods during the start up phase of the reactor and to control the reaction. The gain factor Q of the reaction is determined by

$$Q = \frac{P_{DT}}{P_{heat}}, \quad (1.2)$$

where P_{DT} is the output power of the fusion reaction, mainly due to α -particle generation, and P_{heat} is the input power to heat the plasma [12].

In experimental tokamaks, multiple heating methods are used concurrently to achieve the required plasma temperatures for fusion. In future high Q factor devices, the excess power from the D-T reaction is expected to be sufficient to sustain the operation of the fusion reactor. The α -particle heating resulting from the D-T reaction has been demonstrated at JET, reaching gains up to 0.64, not yet reaching the break even point [12, 13].

Ohmic heating

Plasma, being an electrical conductor, can be heated by ohmic heating, using the central transformer to induce the plasma current. The generated ohmic heat depends on the induced current and on the plasma resistance, which is proportional to $T_e^{-3/2}$. However, as the temperature increases, the plasma resistance decreases and the ohmic heating efficiency is reduced. In addition, the saturation of the magnetic flux through the transformer limits the operation time of this type of heating. Ohmic heating is most useful to start up the reaction, but other heating methods must be used to further increase the temperature and maintain the plasma current [5].

Neutral beam injection heating

In neutral beam injection (NBI) the high energy of the launched neutral atom beam is transferred to the plasma particles through collisions. NBI is an efficient mechanism to directly heat the plasma particles. In addition, NBI provides current drive and toroidal rotation drive which contribute to sustaining the plasma for longer periods of time than possible using only ohmic heating [14, 15].

Wave heating

High frequency electromagnetic waves can be used to heat the plasma. The electromagnetic waves are generated outside the reactor and are launched towards the plasma. Depending on the correct frequency and wave polarization, the wave energy can be transferred to the charged particles in the plasma, which then collide with other plasma particles, increasing the bulk temperature.

Three main wave heating mechanisms have been applied successfully in current tokamaks. Waves in the ion cyclotron range of frequencies (ICRF), between 20 and 120 MHz, heat the bulk plasma ions by the resonant coupling of the wave power to the local plasma ion cyclotron frequency [16, 17]. In lower hybrid current drive (LHCD), waves with frequencies of 1-8 GHz, are damped strongly via Landau damping on electrons with a relatively high phase velocity. It can be used for driving current in low electron temperature conditions, such as in the start up phase, and also for off-axis current profile control in the steady-state and hybrid scenarios [18]. Finally, waves in the electron cyclotron range of frequencies (ECRF), 100-200 GHz, are able to precisely heat the electrons in the plasma core. Electron cyclotron resonance heating (ECRH) additionally provides the means to control some magnetohydrodynamics (MHD) instabilities and promote a soft plasma breakdown [19].

1.3 The ASDEX Upgrade experimental tokamak

This thesis work was developed for the ASDEX Upgrade experimental tokamak [20]. ASDEX Upgrade (Axially Symmetric Divertor EXperiment) is a midsize tokamak at the Max-Planck-Institut für Plasma-physik in Garching, Germany, that started operation in 1991.

Currently, the ASDEX Upgrade (AUG) programme is directed towards the study of critical elements for the ITER design and physics related to ITER operation. The plasma density, plasma pressure and wall loads and materials of AUG match the conditions of future fusion power plants, addressing the physics issues for a future DEMO design [21]. Research topics at AUG include: i) plasma transport, turbulence and instabilities; ii) divertor physics and power exhaust; iii) optimised plasma scenarios.

The AUG tokamak structure is illustrated in Figure 1.2. The vacuum vessel is held within a large toroidal steel structure. The complex arrangement of the D-shaped toroidal field coils, and vertical field, equilibrium and shaping coils, can be seen. Several ports provide access for heating and pumping systems, as well as diagnostics, from the top, mid plane outer wall, and bottom parts of the vessel.

Most of the plasma exhaust is directed along the field lines towards the divertor plates. Here the waste material and impurities from the fusion reaction can be pumped out during the discharge. Still, the heat shield limiters must be able to sustain stray heat loads from the plasma, such as during instabilities.

Due to its thermo-mechanical properties and low H-affinity, tungsten (W) is the most viable material for coating plasma facing components (PFC). ASDEX Upgrade has had a full-tungsten first wall and divertor plates since its 2007 experimental campaign [22]. A major drawback of W-coated PFC is the sputtering of tungsten atoms. These high-Z impurities may enter the plasma and cause radiative losses, eventually leading to accumulation and a degradation of the confinement. W accumulation can be

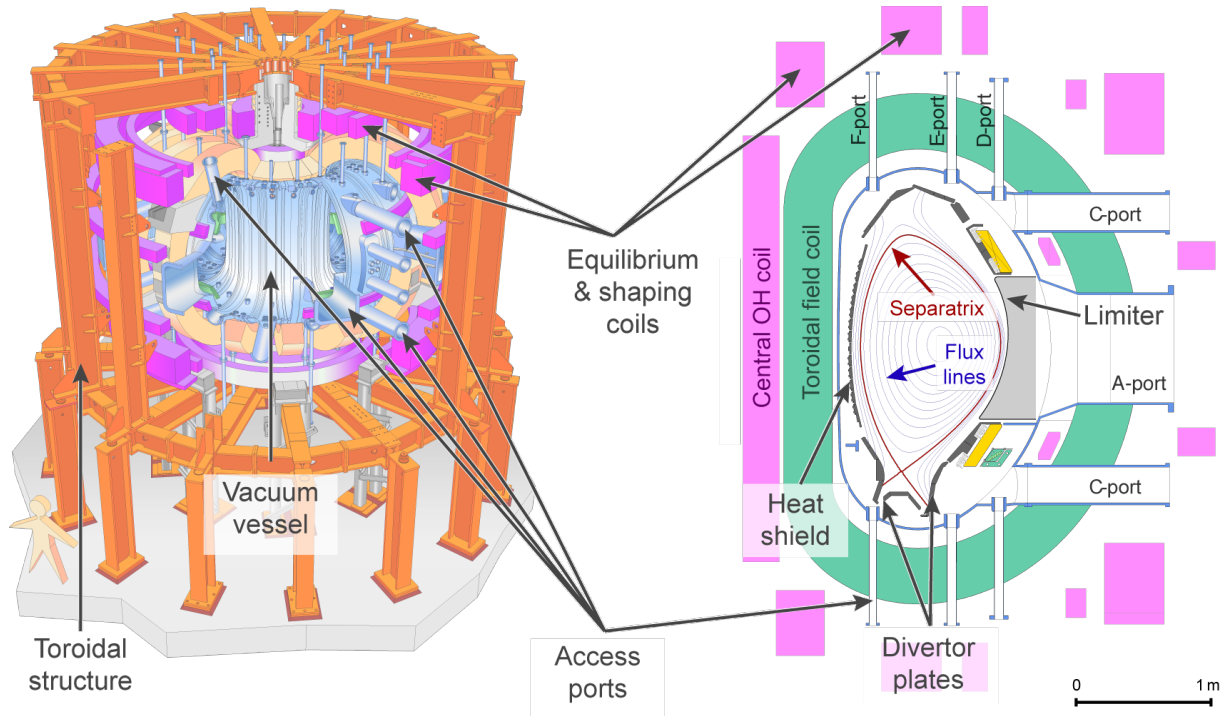


Figure 1.2: Main components of the ASDEX Upgrade tokamak at the Max-Planck-Institut für Plasma-physik in Garching, Germany

prevented by cooling the edge scrape off layer¹ (SOL) with gas puffing, which reduces W influx, or by heating the core plasma to promote W transport using central ECRH or ICRH.

While divertor conditions promote higher W erosion than other W sources in the main chamber, most contributions to the W content in the core plasma originate from increased sputtering of the wall material, such as due to ICRF heating operation.

1.4 Ion cyclotron resonance heating

Ion cyclotron resonance heating (ICRH) uses the ion cyclotron range of frequencies (ICRF) to heat the plasma. This mechanism provides the direct, more efficient, heating of the dominant ion population, leading to higher fusion reaction gain. In the standard ICRF heating scenario, there is a resonant interaction between the launched wave and a small concentration of ions in a plasma layer that efficiently absorbs the ICRF power at the fundamental cyclotron frequency. These ions then redistribute this energy collisionally to the electrons and ions in the plasma bulk [23].

The critical issues with ICRF operation are related to i) the heating efficiency, which depends on how RF waves propagate and are absorbed by the plasma; ii) and the plasma surface interactions, which require the study of the SOL region near the ICRF antenna [24].

While ICRH is the typical acronym used in fusion research for the ion cyclotron heating mechanism, the ICRF term is more common within the ion cyclotron research groups to refer to the range of frequencies. Plasma heating is the consequence of the efficient ICRF power absorption. In this thesis, both

¹Scrape off layer is the typical region between the separatrix and the vessel limiters.

terms are mentioned but refer to the same heating mechanism and can be interchanged for most cases.

1.4.1 ICRH operation principle

A single ion moving perpendicular to a magnetic field, $\vec{v} \perp \vec{B}$, describes a circular trajectory with an oscillating frequency determined by

$$\Omega_i = \frac{qB}{m_i}, \quad (1.3)$$

where q is the ion charge, B is the imposed magnetic field and m_i is the ion mass. An imposed oscillating electrical field, with the same frequency, accelerates the charged particle into a growing spiral orbit. At resonance, energy is transferred from the wave to the ion. This method can be applied to efficiently heat low density plasmas.

In dense plasmas with intense magnetic fields, such as on ASDEX Upgrade (densities typically above 10^{19} m^{-3} and magnetic fields up to 3 T), natural plasma oscillation occurs, called ion cyclotron waves. Plasma heating is possible by coupling ICRF power through the outer plasma boundary layers, to the absorption layer in the bulk plasma, using plasma waves [25].

Power coupling and heating efficiency

ICRF power coupling from the antenna to the bulk plasma where almost total absorption occurs has been shown to depend on the inhomogeneous plasma density profile. Figure 1.3 illustrates the different density regions that affect the coupling efficiency.

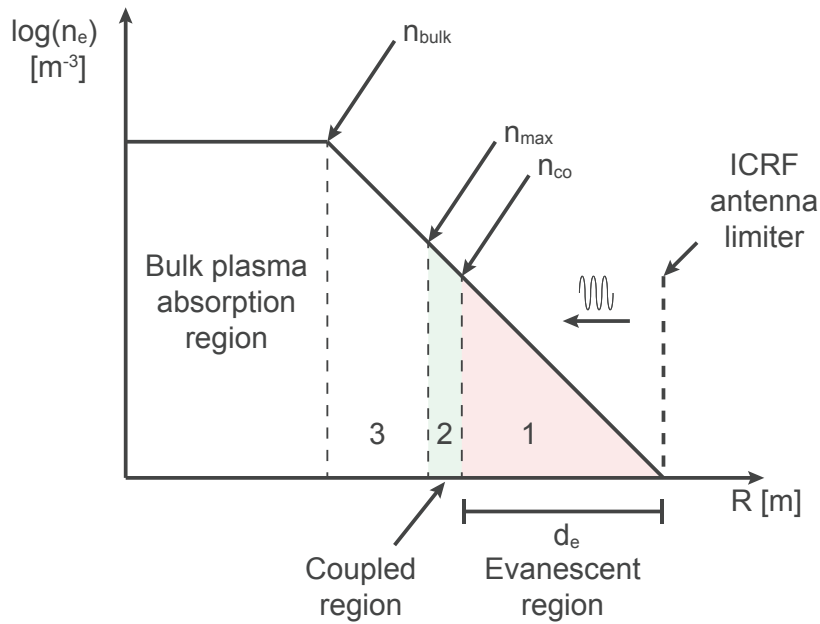


Figure 1.3: Plasma density profile regions for ICRF power coupling and absorption.

The launched ICRF waves must first transition through region 1, from the launching antenna up to

the cutoff density layer, proportional to the plasma frequency of the ion species, $n_{co} \propto (\omega_{pi}^2)_{co}$ [26]. The fast waves are evanescent in this region. The ICRF heating requires that the energy of the fast waves be transported from the launching antenna, through the evanescent layers, up to the region where they are absorbed. It has been observed that power coupling is highly sensitive to the width d_e of this evanescent region, which depends on the edge plasma density profiles. A wider evanescent region attenuates the power of the fast wave, reducing coupling efficiency. The fast wave propagates past the cutoff density layer n_{co} towards the plasma bulk, mainly transferring its energy to the plasma by resonant ion cyclotron absorption, where wave frequency is close to the ion cyclotron frequency (at n_{max}) or its harmonics [27].

Plasma surface interactions

RF rectification of the plasma potential at the edge is a well known occurrence during ICRF operation, which is associated with increased plasma surface interactions [28, 29, 30]. Electrons, being more mobile than the plasma ions, are accelerated towards the wall. To preserve quasineutrality, the plasma develops a negative DC sheath at the wall edge. This DC sheath results in two effects in the AUG SOL plasma region, illustrated in Figure 1.4: convective transport and sputtering of wall material [31].

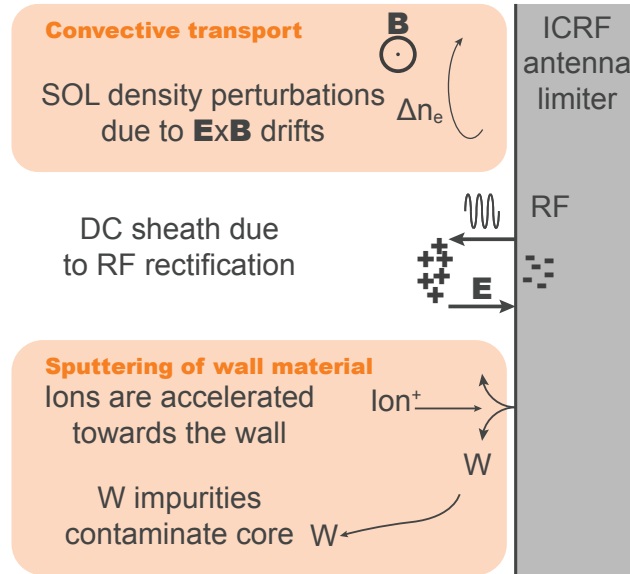


Figure 1.4: Plasma surface interactions due to ICRF operation on ASDEX Upgrade.

The plasma electrons experience $E \times B$ drifts in the SOL, forming convective cells, that displace the plasma density upwards. This convective transport changes the shape of the plasma electron density profile, which may alter the coupling of ICRF power to the plasma, reducing heating efficiency. The increased transport towards the wall may also lead to the formation of hot spots which deteriorate the wall material.

ICRF operation also typically increases core plasma W-impurity content on ASDEX Upgrade. Ions are accelerated in the rectified sheath towards the wall, sputtering the wall material. This wall material contaminates the plasma and, reaching the core, may lead to high radiative losses, eventually leading

to the disruption of the plasma.

1.4.2 ICRF heating system on ASDEX Upgrade

ASDEX upgrade is equipped with four ICRF antennas, allowing up to 8 MW of combined heating power. The ICRF heating system has been in operation since 1992. Power is supplied by four RF generators, which cover a frequency range between 30 MHz and 120 MHz, and can output up to 2 MW each at up to 80 MHz. The ICRF heating system uses antenna pairs, 1-3 and 2-4, which are mounted in the equatorial plane and located opposite to each other inside the vessel, as seen in Figure 1.5. Most recent ICRF antenna designs have arrays of straps to launch the ICRF waves. These strap conductors are surrounded by a limiter frame which protects the antenna elements and also serves as a plasma limiter [32]. The phase and amplitude of the strap currents can be individually controlled to excite the desired wave spectrum for the expected plasma conditions [33]. Antennas 1-3 have a two-strap design and boron (B) coated antenna limiters. ICRF antennas 2-4 adopt a new three-strap design with tungsten (W) limiter tiles. Covering the front of the antenna straps, as seen in Figure 1.6, is typically a Faraday shield or screen that filters out the electric fields parallel to the magnetic field.

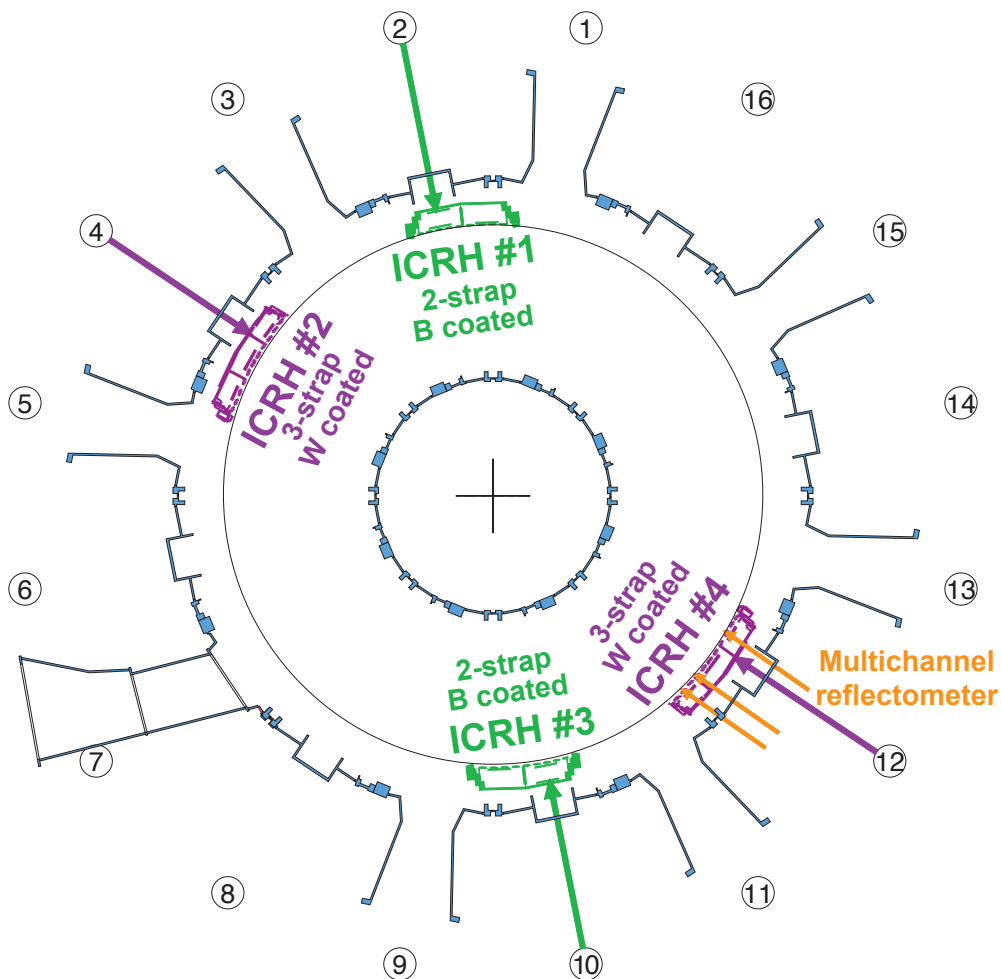


Figure 1.5: Toroidal location of ICRH antennas on ASDEX Upgrade.

The performance of an ICRF heating system depends on the correct coupling between the launching antenna and the inhomogeneous plasma profile in front of it. An incorrect matching of the ICRF system to the low impedance of the plasma load results in a considerable amount of power being reflected back towards the generator. The matching circuits on ASDEX Upgrade are fixed and are set before a discharge [34]. This makes the matching sensitive to fast plasma events such as the L-H transition² and edge localized mode (ELM) instabilities³ [34]. The ICRF system on AUG has undergone several upgrades to facilitate matching to the fast plasma events, including using 3 dB couplers to isolate the generators from reflected power due to a load mismatch [35]. For optimal performance of the ICRH system, a continuous and fast matching during operation is essential. A dynamic matching network using variable vacuum capacitors has been considered for AUG [36]. Additionally, the power coupling has been shown to depend on the phasing and power ratio between the individual antenna straps [26, 37, 38].

1.4.3 The need for a new ICRF antenna

The sputtering of the wall material due to ICRF operation results in the contamination of the discharge plasma and the long-term degradation of the PFC surfaces. The sputtering of high-Z impurities, such as tungsten on ASDEX Upgrade, contribute to increased radiation losses in the core plasma. Two approaches can be used to solve this increased impurity release: i) coating the antenna limiters with a low-Z alternative; ii) reducing the sheath potentials formed during ICRF operation through new ICRF designs. Figure 1.6 shows the evolution of the designs of the ICRF antennas on ASDEX Upgrade.

In 2011, the modified two-strap ICRF antenna 4, with broad limiters and narrow straps, provided a lower increase of W concentration during ICRH operation in AUG than the narrower limiters, allowing a more stable operation at lower gas puffing rate. Broadening the antenna limiters further increases the total area of the W coated PFCs in the vicinity of the ICRF antennas. Despite this, the modified antenna behaved better in terms of balance between the central plasma heating and as the source of W released during operation, showing a 40% reduction in W concentration increase. This improvement may have been compensated by the fact that broad limiters shadow the inside of the antenna from the long magnetic field line and parallel plasma flows. However, it does not explain whether the heating efficiency increased or the W sputtering decreased [39]. In 2012, the side limiters of ICRF antennas 1 and 3 were coated with a 50 μm layer of Boron, a low-Z material. These experiments showed that the side limiters are the dominant source of tungsten impurities [40]. In addition, the density convection induced by the typical antenna feeding configuration is largest with dipole phasing and 1:1 power ratio between straps [41].

The new three-strap ICRF antennas

A new three-strap antenna was designed with the help of the finite-elements EM calculations [39, 42, 43, 44]. The ICRF antennas 2 and 4 on ASDEX Upgrade were substituted by the new design and installed

²The L-H transition is the transition between the low and high confinement modes. Confinement is improved when heating is increased, resulting in steep gradient of the plasma density profile.

³ELMs are instabilities that occur due to the relaxation of the transport barrier in H-mode plasmas. There is an outwards burst of particles towards the wall, which may damage the PFCs and perturbs the density profile, reducing ICRF power.

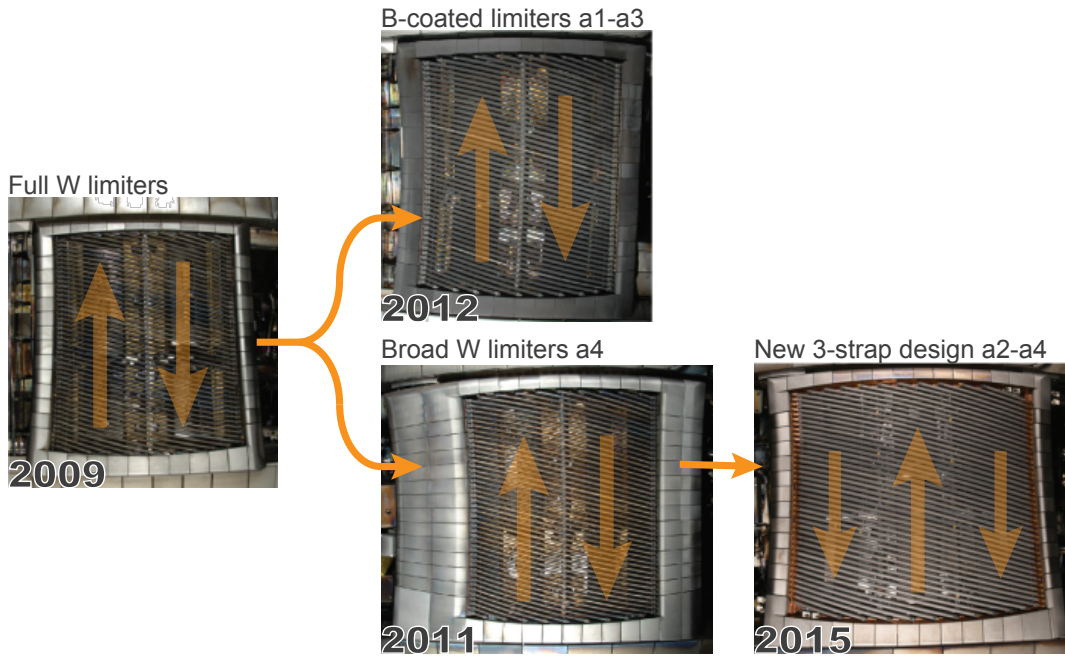


Figure 1.6: Evolution of the ICRF antenna designs on ASDEX upgrade and ICRF. The ICRF antenna is typically surrounded by the limiter structures, which prevent the rotating plasma from going into the antenna, and the oblique metal rods, in front of antenna straps, are the grounded Faraday protection straps. Vertical arrows indicate possible phasing of the individual antenna straps.

in 2015. The principle of this design consists in the minimization of the image currents by balancing the dipole-phased configuration of the contributions of the outer and inner straps through the control of the phase and power distribution. The outer antenna straps are narrowed to increase the distance between the straps and antenna limiter, hence, minimizing the negative impact of the antenna loading. Larger antenna surfaces, were introduced behind the Faraday screen, providing lower impedance and to cancel out the RF image currents.

Embedded reflectometry diagnostic

Measuring the density profiles of the plasma layers in front of the ICRF antennas, during operation, has long been considered useful for the study of local plasma interactions and power coupling. However, the study of these regions required the use of remote diagnostics that were connected along the magnetic field lines. Lithium-beam diagnostics [45], reflectometry diagnostics [46] and reciprocating Langmuir probes [47] have been used for electron density profile measurements on ASDEX Upgrade.

The new three-strap antenna design includes ten access points for a reflectometry diagnostic, which look at the plasma from different toroidal and poloidal locations. Reflectometry is a non-perturbing diagnostic method that uses microwaves to measure plasma density profiles and plasma turbulence. The reflectometry measurement has high temporal and radial resolutions and is not affected by ICRF operation. The diagnostic also has a small access footprint, requiring only small microwave antennas and waveguide routing, making it a viable option to be embedded inside the larger ICRF antenna design.

A new multichannel reflectometry diagnostic was designed and implemented to take advantage of the multiple embedded access points of the new ICRF antenna 4. The location of this new diagnostic inside the vessel can be seen in Figure 1.5.

International collaboration

The new three-strap ICRF antenna design and embedded reflectometry diagnostic were developed as part of an international collaboration between the Max-Planck-Institut für Plasmaphysik from Garching, Germany, ENEA from Frascati, Italy, ASIPP from Heifei, China, and Instituto Superior Técnico from Lisbon, Portugal [48], and the project was funded by the EUROfusion consortium. Figure 1.7 shows part of the large team involved in the design and installation of the new three-strap ICRF antenna and development of the embedded reflectometry diagnostic.

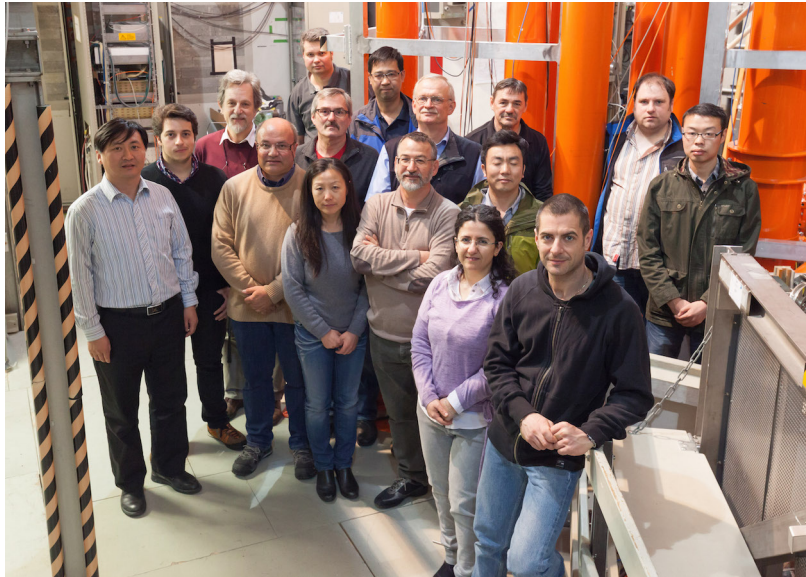


Figure 1.7: Part of the team involved in the design and installation of the new three-strap ICRF antenna and embedded reflectometer (April 2015).

1.5 Objectives of this work

This work is focused on the implementation and commissioning of a new multichannel microwave reflectometry diagnostic embedded on the new three-strap ICRF antenna 4 on ASDEX Upgrade. The main purpose of this diagnostic is to measure the local edge density profile evolution during ICRF operation to aid in the study of plasma interactions and ICRF power coupling. However, other physics studies, such as edge turbulence or poloidal variations, can take advantage of the multichannel topology of this diagnostic. To provide confidence in the density profile measurement data and become a useful addition to the ASDEX Upgrade diagnostic environment, the implementation, calibration and commissioning must be thoroughly and transparently validated. The objectives of this work are:

- Implement a new X-mode microwave reflectometry diagnostic system for edge density profile measurements.
- Commission the diagnostic to ensure reliable operation under most conditions on ASDEX Upgrade.
- Develop and validate automatic X-mode density profile reconstruction codes.
- Contribute to ICRF operation studies with validated density profile measurements.

1.6 This thesis

The structure of this thesis is organized as follows:

Chapter two details the basic principles of microwave reflectometry diagnostics used for fusion plasma measurements.

The design and implementation of the multichannel embedded reflectometer is described in chapter three. The reflectometer microwave architecture and design trade-offs are presented.

Then, the commissioning of the diagnostic is detailed in chapter four. The commissioning and validation of this new diagnostic is the main focus of this work. In this chapter, the raw signal processing algorithms and assumptions are presented, with emphasis on the analysis of the sources of error for density profile reconstruction.

Chapter five presents experimental density profile results obtained with this diagnostic. These results show off the capabilities of the diagnostic in measuring typical plasma phenomena. The measured density profiles have been used in ICRF operation studies: simulations of power coupling under different gas puffing conditions were corroborated experimentally; and the convective transport due to RF rectification was observed experimentally using direct reflectometry measurements.

The final discussion, conclusions and future work are presented in chapter six.

The list of scientific contributions that derived from this work is presented in chapter seven.

Chapter 2

Microwave reflectometry

Reflectometry measurement techniques are based on the reflection of waves on surfaces or interfaces to characterize objects or structures. While reflectometry techniques have been widely used in ionosphere plasma diagnostics for decades, their use in measuring plasma electron density in laboratories was only first proposed in 1961 [49]. However, it was only after recent technological advances in microwave sources and data acquisition systems, that reflectometry was considered a feasible and important diagnostic for fusion plasmas.

The reflectometry measurement in plasmas is similar to a radar technique and depends on the propagation of an electromagnetic wave through the plasma, up to a cutoff layer where the index of refraction goes to zero and the wave is reflected. The frequency and round trip delay of this wave can give us information of the distance of the reflection and the dielectric plasma medium [50].

In this chapter we first analyse the propagation of waves in plasmas to better understand the effects, cutoffs, polarizations and propagation modes. Then we describe how these are applied in reflectometry techniques for the measurement of plasma features, such as electron density profiles. Finally we present different system architectures for reflectometry diagnostics and the requirements for signal processing analysis.

2.1 Propagation of waves in plasmas

To understand wave propagation in plasmas we first describe the plasma medium. Plasma is a hot gas of charged particles: ions and electrons. Electrons are attracted to the positive charges and repel other electrons. As the electrons are more mobile than ions (the protons are around 1836 times heavier than electrons), they rearrange themselves around the plasma to maintain quasineutrality of the plasma medium.

In a nearly neutral plasma equilibrium, a small perturbation of the electrons is compensated by Coulomb force interactions with the remaining charged particles. This originates small oscillations of the charge density. By ignoring the thermal motion of electrons, the electrons oscillate at the plasma

electron frequency

$$\omega_{pe} = 2\pi f_{pe} = \sqrt{\frac{n_e e^2}{m_e \epsilon_0}}, \quad (2.1)$$

where e is the electron charge, n_e is the plasma electron density, m_e is the effective mass of the electron and ϵ_0 is the vacuum permittivity. For typical edge electron densities on ASDEX Upgrade of $1 \times 10^{19} \text{ m}^{-3}$ the plasma electron frequency is approximately 28 GHz.

In the presence of a magnetic field B , the electrons describe an orbital motion with a gyrofrequency [5, 51]. This gyrofrequency is given by

$$\Omega_{ce} = 2\pi f_{ce} = \frac{eB}{m_e}. \quad (2.2)$$

For the typical core magnetic field of 2.5 T on ASDEX Upgrade, the electron cyclotron frequency varies from approximately 70 GHz at the core and 55 GHz at the edge.

A few considerations are now made to further analyse the propagation of waves in fusion plasmas. First we assume the *cold plasma approximation*, in which the thermal oscillations of the plasma are negligible compared to the frequency of the waves. We also assume that the ions are static to the wave perturbations, due to their high inertia at the wave frequency (GHz, microwave range). The plasma medium acts as a dielectric to the wave. When using a plasma slab model, we assume that the plasma is inhomogeneous but its dielectric constant varies only in the direction of propagation of the wave. When waves propagate through an inhomogeneous medium or across the boundaries between different media, they may be absorbed, reflected or refracted [52, 53].

Figure 2.1 shows the inhomogeneous plasma slab model approximation for microwave propagation in typical fusion plasmas with toroidal magnetic field. While several different waves can propagate in a magnetized plasma, only electromagnetic waves propagating into the plasma, perpendicular to the magnetic field ($\vec{k} \perp \vec{B}$), are analysed in this work. The geometry of the microwave probing, illustrated in the Figure 2.1, propagating from the wall towards an increasing electron density and magnetic field strength, makes electromagnetic waves the most interesting for reflectometry measurements.

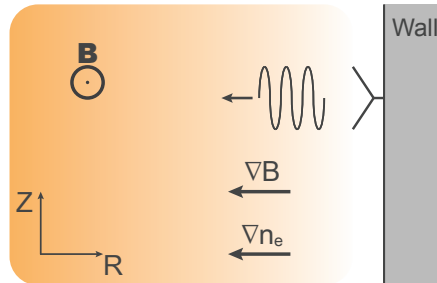


Figure 2.1: Electromagnetic waves propagating in a fusion plasma slab model with a magnetic field gradient.

Using these assumptions, we may analyse the dispersion relation of waves propagating in plasmas with and without magnetic fields using Maxwell's equations, which describe the behaviour of electro-

magnetic fields [54]. Gauss's law relates the electric displacement field \vec{D} [C/m²] in a volume with the electric charge density ρ [C/m³] inside

$$\nabla \cdot \vec{D} = \rho. \quad (2.3)$$

Gauss's law for magnetism states that magnetic flux density \vec{B} [Wb/m²] lines must be closed as there are no magnetic monopoles

$$\nabla \cdot \vec{B} = 0. \quad (2.4)$$

Faraday's law of induction states that the electric field \vec{E} [V/m] induced in a closed loop is proportional to the variation of the magnetic flux density \vec{B} inside the loop

$$\nabla \times \vec{E} = -\frac{\partial \vec{B}}{\partial t}. \quad (2.5)$$

Ampère's law, on the other hand, states that the magnetic field \vec{H} [A/m] induced around a closed loop is proportional to the sum of the electric current \vec{J} [A/m²] and the electric displacement field \vec{D} rate through the loop

$$\nabla \times \vec{H} = \vec{J} + \frac{\partial \vec{D}}{\partial t}. \quad (2.6)$$

The magnetic field strength \vec{H} and electric displacement field \vec{D} are related to the medium properties as

$$\vec{B} = \mu_0 \mu_r \vec{H}, \quad (2.7)$$

$$\vec{D} = \epsilon_0 \epsilon_r \vec{E}, \quad (2.8)$$

where $\mu_0 = 4\pi \times 10^{-7}$ [H/m] is the magnetic permeability in vacuum, μ_r the relative magnetic permeability of the medium, $\epsilon_0 = 8.854 \times 10^{-12}$ [F/m] is the dielectric constant in vacuum and ϵ_r is the relative dielectric constant of the medium.

To solve the Maxwell equations for the propagation of waves in plasmas, the *Wentzel-Kramers-Brillouin* (WKB) approximation is typically used. The WKB approximation is a method of solving linear differential equations, by considering only energy potentials as the coupling mechanisms for the interactions that occur during wave propagation along each infinitesimal small width layer of the plasma [55].

2.1.1 Electromagnetic waves in unmagnetized plasmas

Consider an homogenous plasma with no imposed magnetic field ($B = 0$). The refraction index observed by a wave propagating in an unmagnetized plasma can be derived from the Maxwell's equations and using the fluid approximation. The fluid approximation considers the plasma as two interpenetrating fluids: an electron fluid and an ion fluid [51].

As the wave propagates through the plasma, the perpendicular electric field of the wave induces a small perturbation in the plasma electrons, which results in a Lorentz force, dependent on the magnetic field, given by

$$\vec{F} = q \left(\vec{E} + \vec{v} \times \vec{B} \right), \quad (2.9)$$

where \vec{v} is the velocity of the perturbed electrons. As there is no magnetic field, the particles move to the tune of the electric field. By taking the plane wave solution from the Maxwell set of equations [5, 51], we obtain the electromagnetic dispersion relation

$$\omega^2 = k^2 c^2 + \omega_{pe}^2. \quad (2.10)$$

The index of refraction N of the plasma medium

$$N \equiv \frac{ck}{\omega} = \sqrt{1 - \omega_{pe}^2/\omega^2}, \quad (2.11)$$

is only dependent on the wave frequency and on the plasma electron density n_e

$$N = \sqrt{1 - \frac{n_e e^2}{m_e \epsilon_0} \frac{1}{\omega^2}}. \quad (2.12)$$

For wave frequencies lower than the plasma frequency ($\omega < \omega_{pe}$), N is imaginary and the wave becomes evanescent. The wave amplitude decays exponentially in the skin depth, c/ω_{pe} , of the plasma [52].

The cutoff condition occurs when $\omega = \omega_{pe}$. In this case, the refractive index goes to zero, corresponding to a reflection of the wave at the plasma layer with critical density. This allows determining the density of the plasma layer where the wave is reflected, from the frequency of the probing wave, and is the principle of reflectometry measurements.

2.1.2 Propagation modes of electromagnetic waves in magnetized plasmas

Turning now to the case of fusion plasmas in tokamaks, we analyse propagation of electromagnetic waves in plasmas with an imposed magnetic field. Consider the simple case of an homogenous plasma but with an imposed external magnetic field ($\vec{B}_0 \neq 0$). Using the plasma slab model approximation for fusion plasmas, previously shown in Figure 2.1, we study only electromagnetic waves travelling radially from the wall, perpendicular to the toroidal magnetic field ($\vec{k} \perp \vec{B}_0$). The magnetic field contribution to the plasma electron perturbation must be considered in this regime.

In these conditions, the propagation mode of the waves is classified according to its polarization with respect to the imposed magnetic field \vec{B}_0 . The electric field may be parallel, such that $\vec{E} \parallel \vec{B}_0$, and the wave propagates in the ordinary mode (O-mode). In the perpendicular alignment, such that $\vec{E} \perp \vec{B}_0$, the wave propagates in the extraordinary mode (X-mode). The propagation modes are illustrated in Figure 2.2, where the magnetic field is aligned in the toroidal ϕ direction and the waves propagate along R.

The polarization of a launched wave depends on the alignment of the launching microwave antenna. In tokamaks, the imposed magnetic field is the sum result of the poloidal and toroidal magnetic fields. The average pitch angle of the magnetic fields on ASDEX Upgrade is approximately 15° , and reflectometry antennas are aligned according to this angle. An oblique alignment between the wave's electric field and the imposed magnetic field results in two partial orthogonal components, each propagating in

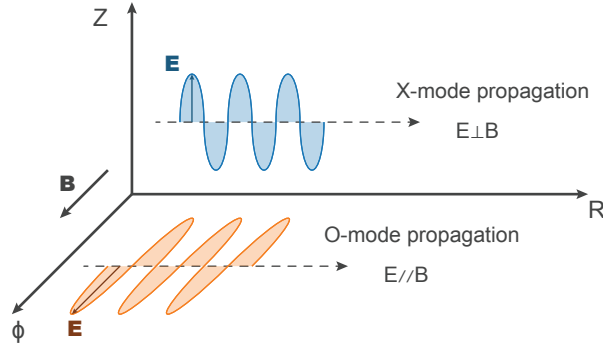


Figure 2.2: Ordinary and extraordinary modes of propagation in magnetized plasmas.

the O- or X-modes.

Ordinary mode

In the ordinary mode, the electric field of the wave is parallel to the imposed magnetic field. In this mode, the small plasma perturbations that arises due to the electric field are also parallel to the magnetic field. As such the $q\vec{v} \times \vec{B}$ force vanishes and the set of equations is reduced to the equivalent equations for an unmagnetized plasma [51]. The dispersion relation for the ordinary waves is then

$$\omega^2 = k^2 c^2 + \omega_{pe}^2, \quad (2.13)$$

$$N_O^2 \equiv \frac{c^2 k^2}{\omega^2} = 1 - \omega_{pe}^2 / \omega^2. \quad (2.14)$$

We can observe that the dispersion relation for the ordinary mode N_O is equal to dispersion relation in an unmagnetized plasma: O-mode waves are not affected by the magnetic field.

O-mode waves can be used in reflectometry to reflect at any density layer where the probing wave frequency f_p matches local plasma electron frequency

$$f_p = f_{pe} = \sqrt{\frac{n_e e^2}{4\pi m_e \epsilon_0}}. \quad (2.15)$$

However, reflecting at the lowest densities requires probing at frequencies lower than the typical microwave bands used in fusion reflectometry diagnostics. In addition, the validity of the WKB approximation, used for density profile reconstruction, depends on the inhomogeneity scale length L and the probing wavelength in vacuum λ . Large wavelengths, when probing low electron densities, can not probe small scale lengths, such as the case of large density gradients, making O-mode unsuitable to probe the low density plasmas [56].

Extraordinary mode

In the extraordinary propagation mode, the waves have a linear polarization, with an electric field perpendicular to the imposed magnetic field. For the cold plasma approximation, only the fundamental cyclotron frequency is considered in the X-mode dispersion relation, which is given by

$$N_X^2 \equiv \frac{c^2 k^2}{\omega^2} = 1 - \frac{\omega_{pe}^2}{\omega^2} \frac{\omega^2 - \omega_{pe}^2}{\omega^2 - (\omega_{pe}^2 + \Omega_{ce}^2)}, \quad (2.16)$$

where ω_{pe} is the plasma electron frequency and Ω_{ce} the electron cyclotron frequency [51].

The extraordinary mode has two relevant properties, the cutoffs and resonance. A cutoff occurs when $N_X \rightarrow 0$, and resonances occur for $N_X \rightarrow \pm\infty$. A resonance occurs at

$$\omega = \omega_{UH} = \sqrt{\omega_{pe}^2 + \Omega_{ce}^2}, \quad (2.17)$$

which corresponds to the upper hybrid frequency. In a real finite temperature (warm) plasma, kinetic effects also lead to resonances at the fundamental electron cyclotron frequency $\omega = \Omega_{ce}$ for O-mode, and at the 2nd harmonic, $2\Omega_{ce}$, for X-mode perpendicular propagation [57, 58]. The cutoff condition has two solutions, ω_R and ω_L

$$\omega_L = \sqrt{\omega_{pe}^2 + \frac{\Omega_{ce}^2}{4}} - \frac{\Omega_{ce}}{2}, \quad (2.18)$$

$$\omega_R = \sqrt{\omega_{pe}^2 + \frac{\Omega_{ce}^2}{4}} + \frac{\Omega_{ce}}{2}. \quad (2.19)$$

In X-mode reflectometry, these two cutoffs are referred to the lower (LC) and upper cutoff (UC) regions, which depend on both the local density n_e and the local magnetic field B

$$f_{LC} = \sqrt{f_{pe}^2 + \frac{f_{ce}^2}{4}} - \frac{f_{ce}}{2} = \sqrt{\frac{n_e e^2}{4\pi m_e \epsilon_0} + \left(\frac{eB}{4\pi m_e}\right)^2} - \frac{eB}{4\pi m_e}, \quad (2.20)$$

$$f_{UC} = \sqrt{f_{pe}^2 + \frac{f_{ce}^2}{4}} + \frac{f_{ce}}{2} = \sqrt{\frac{n_e e^2}{4\pi m_e \epsilon_0} + \left(\frac{eB}{4\pi m_e}\right)^2} + \frac{eB}{4\pi m_e}. \quad (2.21)$$

Both regions can be used in reflectometry measurements. The upper cutoff region has the advantage that the cutoff for the zero density occurs at the local electron cyclotron frequency. For high magnetic fields, the zero density reflection happens for a probing frequency within typical microwave bands, allowing accurate reflectometry measurements without initializations.

Dispersion relation of the electromagnetic modes of propagation

Figure 2.3 shows the squared dispersion diagram for both O- and X-mode waves for a given plasma density and magnetic field. Waves propagate in the region where $N^2 > 0$, and are evanescent for $N^2 < 0$. The cutoff reflections occur when $N^2 = 0$, for each of the modes. Typically, the wave propagates freely in the pass band for frequencies higher than the respective mode cutoff, except at the upper hybrid resonance ω_{UH} where $N^2 \rightarrow \pm\infty$.

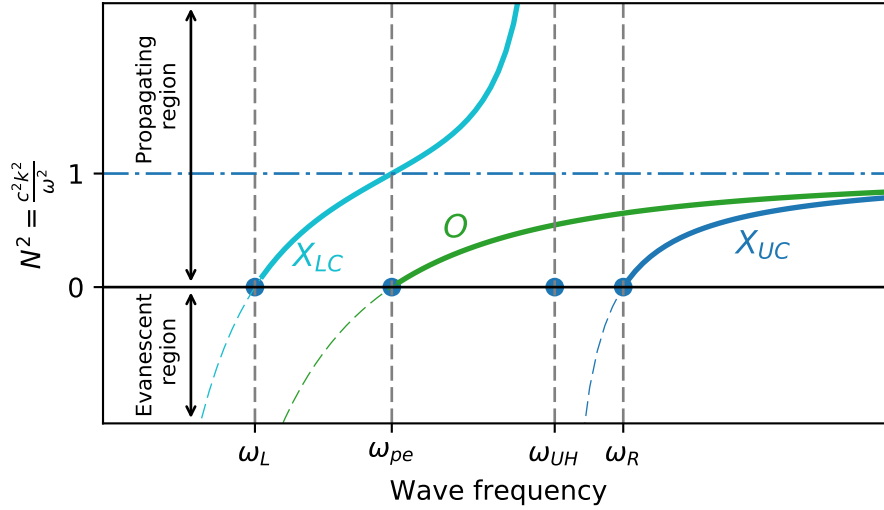


Figure 2.3: Dispersion diagrams for X-mode and O-mode.

2.1.3 Electromagnetic wave cutoffs in fusion plasma

In a typical fusion experiment, the plasma is present within the inner and outer limiters of the vessel, as exemplified in Figure 2.4. There is an electron density profile that has a maximum at the core and a minimum at the limiter walls. In addition, the imposed magnetic field is generated at the center of the machine and has a profile with radially decreasing strength. For this reason, the inner wall is often called the high field side (HFS) while the outer wall corresponds to the low field side (LFS).

The plasma is contained by the magnetic field, within the closed magnetic flux lines, where it revolves around the torus. The last closed magnetic flux line is called the separatrix, indicating the limit of the contained plasma. The region outside the separatrix is called the scrape off layer. This region has a high density gradient, due to the lower confinement and the edge plasma particles being lost to the wall.

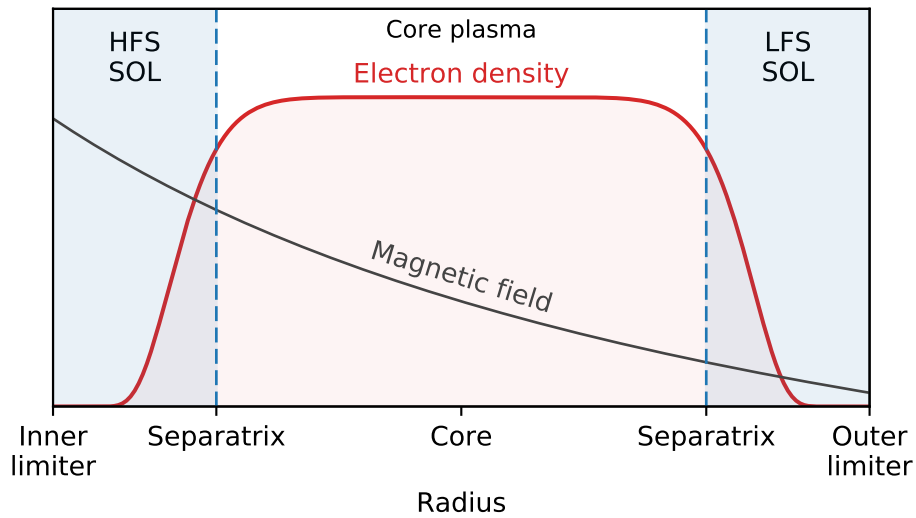


Figure 2.4: Nomenclature of fusion plasma regions.

In microwave reflectometry, a probing wave is launched from the wall into the plasma and reflected at a specific cutoff layer. This cutoff condition depends on the local plasma density, the local magnetic field and the polarization of the wave. In fusion plasmas, the cutoff conditions vary continuously inside the vessel. Typical electron density and magnetic field profiles on ASDEX Upgrade can be observed in Figure 2.5 (top). These have a core electron density of $7 \times 10^{19} \text{ m}^{-3}$ and 2 T magnetic field. These values are taken at the core, which corresponds to the radial middle of the vessel at $R \approx 1.65 \text{ m}$.

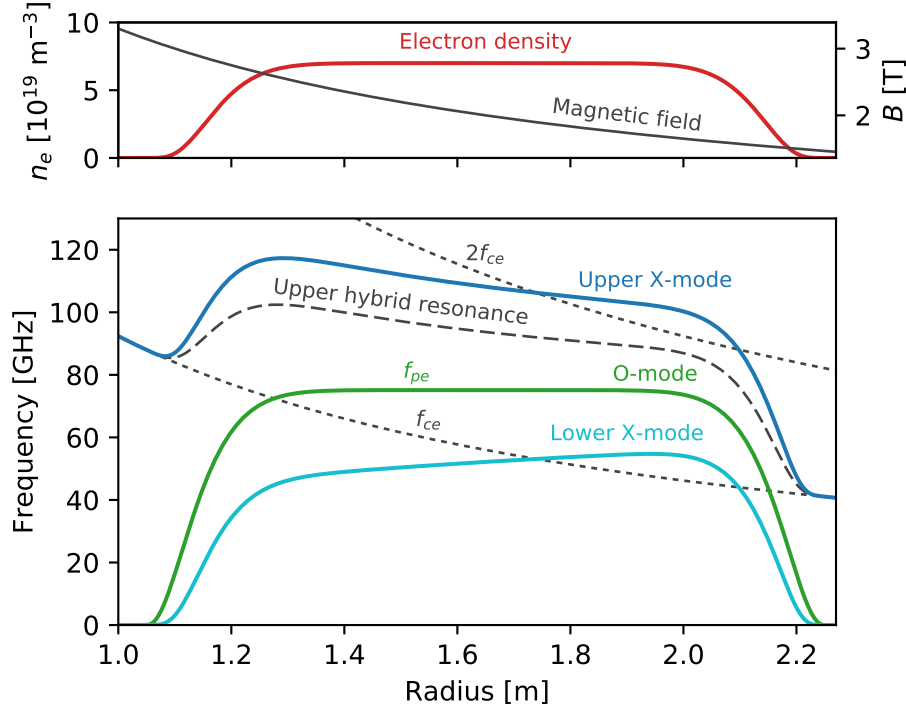


Figure 2.5: cutoff frequencies for a typical ASDEX Upgrade plasma with 2 T magnetic field and $7 \times 10^{19} \text{ m}^{-3}$ electron density.

The cutoffs for O-mode and the two X-mode regions are represented in Figure 2.5 (bottom). The O-mode cutoff occurs at the local plasma electron frequency f_{pe} , depending only the plasma density profile and the frequency of the probing wave. The X-mode cutoffs are additionally influenced by the local magnetic field. The electron cyclotron frequency f_{ce} , its second harmonic, and the upper hybrid resonance are also shown.

A reflectometry probing wave, launched from the outer wall on the right hand side, is going to be reflected at the first cutoff positions it encounters, depending on wave polarization. Waves with frequencies close to the resonance may get absorbed within the narrow absorption region. The $2f_{ce}$ harmonic poses a problem for X-mode propagation from the outer region as it may absorb the probing waves around 82 GHz and above 105 GHz, for these conditions, before reaching the cutoff reflection useful for reflectometry measurements.

The polarization of the wave is dependent on the orientation of its electric field and the sheared magnetic field inside the tokamak. The electric field of the fundamental TE_{10} (transverse electric) mode in a rectangular waveguides is aligned with the shorter edge of the waveguide. This means that O-

mode and X-mode waves must either have dedicated fundamental mode waveguides or share the same circular waveguide, which allows multiple wave polarizations.

Either propagation mode can be used to probe the plasma edge density layers. X-mode reflectometry has the advantage of using the upper cutoff to probe the widest density regions, from the near zero density at the edge up to the flat density region at the plasma core. However, this is not always practical due to the multiple microwave band requirements to accommodate such a broadband probing signal. A combination of both O-mode and X-mode measurements may be used to probe different regions of the plasma to reconstruct the density profile [56, 59].

2.2 Microwave reflectometry diagnostics for fusion plasmas

As described in the previous section, electromagnetic waves can be used to probe fusion plasmas using reflectometry techniques. The waves are launched into the plasma, propagating through it as long as the local plasma electron density is lower than the respective cutoff density for the propagating wave. Then, at this critical density layer, the wave is reflected and the reflection is detected by the reflectometry system. The density of the reflection layer can be estimated from the probing wave frequency. Reflectometry diagnostics are traditionally used for density profile and density fluctuation measurements [60]. New applications include plasma rotation measurements and turbulence imaging [50, 61]. However, this work is focused on reflectometry measurements for density profile reconstruction.

2.2.1 Measurement principle

A reflectometry diagnostic measures the delay of the microwave echo to determine the distance to the reflecting surface. In typical RADAR applications, the reflecting surfaces are far from the diagnostic, and the delay accuracy is mainly dependent on the time resolution of the acquisition method. In a tokamak, the delay corresponds to the round trip of the wave propagating through the plasma medium, which is usually only a few nanoseconds due to the proximity of the reflecting surfaces to the reflectometry antennas.

In reflectometry, the wave delay is measured from the phase difference of the probing wave and a reference wave. The probing wave, with a given frequency f , is phase shifted as it propagates through the plasma medium with a varying refractive index N . In tokamak plasmas, this phase shift ϕ can be approximated to

$$\phi(f) = \frac{4\pi f}{c} \int_{r_0}^{r_c} N(f, r) dr - \frac{\pi}{2}, \quad (2.22)$$

where r_0 is the launching position, r_c is the cutoff layer [60]. The total phase shifts of individual probing waves with different frequencies f are illustrated in Figure 2.6.

In practical terms, the reflectometry system captures the temporal evolution of the interference signal between the reflection and the reference waves

$$sig(t) = A \cos(\varphi(t)), \quad (2.23)$$

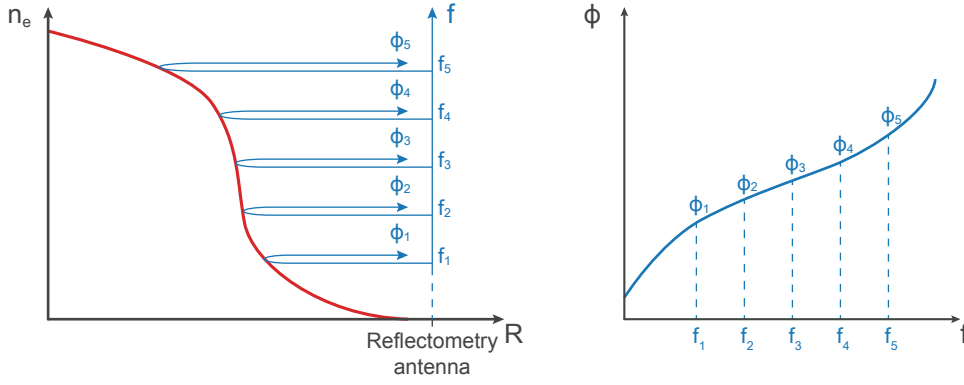


Figure 2.6: Phase shift of probing waves with different frequencies.

where A is the reflection signal amplitude, which is attenuated by the plasma medium, and $\varphi(t)$ is proportional to the difference of the probing wave phase ϕ_p and the reference wave phase ϕ_{ref} , and may have a temporal variation. The phase variation of the probing wave may be the result of the variation of the optical path length, such as in turbulence measurements, or a varying probing wave frequency, such as in the case of density profile measurements.

Constant frequency measurements

Consider a probing wave with a constant frequency which is reflected at a cutoff layer. In O-mode reflectometry, for example, the reflection occurs at the critical density layer. If the cutoff layer is displaced inwards or outwards, the phase shift of the probing wave varies accordingly. This method is useful for density fluctuation measurements, such as illustrated in Figure 2.7, where plasma turbulence displaces the cutoff layer within ΔR along the propagation direction of the probing wave. Here, the phase measurement $\phi(t)$ is modulated by the variation of the optical path length.

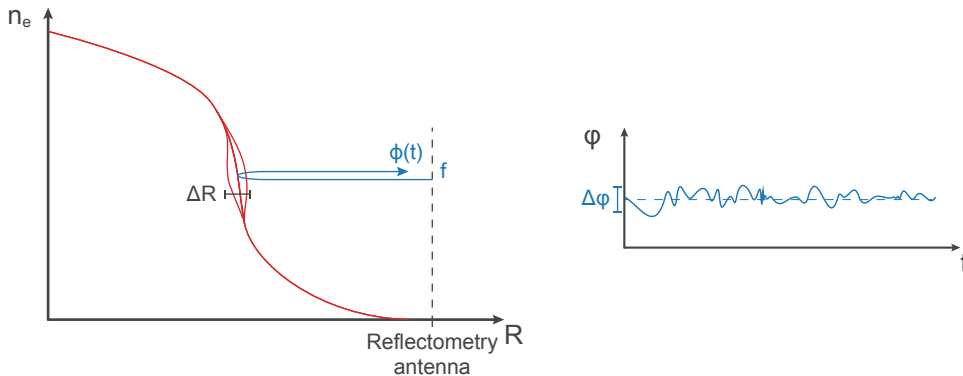


Figure 2.7: Phase measurement of a reflectometry interference signal with constant frequency in a turbulent plasma.

This example is a simple case of fluctuation measurements assuming a stratified plasma slab model.

Fluctuation measurements become more complicated when the multidimensional structure of a tokamak plasma is considered [60].

Varying frequency measurements

By varying the frequency of the probing wave, different cutoff layers of the plasma can be probed. As the cutoff condition depends on the local density, measuring the group delays for multiple probing frequencies allows the reconstruction of the density profile of the plasma along the propagation path, as illustrated in Figure 2.8.

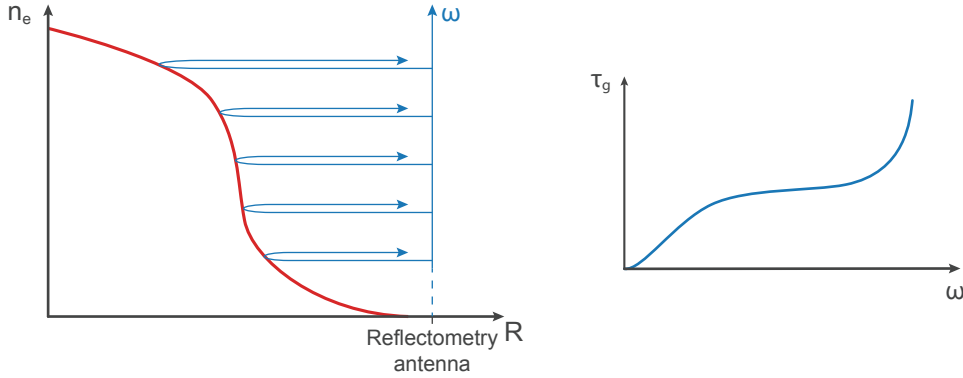


Figure 2.8: Expected group delay measurement of a reflectometry signal with swept probing frequency, in O-mode or X-mode lower cutoff.

2.2.2 Swept reflectometry for density profile measurements

Density profile reflectometry may use a frequency-modulated continuous wave (FMCW) to probe the plasma. In this method, a microwave oscillator sweeps the frequency of the probing band within the frequency range of interest. The acquired reflectometry signal is obtained by mixing the reflected wave with a synchronized reference. This beat signal is given by the phase variation of the reflected signal $d\phi(\omega)/d\omega$. For each probing frequency, τ_g is determined by

$$\tau_g(f) = \frac{1}{2\pi} \frac{d\phi}{df} = \frac{1}{2\pi} \frac{d\phi}{dt} \left(\frac{df}{dt} \right)^{-1} = f_b \left(\frac{df}{dt} \right)^{-1}, \quad (2.24)$$

where f_b is the beat frequency of the acquired reflectometry signal and df/dt is the frequency sweep rate of the oscillator. The sweeping time must be very short, shorter than plasma fluctuation timescales of 100 μ s, in order to probe a mostly static snapshot of the plasma density profile and reduce the effects of density fluctuations on the measurement. As in radar applications, the reflectometry measurement benefits from having a linearly swept FMCW, which improves temporal resolution and reduces system bandwidth requirements [62].

As seen in Figure 2.5, the cutoff frequency range of interest on AUG typically spans multiple microwave bands. This may require multiple microwave sources and respective waveguides. Microwave

oscillators sweep over a broad frequency range in a short time. As microwave oscillator technologies improved, reflectometry FMCW sweeping times have been reduced from 5 ms down to 10 μ s [56, 63, 64]. Shorter sweeping times, such as on the ultra fast 1 μ s X-mode reflectometer [65, 66], require faster acquisition systems. However, the linearisation of the microwave source requires careful dynamic calibrations.

The measured round trip group delay of a wave is dependent on the propagation path of the probing wave, determined by

$$\tau_g = \frac{d\phi(\omega)}{d\omega} = \frac{2}{c} \int_{r_0}^{r_c(\omega)} N(\omega, r) dr, \quad (2.25)$$

where c is the speed of light and N is the refractive index of the propagation medium for the propagating wave. When the cutoff position $r_c(\omega)$ is a monotonic function of the probing frequency, as in the density profile edges observed in Figure 2.5, the density profile can be calculated by inverting equation (2.25).

O-mode

For probing waves polarized in O-mode, the group velocity is dependent only on ω and the local cutoff frequency, the plasma electron frequency $\omega_c = \omega_{pe}$. Equation (2.25) can be converted into an Abel integration equation with the solution

$$r_c(\omega_c) = r_0 + \frac{c}{\pi} \int_0^{\omega_c} \frac{\frac{d\phi(\omega)}{d\omega}}{\sqrt{\omega_{pe}^2 - \omega^2}} d\omega = r_0 + \frac{c}{\pi} \int_0^{\omega_c} \frac{\tau_g(\omega)}{\sqrt{\omega_{pe}^2 - \omega^2}} d\omega, \quad (2.26)$$

where r_c and ω_c are the cutoff layer position and cutoff frequency, respectively [67]. Probing the plasma from the zero density using O-mode is not feasible in practice. Microwave sources have a lower limit to the output frequency ω_0 , which prevent an O-mode reflectometry system from probing the lowest densities. This means that the plasma is not probed in the frequency range 0 to ω_0 and, in order to reconstruct the density profiles, the group delay measurement for the lower density layers must be obtained from other density data, such as X-mode edge density profiles, or approximated, assuming an artificial shape for the edge density profile [68].

X-mode

The equation (2.25) can not be analytically inverted for X-mode since the group velocity is an explicit function of the position. An iterative numerical procedure to reconstruct the X-mode density profile is described in [60]. Consider the discrete measurements of the group delay for each probing frequency $\tau_g(\omega_i)$, removing the delay contribution of vacuum propagation. Assume a known cutoff position for the first measurement, for example $r_0 = 0$ for ω_0 . Let us define the group delay from the reflectometry signal

$$\tau_i = \left. \frac{d\phi(\omega)}{d\omega} \right|_{\omega=\omega_i}. \quad (2.27)$$

The integrated phase shift of the reflected swept frequency probing wave, which propagated through the plasma, is reconstructed from the measured experimental data

$$\phi_i = \sum_{j=1}^i \tau_j (\omega_j - \omega_{j-1}). \quad (2.28)$$

The numerical method for X-mode iterates over the experimental phase measurements ϕ_i to reconstruct the medium up to each cutoff position r_i . Define the short-scale wavenumber

$$A_{i,j} = \frac{\omega_i}{c} \frac{N_{i,j} + N_{i,j-1}}{2}, \quad (2.29)$$

where $1 \leq j \leq i$ and $N_{i,j}$ is the refractive index for frequency $\omega = \omega_i$ and at position $r = r_i$, and $N_{i,i} = 0$. The short-scale phase contributions are integrated to obtain the phase of the i -th measurement

$$\phi_i = \sum_{j=1}^i A_{i,j} (r_j - r_{j-1}). \quad (2.30)$$

In matrix notation the phase is calculated as

$$\phi = \mathbf{M} \cdot \mathbf{r}, \quad (2.31)$$

which translates to

$$\begin{bmatrix} \phi_1 \\ \phi_2 \\ \phi_3 \\ \dots \\ \phi_n \end{bmatrix} = \begin{bmatrix} A_{1,1} & 0 & 0 & \dots & 0 \\ A_{2,1} - A_{2,2} & A_{2,2} & 0 & \dots & 0 \\ A_{3,1} - A_{3,2} & A_{3,2} - A_{3,3} & A_{3,3} & \dots & 0 \\ \vdots & \vdots & \vdots & \ddots & \vdots \\ A_{n,1} - A_{n,2} & A_{n,2} - A_{n,3} & A_{n,3} - A_{n,4} & \dots & A_{n,n} \end{bmatrix} \begin{bmatrix} r_1 \\ r_2 \\ r_3 \\ \dots \\ r_n \end{bmatrix}.$$

However, since the matrix \mathbf{M} is dependent on r , the cutoff positions r_i for each probing wave ω_i must be iteratively calculated, starting at $r_0 = 0$ and $\phi_0 = 0$.

$$\begin{aligned} r_1 &= \phi_1 / A_{1,1} \\ r_2 &= \frac{r_1 (A_{2,2} - A_{2,1}) + \phi_2}{A_{2,2}} \\ &\dots \\ r_n &= \frac{r_1 (A_{n,2} - A_{n,1}) + r_2 (A_{n,3} - A_{n,2}) + \dots + r_{n-1} (A_{n,n} - A_{n,n-1}) + \phi_n}{A_{n,n}} \end{aligned} \quad (2.32)$$

The vacuum distance is added to the radial distances of the cutoff layers r_i . This vacuum distance must be estimated with the aid of the reflectometry measurement and the local magnetic field obtained from the magnetic equilibrium codes. Finally, the local electron density at each radial position is determined from the X-mode cutoff condition using the probing wave frequency and the local cyclotron

frequency.

Typically, the X-mode upper cutoff is used to reconstruct density profiles from the near-zero density. This is possible because the first upper cutoff reflection occurs for typically high frequencies, as determined from equation (2.19). On ASDEX Upgrade, the first upper cutoff reflection near the vessel edge occurs between 35 GHz and 70 GHz, for magnetic fields between 1.5 T and 3 T at the plasma core.

The X-mode lower cutoff reflection, in equation (2.18), poses the same initialization challenges as O-mode reflectometry. On the other hand, higher density layers can be probed with the X-mode lower cutoff, at the same frequencies as the O-mode reflectometry.

2.2.3 Other reflectometry techniques for density profile measurements

Besides FMCW, several other techniques have been used for density profile measurements in experimental nuclear fusion devices.

Pulse reflectometry

An ultrashort pulse has a broadband spectrum in the Fourier space. In reflectometry, this broadband signal can be used to probe multiple regions of the plasma simultaneously to reconstruct a density profile. In a typical ultrashort pulse reflectometry architecture, a Gaussian pulse with a carrier frequency f is generated. The pulse spectrum has a finite bandwidth BW with a Gaussian distribution

$$BW = f \pm \Delta f/2, \quad (2.33)$$

where Δf is the inverse of the pulse width. Several pulses with different carrier frequencies may be used to increase the probed regions of the plasma. Such a short probing pulse allows the measurement of a static snapshot of the plasma. However, the radial accuracy is dependent on the precision of the time of flight measurement. For an accuracy of 1 cm in vacuum, a precision of 60 ps is necessary. Pulse broadening due to waveguide dispersion, plasma fluctuations or low density profile gradients, increases the difficulty in the time of flight measurement [69]. Pulse reflectometry systems have been implemented in fusion machines such as RTP [70, 71], TEXTOR [72], Globus-M [73], START [74] and LHD [75, 76]

Amplitude modulation reflectometry

In amplitude modulation (AM) reflectometry, two closely separated frequencies are launched simultaneously towards the plasma and the time delay, τ , is calculated from the phase difference, $\Delta\varphi$, between their reflections as

$$\tau = \frac{1}{2\pi} \frac{\Delta\varphi}{f_m}, \quad (2.34)$$

where f_m is the modulation frequency. The phase delay is interpreted from the modulating envelopes of the probing and reflected signals, detected simultaneously. This system may be swept or have several discrete frequencies to probe the density profile. AM reflectometry has the advantage of the direct

determination of the time delay. However, it is sensitive to parasitic reflections and the direct time delay measurement is only possible for a dominant plasma reflection, which can be improved by having separate transmitting and receiving antennas in a bistatic configuration [69]. Amplitude modulation reflectometry diagnostics have been used in several fusion devices such as FTU [77], TdeV, [78], PBX-M [79], W7-AS [80] and TFTR [81].

Differential phase reflectometry

In the differential phase technique, similarly to the AM technique, two coherent swept microwave signals with a constant frequency difference are launched towards the plasma. The two signals have different propagation phase shifts, and their phase difference corresponds to the phase shift due to the separation between the lower and higher frequency cutoff layers. This method allows a more accurate phase tracking over the probing frequency range as the phase shifts due to plasma fluctuations, common to both signals, are cancelled out. The difference phase as a function of the sweep frequency is enough information to reconstruct the density profile, providing an almost direct measurement of the average density profile gradient [82]. Reflectometry diagnostics adopting the differential phase measurement have been implemented in TFTR [83], QUEST [84, 85] and Alcator C-mod [86, 87].

2.3 Microwave reflectometry architectures

The generic architecture of an FMCW reflectometry diagnostic uses a microwave oscillator source, transmission lines and antennas to direct the probing wave towards the plasma. The detection mechanism is sensitive to the reflected wave and determines the detection limit of the reflectometry signal of the system.

2.3.1 Homodyne detection

Figure 2.9 illustrates a reflectometry system architecture with homodyne detection. A microwave probing wave is generated by the oscillator and launched by the reflectometry antenna towards the plasma. The reflected wave is received by the same reflectometry antenna and a directional coupler directs the received wave towards the detector.

In this homodyne topology, the reference signal may be generated by a pin inserted into the waveguide in the transmitting branch, close to the launching antenna. This pin reflects part of the probing signal, as a reference, back to the directional coupler and towards the detector. This reflected power depends on the penetration depth of the pin in the transmission line. The voltage response of the detector is proportional to the amplitude of the input signal, which is the modulation result between the reference and the plasma reflection signal. The detector is a microwave sensitive diode and has a typical low pass frequency response, which filters the high frequency components, and the detector output corresponds

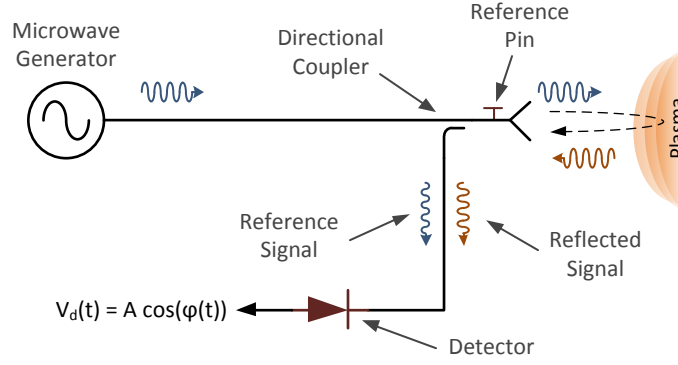


Figure 2.9: Generic architecture of a reflectometer with homodyne detection.

to the beat signal of the plasma reflection

$$V_d(t) = A(t)\cos(\phi(t)), \quad (2.35)$$

where $A(t)$ is the amplitude of the detector output, which considers the reflection signal amplitude and the non-flat response of the detector.

2.3.2 Heterodyne detection

The heterodyne procedure was coined by Reginald Aubrey Fessenden in 1901 and is ubiquitous today in telecommunications as a way to tune information to a carrier frequency [88]. The heterodyne method combines two frequencies to derive their sum and difference frequencies as

$$A_1 \sin(\phi_1(t)) \times A_2 \sin(\phi_2(t)) = \frac{A_1 A_2}{2} [\cos(\phi_1(t) - \phi_2(t)) + \cos(\phi_1(t) + \phi_2(t))], \quad (2.36)$$

$$A_1 \sin(2\pi f_1 t) \times A_2 \sin(2\pi f_2 t) = \frac{A_1 A_2}{2} [\cos(2\pi f_1 t - 2\pi f_2 t) + \cos(2\pi f_1 t + 2\pi f_2 t)]. \quad (2.37)$$

This multiplication is performed in a non linear mixer device. The mixer has two inputs, the local oscillator (LO) and the radio frequency port (RF). The LO corresponds to a stable high power reference signal that polarizes the internal non linear device of the mixer, while the RF is the low power signal to be measured. The sum and difference results of the multiplication are obtained at the mixer intermediate frequency (IF) output. Typically, a low or high pass filter at this port removes the undesired frequency component, resulting in a down- or up-conversion topology, respectively.

In a reflectometer with heterodyne detection, the plasma reflection signal is multiplied with a synchronized reference signal on a microwave mixer. This results in a down-converted signal around a non-zero IF carrier. The heterodyne detection method provides a lower detection limit than homodyne detection, as the detection mixer is partially polarized by the higher power reference signal, resulting in a better signal to noise ratio (SNR). In addition, the IF signal may be bandpass filtered around its carrier to remove frequency features outside the bandwidth of interest. A typical reflectometry architecture with heterodyne detection is represented in Figure 2.10.

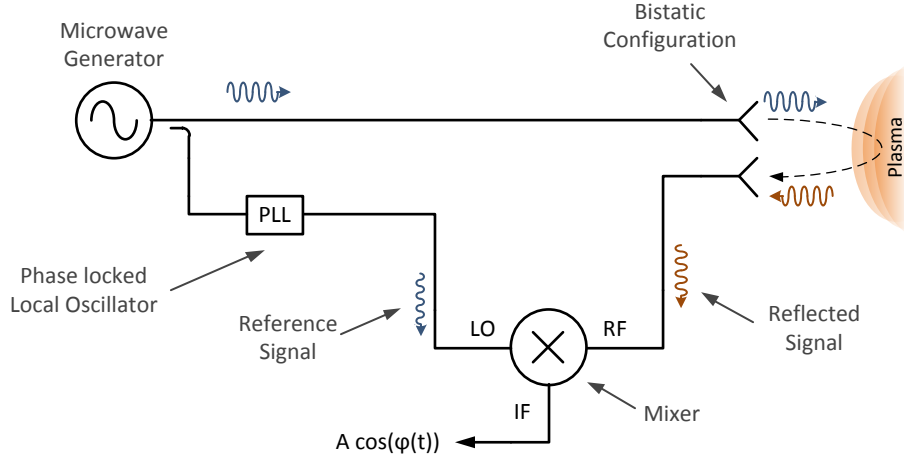


Figure 2.10: Heterodyne reflectometry architecture with bistatic antenna configuration and phase locked local reference generator.

In this topology, the reference signal is generated by a secondary microwave source, which is typically phase locked (PLL) or coherent with the probing generator. This signal may be amplified, if needed, to drive the mixer's local oscillator port. At the front end, a bistatic configuration provides separate transmitting and receiving signal paths and antennas. This reduces cross talk between the probing and detection branches, and reduces the spurious reflections due to waveguide misalignment. The mixer output is low pass filtered and corresponds to the beat frequency difference between the reflected and reference signals. The heterodyne architecture provides a higher dynamic range than the homodyne detection at the cost of increase component and access cost.

Quadrature heterodyne detection

Quadrature heterodyne detection is a technique that is able to extract both the amplitude and phase of a received signal. The procedure uses two orthogonal reference signals, with a phase difference of $\pi/2$, or 90° , with the same frequency as the IF carrier wave, to demodulate the down-converted beat signal into its in-phase and quadrature (IQ) components, using two additional mixers.

The IQ voltage components of the input signal are represented by

$$V_I(t) = A(t)\sin(\phi(t)) \quad (2.38)$$

and

$$V_Q(t) = A(t)\cos(\phi(t)). \quad (2.39)$$

The amplitude of the original signal can be extracted by calculating

$$A(t) = \sqrt{V_I^2(t) + V_Q^2(t)}. \quad (2.40)$$

And its phase is given by

$$\phi(t) = \tan^{-1} \left(\frac{V_Q(t)}{V_I(t)} \right). \quad (2.41)$$

The reflectometer architecture with quadrature heterodyne detection is illustrated in Figure 2.11. The reference signal is obtained by mixing the probing and LO signals, resulting in a signal whose frequency is equal to the IF carrier, accompanying the frequency difference of the probing and LO signals. This reference is split in two and one of these results is delayed by 90° using a phase shifter, such as a calibrated coaxial delay line, and used to drive the quadrature detector mixers. The reflected signal is band pass filtered and split into two branches and used to feed the RF port of each mixer in the quadrature detector. The voltage outputs of the mixers are low pass filtered and correspond to the IQ components of the baseband beat signal, which are the result of the propagation inside the vessel.

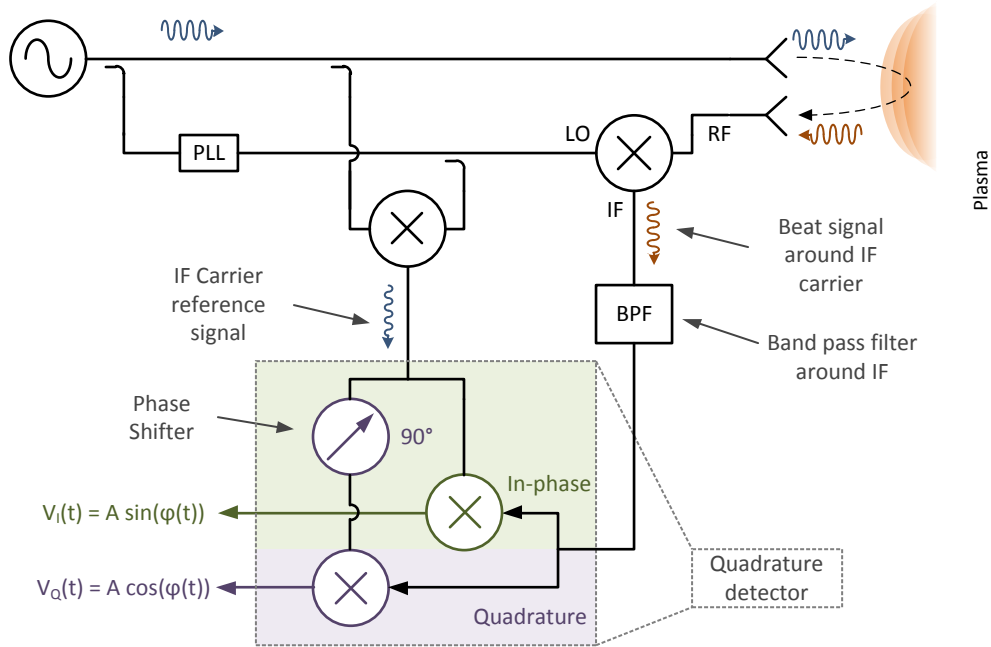


Figure 2.11: Reflectometry architecture with quadrature heterodyne detection.

This topology allows the extraction of the absolute amplitude and phase of the plasma reflection signal. In addition, by using quadrature detection, the usable bandwidth of the reflectometry detection is doubled. Quadrature detection is useful in fluctuation reflectometry as it provides a direct measurement of the phase. In density profile reflectometry, the instantaneous phase and amplitude measurements facilitate the group delay estimation for density profile reconstruction.

2.3.3 Extracting the group delay measurement

In density profile reflectometry, the group delay must be extracted from the detected beat signal. As seen in equation (2.24), the frequency f_b of the beat signal is related to the group delay τ_g , or phase

derivative of the reflectometry interference signal [63, 89, 90], as

$$f_b = \tau_g \left(\frac{df}{dt} \right). \quad (2.42)$$

Evaluating the group delay becomes a problem of estimating the instantaneous frequency of the beat signal. Different techniques are available for frequency estimation: fringe counting [91], zero-crossing, minima/maxima [92], time-based frequency discriminator [93] and complex demodulation [94], and time-frequency spectral analysis.

It is important to note that the beat signal may be contaminated by noise from sources such as plasma emission, plasma heating, or spurious reflections. These contributions may be eliminated through hardware filters or through digital post processing.

2.3.4 Uncertainty of the reflectometry measurement

The detected reflectometry interference signal is acquired using dedicated fast acquisition systems. The acquisition rate and system memory must be able to cope with the fast sweep times and repetition rate of a density profile reflectometer. The analog baseband reflectometry signal typically consists in 10-20 μ s pulses of a transient interference signal with bandwidths up to 100 MHz, depending on the reflectometer.

Density resolution

The density resolution is mainly determined by the resolution of the probing frequency measurement. Assuming a linear probing frequency ramp, the probing frequency resolution Δf_p is

$$\Delta f_p = \frac{df}{dt} \frac{1}{f_s}, \quad (2.43)$$

where f_s is the sampling frequency.

In O-mode, the probed density layer depends only on the cutoff frequency. In X-mode, the probed density layer depends not only on the probing wave frequency but also on the local magnetic field. Here the density and radial resolutions are influenced by the resolutions of the magnetic equilibrium codes (<0.5 cm and 1 ms on ASDEX Upgrade), and may be determined *a posteriori*.

Range resolution

The range resolution is the capability of distinguishing between two close targets. This spatial resolution in vacuum is given by

$$\Delta r = \frac{c\Delta\tau}{2}, \quad (2.44)$$

where c is the speed of light and $\Delta\tau$ is the delay resolution, which may be obtained from the reflectometry signal [69]. In inhomogeneous plasmas, the range resolution depends on the propagation through the medium and can not be directly determined.

When probing a continuously monotonic density profile using reflectometry, the phase difference between the probing and reference waves results in a beat signal that is captured by the acquisition system, whose frequency is proportional to the group delay. The method of frequency estimation, such as the phase of quadrature detection or frequency-time distribution analysis, sets the limitation for the frequency resolution.

The phase measurement for quadrature detection has a relative uncertainty, calculated in Appendix A, approximated by

$$\Delta\phi \approx \frac{\sqrt{2}}{2^N \text{S/N}}. \quad (2.45)$$

where N is the number of bits of the acquisition system and S/N is the signal to noise ratio of the detection mechanism, which depends on a variety of factors: the attenuation of the reflection signal through the plasma, plasma turbulence, linearity of the frequency sweep, the time overlap between the reference and reflected waves and the quadrature demodulator. The phase uncertainty can be reduced by increasing the number of bits N or improving signal quality.

The beat frequency resolution depends on the phase resolution of the detection mechanism. For quadrature detection, this is

$$\Delta f_b = \frac{\Delta\phi}{2\pi} f_s. \quad (2.46)$$

For spectrograms the f_b resolution is

$$\Delta f_b = \frac{f_s}{N_{\text{win}}}, \quad (2.47)$$

where N_{win} is the size of the spectrogram window.

The group delay resolution, is determined from the beat frequency as

$$\Delta\tau = \Delta f_b \left(\frac{df}{dt} \right)^{-1}, \quad (2.48)$$

assuming a linear sweep rate. This delay resolution may be increased by increasing the probing frequency sweep rate df/dt . However, the input bandwidth of the acquisition system and the distance to the reflecting surface set the upper limit for the sweep rate — the beat frequency corresponding to the reflection delay and the sweep rate, must fall within the bandwidth of the acquisition system. The trade off between the sweep rate and the probing frequency resolution must also be considered.

2.4 Summary

In this chapter we described microwave reflectometry diagnostics for fusion tokamaks. First, we analysed the propagation of waves in unmagnetized plasmas, assuming a plasma slab model. The wave is able to propagate through the increasing density regions of the plasma up to the critical density layer, where it is reflected.

Then, we analysed the propagation in magnetized plasmas, as is the case of fusion plasmas in tokamaks. Here, the orientation of wave's electric field to the magnetic field influences its propagation through the plasma. Two electromagnetic propagation modes are determined: O-mode and X-mode.

The cutoff conditions of either propagation mode, used for reflectometry measurements, were analysed. Waves propagating in the ordinary propagation mode are not affected by the magnetic field. The refractive index of O-mode is equal to an unmagnetized plasma. On the other hand, the extraordinary propagation mode is dependent on the magnetic field and has two cutoff conditions.

Reflectometry diagnostics can be used for density profile, using a swept probing frequency or other topologies, and fluctuation measurements, with a fixed probing frequency. Both measurement principles were described with emphasis on density profile measurements using FMCW.

Three different microwave reflectometry architectures were detailed. The simplest case uses homodyne detection with a single detection diode and a pin to generate the reference signal. The heterodyne architecture provides a better SNR at an increased hardware cost. The quadrature heterodyne detection has the advantage of doubling detection bandwidth and providing both amplitude and phase measurements of the reflectometry signal. The conditions that affect the density and range resolutions of reflectometry measurements were described.

Chapter 3

Implementation of the new reflectometry diagnostic

Studying the plasma edge interactions during ICRF heating operation is crucial for the optimization of ICRF power coupling. While some plasma density perturbations can be remotely measured by assuming they propagate along the magnetic field lines, remote measurements are not as reliable as localized measurements, since perturbations become diluted the further they propagate around the torus.

In order to reduce the unwanted RF sheaths that form during ICRF operation, a new ICRF antenna was designed. This antenna uses a 3-strap topology, a central strap and two side straps, which aim to reduce the total DC potentials that form during ICRF operation and reduce the wall material sputtering effects.

Designing a new ICRF antenna for ASDEX Upgrade presented the opportunity to embed a local electron density profile diagnostic to probe the local plasma layers. To aid in ICRF operation studies, this diagnostic would have to: i) measure edge plasma density profiles; ii) provide multiple measurement locations for geometrical studies; iii) not affect or be affected by ICRF operation; iv) be able to work with restricted access port and transmission line routing.

Microwave reflectometry has several advantages towards this purpose. It is a non-invasive diagnostic method, whose low probing power does not affect the plasma, enabling the study of the ICRF effects during operation. It can measure electron density profiles and density perturbations from the edge plasma up to the core, depending on the operational conditions. The comparatively small waveguides required for microwave reflectometry allow the complex routing paths between the much larger ICRF antenna. In addition, small microwave antennas can be embedded in between the protective Faraday straps. Another advantage of using waveguides is that the microwave signals can be routed from inside the vessel to the outside, through a vacuum window, and the more complex microwave diagnostic components can be installed outside the vessel. With these advantages in mind, a microwave reflectometry diagnostic solution was chosen to be embedded in the new ICRF antenna design [95].

This chapter describes the implementation of the embedded X-mode reflectometry diagnostic for density profile measurements [96]. First the specifications of operation are described, followed by a

description of the experimental setup. Then the heterodyne reflectometry architecture and its implementation are detailed.

3.1 Specifications for reflectometry diagnostic operation

The new reflectometry diagnostic design must be compatible with the operational parameters of the ASDEX Upgrade experimental device, seen in Table 3.1. The most relevant parameters affecting the design of the reflectometry diagnostic are the magnetic field, typical plasma densities and discharge duration. The typical core magnetic field values at ASDEX Upgrade are from 1.5 T to 3 T, with the most common magnetic field being 2.5 T.

Table 3.1: ASDEX Upgrade main parameters [20].

Major radius R_0	1.65 m
Minor radius	0.5 m
Plasma height	0.8 m
Core magnetic field B_0	1.5 to 3.1 T
Plasma current I_p	up to 2.0 MA
Pulse duration	up to 10 s
Temperature T_e, T_i	up to 6 keV
Plasma core density n_e	up to $30 \times 10^{19} \text{ m}^{-3}$
Heating power	up to 18 MW

During ICRF heating, the fast wave decays in the evanescent region at the edge, below the cutoff density in the 10^{18} m^{-3} range. For ICRF operation studies, the reflectometry diagnostic must be able to probe the edge plasma located up to a few centimeters from the radiating surface of the ICRF antenna and with a density resolution of less than 10^{18} m^{-3} , up to 10^{19} m^{-3} [27].

The reflectometry diagnostic should be able to provide fast measurements, with sub-millisecond repetition rate, to observe fast plasma events, during the 10 s duration of a typical discharge, which may be limited by the memory of the data acquisition system. The probing sweep time must also be fast, in the order of tens of microseconds, to avoid any phase decorrelation due to fluctuations [95].

3.1.1 Microwave band and probing frequencies

X-mode reflectometry has the advantage of being able to probe the plasma from the near zero density up to the core without recurring to large artificial initializations. This is achieved by using the X-mode upper cutoff region that occurs in the GHz frequency range, depending on the local magnetic field and plasma electron densities.

To illustrate the probing region, Figure 3.1 shows the electron densities of the cutoff layers for different X-mode wave frequencies under the typical core magnetic fields of ASDEX Upgrade. For this analysis, we assumed the measurement layer to be located at the first wall position at mid height $r \approx 2.15 \text{ m}$. The

magnetic field profile along r is approximated by

$$B(r) = B_0 \frac{R_0}{r}, \quad (3.1)$$

where R_0 is the major radius of ASDEX Upgrade, with a typical value of 1.65 m, and B_0 is the core magnetic field. In the figure, the X-mode cutoff condition at the intersection between a probing frequency and a core magnetic field occurs for a given electron density. For example, the cutoff electron density for a 50 GHz probing wave under 1.6 T is approximately $1 \times 10^{19} \text{ m}^{-3}$.

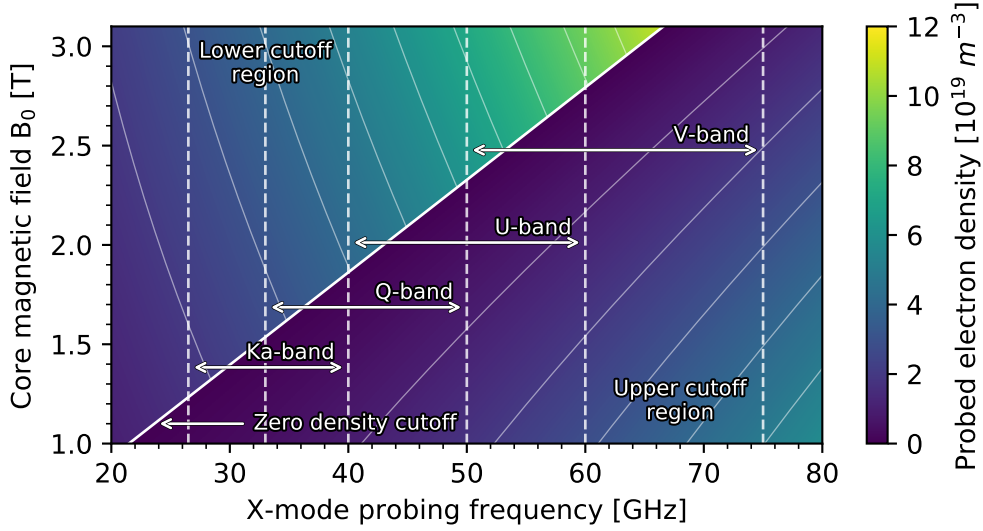


Figure 3.1: Probed electron densities for different cutoff frequencies under the typical core magnetic field range on ASDEX Upgrade.

To standardize the design of commercial applications, the electromagnetic spectrum is divided into several microwave bands with a lower and upper frequency limit. Microwave devices are usually designed to operate within the frequency range specifications of a single band.

The Ka to V microwave bands, typically used in reflectometry diagnostics, are represented within the respective frequency limits in the figure. These probing bands are suitable for reflectometry operation under the 1.5 T to 3.1 T core magnetic field range of ASDEX Upgrade as they can cover the edge electron density layer.

The two, lower and upper, X-mode cutoff regions can be observed to the left and right of the zero density cutoff line, respectively. The upper cutoff region is used for edge density profile reflectometry measurements. This means that the useful probing frequency region of a single microwave band is to the right of the solid line and narrows as the magnetic field increases. Using the U-band as example, the useful frequency region at 2 T is approximately from 43-60 GHz, while for 2.5 T it is reduced to 55-60 GHz, and for magnetic fields above 2.7 T, there is no useful measurement for edge density profile reflectometry. To overcome this, reflectometry diagnostics may aggregate multiple microwave bands to probe a larger region of the plasma.

However, due to the limited access space available to the reflectometry waveguides, the use of the

single U-band was decided for the X-mode reflectometry channels. The U-band restricts the electron density profile measurements to a magnetic field range between 1.85 T and 2.7 T, which is acceptable for ICRF operation studies and most discharges on ASDEX Upgrade. To increase the cutoff density coverage, the probing frequency band was extended to 40-68 GHz. Figure 3.2 shows the operational range of the X-mode upper cutoff reflectometer probing in the extended 40-68 GHz range. As observed, this extended frequency range increases the electron density profile measurement. For the most common 2.5 T discharge of ASDEX Upgrade, the density profile measurement is increased from $0.5 \times 10^{19} \text{ m}^{-3}$ to $1.2 \times 10^{19} \text{ m}^{-3}$ between the original band and the band extended with the additional 8 GHz. For magnetic fields above 1.85 T, the second cyclotron harmonic absorption is well above the extended probing range and does not affect our reflectometry measurement.

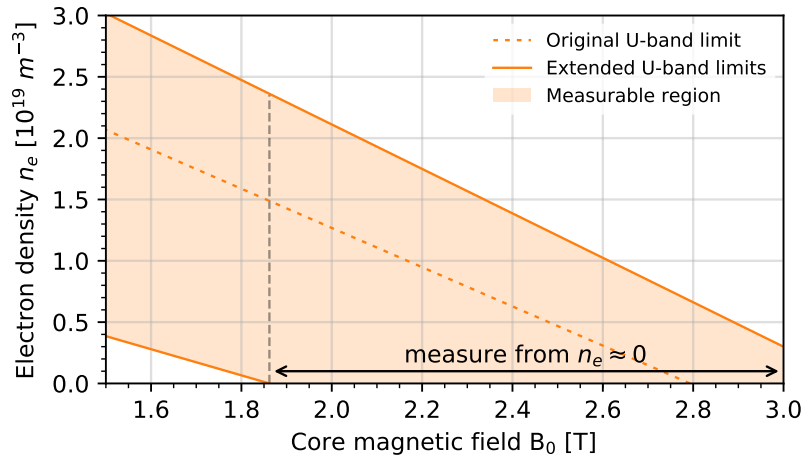


Figure 3.2: Operational range of the extended U-band X-mode edge density profile reflectometer.

3.1.2 Reflectometry antenna locations and lines of sight

A total of ten reflectometry antennas pairs (or channels) are embedded along the radiating surface of the ICRF antenna, probing the plasma from different toroidal and poloidal locations. The reflectometry antenna locations can be seen in Figure 3.3, which shows the front side of the new ICRF antenna #4 installed in sector 12 of ASDEX Upgrade. The reflectometry antennas are grouped in a bistatic configuration, using dedicated waveguides for the transmitting (TX) and receiving (RX) branches. The bistatic configuration increases the isolation between the TX and RX branches by preventing internal crosstalk between the transmission and reception. However, this configuration comes at the cost of increased space requirements for both TX and RX waveguides. In this work, the nomenclature of reflectometry channel or reflectometry antenna refers to the pair of TX and RX antennas in bistatic configuration at each location.

Microwave power transfer between different mediums requires a correct impedance matching at their interface. Horn antennas provide a gradual transition from the characteristic impedance of the waveguide, 50Ω , to the impedance of free space, 377Ω , improving the efficiency of transmission [97].

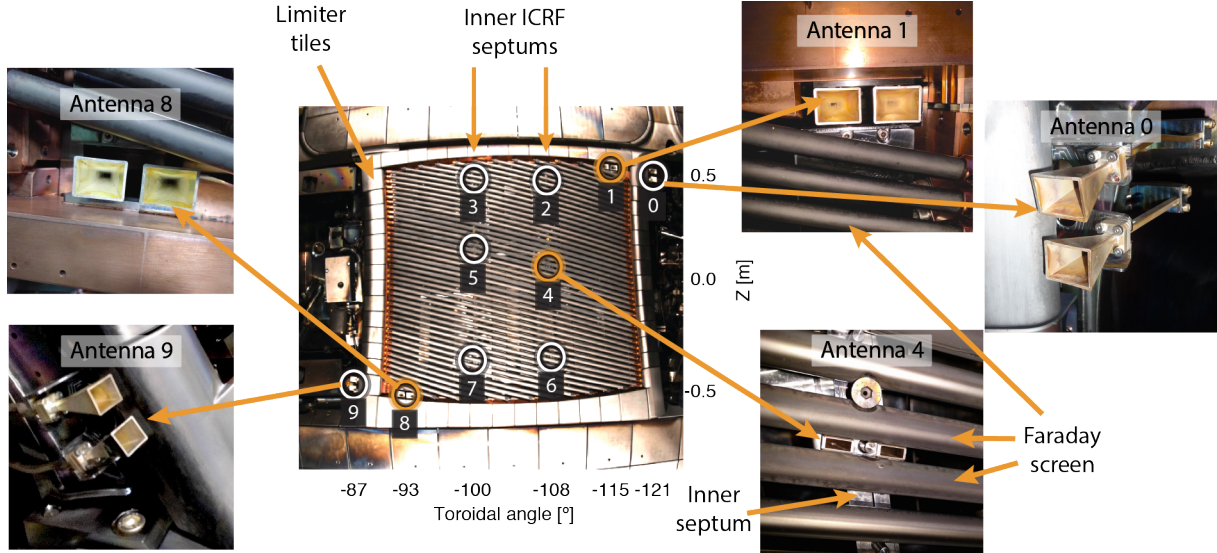


Figure 3.3: Location and details of the reflectometry antenna pairs embedded along the radiating surface of ICRF antenna 4 in sector 12 of ASDEX Upgrade.

The reflectometry antennas in the outer extremities (0, 1, 8 and 9, seen in the figure) are attached to the back structure of the ICRF limiter and consist of pyramidal horn antennas. Antennas 1 and 8 are located in the open region between the last Faraday straps and the ICRF antenna limiter, while antennas 0 and 9 are located outside the limiter. The central reflectometry antennas (2-7) are attached to the two parallel inner septums near the centre of the ICRF antenna structure. These have to look through the small gap between the Faraday shield straps, as seen in the antenna 4 detail in the figure, and use smaller WR19 to WR42 waveguide¹ tapers as antennas.

The pitch angle of the magnetic field on a tokamak depends on the toroidal magnetic field and the plasma current. The average pitch angle of discharges on ASDEX Upgrade is around 15° at the mid-plane separatrix, also corresponding to the tilt of the Faraday rods. The midplane reflectometry antennas are aligned with these Faraday straps so that the probing waves are polarized for X-mode propagation: the electric field of the probing waves, parallel to the shorter edge of the rectangular waveguide, is perpendicular to average magnetic field. The outer horn antennas, on the other hand, are parallel to the equatorial plane of the tokamak, launching electromagnetic waves with a main component in X-mode but also with a small O-mode component. This reduces the efficiency of the X-mode reflectometry measurement, as the probing wave energy is divided between both components. There is an approximate additional 2 dB plasma coupling loss in these channels, due to this misalignment of the horn antennas, during a typical discharge on ASDEX Upgrade.

Only three (antennas 1, 4 and 8, highlighted in Figure 3.3) of the ten available channels were instrumented in this work. However, the remaining available antennas may be instrumented in future upgrades of the reflectometry diagnostic. In this work, these channels were selected to provide poloidally distributed measurements of the plasma, aimed for ICRF operation studies. Channels 1 and 8 were chosen as they were expected to provide high quality measurements, due to the standard pyramidal

¹WR19 and WR42 are standard rectangular waveguide designations [98].

horn antennas, near the top and bottom parts of the ICRF radiating surface. Channel 4 was selected to provide a mid plane measurement and to evaluate the quality of the reflectometry signal due to the smaller antennas and proximity of the reflective Faraday straps. These metallic obstacles in front of channel 4 may result in secondary reflections, which contaminate the reflectometry signal. This has been observed experimentally by the appearance of a low power reflection very close to the antenna at low probing frequencies, which can be distinguished from the higher power main plasma reflection.

The lines of sight (LOS) of the installed antennas can be seen in the poloidal and toroidal cross sections of ASDEX Upgrade in Figure 3.4 a) and b), respectively. The LOS are taken at the middle point between the TX and RX antennas of each channel and are parallel to the propagation direction of the probing beam. The probing beam is oriented towards the magnetic axis to reduce the scattering of the beam energy and maximize the reflection power towards the receiver antenna. It can be observed from the top view b) that the LOS of antenna 4 is misaligned toroidally with the LOS of antennas 1 and 8, which are oriented towards the machine origin. This is due to antennas 2-7 being attached to the inner septums of the ICRF antenna, which are parallel to each other. In the case of antenna 4, it is expected that this slight misalignment of the LOS contributes to an increased signal loss due to scattering, which reduces the received plasma reflection power.

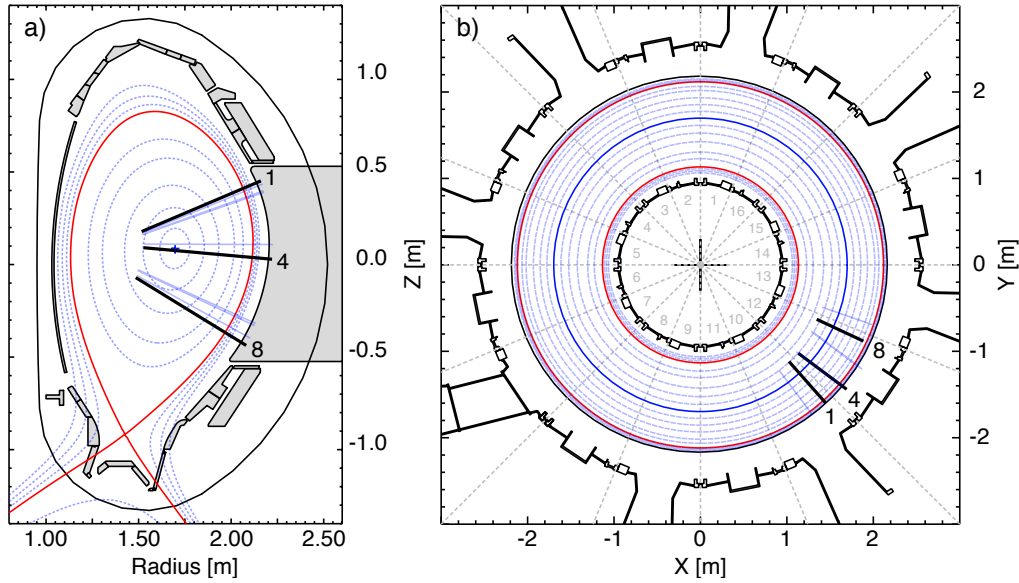


Figure 3.4: a) Poloidal and b) toroidal cross section views of the ASDEX Upgrade tokamak and lines of sight of the installed reflectometry channels 1, 4 and 8.

No crosstalk was observed between the installed channels during the commissioning of the diagnostic. This was verified by having each of the transmitters operating and receiving on all channels, with and without plasma. The installation of additional channels may introduce crosstalk issues between channels close to each other, mainly channels 2 to 7, which must be accounted for during their commissioning. The misalignment of the LOS of channels 2-7 from the orthogonal direction of the plasma center, may contribute to the signal scattering in opposite directions, reducing the eventual crosstalk between channels installed in the future.

3.2 Experimental setup of the diagnostic

To implement a new diagnostic for fusion research, the location and conditions of the experimental setup must first be analysed. The environment inside the ASDEX Upgrade torus hall can become quite harsh during operation. In addition to the temperature increase, there are high magnetic fields, X-ray radiation, neutron release and machine vibrations that can damage sensitive hardware. Existing diagnostics are typically divided between two distinct areas, with the sensors and actuators installed in the torus hall, or even inside the vessel, and the data acquisition and control systems placed in the control room. Communication between these two areas is performed using optical fiber links, which enable galvanic isolation but may cause distortions in the analog signals. To prevent these issues, the implemented reflectometry diagnostic was designed to be installed inside the torus hall and survive the operation conditions.

The main components of the reflectometry diagnostic are the microwave reflectometry hardware, the waveguides connecting to the antennas inside the vessel and the diagnostic support systems, as illustrated in Figure 3.5. The diagnostic support systems include i) the host computer that controls operation and network communication; ii) the trigger controller synchronized with ASDEX Upgrade; iii) the data acquisition system.

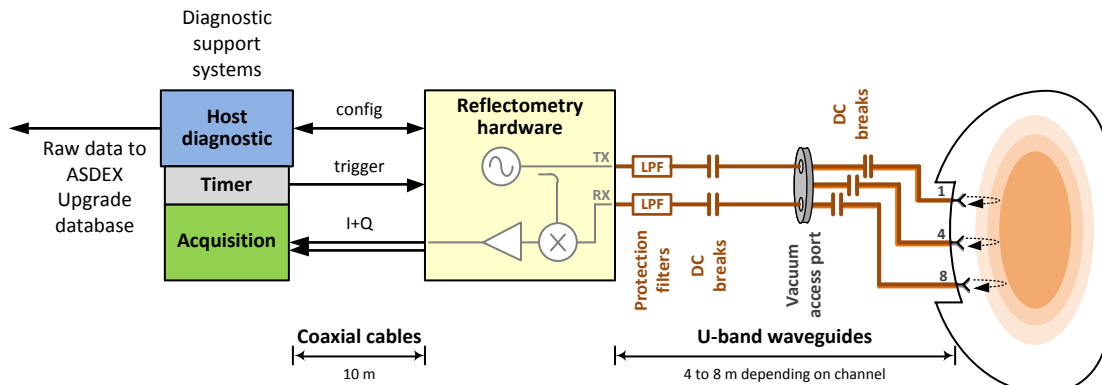


Figure 3.5: Main components of the reflectometry diagnostic system.

The reflectometry hardware is configured through an ethernet connection by the host diagnostic computer. The trigger for each acquisition is supplied, using a coaxial cable, by a dedicated timer subsystem synchronized with the central timer of ASDEX Upgrade. The resulting baseband quadrature reflectometry signals are routed using coaxial cables to the acquisition system.

The reflectometry diagnostic is divided between two standard 19" cabinets, which are installed inside the torus hall, at the locations seen in Figure 3.6. The diagnostic control and support systems are placed in a cabinet away from the high magnetic fields that occur during a discharge, seen in Figure 3.7. The reflectometry hardware is placed in another cabinet near the tokamak vessel, and attached directly to the waveguides, seen in Figure 3.8.

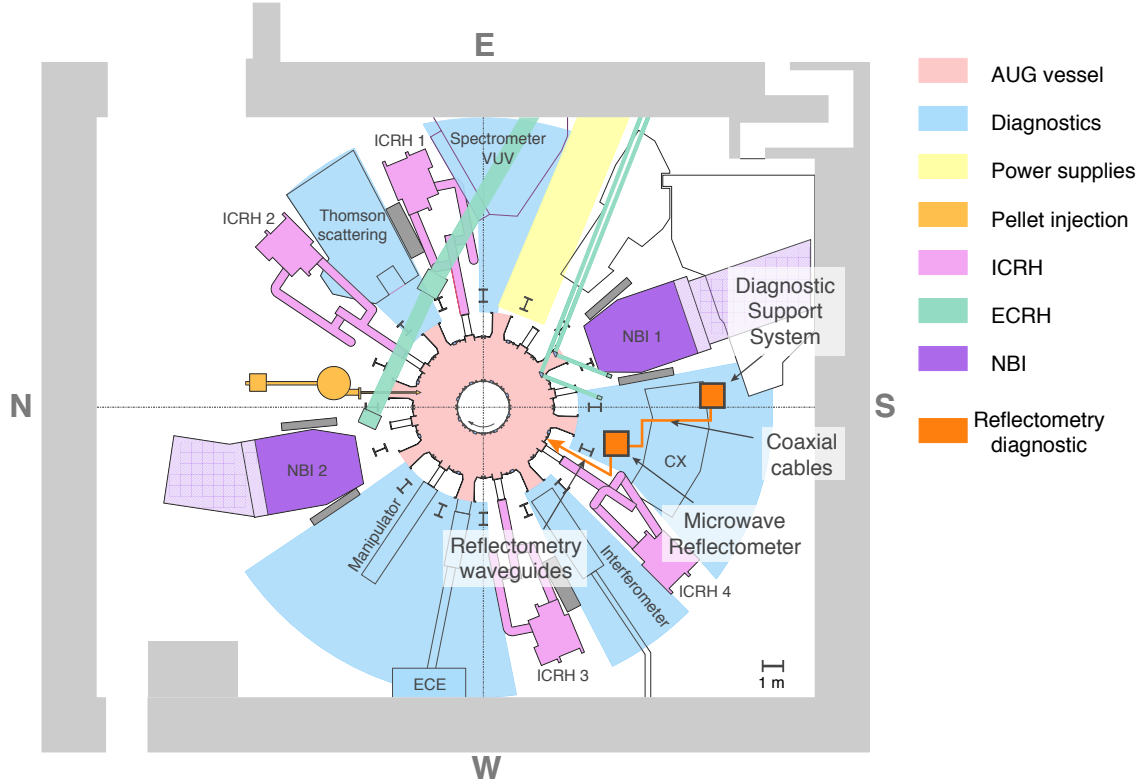


Figure 3.6: Placement of the reflectometry diagnostic system cabinets installed inside the ASDEX Upgrade torus hall.

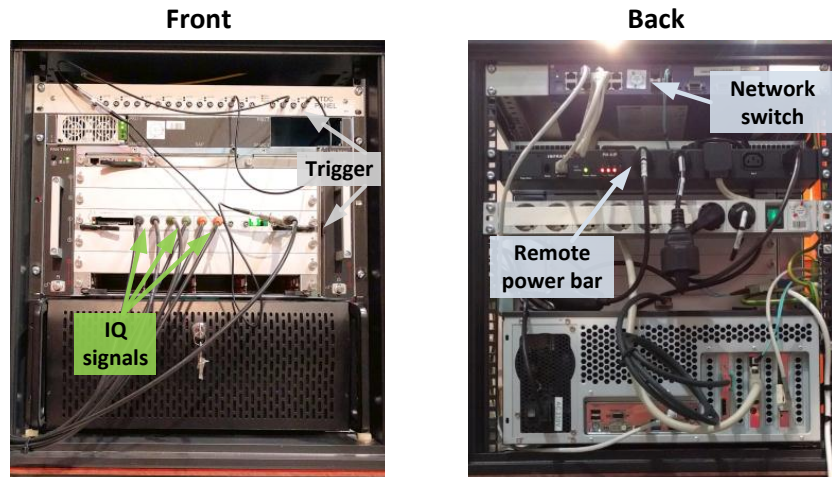


Figure 3.7: Cabinet containing the diagnostic support hardware: host computer, acquisition system, trigger controller and network interfaces; placed away from the vessel.

Waveguide routing

The microwave signals are routed between the reflectometry hardware and the antennas inside the vessel using fundamental U-band WR19 waveguides. The interface with the outside of the vessel is made through the upper vacuum port (CO12) on sector 12 of ASDEX Upgrade. Due to the restricted

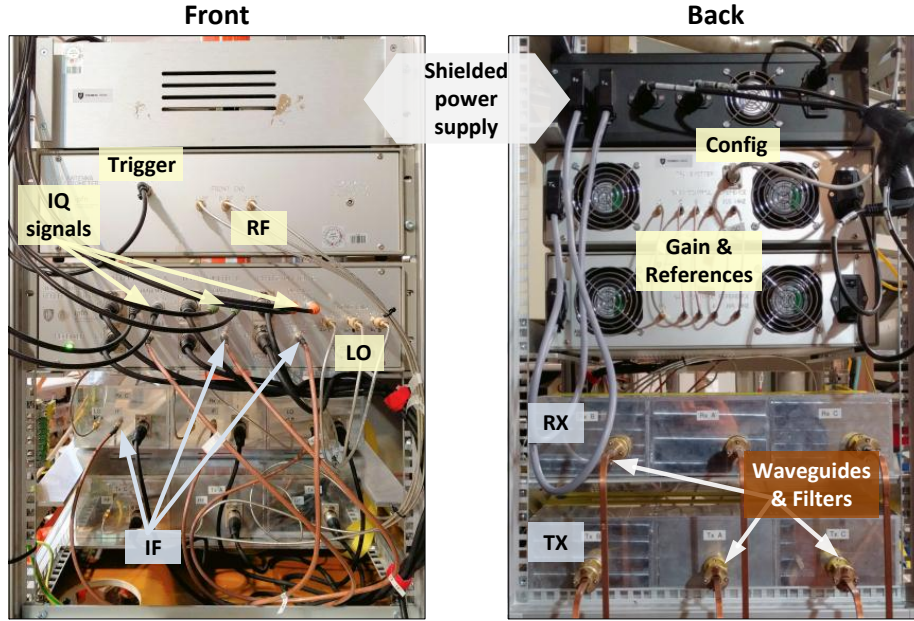


Figure 3.8: Cabinet containing the microwave reflectometry hardware: shielded power supplies, reflectometry signal generation and conditioning hardware, and front ends attached to waveguides; close to the vessel.

port size, the vacuum flange was specially designed with only 14 pass through WR19 windows (seen in Figure 3.9 left). Each window has a 0.1 mm Mica with a measured insertion loss of less than 0.5 dB in the 40-68 GHz frequency range [95]. The waveguide routing from the vacuum port to the embedded reflectometry antennas along the back side of the ICRF antenna is shown in Figure 3.9 (right). Only seven reflectometry antenna pairs, or channels, may be connected at a time without rerouting the in-vessel waveguides.

During a discharge the electric potentials between the different ground planes may reach thousands of volts. To protect diagnostic equipment and ensure personnel safety, the plasma facing components, the vessel chamber and the equipment in the torus hall have dedicated ground planes. The waveguides traversing across these different grounds are interrupted by DC breaks that ensure galvanic isolation while still allowing the microwave signals to propagate. Protection filters are attached to the waveguides to protect the microwave components from stray microwave radiation, such as ECRH at 105 GHz or 140 GHz.

Shielded power supplies

In a first approach, the diagnostic computer and acquisition system were placed in the same cabinet as the microwave reflectometry hardware, close to the vessel. However, during the start of the commissioning phase in November 2015, it was detected that the switched power supplies inside both the host computer and the reflectometry back end would fail during a discharge. This was attributed to the high stray magnetic field (up to 30 mT, depending on operation conditions) that arise at this location. It is believed that the internal transformer cores would saturate during operation, triggering the voltage

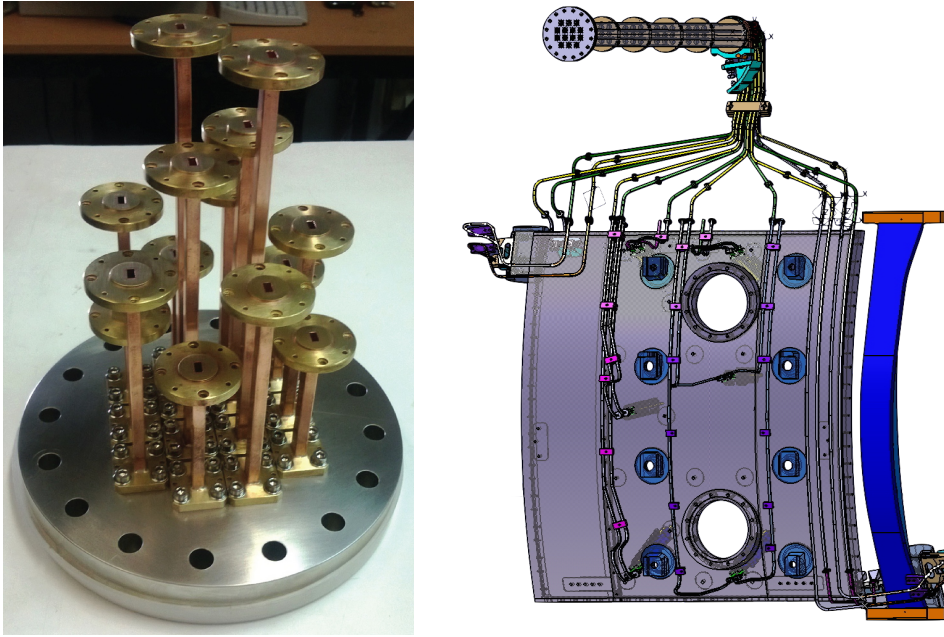


Figure 3.9: Vacuum flange with 14 WR19 pass through windows (left). CAD setup of the in-vessel waveguide routing along the back side of the ICRF antenna (right).

protection circuits and the shutdown of the power supplies. To reduce the influence of the magnetic field on the switched power supplies, the host computer and acquisition system were moved to a new cabinet over 10 meters away from the vessel.

In addition, a new power supply with magnetic shielding, seen in in Figure 3.10, was designed for the reflectometry hardware and was placed in the same cabinet, close to the vessel. The magnetic shielding consists in a 10 mm thick iron casing with side openings that surrounds the power supplies. The high magnetic permeability of the iron case and its orientation force the magnetic flux lines to go through the iron case, reducing the magnetic field strength near the internal power supplies.

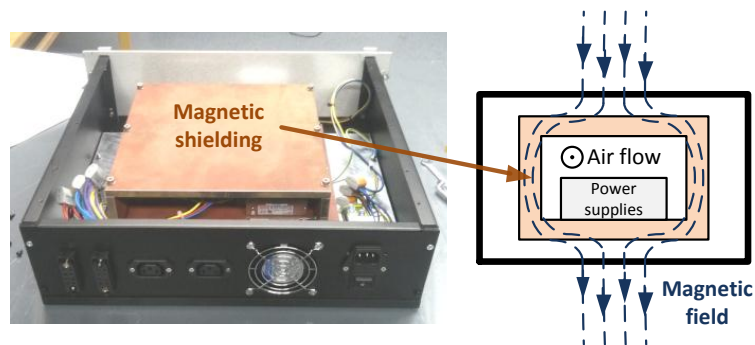


Figure 3.10: Reflectometer power supply with magnetic shielding and theoretical diagram of operation.

3.3 Microwave reflectometry system design

The design of the microwave reflectometry system is analysed in this section. First the architecture and operation are described. Then the individual blocks of the diagnostic architecture are detailed. These blocks include i) the generation and calibration of the microwave signals and references; ii) the transmitter and receiver front ends; iii) the amplification and quadrature detection; iv) and the bandwidth requirements and delay line compensation.

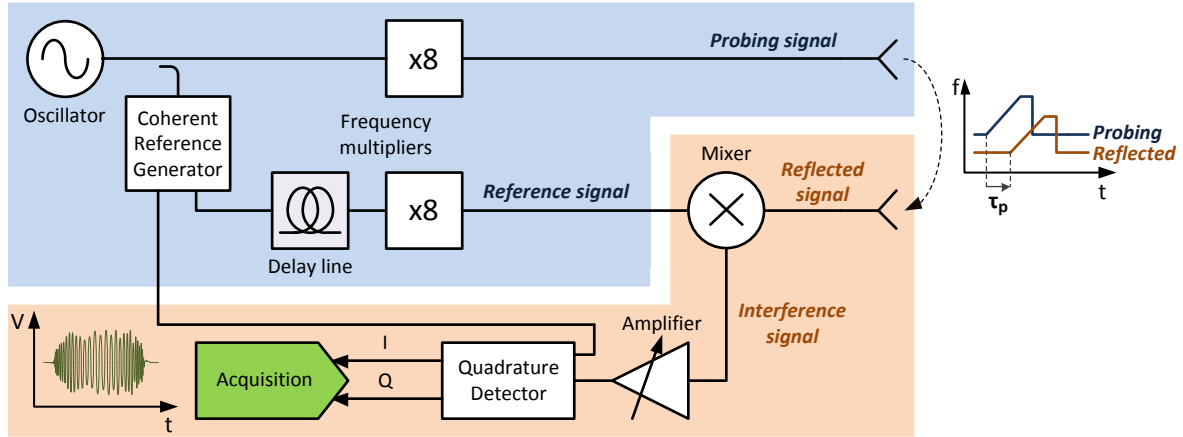


Figure 3.11: Heterodyne quadrature detection topology implemented in this microwave reflectometry system.

The reflectometry system uses an heterodyne architecture with quadrature detection, whose basic topology is illustrated in Figure 3.11. A single broadband microwave oscillator is used to generate the probing signal with a linear frequency ramp. The reference signals, used for the heterodyne down-conversion and quadrature detector, are derived from the same microwave source, ensuring coherency. The probing signal is synthesized from the base oscillator signal using frequency multipliers. The probing signal is launched towards the plasma and is reflected at specific cutoff layers back towards the receiver antenna. The reflected signal corresponds to a delayed probing signal, whose delay τ_p is proportional to the distance between the reflectometry antennas and the cutoff layers, and is dependent on the probing frequency f . The received signal is mixed with the coherent reference to obtain the reflectometry interference signal whose beat frequency is proportional to τ_p , around the IF carrier. A quadrature detector is used to obtain the in-phase and quadrature components (IQ) of the interference signal, which are then acquired.

3.3.1 Reflectometry architecture

The implemented reflectometry system architecture is detailed in Figure 3.12. The diagnostic is divided into back ends, which handle the lower frequency microwave signals, and front ends, which handle the 40-68 GHz U-band microwave signals. The back end transmitter generates the probing and reference signals used for the mixer and quadrature detectors of each channel. The front end transmitter, front

end receiver and back end receiver modules are replicated for each of the three reflectometry channels.

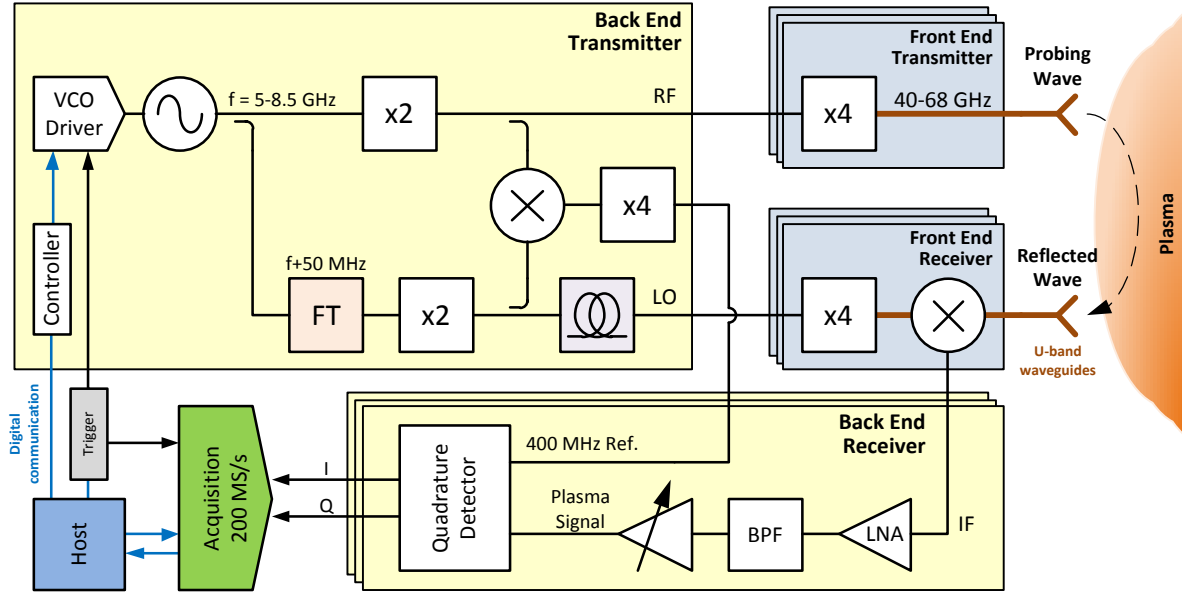


Figure 3.12: Complete architecture of the microwave reflectometry diagnostic system.

Operation description

For each trigger pulse, the microwave oscillator generates a sinusoidal signal with a linear frequency sweep between 5 GHz and 8.5 GHz. This sweep signal is doubled and quadrupled by frequency multipliers to generate the 40-68 GHz probing wave, which is launched towards the plasma by the front end transmitter. A coherent reference is derived from the same oscillator source to create the heterodyne receiver using a frequency translator (FT). The FT adds a 50 MHz offset to the LO from the probing signal, which results in a 40.4-68.4 GHz reference signal after the frequency multiplication.

The wave reflected by the plasma is mixed with the reference (LO) in the front end receiver, generating a beat signal at an intermediate frequency carrier (IF) of 400 MHz. The beat signal frequency around IF is proportional to the delay difference between the reference and the reflected waves. A coaxial delay line in the LO branch partially compensates the delay introduced by the long waveguide transmission line.

The beat signal is amplified, filtered and fed into a quadrature detector. The 400 MHz reference of the quadrature detector is coherent with the IF carrier frequency, resulting in the baseband in-phase and quadrature components of the beat signal. These are then acquired at 200 MSamples/s and uploaded to the rawfile database.

3.3.2 Microwave generation

In reflectometry, a good microwave signal quality is crucial for the correct determination of the group delays used for density profile reconstruction. The main requirements are: i) good linearity of the fre-

quency ramp; ii) fast variation of the frequency sweep ramp, in the order of a few μs , for a mostly still plasma snapshot; iii) fast reset time of the oscillator to allow repetition of the frequency sweep.

As seen in the architecture (Figure 3.12), the probing and reference signals are derived from a single fundamental oscillator using $\times 2$ and $\times 4$ active multipliers. This common source allows for a fully coherent heterodyne topology as the phase difference is maintained constant between launching antenna mouth and the reference of the mixer at the receiver front end. The resulting beat signal frequency depends only on propagation delay difference between the probing and reference signals. In addition, using a common source for all channels facilitates the calibration procedure of each channel as well as the post processing of the raw data.

Frequency sweep generation

In this reflectometer a wideband Voltage Controlled Oscillator² (VCO) is used to generate the swept frequency signal. This broadband fundamental frequency oscillator is tunable between 5-8.5 GHz with tuning voltages within 0-20 V. The VCO driver³ consists in a 16-bit, 200 MHz digital to analog converter (DAC), followed by an amplifier to generate the 0-20 V tuning signal. An internal frequency calibration lookup table calculates the correct DAC values to generate the desired frequency ramp signal with rise times between 1 μs and 10 ms. Sweep times are typically set to 15 μs in this diagnostic. The beginning of each sweep is triggered by the centrally-synchronized timer controller signal.

Linearisation of the microwave generation

Microwave VCOs do not typically have a linear output frequency response to the tuning voltage. In a first approach to linearise the frequency ramp, a coarse static frequency calibration of the tuning lookup table is performed. For each desired output frequency of the lookup table, a 16-bit DAC value, used to set the 0-20 V tuning voltage, is manually set. This calibration procedure is executed after thermal stabilization of the microwave hardware (approximately 90 minutes after power up). The calibration table shown in Figure 3.13 approximates the non-linear tuning curve of the VCO. This table uses the diagnostic output frequency instead of the fundamental frequency of the VCO. The output probing frequency may have up to 24 MHz/ $^{\circ}\text{C}$ temperature drift. This effect is attenuated by performing the calibration procedure with a warm system, at least two hours after a cold boot to stabilize temperature. However, static tuning calibration does not compensate for daily temperature variations of the oscillator, which depend on the room temperature and the types of discharges being performed. A 10°C variation may introduce around 240 MHz shift in the output 40-68 GHz probing frequency. This may be improved in future upgrades by implementing an online absolute frequency calibration method similar to the markers method described in [56].

²VCO VO4280C/00 from Sivers Ima (<https://www.siversima.com/>) [99]

³The VCO driver used is the RAWGv04 from LC Technologies (<http://www.cupidotech.com/>) [100].

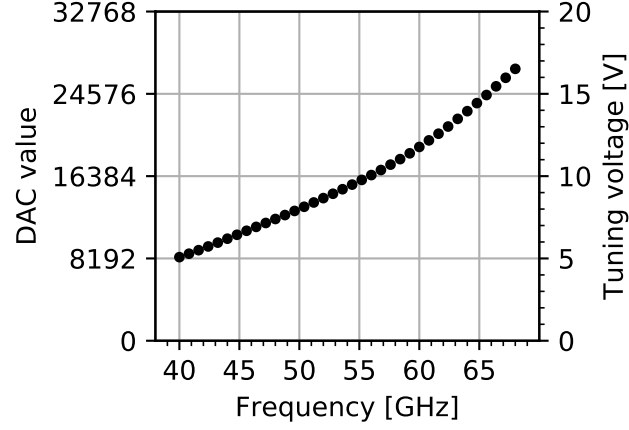


Figure 3.13: Coarse calibration of the VCO tuning lookup table for output frequency of the reflectometer.

Calibration of the dynamic oscillator tuning response

The static calibration table determines the constant output frequency for a given tuning voltage. However, in this diagnostic we require frequency sweep ramps with fast rise times of 15 μs . VCO devices present a dynamic response when the tuning voltage changes very rapidly. This dynamic response must be correctly compensated to produce a linear output frequency ramp, required for reliable density profile reconstruction [64].

Assume a chirp signal with a linearly increasing frequency f over time

$$f(t) = m * t + f_0 = \frac{df}{dt}t + f_0, \quad (3.2)$$

where f_0 is the starting frequency 40 GHz and m is the frequency sweep rate. A linear frequency sweep between 40 GHz and 68 GHz, with a sweep time of 15 μs , should have a constant sweep rate of $m \approx 1.87 \text{ GHz}/\mu\text{s}$.

The circuit represented in Figure 3.14 can be used to measure the frequency sweep rate. The frequency sweep signal is generated by the oscillator and a directional coupler splits the input signal into two branches, LO and RF. A delay τ_{dl} is introduced in the RF branch using a coaxial delay line having a known constant group delay versus frequency response, measured with a Vector Network Analyzer (VNA). The mixer produces a beat signal whose frequency is proportional to the introduced delay and the sweep rate.

The dynamic calibration setup is installed at one of the RF output ports of the back end transmitter. The signal here is doubled from the base frequency using $\times 2$ multipliers to 10-17 GHz. A delay of $\tau_{dl} = 17.980 \text{ ns}$ is introduced between LO and RF. The sweep rate evolution during a 15 μs sweep, using the original static calibration, is shown in Figure 3.15 (left), corrected to the system's output 40-68 GHz probing frequency range. It can be seen that the actual sweep rate differs slightly from the expected linear sweep, represented by the horizontal line. The corresponding frequency ramp in Figure 3.15 (right) deviates up to 113 MHz from the linear response.

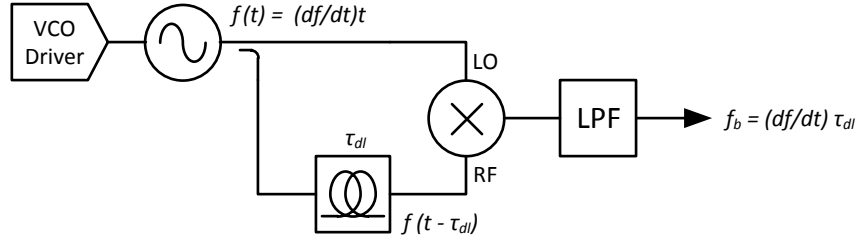


Figure 3.14: Dynamic frequency calibration setup. The resulting beat signal frequency is proportional to the sweep rate and the delay between the LO and RF signals.

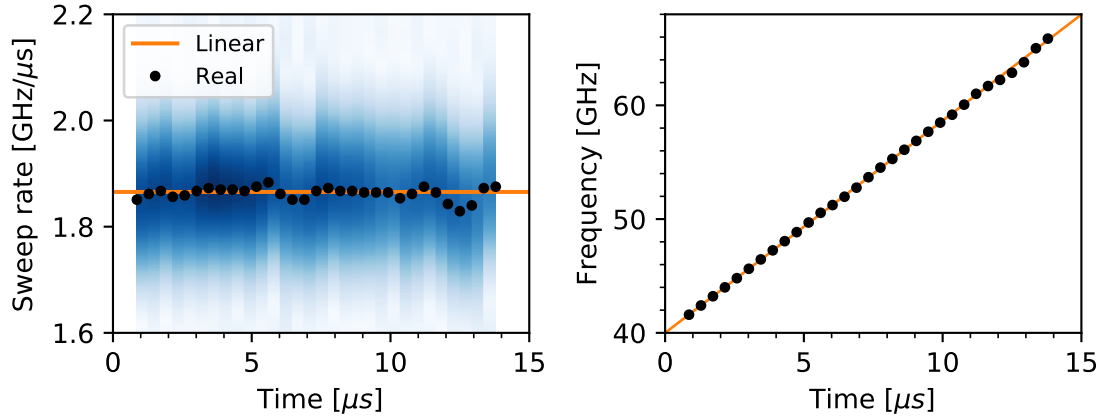


Figure 3.15: Sweep rate variation (left) of the VCO response using a static calibration and resulting frequency ramp (right). The maximum frequency non-linearity is 113 MHz.

The calibration table may be recalculated using this sweep rate information in order to compensate for the dynamic frequency response of the VCO. An iterative algorithm was developed to perform this dynamic calibration automatically. First, for a given calibration table, the corresponding instantaneous sweep rates are obtained. Then the error between the real and the linear frequency ramps is calculated, and this error is compared with the DAC look up table. The starting table value, corresponding to f_0 , is initially estimated using precise frequency counter measurements. Then, for each calibration point, a new DAC value is recalculated from the previous DAC point and the frequency error in the corresponding interval. By executing this algorithm iteratively, the calibration table will converge to a linear dynamic frequency response. The final calibrated response is shown in Figure 3.16, improved over 27 iterations. The maximum frequency non-linearity was improved to 38 MHz ($<0.01\%$). This calibration is performed once per operational campaign, to compensate for the aging of the oscillator. An online dynamic calibration module may be added in the future to recalibrate the oscillator between discharges and correct the acquired reflectometry measurements in post processing.

Beat frequency uncertainty regions

The reference signal has a linearly increasing frequency ramp, coherent with the probing signal. The plasma reflection signal is affected by different propagation delays which depend on the frequency of the

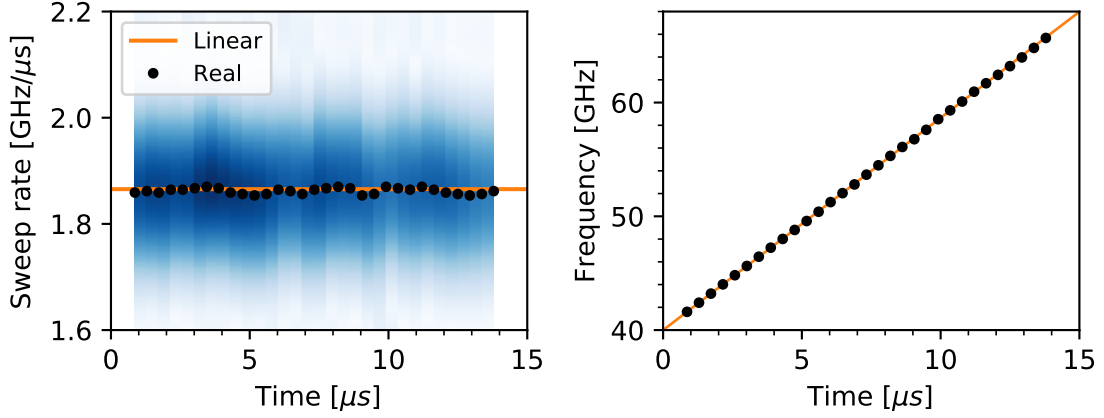


Figure 3.16: Sweep rate variation (left) of the VCO response using after 27 iterations of the dynamic calibration algorithm and resulting frequency ramp (right). The maximum frequency non-linearity is 38 MHz.

probing wave: $\tau_g(f_p)$. The reflectometry interference signal is the instantaneous frequency difference between the reference and the received plasma reflection signal. Since there is a necessary delay between these two signals, there are two uncertainty regions at the beginning and end of the frequency ramp, with a time width equal to the instantaneous delay, as illustrated in the exaggerated case of Figure 3.17.

These uncertainty regions effectively reduce the valid probing bandwidth of the diagnostic. However, this uncertainty typically corresponds to less than 3 samples at either end of the probing band, using our acquisition system, and are negligible to the reflectometry measurement, corresponding to $<0.2\%$ of the probing range.

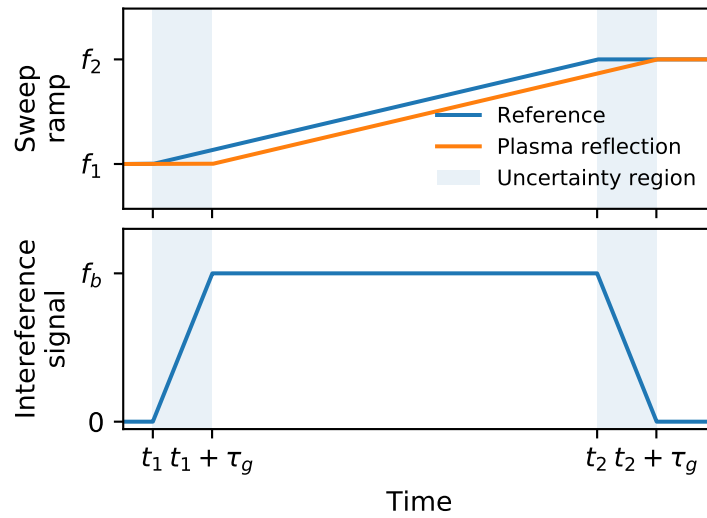


Figure 3.17: Beat frequency uncertainty due to reflection delay.

3.3.3 Generation of coherent references

Heterodyne receivers and quadrature detectors provide a better sensitivity and selectivity of the plasma reflection signal than homodyne detection. In addition, the quadrature detection also allows a direct measurement of the phase, contrary to homodyne architectures. The heterodyne topology adopted in this system uses two reference signals coherent with the probing signal. The frequency difference between the references and the probing signal is deterministic since they are derived from a single oscillating source. This coherency means that thermal variations or non-linearity of the source signals equally affect the references and the RF signal, making the heterodyne down-conversion procedure immune to these variations.

The first LO reference is a swept frequency signal shifted 400 MHz from the swept probing RF frequency. Mixing the LO and the reflection RF signals in the receiver results in a intermediate frequency signal centered at 400 MHz. The second reference is a 400 MHz baseband signal used to demodulate the beat signal into its in-phase and quadrature components. The frequency shifts of these references are generated using a frequency translator and derived from a pure 50 MHz source.

Frequency translator

The frequency translator (FT) uses a double frequency conversion design similar to the technique implemented in [101]. This double frequency conversion uses two mixers and two synchronized local oscillators to introduce a frequency shift on the LO signal. The diagram for the frequency translator, and relevant frequencies, is shown in Figure 3.18.

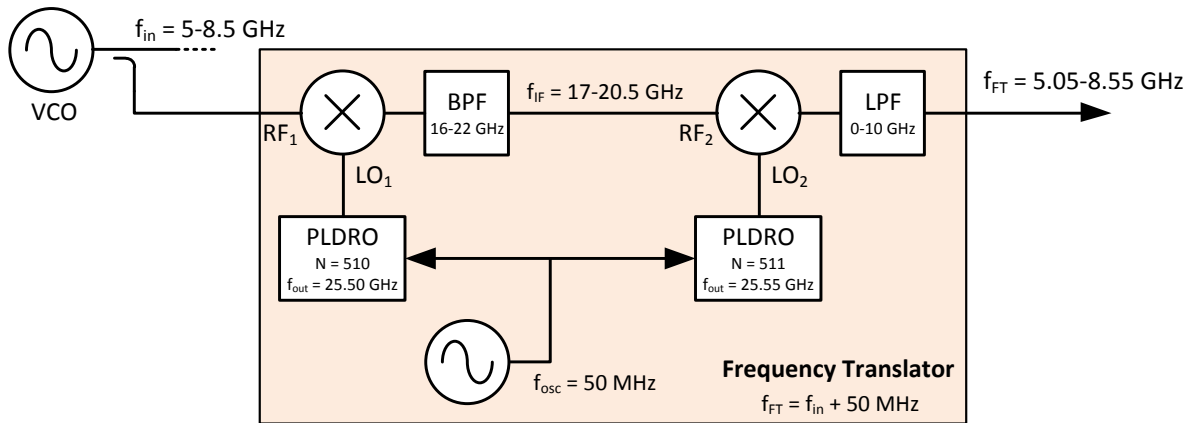


Figure 3.18: Diagram of the frequency translator module that introduces a +50 MHz shift to the input signal.

Two phase locked dielectric resonant oscillators (PLDRO)⁴ are synchronized with a fundamental oscillator clock. This temperature controlled oscillator clock⁵ generates a pure 50 MHz signal to derive the frequency shifts of the references. The output frequency of each PLDRO is a multiple ($N = 510$ or 511) of the base clock.

⁴PLDRO from Microwave Dynamics

⁵Oven controlled 50 MHz Sprinter Crystal Oscillator 501-27513-32 from Wenzel Associates, Inc. [102]

The input 5-8.5 GHz RF_1 signal is mixed with the first LO_1 signal of 25.50 GHz, and up converted to a higher intermediate frequency (IF) signal

$$f_{IF} = f_{LO_1} \pm f_{RF_1}. \quad (3.3)$$

A band pass filter removes the higher frequency sideband ($f_{LO_1} + f_{RF_1}$) and the lower frequency (f_{RF_1}) components that may still contaminate the mixer product signal. The filtered up converted IF signal varies between 17-20.5 GHz. This IF signal is mixed with the second LO_2 signal of 25.55 GHz, and low pass filtered, resulting in baseband output signal of 5.05-8.55 GHz: a 50 MHz up shift of the input signal.

The FT setup was designed so that the frequency windows from each step do not overlap and are appropriately filtered. This facilitates image rejection, improves isolation between the input and output, and decreases the effect of spurious signals.

Generation of reference for quadrature detectors

The quadrature detectors demodulate the beat signal, with a 100 MHz bandwidth around 400 MHz, to its baseband in-phase and quadrature components. A coherent 400 MHz reference is obtained from the RF and LO branches, as shown in Figure 3.19. A base 100 MHz signal is obtained by mixing the 10-17 GHz RF and the 10.1-17.1 GHz frequency shifted LO signals, after the respective $\times 2$ multipliers. A $\times 4$ multiplier⁶ provides the 400 MHz reference used in the quadrature detectors. This 400 MHz reference is coherent with the 400 MHz IF carrier signal.

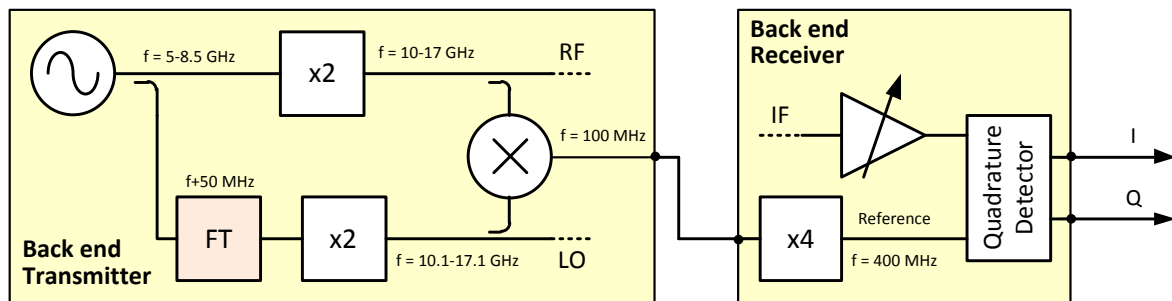


Figure 3.19: Diagram of the 400 MHz reference generation.

3.3.4 Transmitter and receiver front ends

Each reflectometry channel has dedicated front end pairs for a total of three transmitter and three receiver front ends, as illustrated in Figure 3.20. The TX front ends contain a single active $\times 4$ multiplier each, which generate the output 40-68 GHz probing signal. Each RX front end contains a heterodyne mixer detector, whose LO port is driven by a coherent 40.4-68.4 GHz reference signal.

The active multipliers and the detection mixers connectors are U-band waveguide ports, which allow the front ends to be attached directly to the transmission and reception waveguides. Microwave isola-

⁶RM040H from LCTech [100]

tors, with magnetic shielding, are placed at the output of the TX front end and at the input of the RX front end. The TX isolator prevents the reflected signal and stray radiation from the vessel from damaging the active multiplier. The RX isolator reduces the LO signal leaking to the waveguides, which might result in spurious reflections. In addition, low pass filters⁷ are placed between the front ends and the connected waveguides. These filters provide protection of the microwave components from stray microwave radiation that may creep into the waveguides, such as due to 105 GHz and 140 GHz ECRH operation or runaway electrons.

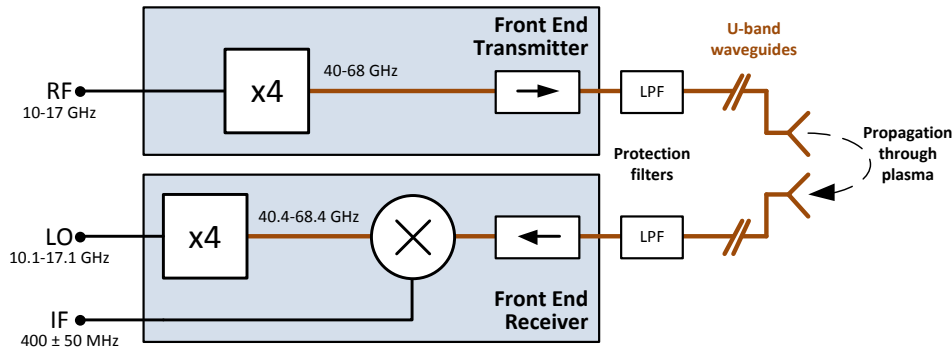


Figure 3.20: Diagram of the microwave reflectometry front ends, protection filters and connecting waveguides.

Output power of the active multipliers

The output power of the active multipliers, shown in Figure 3.21, was tested for the extended U-band operation by the manufacturers⁸. The power is maintained above +15 dBm up to 60 GHz but drops in the 60-68.40 GHz range. This drop is an inherent condition of the multiplier and results in a loss of reflectometry measurement quality for probing frequencies above 60 GHz. The three multipliers with the highest output power were selected to produce the probing beams while the remaining three are used to generate the LO signals used to drive the receiver detection mixers.

Mixer conversion losses

The conversion loss of the mixer⁹ used for coherent detection depends mainly on the frequency and power of the LO signal. Figure 3.22 shows the measured conversion losses of the mixer for different LO driving powers. The high LO power up to 60 GHz provides the lowest conversion loss of the mixer. However, the combination of both the reduced LO power and increased conversion losses results in a worse detection performance in the 60-68 GHz range.

⁷Spacek Labs LPF3-Q-7 low pass filters with 40 dB rejection at 104-142 GHz.

⁸Active multipliers model AMC-19-RFH00 from millitech [103]

⁹Mixers model CMB68680211-01 from CernexWave [104]

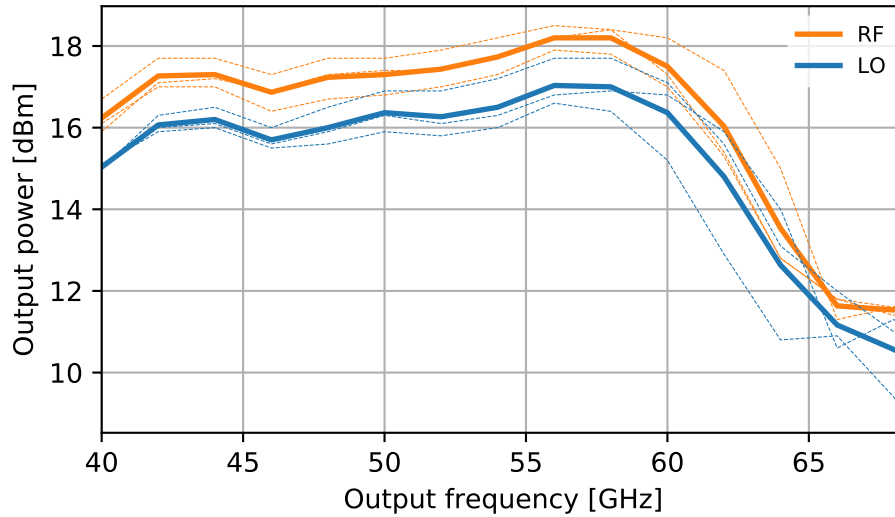


Figure 3.21: Output powers of the $\times 4$ active multipliers used for probing the plasma (RF) and driving the receiver mixer (LO). The dashed lines represent the output power of each device, while the solid lines represent the average output power for the RF and LO drivers.

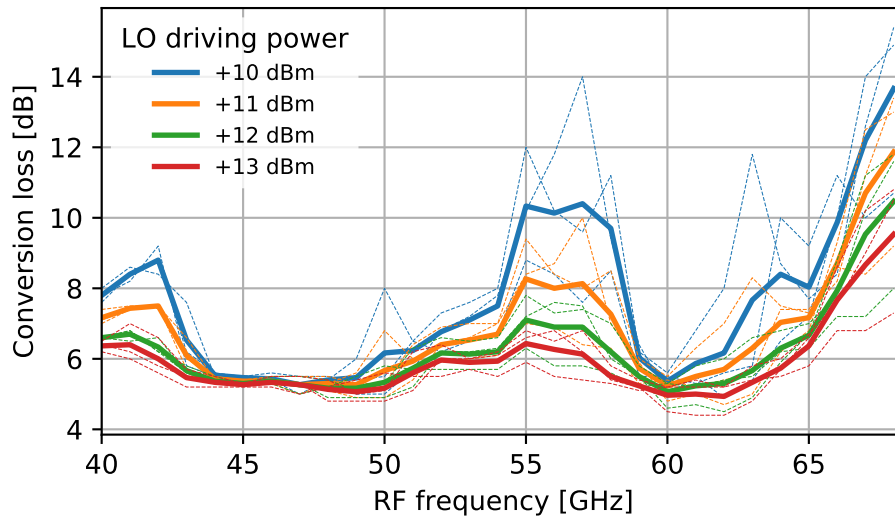


Figure 3.22: Conversion losses of the front end mixers for different LO driving powers and a -5 dBm RF signal with a +400 MHz frequency difference from the LO. For each LO driving power, the dashed lines represent the individual conversion losses of the three detection mixers, while the solid lines represent the respective averaged conversion losses.

Microwave power balance

Mixer detectors typically have noise floors lower than -60 dBm. In order to estimate the expected SNR of our diagnostic, all the loss contributions along the signal path were calculated and are shown in Figure 3.23 (left). These loss measurements were obtained from either experimental data provided by the component manufacturer or measured after the assembly and installation of the ICRF antenna and reflectometry waveguides. Lossy microwave components consist of: i) two protection isolators on each TX and RX front end; ii) four DC breaks that separate the TX and RX waveguides in contact with the

torus hall ground, the vacuum vessel ground and the inner plasma facing components ground; iii) the vacuum window flanges; iv) the TX and RX waveguides, which have different lengths for the different reflectometry channels; v) and the mixer conversion losses.

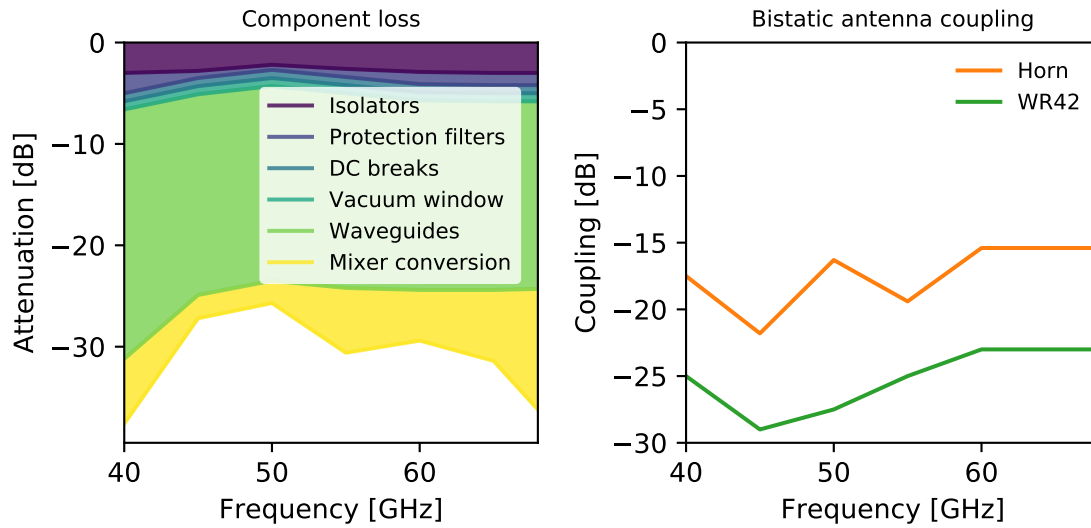


Figure 3.23: Losses of the microwave components and coupling of the bistatic horn and WR42 antennas.

The coupling between the TX and RX bistatic antennas depends on the kind of antenna being used: horn or WR42 taper. The coupling using either of these antenna types is shown in Figure 3.23 (right). The coupling measurement was performed using a metallic mirror 10 cm away from the reflectometry antenna, aligned perpendicular to the beam path for maximum coupling. It is expected that the channels 1 and 8, using horn antennas, have a better reflection signal power than channel 4, which uses WR42 tapers as antennas. It can be seen that the long waveguide length, the coupling between the plasma and the antennas, and the mixer conversion losses introduce the most losses in the reflectometry signal.

Figure 3.24 shows the average transmission power and the expected received signal power when using either of the antenna types. Despite the high signal losses, the estimated SNR is at least 10 dB.

3.3.5 Amplification and quadrature detection

The beat signal has an intermediate frequency around a 400 MHz carrier. This beat signal is filtered and amplified before being demodulated into its baseband in-phase and quadrature components. The amplification and quadrature detection procedure is illustrated in Figure 3.25. A 30 dB low noise amplifier with embedded band pass filter¹⁰ (400±50 MHz) is used at the input stage of the receiver back end, followed by a 0-60 dB variable gain amplifier¹¹. The gain of each channel can be adjusted independently and is digitally set by the reflectometry controller, with a 0.15 dB resolution. The quadrature detector¹² down converts the beat signal to the DC ±50 MHz quadrature components, which are then acquired at 200 MSamples/s.

¹⁰Band pass filtered low noise amplifier IFA0401 from LCTech [100].

¹¹IFVA0515/A from LCTech [100]

¹²QDet from LCTech [100]

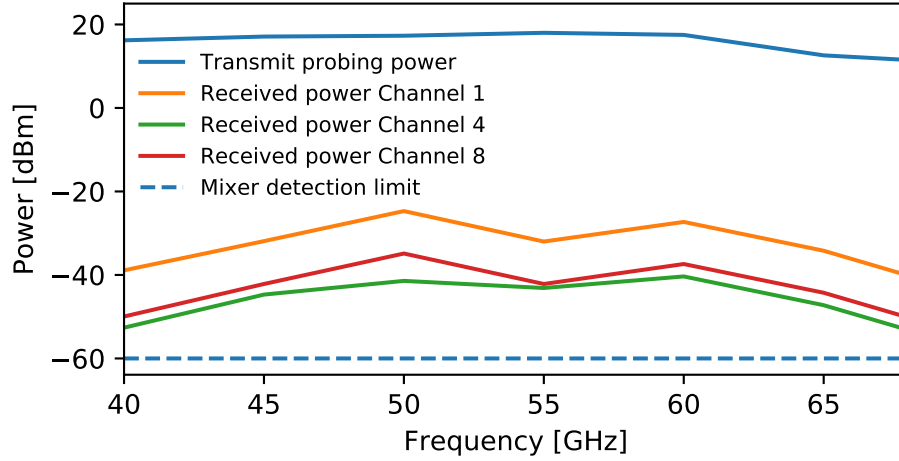


Figure 3.24: Power output and expected measurement signal power of horn and WR42 antennas.

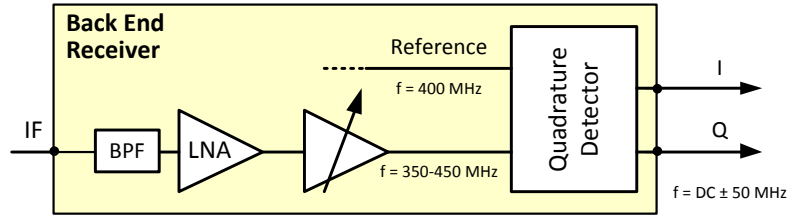


Figure 3.25: Intermediate signal conditioning diagram and quadrature detection.

3.3.6 Reflectometer bandwidth

The bandwidth (BW) of the reflectometer must accommodate the maximum beat frequency of the reflectometry interference signal. The beat frequency is determined by the frequency sweep rate df/dt and the group delay difference τ_g between reflection and reference signals.

$$\max(f_b) = \frac{df}{dt} \max(\tau_g) < BW \quad (3.4)$$

This delay difference is proportional to the propagation inside the waveguide τ_{wg} and through the plasma τ_p , inside the vessel, minus the delay compensated with dedicated delay lines τ_{dl} .

$$\tau_g = \tau_{wg} + \tau_p \quad (3.5)$$

Waveguides are dispersive mediums that have a non-linear frequency-dependent propagation delay that is proportional to the length of the waveguide. The propagation delay curve of a 10 m long WR19 waveguide is shown in Figure 3.26. This waveguide propagation delay is the accumulated delay introduced in the received signal, as the probing signal propagates through the TX and RX waveguides up to the detector. Such a high delay difference between the received and reference signals results in an unnecessarily high beat frequency. To reduce the beat frequency, we introduce a delay line in the

reference signal path with a constant delay τ_{dl} ,

$$\tau_{wg} = \tau - \tau_{dl}. \quad (3.6)$$

Still, the resulting variation of the waveguide delay τ_{wg} is approximately 15 ns for a probing frequency of 40 GHz, and 1 ns for 68 GHz. This non-linear delay variation is added to the plasma propagation delay, and must be accommodated by the input bandwidth of the reflectometry system.

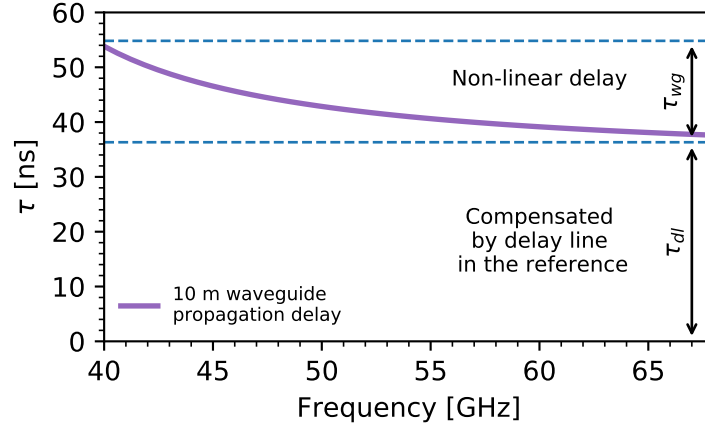


Figure 3.26: Non-linear propagation delay of a 10 m long WR19 waveguide as a function of wave frequency.

Delay line compensation

Each reflectometry channel has dedicated TX and RX waveguides, resulting in different electrical paths for the probing waves. In order to reduce the beat signal frequency to within the receiver ± 50 MHz bandwidth, the delays for each channel, $\tau_{dl1,4,8}$, must be individually compensated.

The delay compensation is performed by adding coaxial delay lines to the reference paths. This is performed in two steps using a coarse and fine delay adjustments. A first step adds a coarse delay contribution, matching most of the common waveguide delay of all channels. This delay was achieved by using a long coaxial line of around 8.05 m compensating a constant 38.21 ns delay¹³. This delay line (DL) is then power split by three¹⁴ and connected to three shorter coaxial delay lines that compensate the individual channel waveguide delays. The structure of the coarse and fine delay lines is illustrated in Figure 3.27.

Even though the delay lines have a constant delay in the desired frequency band, they have different attenuations that increase with the frequency. The reference branch, where these DLs are located, must be used to drive the input port of the front end $\times 4$ multiplier. The DL design must guarantee enough driving power in the worst case, but still below the maximum input power for all the frequencies. For this purpose, the attenuation of each DL segment and the power divider were measured for the best

¹³Coaxial delay measurements were performed using an Anritsu 37269D Vector Network Analyzer.

¹⁴3-way power splitter AS7392 from AtlanTecRF.

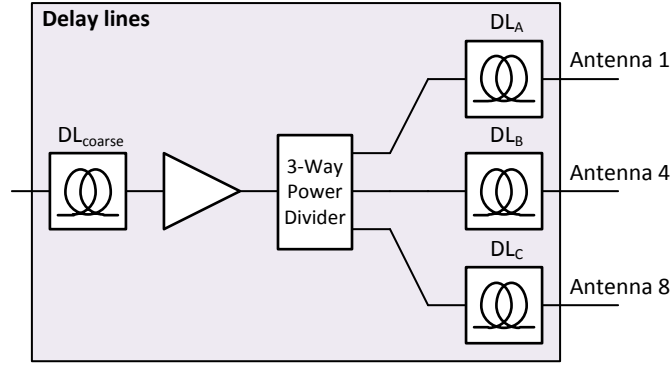


Figure 3.27: Diagram of the coarse and fine delay lines.

(40 GHz) and worst (68 GHz) cases. The lengths, delays and attenuation of the coarse and fine DL are represented in Table 3.2. The maximum attenuation difference between 40 GHz and 68 GHz in these delay lines is 7.7 dB, which falls within the LO driving power range of the front end mixers. If necessary, an amplitude equalizer may be added to compensate the amplitude difference between the frequency limits.

Table 3.2: Measured lengths, delays and attenuations of each delay line segment.

	Length [m]	Delay [ns]	Attenuation [dB]	Accumulated	
DL_{coarse}	8.05	38.21	12.5 to 19	Delay [ns]	Attenuation [dB]
DL_A	0.35	1.23	0.6 to 1.2	39.44	13.1 to 20.2
DL_B	1.34	6.41	2.2 to 3.4	44.62	14.7 to 22.4
DL_C	1.63	7.73	2.7 to 3.7	45.94	15.2 to 22.7

Determining the optimal sweep rate

Figure 3.28 illustrates the beat frequency distribution for different sweep rates and group delays. It can be seen that the beat frequency is proportional to both the group delay and sweep rate. The diagnostic was designed to have 50 MHz single sided bandwidth, which corresponds to the maximum measurable beat frequency, signaled by the contour line in the figure.

The measurement bandwidth of the diagnostic and the expected group delay variation within the probing band determine the required sweep rate of the diagnostic. The maximum non-linear group delay variation of the waveguides of channels 1, 4 and 8 are also represented as $\tau_{wg1,4,8}$, respectively. These set the minimum required bandwidth, or maximum sweep rate, for the reflectometry system. For example, a reflectometry system with an input bandwidth of 50 MHz is able to observe reflections up to 18 ns with a sweep rate of (40-68 GHz)/10 μ s. However, at this sweep rate, the waveguide propagation delays already contribute with a group delay above the reflectometer 50 MHz bandwidth threshold, except for channel 1. Since all channels share the same microwave source, the maximum sweep rate of the diagnostic must accommodate the highest waveguide delay.

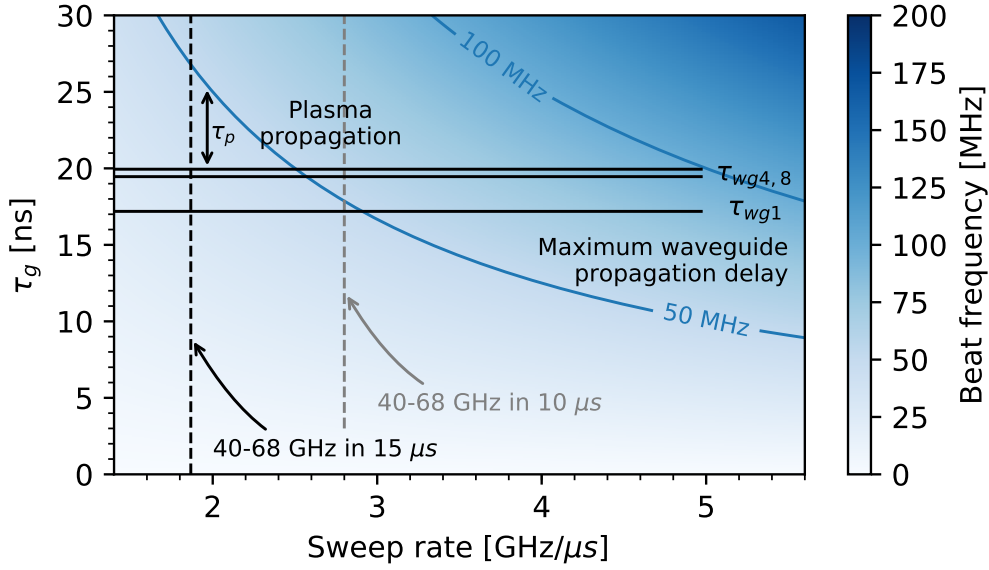


Figure 3.28: Distribution of the beat signal frequency as a function of the sweep rate and total delay of the received reflectometry signal.

A slower 15 μs sweep, on the other hand, can measure delays up to 27 ns. This slower sweep rate is able to accommodate the waveguide dispersion delay and also provides an approximately 7 ns margin for the plasma propagation measurement (τ_p), which is enough for the typical X-mode upper cutoff group delays on ASDEX Upgrade.

With this analysis, the reflectometry diagnostic was specified to operate with a 28 GHz/15 μs sweep rate. This sweep time allows approximately 3000 samples to be acquired per reflectometry measurement using the maximum sampling frequency of the acquisition system.

The repetition rate of the measurements is limited by the reset time of the HTO, which imposes a dead time between sweeps. Tests have shown that the HTO behaves differently during frequency ramp up and ramp down. An input voltage step down takes approximately 10 μs before settling the output frequency at the start frequency of 40 GHz (8×5 GHz). Reducing this dead time would not give the HTO enough time to settle at the expected frequency — the sweep ramp would start at a higher than expected frequency. For this reason, the maximum repetition rate is set at 25 μs to ensure that the frequency sweep rate starts at 40 GHz. Typically, the repetition rate is set at 100 μs to capture the whole discharge, due to memory constraints of the acquisition system. The diagnostic is capable of measuring plasma density profile fluctuations up to 40 kHz using the 25 μs rate.

3.4 Diagnostic support systems

The diagnostic support system consists in the data acquisition system and the host computer that configures and triggers the reflectometry hardware and handles its integration within the ASDEX Upgrade infrastructure.

Data acquisition

The acquisition system uses the Advanced Telecommunications Computing Architecture (ATCA) standard and communicates with the host computer through a PCI Express link. In this system, a single acquisition board with eight channels is installed in the ATCA case. This acquisition system was developed by IPFN and is further described in [105]. Up to five acquisition boards can be installed in a single ATCA crate, enabling future upgrades of the number of reflectometry channels.

The acquisition system has a ± 1.1 V 13-bit resolution, 190 MHz input bandwidth, and a maximum sampling rate of 200 MSamples/s. Each group of four channels share 2 GB of internal memory, allowing 512 MB of data to be acquired per discharge per channel. A total of six acquisition channels are used to acquire the in-phase and quadrature reflectometry signals from antennas 1, 4 and 8.

Before the discharge, the host computer configures the acquisition sampling rate, number of samples per sweep and total number of sweeps. The maximum number of sweeps that can be acquired, or density profiles that can be measured, during a discharge is limited by the allocated memory to each channel. Around 89 thousand profiles are acquired per discharge in the typical three-channel operational configuration.

Host computer

The host and control computer connects to the ASDEX Upgrade network through an optical fiber network switch. This host computer handles the configuration of the reflectometry hardware and of the data acquisition system. It integrates a universal time-to-digital converter (TDC) [106] to generate synchronized triggers for the frequency sweep generation and acquisition. The host computer uses an Intel 3.1 GHz quad-core CPU¹⁵ and has 4 GB of RAM. A local 240 GB solid-state drive (SSD) temporarily stores the acquired raw data files before uploading to the shotfile database. Using an SSD is a requirement for this diagnostic as it is unaffected by strong magnetic fields, while typical mechanical hard disk drives might fail during a discharge. Two ethernet network interfaces are installed on the computer: one connects to the ASDEX Upgrade network while the other is isolated to communicate with the reflectometry hardware on a local network, for security reasons. The host computer is dedicated to operating the diagnostic while the density profile reconstruction is outsourced to the computation facilities. A remotely controlled power bar allows shutting down the mains power supply separately to the host computer, the acquisition system and the reflectometry hardware.

3.5 Summary

This chapter describes the development and installation of the new microwave reflectometry diagnostic for density profile measurements. The operational range of ASDEX Upgrade sets the main specification requirements for the reflectometry system. Ten reflectometry antennas and waveguides were embedded in the new three-strap ICRF antenna design installed on ASDEX Upgrade. The poloidal and toroidal

¹⁵Intel® Core™ i5-4440 CPU @ 3.10GHz

distribution, and corresponding lines of sight, of the available reflectometry channels were shown. Only three of the ten available reflectometry channels are currently instrumented, with the possibility of more channels to be added in the future.

The reflectometry architecture has a coherent microwave generation which improves the reliability of the heterodyne detection. The microwave generation was linearised using an initial static procedure, followed by a calibration of the dynamic frequency response of the oscillator to improve the accuracy of output frequency during fast sweeps. The power balance analysis showed that the received signal power is above detection limit. A delay line brings down the reflectometry beat signal frequency to within the bandwidth of the detector. A sweep time of 15 μs was specified, which allows the measurement of group delays up to 27 ns.

Chapter 4

Commissioning of the reflectometry diagnostic

The new reflectometry system was installed in November 2015 on ASDEX Upgrade and has been operating throughout the 2016 and 2017 experimental campaigns. During this period, the diagnostic was commissioned to ensure reliable operation under most conditions. This chapter describes the different stages of the diagnostic commissioning. First we analyse the raw X-mode reflectometry signal measurement under different conditions and the calibration of the waveguide dispersion [107]. Then the first fringe estimation algorithms are detailed [108]. These must provide a reliable estimation of the vacuum distance and the start of the upper cutoff reflection. Finally, the steps required for the density profile reconstruction are explained, including group delay measurements, data validation tests, and automatic profile processing.

4.1 Analysis of the raw reflectometry measurement

The microwave reflectometry diagnostic works similarly to a radar measuring reflective surfaces inside the vessel. These reflective surfaces can be the plasma layers or any metallic object inside the vessel, such as the back wall or the Faraday screen protecting the ICRF antenna.

The multiple reflections present in the reflectometry measurement can be easily distinguished by analysing the spectrogram of the beat signal. The total group delay τ of the reflections is given by

$$\tau = \tau_{wg} + \tau_g, \quad (4.1)$$

where τ_{wg} is the delay of the propagation inside the waveguides and τ_g is the delay of the propagation inside the vessel. The reference must be set at the mouth of the antennas, at the end of the waveguides, so that reflections close to the reference position have a lower delay signature than those further away. An example of the raw reflectometry measurement of the three installed channels 1, 4 and 8, is detailed in Figure 4.1. To increase contrast and improve visibility, the spectrograms were normalized within each

window and the amplitude is represented in logarithmic range. Multiple reflections can be observed in the measurements, besides the main plasma reflection.

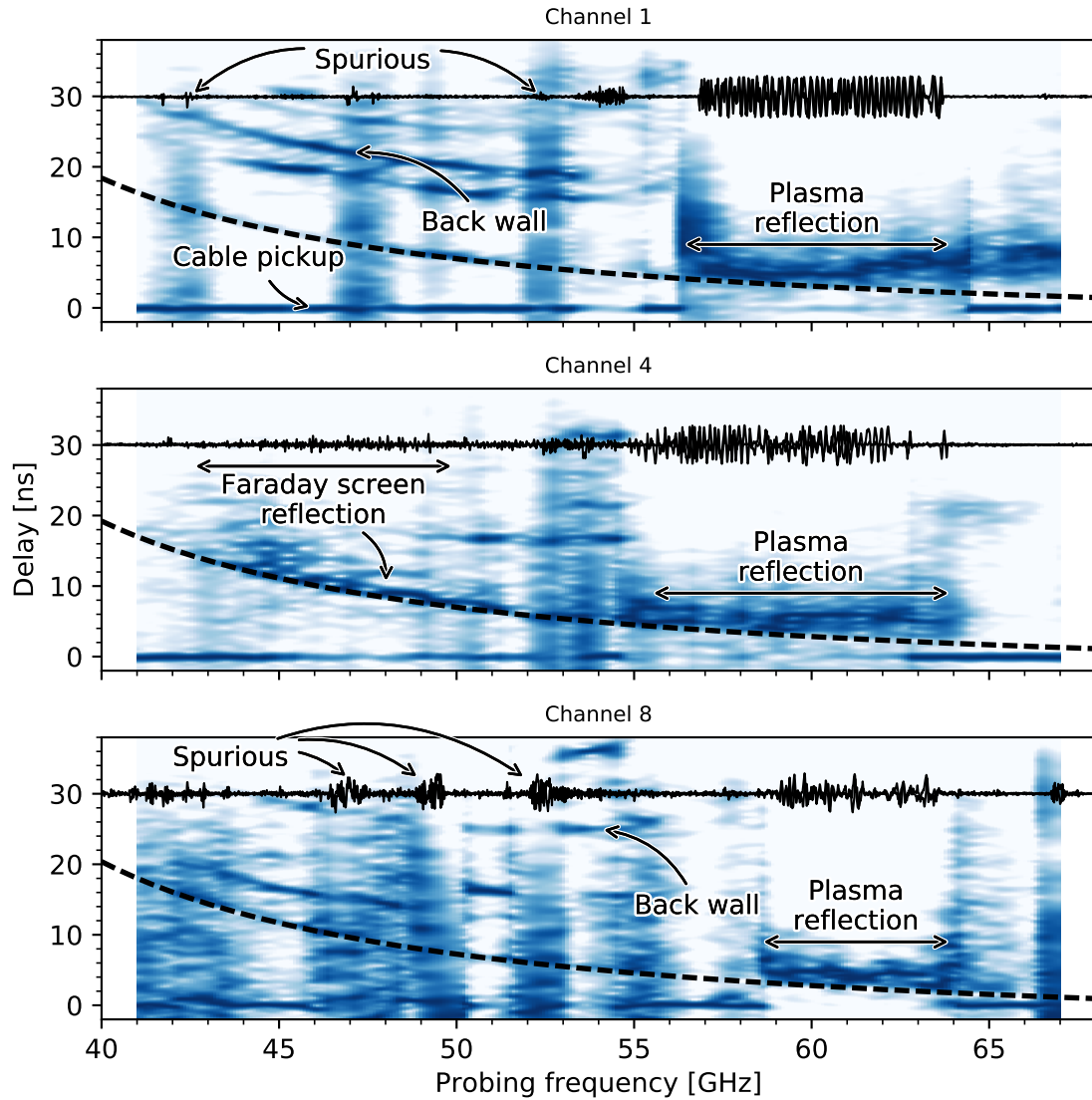


Figure 4.1: Reflectometry group delay reflection signals measured at the beginning (70 ms) of discharge #33490 with $B_0 = -2.6$ T. The reflection signatures of the edge plasma, the back wall and the Faraday screen can be seen.

Firstly, the plasma reflection signal can be distinguished by the clear rise of the amplitude of the raw signal around 55-60 GHz. The cutoff frequencies at which the plasma reflections occur vary between the channels since the reflectometry antennas have different radial positions and, consequently, different local magnetic fields. Antenna 4 is the furthest away from the machine center, resulting in a lower magnetic field and lower cutoff frequencies of the plasma reflections than antennas 1 and 8.

The consequences of the low transmitter power and high conversion losses of the microwave front ends are clearly observed in the low signal power towards the end of the probing band.

Multiple low amplitude spurious signals contaminate the measurement. These spurious result in a lower SNR in channel 8, which has an increased amplification gain than other channels.

The curved shapes of the waveguide dispersion are clearly visible in each channel. The reflectometry antenna references, represented by the dashed lines, follow the shape of the waveguide dispersion. These are later removed using the calibration procedure described in section 4.2.

A DC component is observed in all measurements. This signature does not follow the delay curve of the waveguide dispersion, indicating that it might be the result of low frequency cable pickup due to the long coaxial cables that connect the baseband reflectometry beat signals to the acquisition system.

The reflectometry antennas are located along the outer vessel wall. The distance between the inner and outer vessel walls is approximately 1.3 m. Waves launched by the reflectometry antennas propagate inside the vessel and may be reflected by the inner vessel wall. This back wall reflection appears in the measurements of channels 1 and 8.

A high reflection signal is detected with a group delay very close to the antenna 4 reference. This signature is consistent with the reflectometry signal being partially reflected at the straps of the Faraday screen.

Nonetheless, the plasma reflection provides a very clear spectral signature in all channels. The spurious features of the spectrogram are overwhelmed by the higher plasma reflection power and the back wall ceases to be visible. The group delay used for density profile reconstruction is determined at this plasma reflection layer.

4.2 Calibration of the waveguide dispersion

Microwave waveguides are dispersive mediums. A wave propagating in a dispersive medium suffers a delay that depends on its frequency and is proportional to the length of waveguide. These delays can be understood by analyzing the propagation modes inside waveguides. The modes inside a hollow rectangular waveguide have cutoff frequencies given by

$$f_c = \frac{1}{2\sqrt{\mu\epsilon}} \sqrt{\left(\frac{m}{a}\right)^2 + \left(\frac{n}{b}\right)^2}, \quad (4.2)$$

where m, n correspond to the propagation mode, a and b are the longer and shorter edges of the rectangular cross section, respectively, and μ is the permeability and ϵ is the permittivity of the medium inside the waveguide. The fundamental TE₁₀ mode in a U-band WR19 waveguide¹ has a cutoff frequency given by

$$f_c = \frac{c}{2a} \approx 31.391 \text{ GHz}, \quad (4.3)$$

where a is the longer edge of the rectangular waveguide. The group velocity of a wave with frequency f inside a waveguide can be calculated by

$$v_g = c \sqrt{1 - \left(\frac{f_c}{f}\right)^2}. \quad (4.4)$$

¹WR19 waveguides have standard dimensions of 4.775 mm per 2.388 mm.

And the delay of a wave propagating inside a waveguide of length l is

$$\tau_g = \frac{l}{v_g}. \quad (4.5)$$

Figure 4.2 shows the non-linear group delays of waves propagating in waveguides of different lengths.

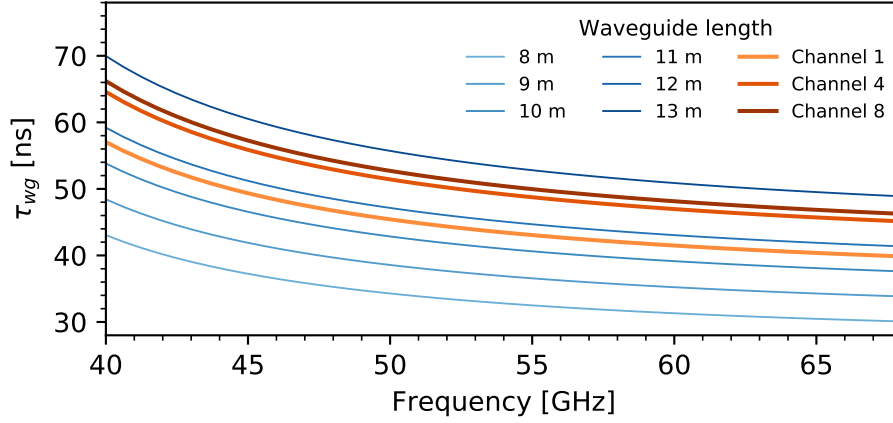


Figure 4.2: Non-linear wave propagation delays inside WR19 waveguides of different lengths.

4.2.1 Calibration setup

The probing waves of each reflectometry channel propagate through dedicated waveguides of different lengths. These must be properly calibrated to correctly determine the reference at the mouth of the antenna.

The individual coaxial delay lines installed in the reflectometry hardware compensate up to 46 ns of the waveguide dispersion delay, reducing the beat signal frequency to within the input bandwidth. This allows using the installed reflectometry and acquisition system setup to calibrate the waveguide dispersion response.

The waveguide dispersion calibration procedure uses a metallic mirror placed at known distances in front of the reflectometry antennas, and the delays for each distance are individually measured. The free space propagation delay, which accounts for the distance between the reflectometry antenna and the metallic mirror, is removed from each measurement. The resulting measurements correspond only to the delay through the microwave waveguide and should overlap. Then, the waveguide delays are fit to the delay function [109]

$$\tau_{wg} = a + \frac{b}{\sqrt{1 - \left(\frac{f_c}{f}\right)^2}}, \quad (4.6)$$

to obtain the parameters a and b , where a includes the contribution of any constant delay introduced by the microwave components and connections inside the reflectometer, b the contribution of waveguide length, and f_c is the lower order cutoff frequency of the waveguide. These a and b parameters are stored for each channel and used to recalibrate the raw signal response.

The in-vessel calibration setup to measure waveguide dispersion of reflectometry channel 1 is shown in Figure 4.3. As this procedure requires in-vessel access, it is performed only outside the ASDEX Upgrade experimental campaigns. The calibration procedure is:

1. A metallic mirror is mounted on a standing structure inside the vessel;
2. The metallic mirror is fixed to the structure and placed in front of the reflectometry antenna;
3. The mirror is oriented perpendicular to the beam path so as to maximize reflection signal;
4. A reflectometry measurement is acquired;
5. The distance between the metallic mirror and the central point between the bistatic reflectometry antennas is taken using a measuring tape;
6. The metallic mirror is repositioned and steps 2-5 are repeated.

Multiple distances are taken to minimize the error of free space propagation. A portable computer is used to control the diagnostic and to verify the calibration measurement signal.

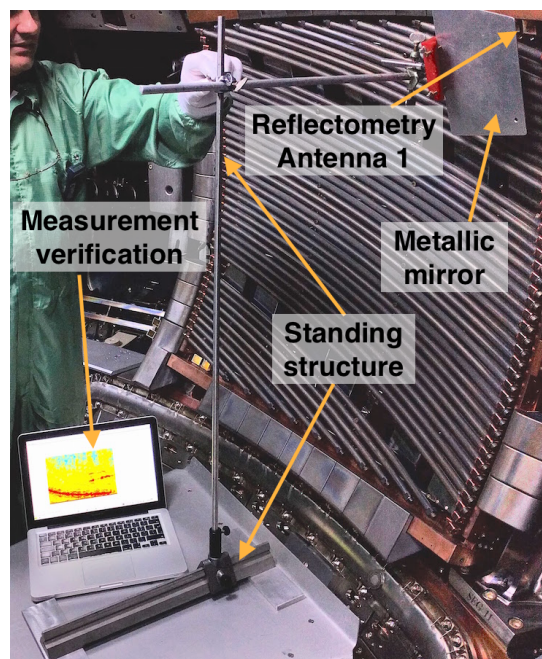


Figure 4.3: In-vessel calibration setup to measure waveguide dispersion of reflectometry channel 1.

4.2.2 Group delay measurements for multiple distances

The calibration measurement results for multiple mirror distances in front of channel are represented in Figure 4.4. There is usually a large low frequency component (near-DC) in most measurements. Tests indicated that this is the result of noise pick up in the long baseband coaxial cables between the

reflectometry back ends and the acquisition system. These do not affect the operation of the diagnostic but should be filtered in post processing.

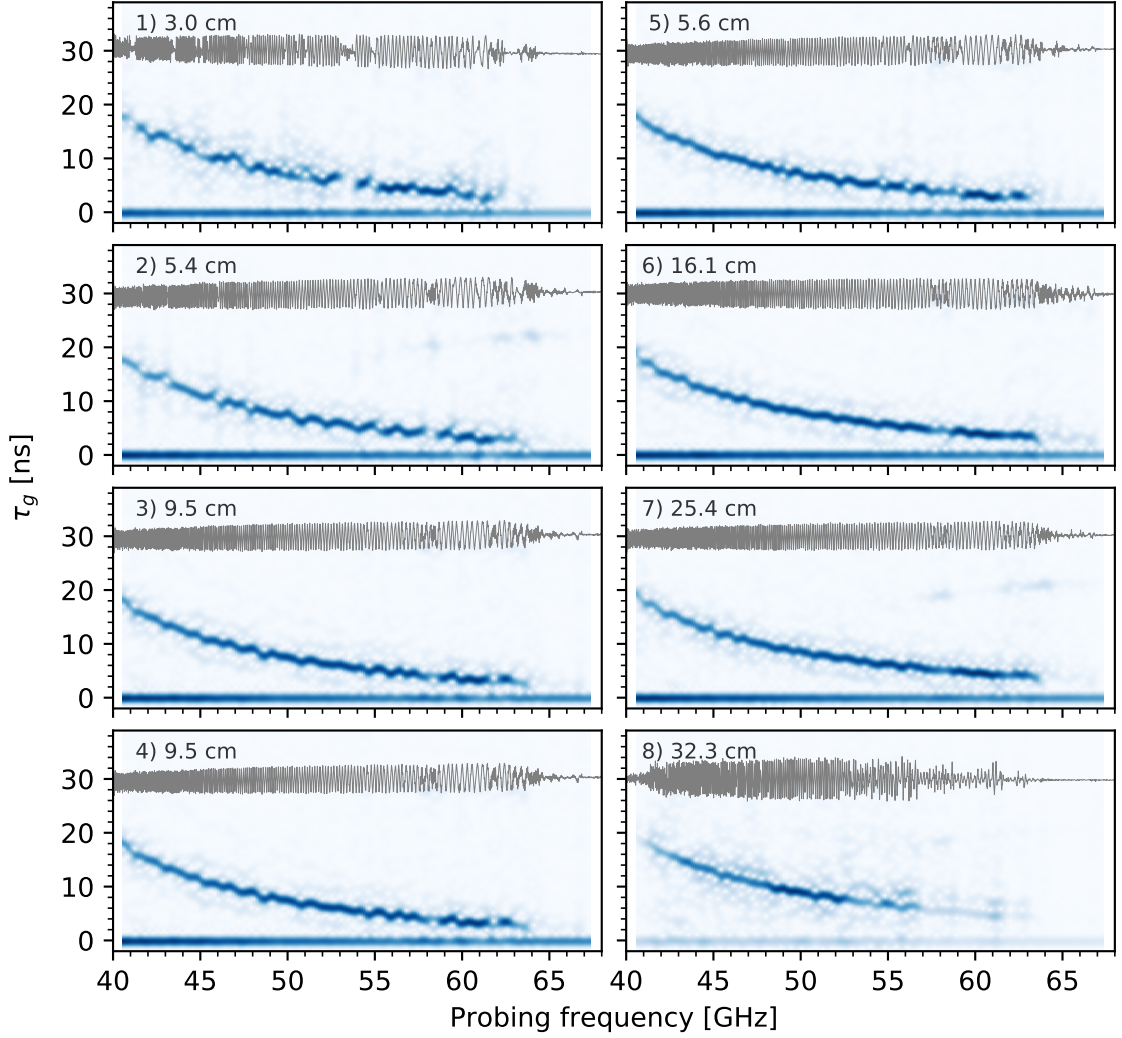


Figure 4.4: Raw beat signal and group delay spectrogram measurements for multiple metallic mirror distances using reflectometry channel 1.

A small modulation of the beat signal is observed when the metallic mirror is placed close (< 6 cm) to the reflectometry antenna, due to the multiple reflections that result in the small region between the mirror and the metallic components on the vessel wall. This modulation affects the determination of the reflection group delay measurement of plasmas very close to the outer wall. In addition, the measurement signal power at the end of the probing band is too low to get an accurate response. This 64-68 GHz region is discarded.

Improving signal quality and overlapping spectrograms

To improve the signal quality, the low frequency components are filtered out for each individual measurement. This is achieved using a 5th order high pass digital Butterworth filter on the raw quadrature signal. An offline forward-backward² digital filter implementation is used, which duplicates the order of the filter while providing a flat amplitude response and zero phase distortion, preventing artificial deformation of the reflectometry signal.

The free space propagation d between the reflectometry antenna and the metallic mirror introduces a constant delay τ_{vac} to the reflectometry measurement equal to

$$\tau_{vac} = \frac{d}{c}. \quad (4.7)$$

This delay contributes with a phase to the acquired sample of

$$\phi_{vac} = \tau_{vac} \frac{2\pi}{f_s} \frac{df}{dt} = \frac{d}{c} \frac{2\pi}{f_s} \frac{df}{dt}, \quad (4.8)$$

where c is the approximate wave velocity, df/dt is the linear probing frequency sweep rate and f_s is the sampling rate of the acquisition system.

The phase contribution ϕ_{vac} of each mirror distance is removed from the respective measurement signal samples. The resulting spectrograms may be combined, by averaging each point in the spectrogram matrices, to obtain a better representation of the group delay. The normalized median spectrogram of the eight calibration measurements of channel 1 is shown in Figure 4.5. The peaks of maximum amplitude correspond to the group delay of the mirror reflection.

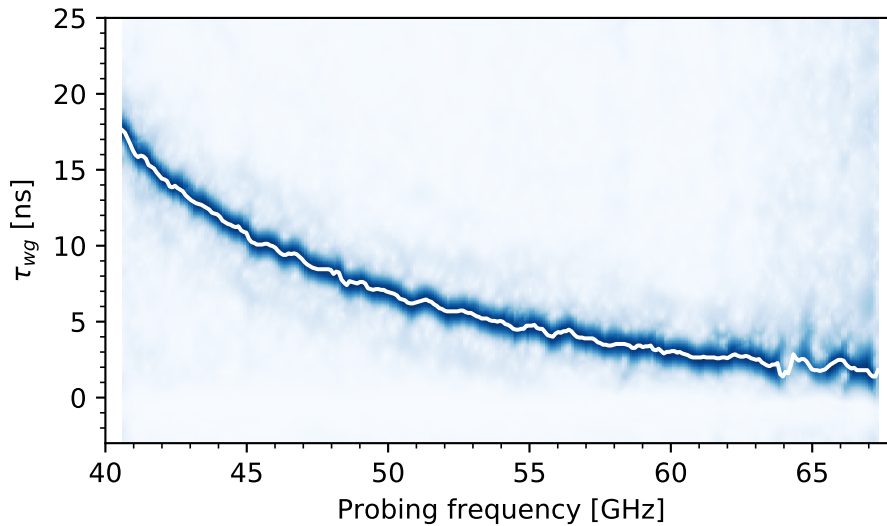


Figure 4.5: Combined spectrogram of normalized calibration waveguide delay measurements of channel 1.

²SciPy Signal's forward-backward *filtfilt* implementation.

4.2.3 Fitting the calibration measurements

The overlapped mirror measurements for the three installed reflectometry channels are shown in Figure 4.6. The delay peaks were approximated to the fitting function in equation (4.6) and the respective parameters a and b were obtained for each channel. The waveguide dispersion is a static feature that does not change during the operational campaign. The fitting parameters obtained during this procedure are used to reconstruct the phase corresponding to the waveguide delay and calibrate the reflectometry raw signal. The calibration sets the delay reference to the origin of the reflectometry antenna.

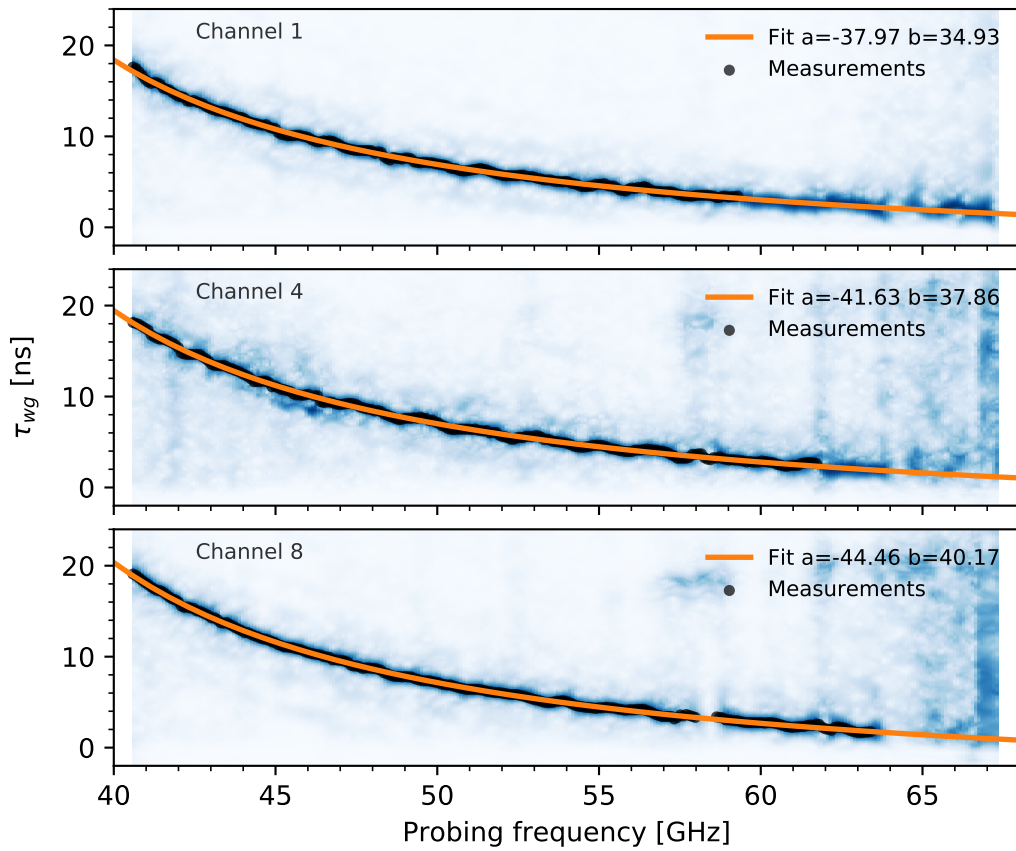


Figure 4.6: Calibration results and fitting parameters for each reflectometry channel.

The first waveguide dispersion calibration was performed in April 2015, using a test reflectometry front end setup and a high bandwidth oscilloscope to acquire the reflectometry beat signal. This procedure allowed the crude approximation of the waveguide dispersion and the design of the delay lines described in section 3.3.6. The final calibration was performed in September 2016, with the complete diagnostic setup installed. This data was used to recalibrate the reflectometry measurements acquired during the 2015-2016 ASDEX Upgrade operational campaign.

4.2.4 Calibrating raw signal by removing waveguide dispersion

The reflectometry measurements of each channel have the plasma propagation delay on top of the waveguide dispersion. This waveguide dispersion must be removed by using the fitting parameters obtained in the calibration procedure. The calibrated delay then corresponds solely to the propagation between the mouth of the reflectometry antenna and the reflection layer inside the plasma.

An example of a real uncalibrated raw signal can be seen in Figure 4.7 (left). The in-phase and quadrature signals show an X-mode upper cutoff plasma reflection appearing at around 48 GHz. The corresponding spectrogram shows the main reflection delay appearing on top of the waveguide dispersion, which represents the reference of the antenna position.

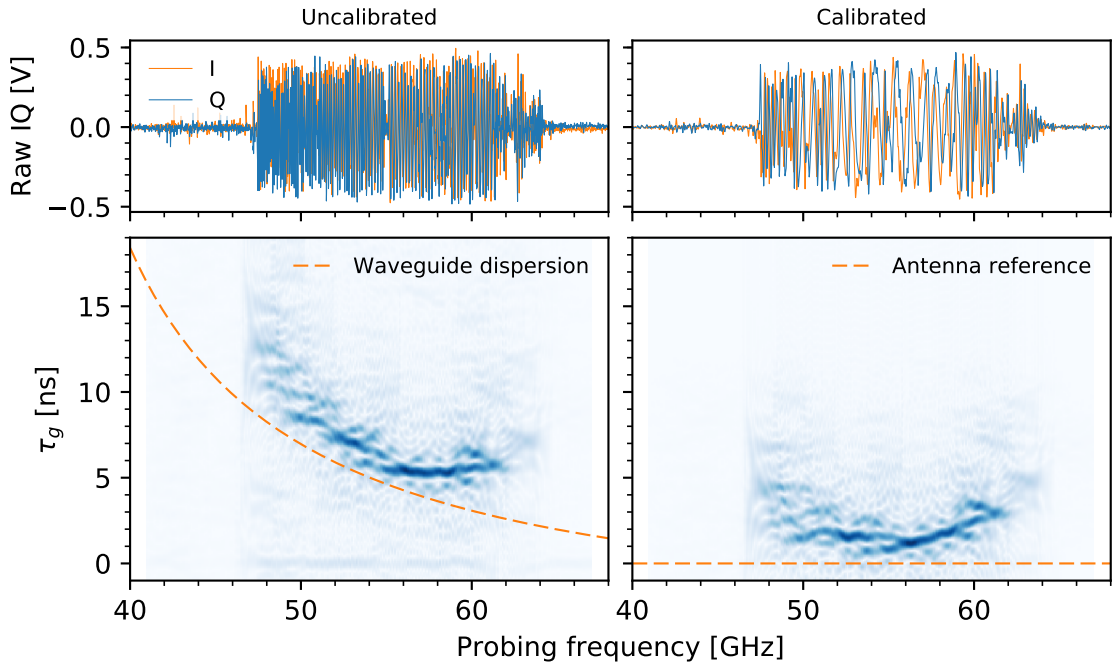


Figure 4.7: Comparison of a plasma reflection signal before (left) and after (right) calibration by removing the respective waveguide dispersion. H-mode He discharge #32774 at 1.5 s with -2.1 T using reflectometry channel 1.

The phase of the raw measurement depends on the accumulated delay of the reflection signal. By removing the phase corresponding to the waveguide, we are left with the propagation delay between the antenna and the reflection surfaces. In order to do this, the quadrature raw signal is first represented in the exponential form

$$sig(n) = A(n) e^{i\phi(n)}, \quad (4.9)$$

where the amplitude is given by

$$A(n) = \sqrt{I^2(n) + Q^2(n)}, \quad (4.10)$$

and the phase is

$$\phi(n) = \tan^{-1} \left(\frac{Q(n)}{I(n)} \right). \quad (4.11)$$

For each raw signal sample, the phase corresponding to the delay inside the waveguide is calculated

$$\phi_{wg}(n) = \sum_{n_i=0}^n \tau_{wg}(f(n_i)) \frac{2\pi}{f_s} \frac{df}{dt}, \quad (4.12)$$

where τ_{wg} is calculated using the previously determined calibration fitting parameters a and b using equation (4.6). This phase contribution is then removed from the raw signal using

$$sig_{cal}(n) = A(n) e^{i(\phi(n) - \phi_{wg}(n))}. \quad (4.13)$$

The calibrated signal is shown in Figure 4.7 (right).

Raw signal filtering

The raw signal is filtered during this calibration procedure in two steps. First, the ubiquitous low frequency cable pick up is removed from the uncalibrated raw signal using a high pass filter. Then, the signal is calibrated to the antenna origin reference as in Figure 4.7 (right). Finally, a low pass filter removes the high beat frequency components and limits the signal to the delay region of interest, typically between 0 ns and 10 ns.

4.3 Analysis of the X-mode reflectometry signal

The reflectometry system is specified to operate with core magnetic fields between 1.8 T and 2.7 T on ASDEX Upgrade. In these conditions the diagnostic is capable of probing the plasma from the near zero density by using the X-mode upper cutoff (UC) reflection.

The first upper cutoff reflection occurs when the probing wave frequency f_p matches that of the local cyclotron frequency f_{ce} , while the local plasma electron density is ≈ 0 . The frequency of this first reflection is called the first fringe (FF) frequency f_{FF} . For probing frequencies higher than the f_{FF} , the wave is reflected when its frequency matches the upper cutoff condition given by

$$f_{uc} = \sqrt{f_{pe}^2 + \frac{f_{ce}^2}{4}} + \frac{f_{ce}}{2}. \quad (4.14)$$

It is important to note that in the limit where the probing wave frequency matches the local cyclotron frequency where the plasma density is zero

$$f_p = f_{ce}(r(n_e = 0)), \quad (4.15)$$

the wave energy is absorbed. We assume that the first reflection occurs at the first plasma layer with a low residual electron density.

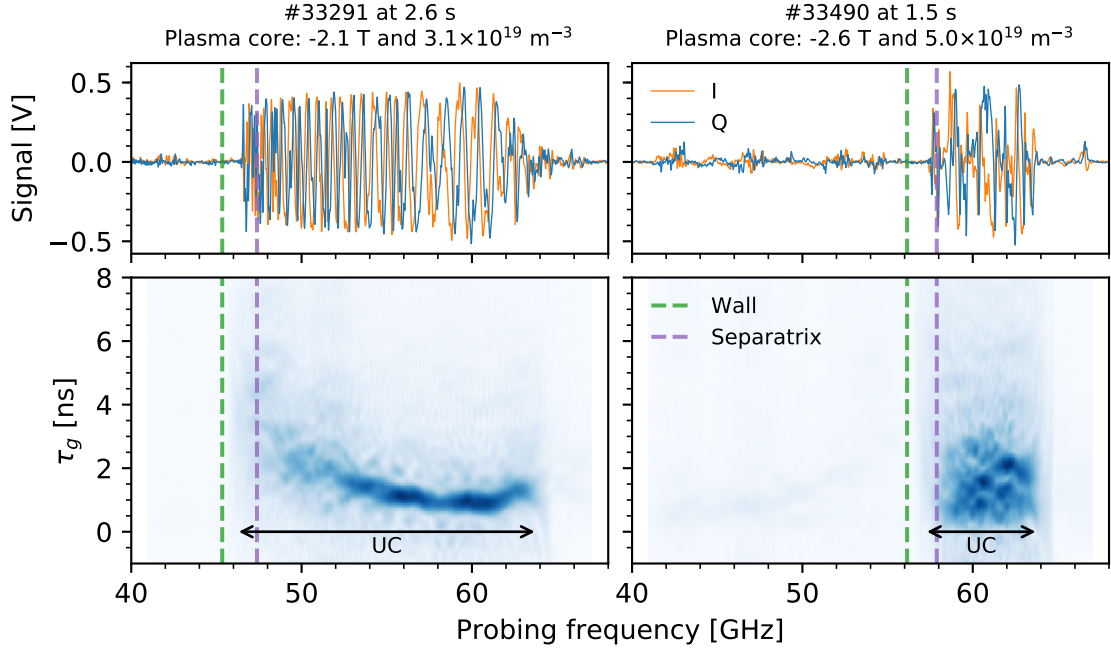


Figure 4.8: Raw signal of discharges with low and high magnetic fields measured using channel 1. The bandwidth of the plasma reflection decreases with the magnetic field strength.

Two typical plasma reflection signals can be observed in Figure 4.8, for low (left) and high (right) magnetic fields. By definition, we know that the first fringe reflection must occur somewhere between the reflectometry antenna on the vessel wall, where there is no plasma, and the separatrix position, necessarily inside the plasma. The cyclotron frequencies at both these locations are represented in the figure by the vertical dashed lines.

The group delay measurement corresponds to the main UC reflection component, represented by the darker regions, starting at the FF frequency up to the end of the probing window. The reflection bandwidth in the lower magnetic field case (-2.1 T, left) spans around 17 GHz from the first reflection at 47 GHz up to the end of the probing range. On the other hand, the measurement bandwidth under a stronger magnetic field (-2.6 T, right) is much smaller, spanning around 6 GHz starting at around 58 GHz. The maximum measurable density is dependent on the width of this reflection signal.

4.3.1 Appearance of lower cutoff reflection

The X-mode upper cutoff reflections occur at the outer edge plasma layers. Typically, probing waves with $f_p < f_{FF}$ propagate freely through the plasma and get scattered by the back vessel wall. If not for the increased attenuation due to the wave propagating through the plasma and the energy loss to scattering, the back wall reflection would be observable in this lower frequency region, as demonstrated previously in Figure 4.1.

However, for high plasma core electron densities, the X-mode lower cutoff (LC) reflection may occur

within the probing window, in addition to the UC reflection. Figure 4.9 shows two situations where the high core n_e results in the appearance of both UC and LC reflections in the reflectometry measurement. In these high core density situations, the high LC reflection amplitude is clearly observed near the start of the probing band up to the f_{FF} . Since we are probing the plasma from the lower field side, the UC reflection always occurs in front of the LC reflection. In the cases where there is an overlap between both cutoff conditions, for a given probing frequency, the upper cutoff reflection is always observed first.

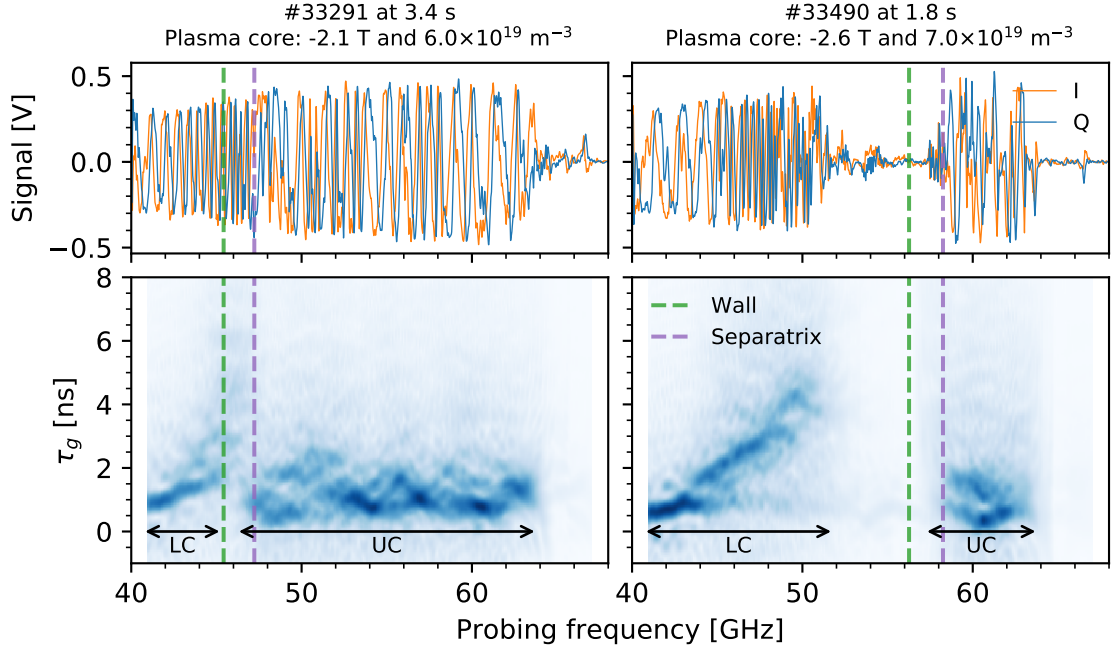


Figure 4.9: Raw signal of discharges with high core plasma electron density and low and high magnetic fields, showing both X-mode upper and lower cutoff reflections measured using channel 1.

These results are consistent with the simulations in Figure 4.10. The simulations show the X-mode cutoff conditions for the corresponding plasma density profiles shown in Figures 4.8 (blue, UC reflection) and 4.9 (orange, UC and LC reflections). The unshaded regions represent the frequencies probed with the diagnostic. The solid lines represent the detected cutoff reflections. The lower cut reflection in the #33291 case is partially obscured by the upper cutoff. The measurement gap between the LC and UC reflections in the #33490 case is also observed.

4.3.2 Evolution of the reflectometry signal during a discharge

The reflectometry measurement varies throughout a discharge, depending on the varying conditions. Figure 4.11 demonstrates this evolution. The amplitude of the reflectometry beat signal for each probing frequency is represented (darker regions represent higher amplitude, left). The core and edge plasma electron densities provided by the interferometer diagnostic are also shown (right). The electron cyclotron frequencies at the wall and separatrix positions delimit the region where the upper cutoff

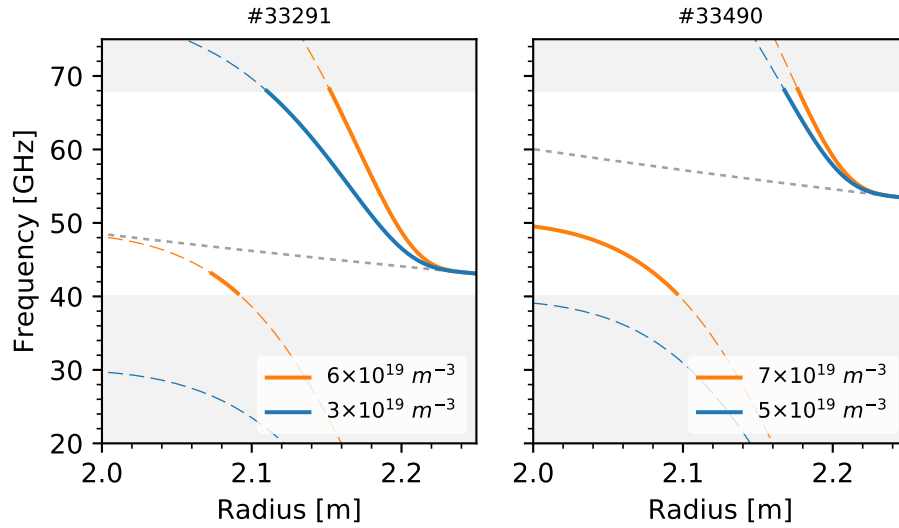


Figure 4.10: Simulated probed plasma regions (solid lines) using the X-mode reflectometry diagnostic for plasmas with low and high density profiles.

reflection should begin, as is observed by the increase in signal amplitude, signalling the first fringe reflection.

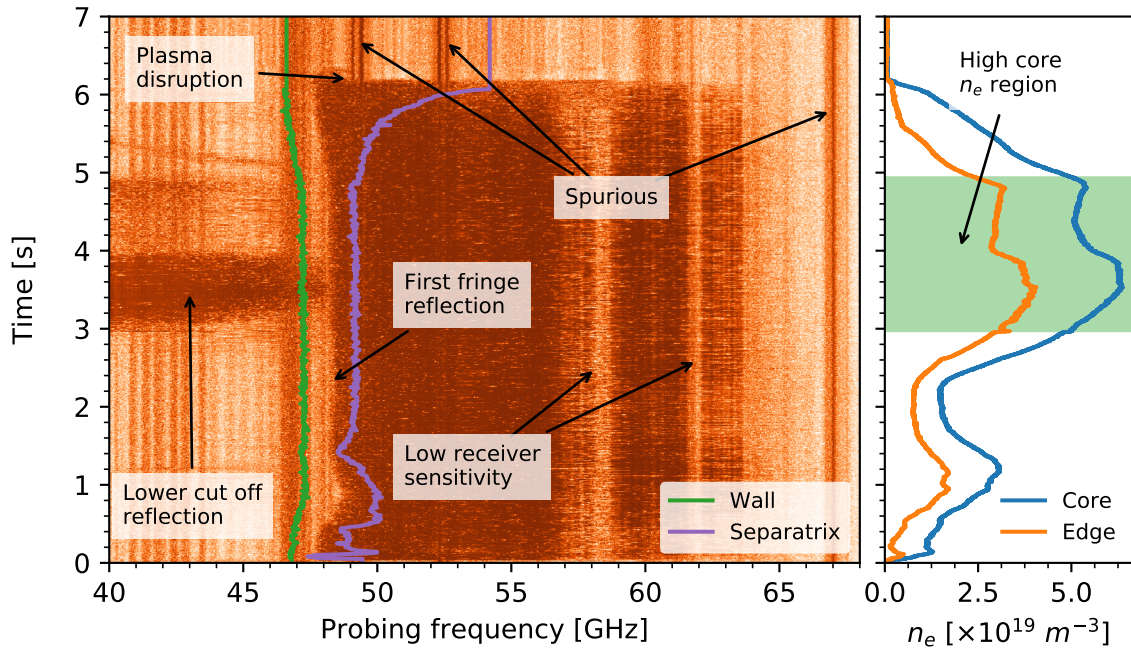


Figure 4.11: Amplitude evolution of the reflectometry measurement on channel 1 during ASDEX Upgrade discharge #33291

The amplitude of the upper cutoff reflection is maintained high up to the plasma disruption at around 6.1 s. Two systematic low signal power regions exist around 57 GHz and 62 GHz, which are attributed to low receiver sensitivity. Low power spurious components are seen at around 50 GHz, 53 GHz and

67 GHz, and in the lower 41-44 GHz frequency region.

Lower cutoff reflections start to be measured as the plasma core electron density goes above approximately $6 \times 10^{19} \text{ m}^{-3}$. This can be observed between 3 s and 5 s. The co-existence of both UC and LC make it difficult to discern the first fringe frequency from the amplitude signal alone.

4.4 First fringe reflection estimation

One of the main issues in X-mode plasma density profile reflectometry is the correct estimation of the start of the upper cutoff plasma reflection. Figure 4.11 showed that the FF frequency is not constant during a discharge and the f_{FF} may occur anywhere in 40-68 GHz probing band window, depending on the local magnetic field. A reliable estimation algorithm is mandatory for the correct automatic reconstruction of the density profiles, since FF estimation errors consequently propagate towards radial and density errors during reconstruction. In addition to being able to track this FF evolution, this algorithm must be robust enough to operate in any condition, such as high or low magnetic fields, and in the presence of both UC and LC reflections.

4.4.1 Influence first fringe estimation errors on density profile reconstruction

The influence of a wrong FF estimation can be interpreted from Figure 4.12. The upper cutoff region used for profile reconstruction is expected to start when the amplitude of the raw reflectometry signals (I and Q) increases, seen at around 46.4 GHz in a). The spectrogram visualization in b) shows the main UC reflection starting at around the first fringe frequency f_{FF} . The electron cyclotron frequency profile f_{ce} in front of the reflectometry antenna, obtained from the magnetic equilibrium codes, is shown in c). The vacuum distance d_0 between the launching antenna and the first plasma reflection is determined when the FF matches the local electron cyclotron frequency $f_{FF} = f_{ce}(d_0)$. At f_{FF} , the plasma is estimated to be around 5 cm away from the wall and the reconstructed density profile is shown in d).

However, misjudging the frequency of the first fringe reflection introduces errors in the density profile reconstruction. Two other FF estimations at 46.2 GHz and 46.6 GHz are shown in the figure, corresponding to two different density profile reconstructions. It can be seen that a small ± 200 MHz shift of the estimated f_{FF} results in a ± 10.1 mm variation of the vacuum distance, and of the group delay measurement. This, in turn, shifts the reconstructed density profiles radially, since the profiles move inwards or outwards. This high radial shift is an alarming indication of the sensitivity requirements of a first fringe estimation algorithm.

4.4.2 Amplitude based first fringe estimation algorithms

In the ideal X-mode conditions, the plasma reflection is distinctly correlated with the increase in reflectometry signal amplitude. The probing frequency at the sharp amplitude gradient indicates the start of the plasma UC reflection. This feature has been used to estimate first fringe frequency in X-mode

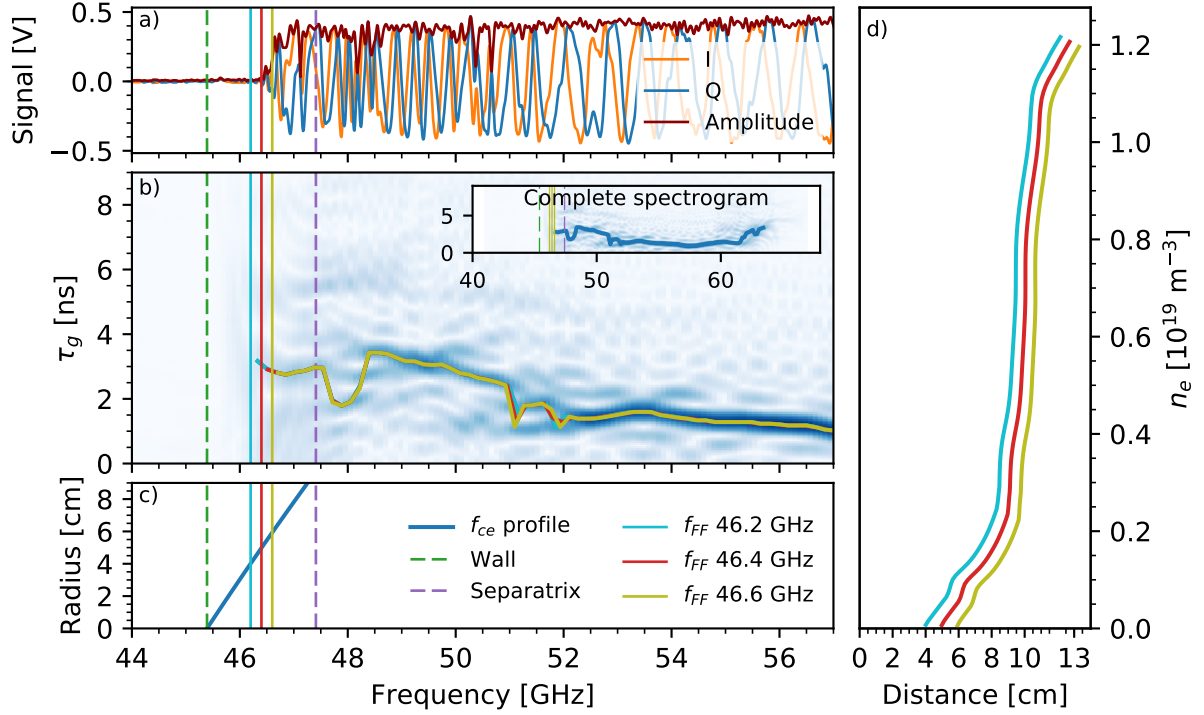


Figure 4.12: Influence of small FF estimation shifts in resulting density profile reconstruction of reflectometry channel 1 measurement at 2.452 s of #33291.

reflectometry diagnostics at several experimental fusion devices such as DIII-D [110], Tore Supra [111], and EAST [112].

This phenomenon can also be observed using our implemented reflectometry diagnostic, as shown in Figure 4.13. Here, the normalized amplitude³ of the raw reflectometry signal acquired in channel 1 is plotted under different magnetic field conditions. We can clearly distinguish the start of the upper cutoff reflection by the amplitude increase that falls within the wall-separatrix region.

Amplitude based methods require a high dynamic range of the diagnostic measurement and assume that the plasma reflection signal power is consistently higher than other reflections, such as back wall reflection, spurious noise, or LC reflection.

However, a simple amplitude based FF estimation algorithm may not be reliable enough in the large operational range of this diagnostic, specially in high core electron density conditions which result in LC reflection. Over half of the plasma discharges at ASDEX Upgrade, acquired during the commissioning phase of the diagnostic, meet the high core density conditions for the appearance of a lower cutoff reflection in the 40-68 GHz probing window sometime during the discharge. The consistent high amplitude of the LC reflection signal typically breaks amplitude based FF estimation algorithms, which can not easily distinguish between UC and LC regions.

More advanced techniques contemplate both the amplitude and frequency response to estimate the first fringe location. These methods may be able to recognize the typical group delay signature and

³The amplitude signal was smoothed, using a moving average window with $N=75$, to attenuate the jitter and provide a clearer signal.

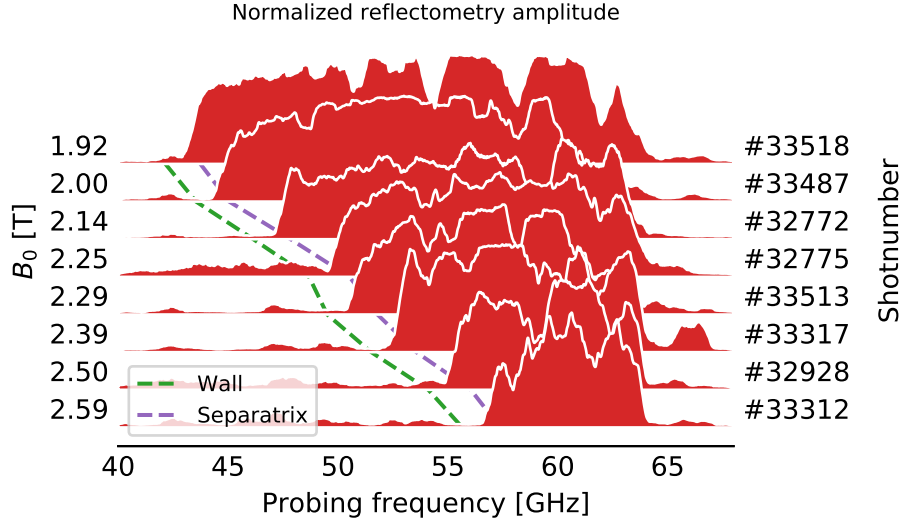


Figure 4.13: Smoothed raw signal amplitude in different magnetic field conditions.

ignore other coexisting broadband spurious signals or undesired spectral features. For example, in theory, the FF reflection occurs immediately after an absorption layer where $n_e \rightarrow 0$ and the probing frequency matches the local f_{ce} . In this positive vicinity, the probing wave is slowed down resulting in a high group delay measurement followed by an exponential decrease of the delay. Spectral and amplitude based algorithms have been used at JET [113], Alcator C-Mod [114], and DIII-D [115].

4.4.3 The *ampfilt* first fringe estimation algorithm

A first fringe estimation algorithm was developed to estimate the start of the X-mode UC reflection used for density profile reconstruction. This algorithm is based on the existing estimation algorithm, used at DIII-D [115], and was given the name *ampfilt*.

The most challenging situation for the FF estimation algorithm is the presence of a consistently high reflection power around the FF frequency, such as overlapping UC and LC reflections. To solve this, the *ampfilt* algorithm first distinguishes under which cutoff regime it is measuring, and then applies one of two methods:

- UC Regime: FF estimation from a signal with only upper cutoff reflection;
- UC+LC Regime: FF estimation of a signal with both upper and lower cutoff reflections.

Determining the regime of FF estimation

To determine the cutoff regime, the probing band is separated into two distinct regions. The first region is determined by where the upper cutoff reflection must appear, which is the region of probing frequencies above the electron cyclotron frequency at the separatrix (f_{sep}): region to the right of the separatrix. The second region is where a lower cutoff reflection may exist, which is from 40 GHz up to the electron cyclotron frequency at the wall (f_{wall}): region to the left of the wall.

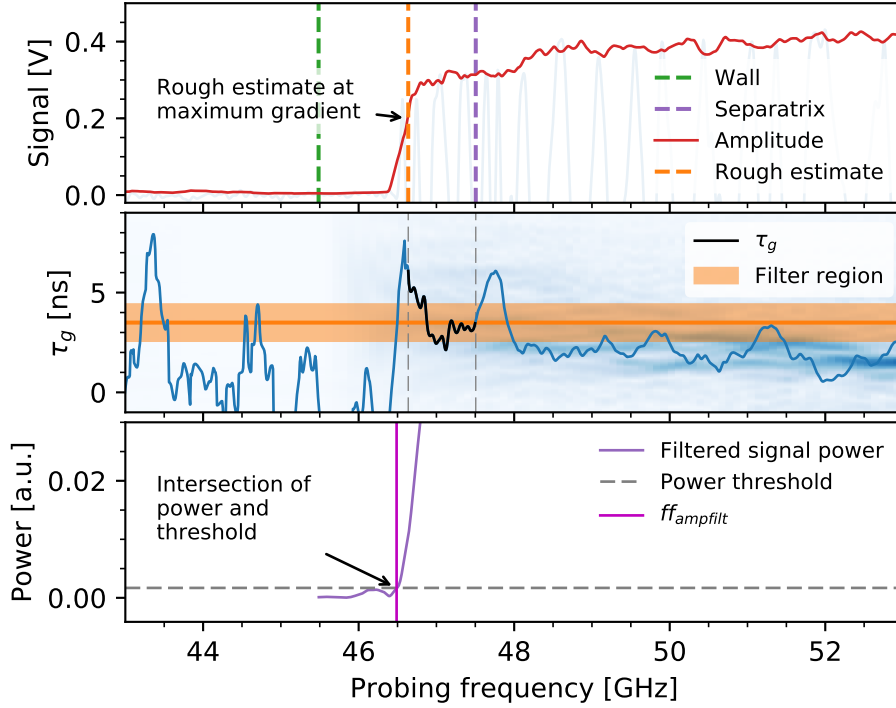


Figure 4.14: FF estimation steps using the *ampfilt* algorithm of the reflectometry raw signal at 2.45 s of #33291 with only X-mode upper cutoff reflection.

A LC reflection is characterized by a high signal amplitude from the beginning of the probing band, at 40 GHz, up to the expected FF frequency. If the average signal amplitude in the left region is more than 0.8 times the signal amplitude in the right region, then the reflectometry signal is in the UC+LC regime, otherwise, it is in the purely UC regime.

FF estimation in the UC regime

The steps of the FF estimation procedure in the UC regime are described below and shown in Figure 4.14.

1. The amplitude of the raw signal is calculated, showing a clear increase of signal power in the upper cutoff region.
2. A probing band region of interest is delimited between the f_{wall} and the f_{sep} .
3. A rough frequency estimate of the start of the upper cutoff reflection is taken at the point of highest amplitude gradient within this small region, as seen in the top plot of Figure 4.14.
4. The instantaneous group delay $\tau_g(n)$ is calculated using the quadrature signal phase $\phi(n)$, sampling frequency f_s and the sweep rate df/dt

$$\tau_g(n) \frac{df}{dt} = \Delta\phi(n) \frac{f_s}{2\pi} = [\phi(n) - \phi(n-1)] \frac{f_s}{2\pi}, \quad (4.16)$$

and shown in the middle plot⁴.

5. The average delay and standard deviation (σ) of the raw signal, in the small region to the right of the rough estimate, are calculated.
6. The raw signal is then filtered with a band pass filter centered at this average delay with width 2σ . This filtering emphasizes the group delay signature at the start of the upper cutoff reflection.
7. The power of the filtered signal within the small region is calculated and shown in the bottom plot.
8. A threshold is set at 2% of the peak-to-peak power.
9. The *ampfilt* first fringe frequency in the UC regime is determined at the first position where the signal power crosses the threshold, coming from the right.

This FF estimation procedure provides good detection of the start of the UC reflection. However, it is greatly dependent on a clean amplitude signal and does not provide reliable results in the UC+LC regime.

FF estimation in the UC+LC regime

In the presence of the lower cutoff reflection, there is a consistent reflection signal on both sides of first fringe frequency. However, in the FF boundary, where the probing frequency matches that of the local f_{ce} and $n_e = 0$, there is an absorption layer that should have no reflection. In reality, due to plasma turbulence and other effects, this absorption layer only introduces an attenuation in the reflectometry measurement, which is hard to interpret and to distinguish from other dips in reflection amplitude. This amplitude valley can be observed in the top plot of Figure 4.15.

In addition, we know that the group delay signature to the right of the FF starts typically high, followed by an exponential decrease. With this understanding, we can assume that the signal around the FF has a high group delay simultaneously with an amplitude attenuation.

In the UC+LC regime, the *ampfilt* algorithm implements another FF estimation procedure than in the UC regime. The steps are represented in Figure 4.15 and described below.

1. The amplitude and instantaneous group delay of the raw reflectometry signal are calculated and shown in the top and middle plots.
2. A small region of interest is delimited by the f_{ce} at the wall and at the separatrix positions.
3. The valley of the signal amplitude and the peak of its group delay in this small region is consistent with the expected first fringe signature.
4. A rough probing frequency estimate is taken at the maximum of the ratio between the delay and the amplitude. This rough estimate is shown in the figure, but is biased to the left of where the FF should be.

⁴The instantaneous group delay shown in the figure is smoothed with a moving average (window=10) to reduce jitter and improve interpretation.

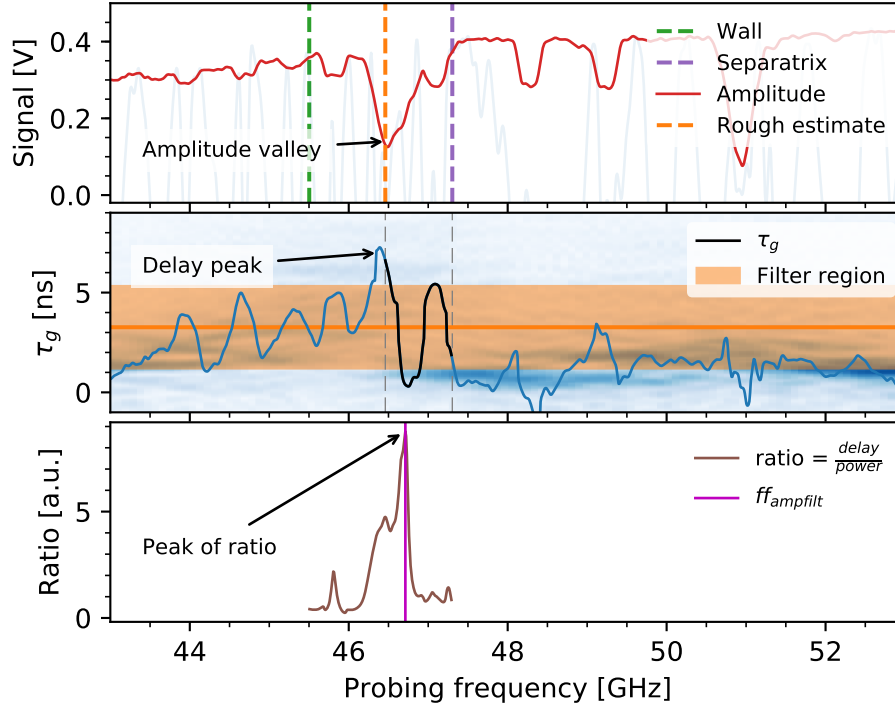


Figure 4.15: FF estimation steps using the *ampfilt* algorithm in the UC+LC regime for a reflectometry raw signal of a high core density plasma, at 3.4 s of #33291.

5. The average delay and standard deviation of the raw signal, in the small region to the right of the rough estimate, are calculated.
6. The raw signal is filtered with a band pass filter centered at this average delay with width 2σ .
7. Again, the ratio between the delay and the amplitude of the now filtered raw signal is calculated and shown in the bottom plot.
8. The *ampfilt* first fringe frequency in the UC+LC regime is determined at the maximum of this filtered signal ratio.

Experimental results of the *ampfilt* algorithm

The *ampfilt* algorithm was used to estimate the first fringe frequency, with a 100 μ s interval resolution, along two discharges with different magnetic fields and with UC and UC+LC regimes. The raw reflectometry signal amplitude and the estimated first fringe frequency evolution are shown in Figure 4.16. The *ampfilt* algorithm is capable of estimating the FF frequency evolution, and corresponding vacuum distance r_0 .

The average values of the vacuum distance $\overline{r_0}$ within a 5 ms moving window are shown in the bottom plots. The vacuum distance remains more or less constant during the UC regime. However, the plasma seems to move outwards towards the wall in the UC+LC regime in the right plot, which is correlated with the transition to an H-mode plasma at 1.6 s.

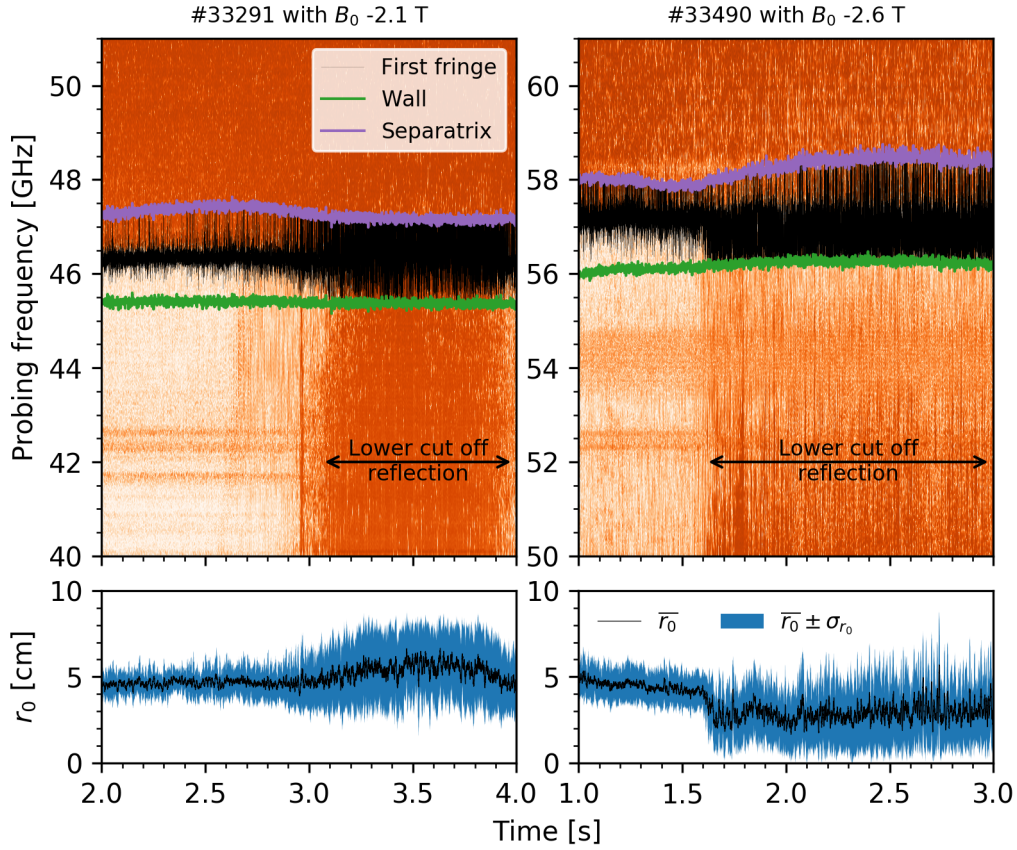


Figure 4.16: First fringe estimation along two discharges with low and high core magnetic fields and with UC+LC regimes.

The precision of the FF estimation measurement is analysed by the standard deviation of the vacuum distance σ_{r_0} in a small time window, assuming the plasma does not move within this interval. The FF estimation imprecision increases during the UC+LC regimes. The maximum deviation within a 5 ms interval is 2.9 cm for discharge #33291, and 3.3 cm for #33490, with peaks of up to 9 cm between consecutive 100 μ s sweeps. Such high radial displacement is not expected for a confined plasma within such a small time frame, and it is attributed to the algorithm's artificial imprecision.

4.4.4 Improving vacuum distance measurements with Kalman filtering

In order to improve the precision of the first fringe estimation algorithm, a Kalman filter was applied to the consecutive vacuum distance measurements. A Kalman filter, also known as linear quadratic estimation, is capable of providing more accurate estimates of unknown variables using a series of measurements, containing some statistical noise or other inaccuracies, than if a single measurement was used [116]. This filter is widely used in signal processing and for navigation and control of autonomous vehicles.

The Kalman filtering works in two steps. In the first prediction step, the filter provides an estimate for the new measurement and its uncertainty, based on its own internal state. Then, the filter compares

these predictions with the next noisy input measurement, and updates the original estimates using a weighted average. No additional information other than the previous state, the uncertainty matrix, and the current input, is required, enabling the use of Kalman filtering in real-time applications.

The previous FF estimation results showed that the *ampfilt* algorithm may result in artificial radial jumps of up to 9 cm between consecutive 100 μ s measurements. A Kalman filter was designed assuming a radial displacement limit of 1 mm per 100 μ s (corresponding to an upper limit for the outwards plasma radial velocity of 10 m/s). This filter is used to improve the estimate of the radial position of the first fringe by reducing the artificial jitter.

The average and standard deviation of the vacuum distance, using the Kalman filtered *ampfilt* estimation, are shown in the bottom plots in Figure 4.17. The filtered response improves the tracking of the first fringe position similarly of the original estimation. The maximum standard deviations decreased from 2.9 cm (original) to 0.43 cm (Kalman filtered) in discharge #33291, and from 3.3 cm to 0.89 cm in discharge #33490. Overall, the Kalman filter provides a more precise estimation.

The more accurate estimation of the vacuum distance is then used to interpolate the new first fringe frequency value. These results show that the standard deviation of the Kalman filtered vacuum distance is negligible, improving measurement precision.

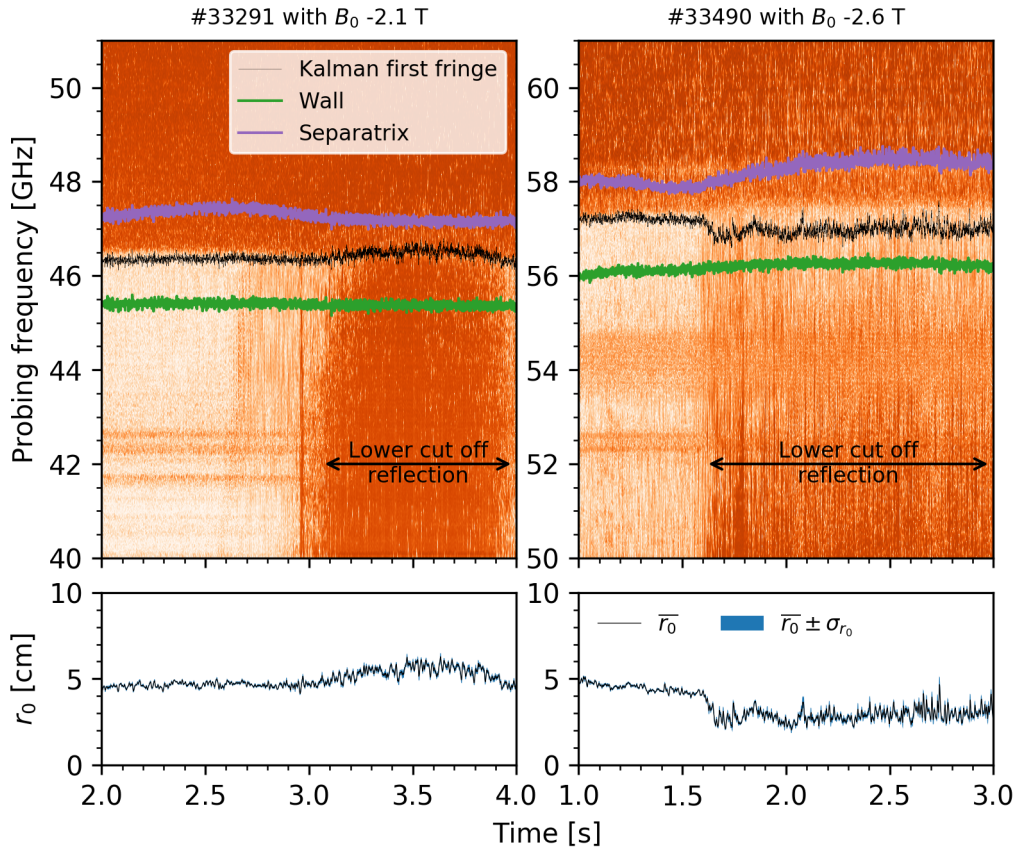


Figure 4.17: Improved precision of the Kalman filtered first fringe and vacuum distance estimations along two discharges with antenna 1.

The Kalman filter is applied to the estimated vacuum distance instead of directly to the first fringe frequency. The reason for this is that the Kalman filter must be applied to an independent input measurement, and the FF frequency is dependent to the instantaneous magnetic field profile, which is changing constantly. Then the frequency of the start of the upper cutoff reflection is recalculated using the more precise Kalman estimation of the vacuum distance.

It was shown that the combination of the *ampfilt* algorithm and Kalman filtering provide a reliable estimate for the first fringe position.

4.4.5 Developing a first fringe estimation algorithm based on Neural Networks

Generally, an experienced human diagnostician analysing the different X-mode group delay spectrograms may detect certain patterns that give hints of the start location of the upper cutoff reflection. These patterns may be a combination of frequency peak evolution, amplitude dynamics and knowledge of the wall and separatrix positions. Translating these cues into discriminating rules and programming these into explicit procedural algorithms, such as the *ampfilt* algorithm, is not an easy task. In this section, the implementation of a first fringe estimation method based on neural networks is described. The purpose of this new method is to improve the precision of the FF estimation when compared with the *ampfilt* algorithm.

Introducing neural networks

Biological brains consist of complex interconnections between neurons. Individual neurons respond to the sum of their input signals and become activated when it goes above a certain threshold, sending another potential signal to the next neuron, which reacts differently. This interconnected network is supported by stronger or weaker links between the neurons. The brain learns by training these links with different stimuli, such as visual images, sounds or by touching objects.

Artificial neural networks (NN) are computational methods ubiquitously used in machine learning systems. Similar to biological brains, these networks consist of several layers of mathematical neurons, interconnected by weighted links, that can be trained to mimic the pattern recognition procedures of humans. The training of these networks is achieved by providing a large dataset of input stimuli to the network and compare its output with the expected result. The error between the output and the expectation is used to recalibrate the weights of the individual links between the neurons using backpropagation algorithms [117]. This allows the network to *learn* how to react to different input signals to reach an expected result. Neural networks are used to recognize objects, classify images, transcribe and translate speech, provide accurate web search results, or make financial market predictions [118].

With the recent increasing popularity of machine learning and artificial intelligence, several tools have been developed to create, train and use neural network models. Google has open sourced its versatile TensorFlow [119] tool to express machine learning algorithms. Keras [117, 120] is a deep learning Python library interface that can work with TensorFlow or other machine learning back ends. These open source initiatives greatly reduce the barrier to entry and eased the learning curve needed to

implement machine learning techniques in new fields of application, such as statistics, physics, health, and biology research.

Neural network models have also been used in fusion research to substitute existing computationally complex reconstruction algorithms. A well trained NN model may be capable of reproducing the same results as an explicit algorithm, within acceptable accuracies, while sometimes being faster to compute than their original counterparts. NN applications in fusion research include the tomographic reconstruction of bolometry data [121], real-time plasma impurity monitoring [122], and real-time evaluation and reconstruction of reflectometry density profiles for plasma position control [123, 63]. In addition, the pattern recognition capabilities of neural networks have been used to classify and predict tokamak disruptions [124, 125].

A new neural network approach was developed to further improve the precision of the first fringe frequency estimation, when compared with the *ampfilt* algorithm [108]. The aim of this NN model is to mimic the same pattern recognition of human diagnosticians looking at reflectometry spectrogram results. The supervised training of the NN model uses a large comprehensive training dataset, created by experienced X-mode reflectometry diagnosticians using experimental data acquired during the 2016 ASDEX Upgrade campaign. By using a well defined training dataset, the NN is capable of extrapolating accurate first fringe estimation predictions from new input data.

Creation of the training dataset

The training dataset must be comprehensive, with good enough variability of the operational parameters, so that the trained NN is capable of predicting the correct answer in most cases.

A total of 695 discharges were acquired with the new X-mode reflectometry diagnostic during the 2016 ASDEX Upgrade campaign. The distribution of these discharges depending on their magnetic field and core electron density is shown in Figure 4.18.

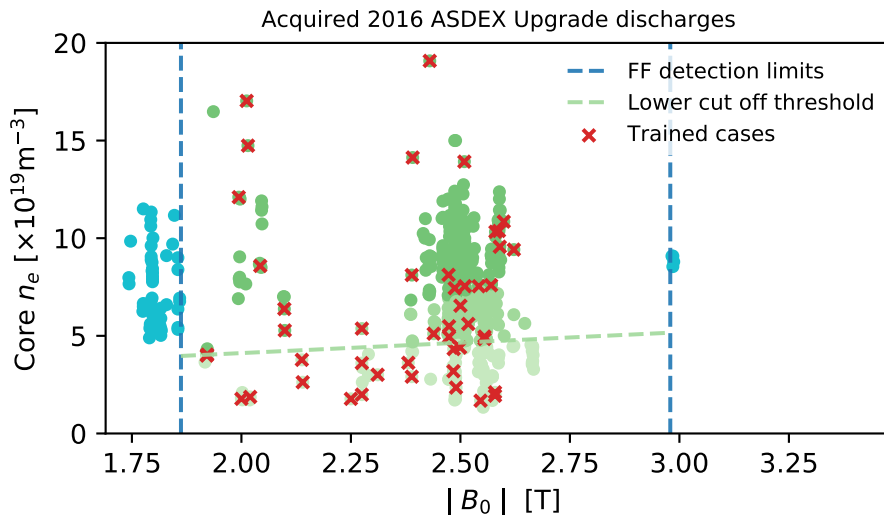


Figure 4.18: Distribution of the plasma discharges depending on their magnetic field and core electron density acquired during the 2016 ASDEX Upgrade campaign.

The vertical magnetic field limits indicate the discharges where the start of the upper cutoff reflection can be detected inside the 40-68 GHz probing frequency band. Most discharges on ASDEX Upgrade have a magnetic fields around 2.5 T and core plasma electron densities of around 10^{20} m^{-3} . These conditions are propitious for the measurement of the lower cutoff reflection sometime during the discharge. The density threshold for the UC+LC regime to occur is indicated by the dashed curve.

A total of 2209 training cases were selected from 47 distinct discharges, dispersed along the measurable operational range, marked with a cross in Figure 4.18. A graphical tool was developed to plot the raw data, group delay spectrogram and relevant information such as signal amplitude, and the wall and separatrix locations, to aid the diagnostician in selecting the correct FF frequency for each individual case. It is important to note that the NN is trained to be as good as the experienced diagnostician. Any bias or uncertainty in the diagnostician selection is passed on to the trained model.

Different heating scenarios, ELM events and LC reflection within the probing band, were considered when selecting the training dataset, to add variability, as detailed in Table 4.1.

Table 4.1: Variability of dataset

Variability	Percentage of cases
ICRH operation	14.2%
ECRH operation	56.6%
NBI operation	34.3%
ELM events	2.6%
With LC reflection	24.5%

Preprocessing the raw data

The neural network is expected to interpret the calculated group delay spectrogram data and determine the corresponding FF frequency. The neural network input is a 2D image of the spectrogram data of the raw reflectometry signal. The NN output is the location of the start of the upper cutoff reflection, along the x axis of the image.

Each case in the dataset is first preprocessed to generate the input spectrogram image and the discretized FF output solutions. This procedure is called feature engineering and consists in using high level knowledge of the dataset to partially digest the input data before it goes into the neural network model.

First, a region of interest (ROI) is defined to restrict the FF search and increase NN prediction performance. The vertical ROI is restricted to the 0-25 MHz beat frequency region (0-13.4 ns group delay), since, by design, there is no useful X-mode reflection data outside this range. Then, the horizontal ROI is delimited to the wall-separatrix region. An example of the raw spectrogram data and the ROI delimiters are shown in Figure 4.19.

The data outside the ROI is zeroed out, resulting in the 2D spectrogram image shown in Figure 4.20. Tests showed that the FF localisation performance is increased by zeroing the input matrix outside the ROI, since only the NN neurons connected to the inputs in the ROI are activated.

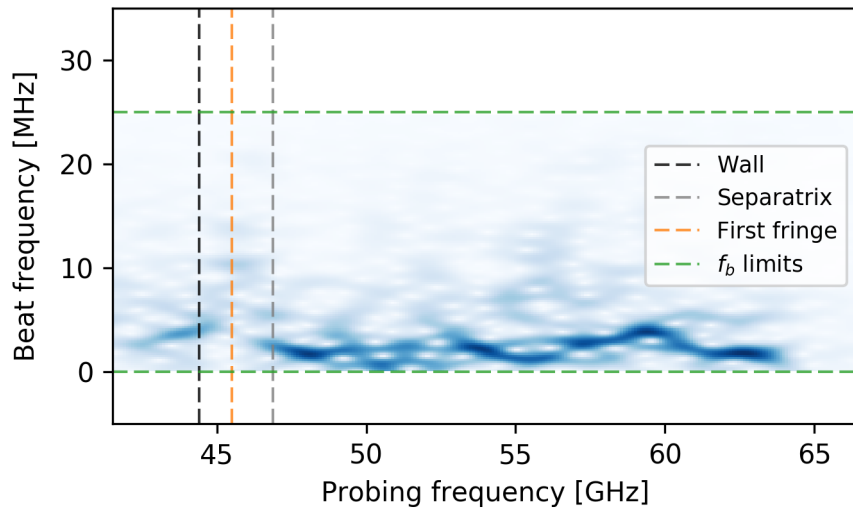


Figure 4.19: Raw spectrogram data and ROI limits.

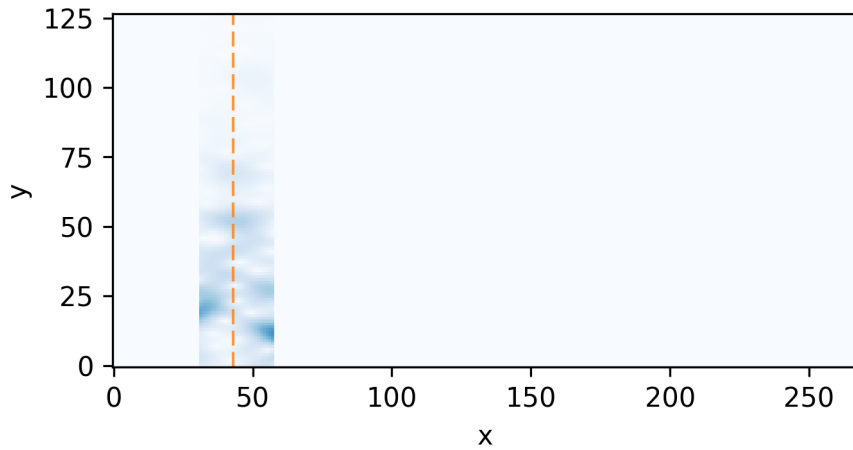


Figure 4.20: Preprocessed 2D spectrogram matrix used as input image for the neural network; x and y axis correspond to the grid points of the image.

The output FF frequency is discretized into a one-hot vector⁵ with 1120 possible discrete values between 40 GHz and 64 GHz (signal quality decreases above 64 GHz). This improves the horizontal FF frequency prediction resolution to 21 MHz. However, there is a trade off between acceptable FF discretization resolution and the FF coverage of the training dataset. A higher discretization results in fewer cases per discrete FF value, which reduces the efficacy of the dataset for training the network.

⁵A one-hot vector is a sequential vector with 1 at the single position corresponding to the true value and 0s in the remaining positions.

Definition of the neural network model

The neural network includes a 2D convolutional input layer. Convolutional neural networks use several 2D filters, trained to detect specific features, to scan the input image matrix. The different feature contributions of each filter are weighed in a fully-connected layer, where all neurons are connected to each other. For each training case, the filters and the weights of the neuron interconnections of the NN model are recalculated to approximate their output vector to the one-hot vector answer. The NN model prediction is the likelihood distribution of the FF along the 1120 discrete FF values. The highest probability is assumed as the first fringe frequency.

The neural network model was defined using the Keras Python library and trained with the Tensor-Flow back end. The input layer of the neural network model is a 2D convolutional layer with 127x268 input grid shape, 50 5x5 filters, using a rectified linear unit (ReLU) activation and set to scan the input image with a stride of 3 pixels. A 2×2 pooling layer was used to down sample the data, which was then flattened. Then, there is a fully-connected (FC) layer with ReLU activation and 1024 elements, followed by the output FC layer with sigmoid activation and 1120 output shape. The network was trained using a categorical cross entropy loss function and Adam optimization [126].

Training the neural network model

The NN weights are calculated by training the NN model several times, each iteration called an epoch, over the same randomly sorted training dataset. In order to validate the model training and ensure the convergence of the weights, the NN performance must be constantly checked against an unseen validation dataset. The source dataset was randomly split with 90%-10% for training and validation, respectively, maintaining FF coverage distribution in both datasets.

The accuracy of the neural network predictions typically improves with each training epoch. However, the model training must be carefully analysed to prevent overfitting. Overfitting implies that the model becomes too familiar with the training dataset and is reluctant to extrapolate to other cases. The decrease of the validation dataset accuracy as the number of epochs increases is a symptom of model overfitting, and should be prevented by choosing the trained model with the best accuracy instead of the most intensely trained.

The model training was performed on the Max-Planck Computation and Data Facility clusters, using the available GPU acceleration. Training ranged from a few minutes for small datasets up to three hours for the extended dataset. The peak model accuracy was reached after approximately 50 training epochs before the starting to decrease. Training accuracy was measured by comparing the average absolute difference between the predictions and the validation dataset answer.

Artificially extending the dataset

The sparse FF distribution of our original dataset does not cover all possible discretized FF values, resulting in high prediction errors for inadequately trained cases. A broader training set, with a better defined FF distribution, is required to improve prediction performance.

Extending the sparse dataset is possible by making a few assumptions on the raw data and the preprocessed inputs. For example, the reflectometry group delay spectrogram signature is similar for consecutive measurements. We can make the assumption that these signatures also remain similar under slightly higher or lower magnetic fields.

Under these assumptions, we define a vicinity around the FF where the delay signatures are assumed similar. Since the spectrogram data outside the ROI is zeroed out, the ROI may be shifted within this vicinity, and we assume that it corresponds to a new case where the respective FF value is equally shifted.

A new extended dataset was created by rearranging each of the original dataset case 51 times within ± 1 GHz in its vicinity. The dataset was extended from 2209 to 112 659 total cases, providing a much better FF coverage of the valid probing frequency band.

Analysis of the neural network first fringe estimation

Two neural networks were trained based on the same model definition. The first NN was trained using the sparse dataset created by the experienced human diagnosticians. The second NN uses the extended dataset.

The first fringe frequency distribution of the sparse and extended datasets can be seen in the top histograms of Figures 4.21 and 4.22, respectively. The horizontal axis corresponds the FF values between 40-64 GHz that NN model may predict, with a 21 MHz resolution.

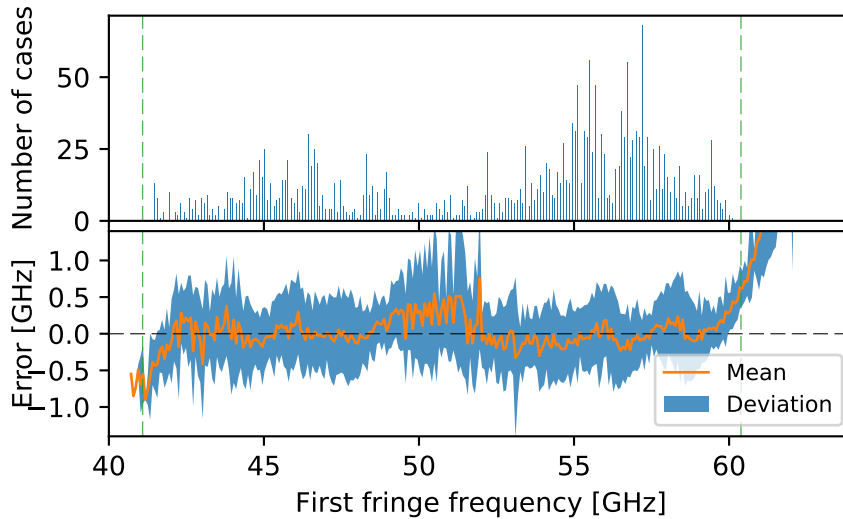


Figure 4.21: First fringe frequency distributions of the sparse dataset and corresponding prediction error.

The extended dataset has a much better coverage of the FF values than the sparse dataset. It can be seen that the dataset FF histograms have two main peaks which correspond to the most typical magnetic field settings on ASDEX Upgrade, 2 T and 2.5 T.

Prediction performance of both neural networks was analysed using the same validation dataset. This validation dataset is a 10% subset of the extended dataset, and none of its test cases was used for

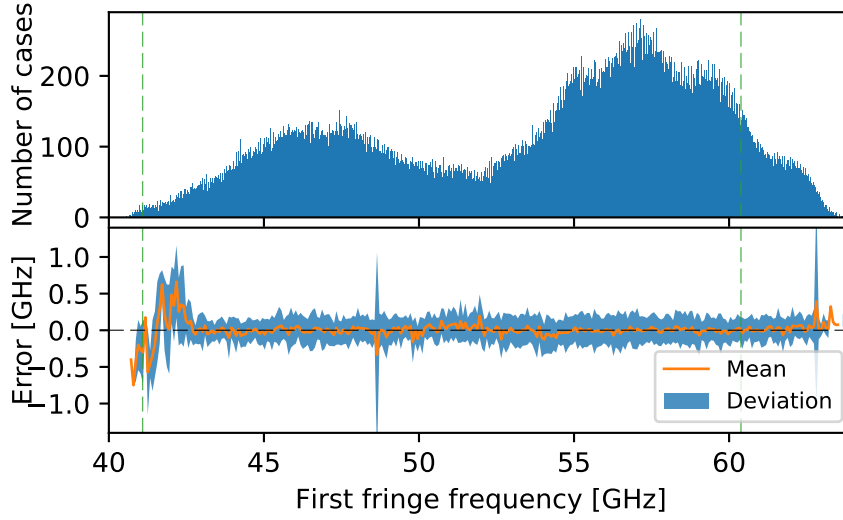


Figure 4.22: First fringe frequency distributions of the extended dataset and corresponding prediction errors.

training either network. The errors were calculated between the FF prediction and the *true* FF value. The results can be seen in the bottom plots of Figure 4.21. The error distribution is obtained by discretizing the FF frequency axis into a smaller number of bins and calculating the average and standard deviation errors within these bins.

The sparse NN model has a much larger error deviation than the extended NN model. This is attributed to a better FF coverage of the extended training dataset. Still, both models fail to provide accurate predictions near the edges of the FF range, which are uncommon for most discharges. The average error of the extended NN model stabilizes close to zero when more than 40 training cases are used for each discrete FF value.

We used the sparse dataset to validate the original *ampfilt* algorithm. The resulting error distribution is shown in Figure 4.23. The *ampfilt* algorithm has a much higher error deviation throughout the dataset than the NN model, with error peaks of over 1 GHz.

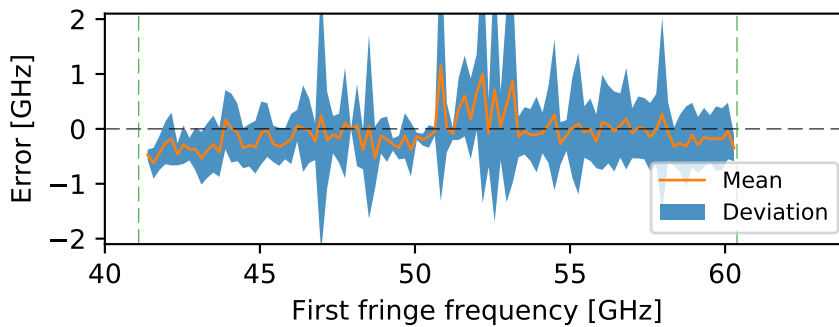


Figure 4.23: First fringe error distribution of the *ampfilt* algorithm using the known sparse dataset.

The estimation errors of each algorithm over their validation dataset are presented in Table 4.2.

These errors were calculated within the sparse dataset frequency limits, represented by the vertical dashed lines, to avoid biasing due to the extrapolated results.

Table 4.2: Estimation errors of first fringe estimation algorithms.

Algorithm	Mean error	Standard deviation σ	Validation dataset
<i>ampfilt</i>	-80 MHz	790 MHz	Sparse dataset
Sparse NN	+30 MHz	550 MHz	10% of extended dataset
Extended NN	-0.5 MHz	230 MHz	10% of extended dataset

These estimation results were obtained by using single measurements, which are prone to high deviations. While these high errors may be disconcerting for individual sweeps, we may improve their performance by using the Kalman filtering technique on multiple consecutive measurements, such as when reconstructing the density profiles of a discharge sequentially.

4.4.6 Reconstructed density profiles using both first fringe algorithms

The density profile evolutions of discharge #33841 of ASDEX Upgrade were reconstructed using vacuum distances estimated by the *ampfilt* algorithm and the extended neural network model. This discharge, represented in Figure 4.24, allows the analysis of critical operational parameters that affect the estimation of the first fringe:

- A high core electron density (Core n_e) H-mode plasma resulted in the UC+LC regime in the 1.2-4.3 seconds interval, represented by the shaded region. The FF estimation algorithms should not be affected during this regime.
- A 2 cm outer radial scan of the separatrix position occurred at around 3 seconds. The reconstructed density profiles should be able to track this radial variation.
- The core magnetic field varied from 2.47 T up to 2.54 T, as can be observed by the corresponding cyclotron frequency evolution at the wall (f_{wall}). The vacuum distance estimation should not be affected by a varying magnetic field.

The FF frequencies estimated with the *ampfilt* and NN algorithms are shown in b) of Figure 4.24. It can be seen that the FF algorithms correctly estimate frequencies between f_{wall} and f_{sep} . However, there is a relatively high jitter of the FF estimations, specially for the *ampfilt* algorithm. This jitter corresponds to high frequency estimation jumps between consecutive measurements, which are increased during the UC+LC regime. On the other hand, the neural network predictions show a better precision throughout the discharge. It can be seen that the FF_{NN} predictions are not affected by the UC+LC regime, and are just as good as in the UC regime.

The FF frequency estimations are then used to calculate the vacuum distances between the reflectometry antenna and the first plasma reflection, for each measurement. The Kalman filtered vacuum distance measurements are shown in c). The estimated vacuum distances using the NN algorithm

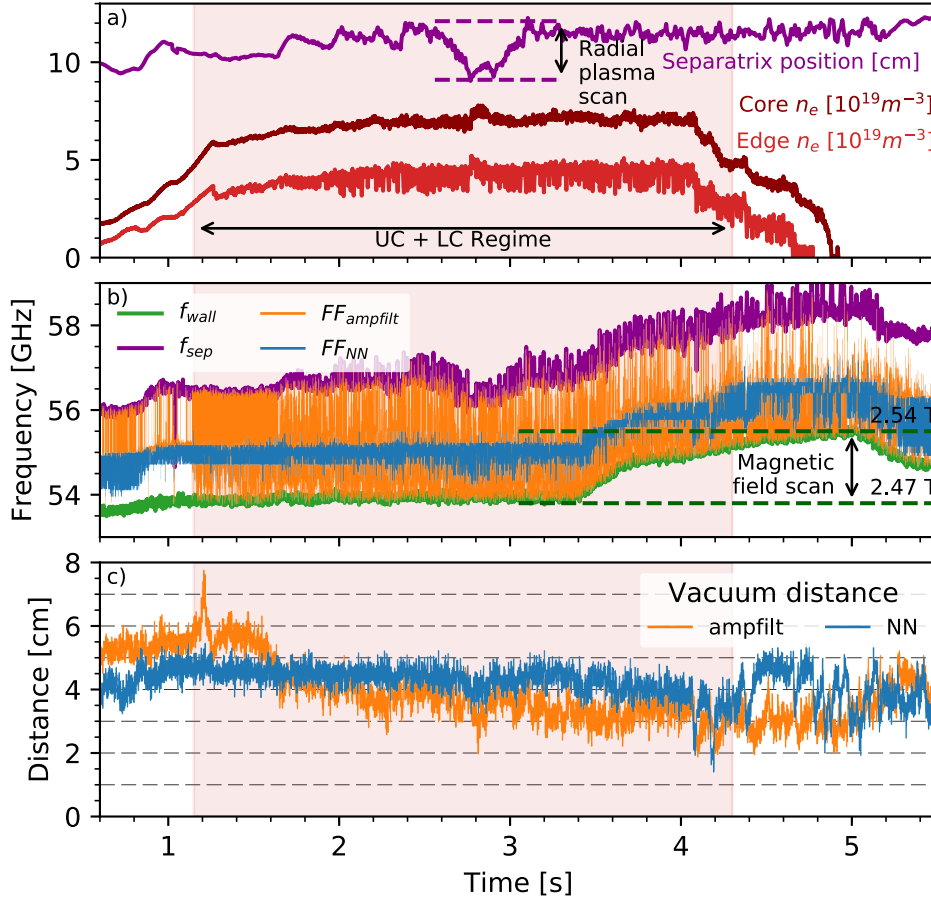


Figure 4.24: Estimated first fringe frequencies and Kalman filtered vacuum distances during discharge #33841 using the *ampfilt* and neural network algorithms.

appear to be more constant during the discharge, than the ones provided by *ampfilt*. The distance estimations do not seem to be affected by the magnetic field scan.

In this discharge, large D pellets were injected into the plasma between 4 s and 6 s at around 10 Hz. Pellet injection typically results in a sudden increase of plasma electron density, which result in outwards bursts of the edge density profile. The vacuum distances measured by the reflectometer are able to observe these density bursts. On the other hand, the interferometer density measurements at the core and edge are affected by these sudden bursts and lose their reference, erroneously indicating as if there is no plasma at around 4.8 s and the discharge ends.

The exact error of the vacuum distance estimation can not be directly analysed. To analyse the performance of the algorithm estimations we analyse the imprecision of the measurements within small 5 ms intervals during the discharge. It is assumed that the vacuum distance should remain constant within 5 ms and any deviation is a result of the artificial jitter. The imprecision is calculated as two standard deviations σ_{dist} of the vacuum distance measurement, which gives an indication of the jitter amplitude within the interval. The *ampfilt* and NN measurements are shown in Figure 4.25 a). The darker lines indicate the corresponding average of the measurement within the interval, showing the approximate expected evolution of the vacuum distance.

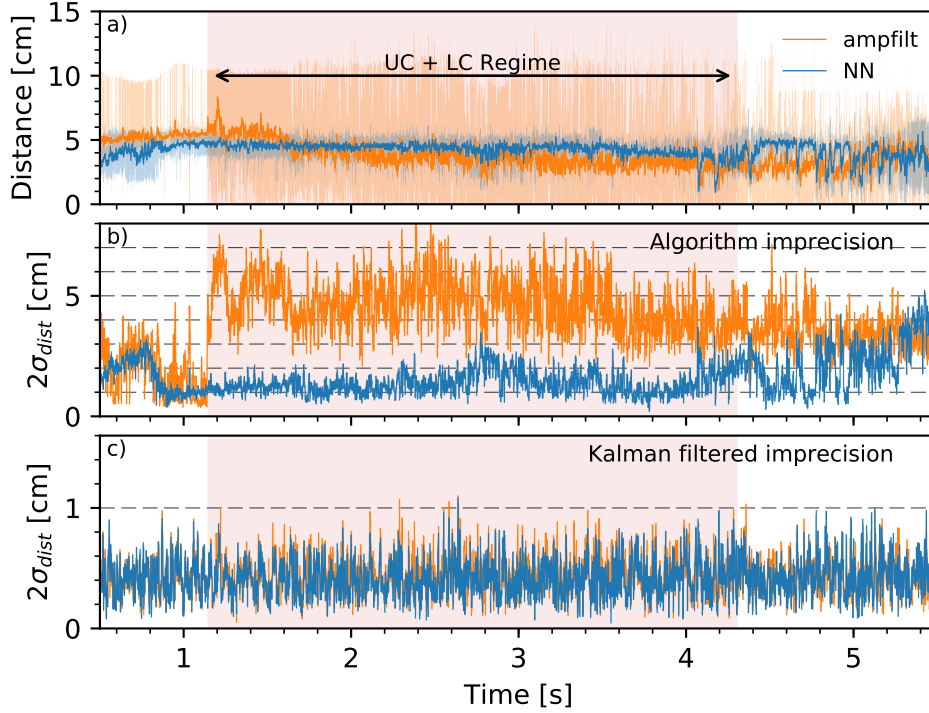


Figure 4.25: a) Estimated vacuum distances and moving 5 ms average distance during discharge #33841 using the *ampfilt* and neural network algorithms; b) Imprecision of the algorithms' measurements; c) Imprecision of the Kalman filtered measurements.

The imprecision of both algorithms is shown in b). The NN algorithm provides a much better imprecision throughout the discharge than *ampfilt*. It can also be seen that the *ampfilt* imprecision increases during the UC+LC regime, from around 2-3 cm to over 5 cm, while the NN imprecision is unaffected and remains below 2 cm for most of the discharge.

Implementing the Kalman filter to the estimation measurements improves both imprecisions to below 1 cm, shown in c). This is a direct consequence of the assumed measurement error limits for the Kalman filters. The accuracy of the measurements, however, depend on the absolute FF estimation and not on the relative deviation from the mean. Errors in vacuum distance estimations propagate to the reconstructed density profiles.

The density profiles reconstructed with the vacuum distances estimated by the *ampfilt* and neural network FF algorithms are represented in Figure 4.26 b) and c), respectively. The profile positions are referenced as the distance from the antenna origin, along the reflectometer line of sight.

The radial scan of the separatrix position can be observed in both density profile reconstructions, in the higher density layers. The profiles also show independence from the magnetic field variation, represented by the green shaded area.

The main differences between reconstructions is the distance between the wall and the first plasma reflection layer. The *ampfilt* reconstruction shows a plasma that moves outwards past the L-H transition, which occurs at around 1.2 s, and comes closer to the wall than the NN reconstruction. On the other hand, the neural network method shows an approximately constant vacuum distance throughout the dis-

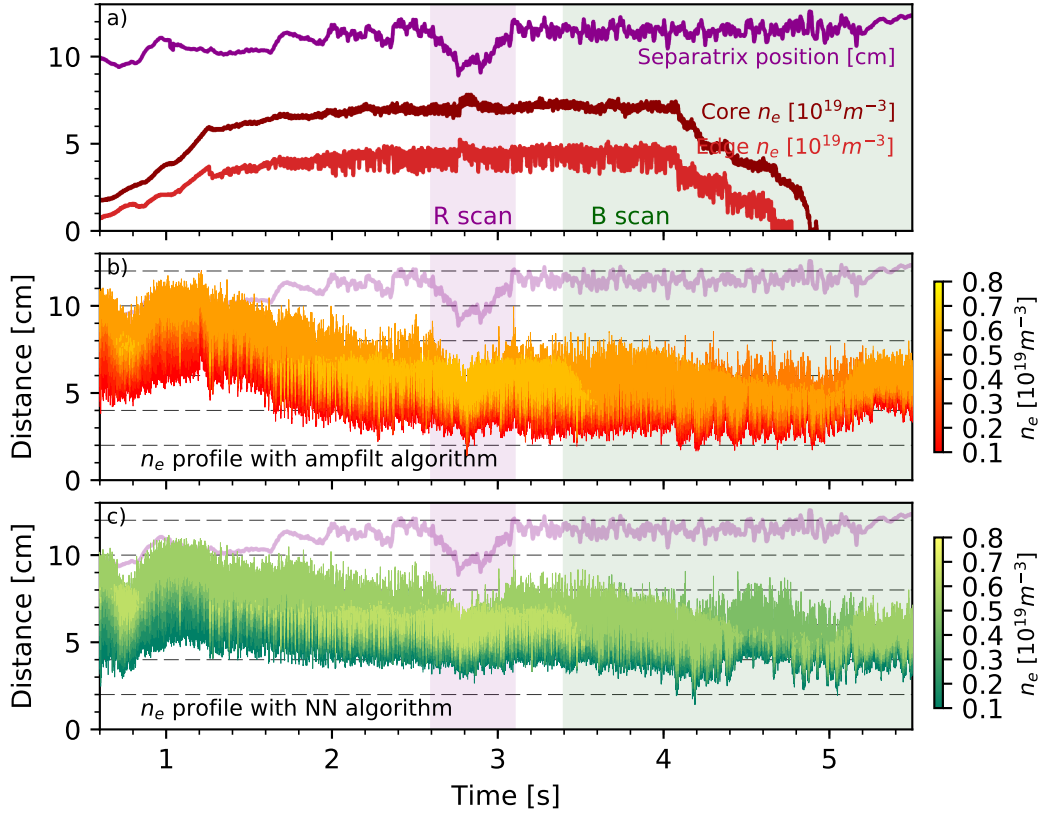


Figure 4.26: Reconstructed density profiles for discharge #33841 using the vacuum distances estimated by the *ampfilt* and neural network algorithms.

charge. A constant distance of the lower density plasma layers can be expected since the reflectometry antenna is embedded in the shadow, but very close, to the ICRF antenna limiters, forcing a steep profile at around 3-4 cm.

4.4.7 Conclusions of the first fringe estimation algorithms

The *ampfilt* algorithm provides a reliable first fringe estimation during most operational conditions. The Kalman filter uses consecutive measurements to improve the estimation precision of the first plasma layer position, determined from the first fringe frequency and the magnetic field profile obtained from the equilibrium codes.

A neural network was trained, using a comprehensive dataset, to mimic the first fringe estimation of an experienced X-mode reflectometry diagnostician. The neural network approach improves the precision of the FF estimation by up to a factor of three during the UC+LC regime.

Unfortunately, there is no way to verify the exact values of the first fringe frequency or position of the first plasma layer to calculate the accuracy of either method. However, by using multiple consecutive measurements and Kalman filtering, the first plasma layer estimation tends towards the most probable

location along the line of sight. The radial distance precision of the *ampfilt* and NN algorithms are reduced to less than ± 1 cm with Kalman filtering.

4.5 Processing the group delay measurement

This diagnostic uses the methodology described in [60] to reconstruct the electron density profiles from the reflectometry group delay data. The edge plasma layer is probed using the X-mode upper cutoff. The probing waves propagate a certain small vacuum distance and through the edge plasma, up to the corresponding cutoff layers, where they are reflected. This round trip delay is directly proportional to the phase of the measurement signal, and used in the reconstruction.

The reconstruction process is iterative, as the density profile is reconstructed inwards from the outer edges. For each iteration, the refractive index of the propagation medium is calculated using the probing frequency, the magnetic field profile, and the previously calculated electron density profile points. The phase shift of a probing signal propagating through this medium is integrated. The position of the cutoff layer (r) is determined from the phase difference between the new reflectometry measurement and the integrated phase. Finally, the local plasma electron density (n_e) is calculated from the upper cutoff condition:

$$f_{pe}^2 = f_{uc} (f_{uc} - f_{ce}). \quad (4.17)$$

This new (r, n_e) point is added to the reconstructed density profile, which is used in the next iteration.

4.5.1 Extracting reflectometry group delay measurement

The first fringe frequency indicates the start of the upper cutoff reflection, where the group delay measurement should start. The group delay measurement can be determined i) directly from the input quadrature signal phase, or ii) from the spectrogram data.

Using the raw quadrature signal phase has the advantage of increased density resolution enabling better feature representation. However, it comes at the cost of increased processing time and a higher dependence of noisy broadband spurious signals. Using the spectrogram data allows distinguishing different reflections but introduces aliasing and a decrease of the radial and density resolutions.

The simplest spectrogram extraction method assumes that the maximum reflection energy corresponds to the plasma reflection: the delay measurement is obtained at the peaks of the power spectrum for each probing frequency. Other methods from the literature [127] have been explored.

Both group delay measurements, taken from the raw signal phase and the spectrogram peaks, are shown in Figure 4.27 (left). Here, the raw phase delay is scattered all over the spectrogram due to unfiltered noise. On the other hand, the spectrogram⁶ peak delays follow the expected X-mode reflection signal shape, with much less scattering.

Despite these delay differences, the reconstructed density profiles have similar shapes, as shown in the Figure 4.27 (right). A step of 10 samples was chosen for the spectrogram windows, which reduces

⁶The spectrogram configuration uses a rectangular window of size 214, step 10 and padding of 2048.

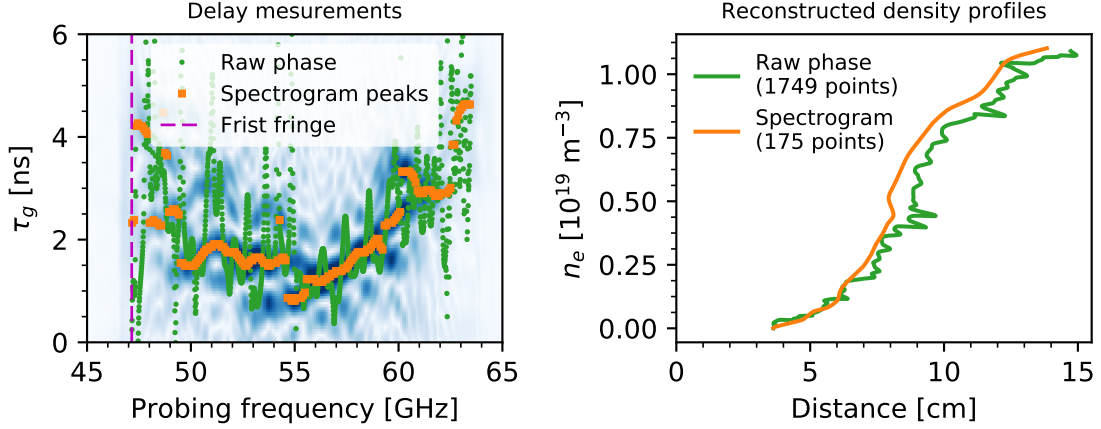


Figure 4.27: Reconstructed density profiles using group delays calculated from raw phase and spectrogram peaks using channel 1 at 1.5 s of #32774.

the number of output measurements, resulting in a less detailed density profile.

While both density profiles overlap up to $0.4 \times 10^{19} \text{ m}^{-3}$, the profile reconstructed from the raw phase shows a radial shift, due to a delay bump at around 54 GHz, which is not recovered. This reconstruction also presents a fine detailed structure. However, it is an artificial consequence of the scattered delay signal and does not directly represent the plasma structure. Such noise influence on the delay measurement is the main drawback of using the raw phase for density profile reconstruction. Using the main reflections shown in the power spectrum provides confidence in the group delay measurement and is the preferred method for this diagnostic.

4.5.2 Improving group delay spectrogram

The reflectometry measurement is not a static snapshot of the plasma. A single sweep takes $15 \mu\text{s}$ to probe the plasma in the 40-68 GHz range. Fast plasma events, such as turbulence, may be reflected along the reflectometry interference signal. The corresponding spectrogram may have shifts or scattered components of the group delay, which difficult the determination of the main reflection for density profile reconstruction.

Optimizing spectrogram parameters

A spectrogram is constructed by calculating the Discrete Fourier Transform, such as the Fast Fourier Transform algorithm (FFT), of a moving window. This Short-Time Fourier Transform allows visualizing the time evolution of the frequency components, which translates to a probing frequency evolution and respective group delay components. The group delay resolution of the FFT sets the minimum delay difference between two delay components to be distinguished. This group delay resolution $\Delta\tau_g$ depends on the window size N and sampling frequency f_s

$$\Delta\tau_g = \frac{f_s}{N} \frac{dt}{df}. \quad (4.18)$$

Spectrograms with multiple window sizes can be observed in the first column of Figure 4.28. Increasing the window size improves resolution and reduces group delay modulation. However, a large window size results in aliasing of the reflectometry measurement within a probing frequency interval Δf_p

$$\Delta f_p = \frac{df}{N} = \frac{|40 - 68| \text{ GHz}}{N}. \quad (4.19)$$

This aliasing can reduce the quality of group delay estimations in fast transients, such as at the start of the upper cutoff reflection, or in flat plateaus of the density profile. An acceptable probing frequency aliasing of 2 GHz was selected, which corresponds to a window size of 214.

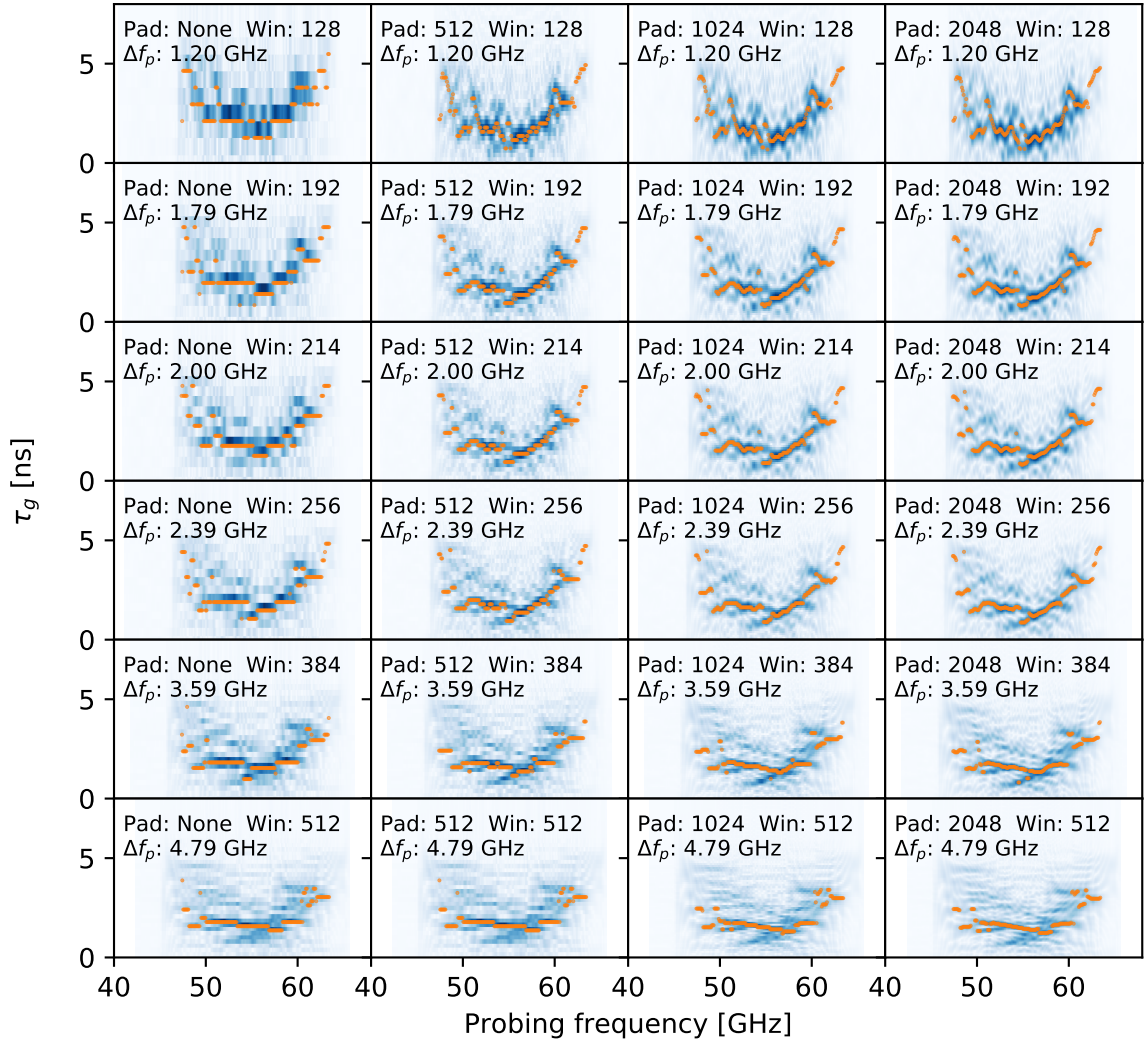


Figure 4.28: Effect of different window and padding parameters on group delay spectrogram.

Another optimization is zero-padding each windowed signal before calculating the FFT. This artificially increases the window size N , without adding more signal information. Zero-padding does not improve distinguishing between similar group delay components, but it does improve the accuracy of the delay feature. The columns in Figure 4.28 correspond to different padding values and their effect on

group delay estimate. A padding of 2048 improves group delay resolution $\Delta\tau_g$ from 0.5 ns to 0.052 ns.

Persistence of consecutive spectrograms

A persistence method was adopted, similar to the burst-mode analysis in [127], to average the delay spectrograms of multiple consecutive periodic (T) measurements. The common features are accumulated while random spurious are diluted, improving the SNR of the group delay measurement. The group delay is extracted from the persisted spectrogram to reconstruct the density profile. Figure 4.29 shows the spectrograms calculate with increasing persistence (p), and corresponding group delays. A persistence of $p = 1$ means only a single reflectometry measurement is used. It can be seen that the increased persistence smooths the delay signal, with diminishing returns past four sweeps.

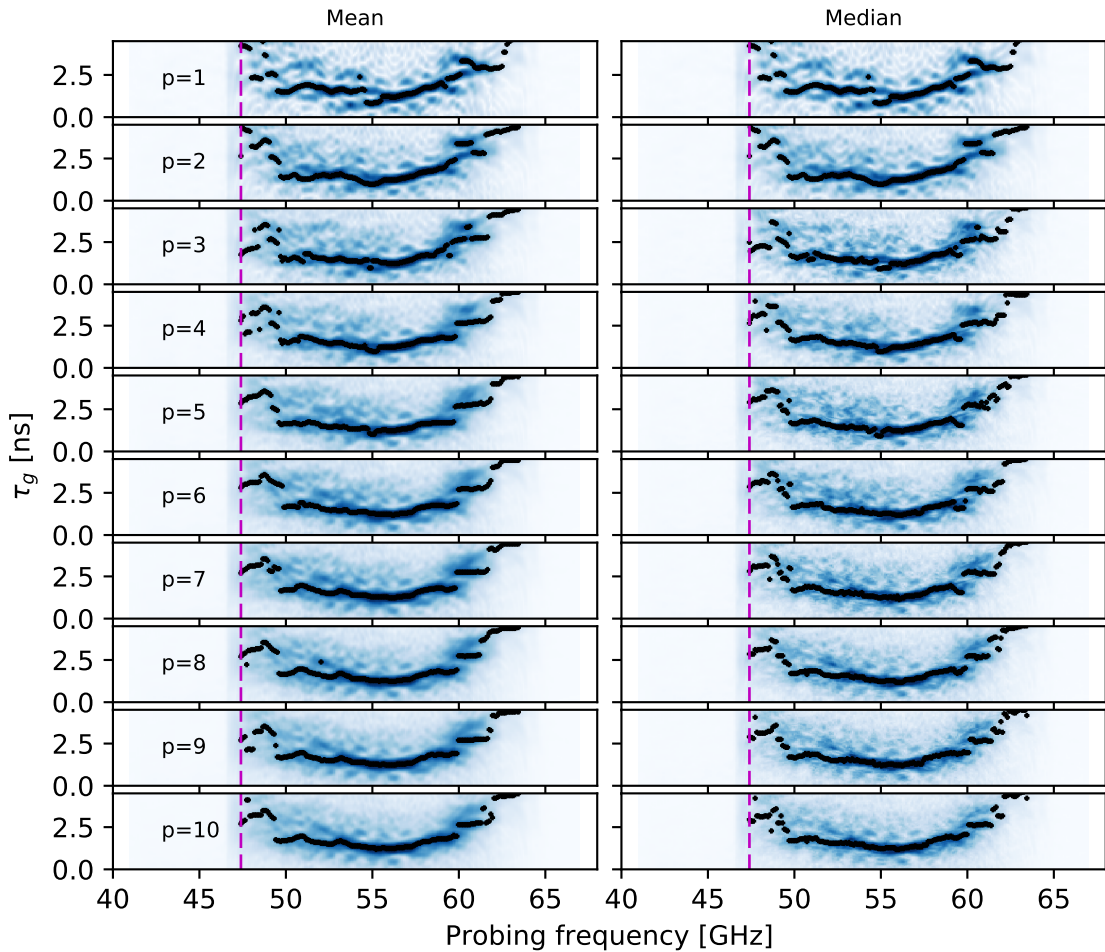


Figure 4.29: Spectrogram evolution with increasing persistence window using mean and median averaging using channel 1 at 1.500-1.501 s of #32774.

Two averaging functions are compared: for each data point in the two dimensional spectrogram matrix, the average value of the p previous measurements is calculated using the mean (left) or median (right) functions. The arithmetic mean of a large sample provides a good indication of the average value

of that sample. However, an outlier may contaminate result when calculating the mean of a smaller sample. The median function, on the other hand, provides an existing value in the sample and is immune to contaminating outliers.

The reduced reflection power near the first fringe typically results in a scattered reflectometry reflection signal, which gives different group delay signatures. A good definition of the group delay is necessary to prevent large radial jumps in the reconstructed density profile. For example, the median spectrogram for $p=6$ provides better continuity around 50 GHz than the corresponding mean spectrogram.

Figure 4.30 shows the analysis of the spectrogram persistence on the group delay gradient definition of the mean and median averaging functions. The derivatives of the group delays were calculated for 150 measurements, from three different discharges, using persistences 1 to 10. A low standard deviation of the group delay derivative $\sigma(d\tau_g/df_c)$ corresponds to less signal scattering and a better measurement. We can see that the average deviation is reduced with increased persistence, as expected, with minimums for persistence of six.

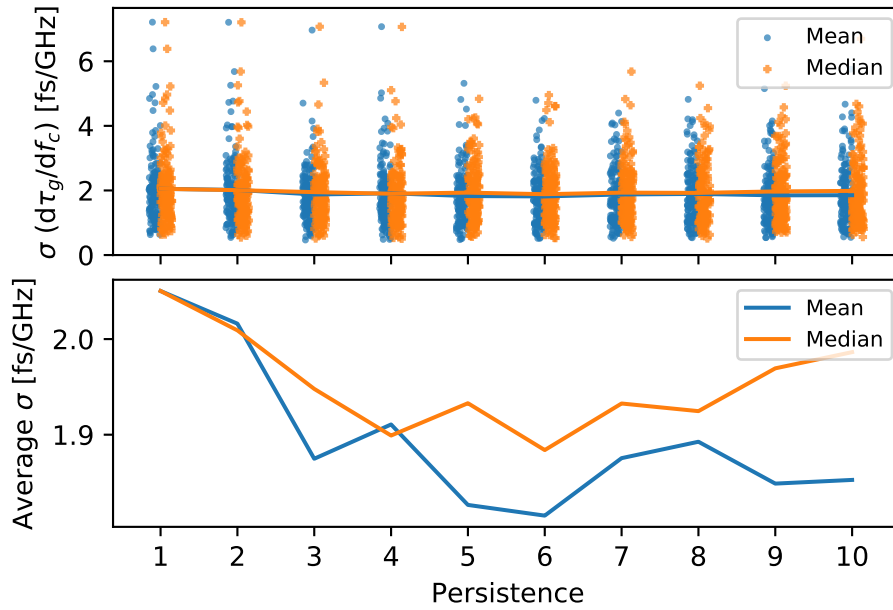


Figure 4.30: Analysis of the deviation of group delay gradients with increasing persistence using mean and median spectrogram averaging.

Evaluating spectrogram persistence on reconstructed density profiles

The reconstructed density profiles of the averaged reflectometry reflections are shown in Figure 4.31. Here we see the pronounced scattering of the group delay measurement with $p = 1$, which results in radial artifacts in the reconstructed density profile. However, the increased persistence solves most of the scattering issues, and both averaging methods provide similar results.

Although this persistence procedure reduces the effective temporal resolution of the reconstructed

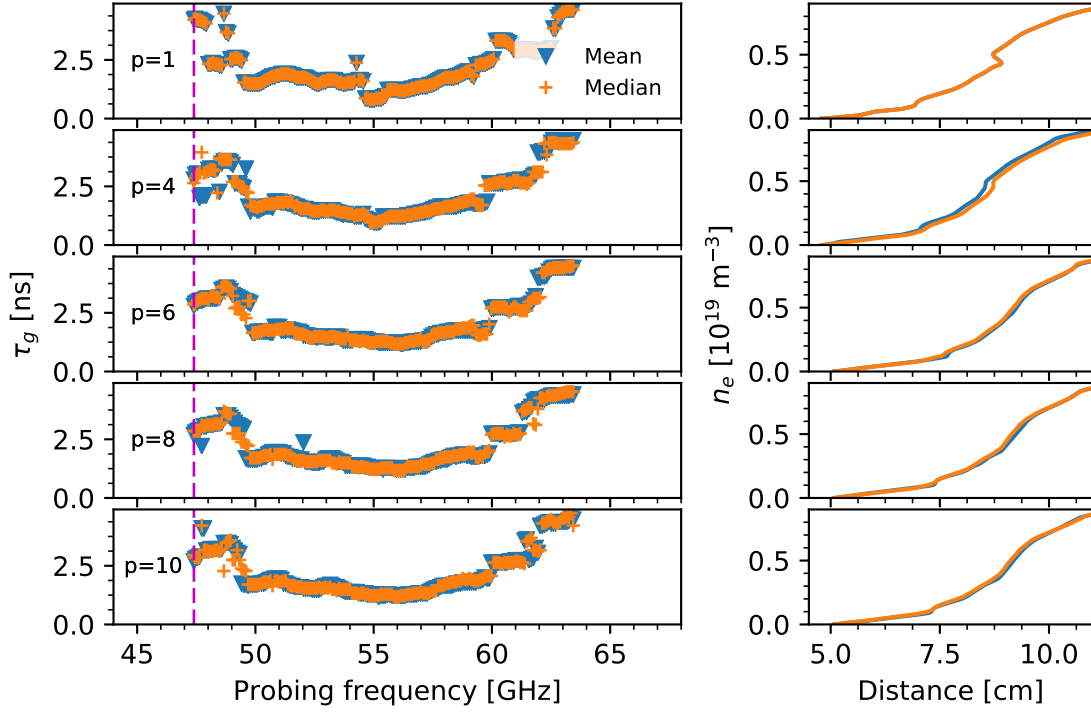


Figure 4.31: Comparing the group delays of mean and median persistences and corresponding reconstructed density profiles.

density profiles, a moving persistence window is used so that transient events may be observed with a maximum of $p \times T$ delay, where T is the acquisition period, typically $100 \mu\text{s}$. The default value for persistence in this system is four sweeps, which smooths the group delay over $400 \mu\text{s}$. This time resolution is sufficient for ICRF operation studies while still providing better time resolution than the 1 ms resolution of the magnetic equilibrium used for density profile reconstruction.

4.5.3 Estimation of the residual density at the first reflection

Ideally, the upper cutoff reflection occurs at the estimated first fringe frequency, which is the cyclotron frequency at the $n_e \rightarrow 0$ plasma position. However, the first plasma reflection occurs at a thin plasma layer with a non-zero residual electron density n_{e0} . In addition, edge plasma turbulence scatters the already low power of the reflection signal, resulting in a further loss of the of the reflected power around the $f_p \approx f_{ce}$ condition. This low reflection power may even be lower than the diagnostic detection limit.

Take the X-mode upper cutoff condition

$$f_{uc} = \sqrt{f_{pe}^2 + \frac{f_{ce}^2}{4}} + \frac{f_{ce}}{2}. \quad (4.20)$$

The electron cyclotron frequency is calculated from the first fringe frequency and used to determine the

location of the first plasma layer, using the magnetic field profile.

$$f_{ce} = f_{uc} - \frac{f_{pe}^2}{f_{uc}}. \quad (4.21)$$

By assuming a zero residual density, $n_{e0} = 0$, the electron cyclotron frequency becomes $f_{ce} = f_{FF}$ and the estimated ideal position of the first plasma layer is $r_0 = R(f_{ce} = f_{FF}) = r_{ideal}$. But for $n_{e0} > 0$, the first plasma position is closer to the wall, $f_{ce} < f_{uc} \rightarrow r_0 < r_{ideal}$.

Figure 4.32 shows the reconstructed density profiles for increasing n_{e0} , compared with the density profile measured with the Lithium beam diagnostic. Here we see that the first density profile data point (r_0, n_{e0}) moves closer to the wall with increasing residual density. We also see that the density profile for $n_{e0} = 0$, has an offset when compared with the Lithium beam profile. The reconstructed density profile closest to the lithium beam profile assumed a residual density $n_{e0} \approx 2 \times 10^{17} \text{ m}^{-3}$. The Li-beam density profiles are remapped to the reflectometry diagnostic line of sight assuming symmetry along the poloidal magnetic flux lines, ρ_{pol} . This example shows that a non-zero density for the first plasma layer must be estimated to improve accuracy of the density profile reconstruction, when compared with other diagnostics.

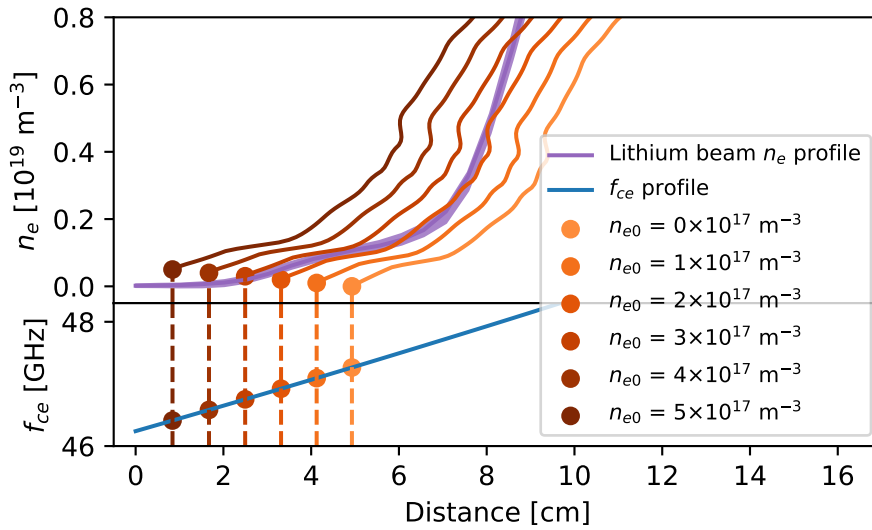


Figure 4.32: Reconstructed density profiles with different residual density n_{e0} initializations and compared with Lithium beam density profile at 1.6 s of #32774

Figure 4.33 (top) shows the evolution of the estimated position of the first plasma layer, assuming different residual densities n_{e0} from zero up to $4 \times 10^{17} \text{ m}^{-3}$. Two intervals of UC regime (2.3-2.7 s) and UC+LC regimes (3.4-3.8 s) were selected. The average reconstructed density profiles within these intervals, assuming the different residual densities, are shown in the bottom two plots. The density profiles provided by the Lithium beam diagnostic are also represented (orange). The shaded regions represent the 95% interval of the density profiles around the mean profile. This variation is measured as two standard deviations from the radial mean for the reflectometer and two deviations from the density mean for the Lithium beam diagnostic.

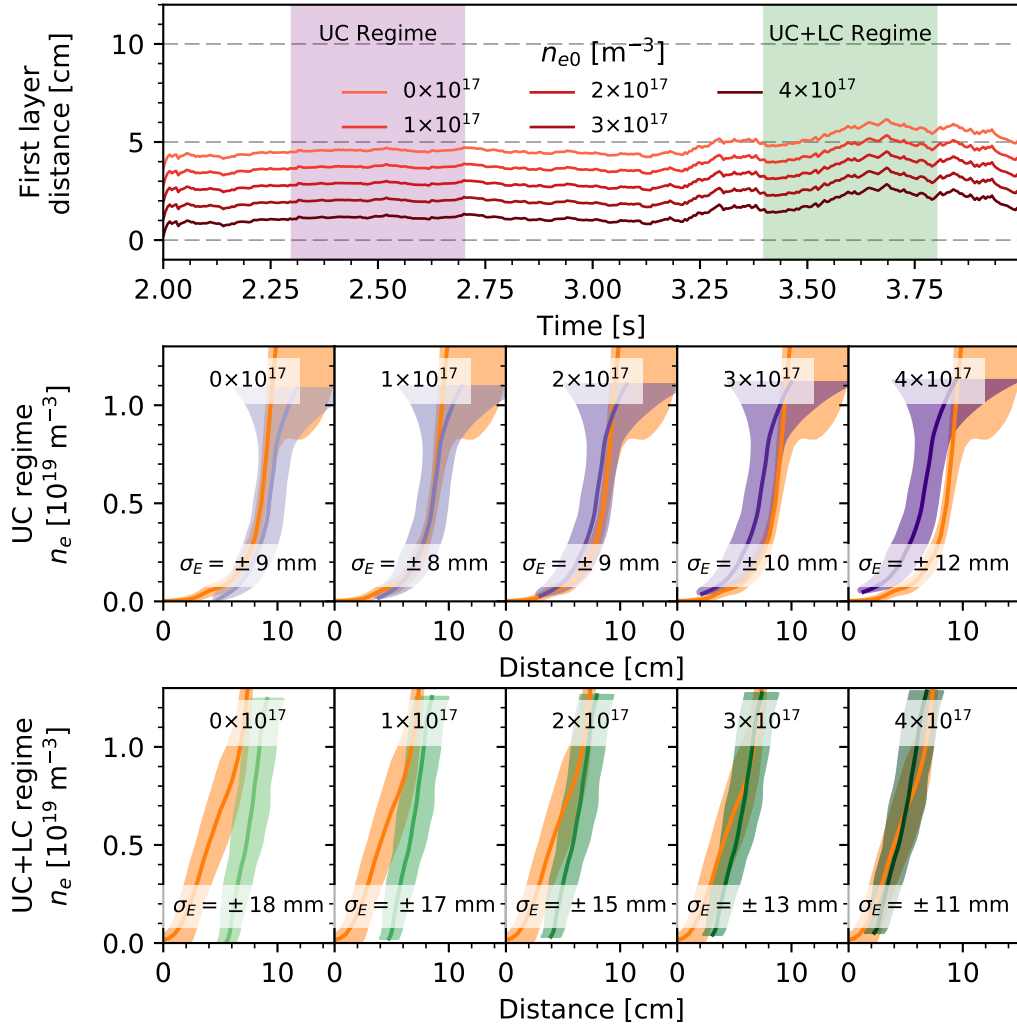


Figure 4.33: Comparison of the radial mismatch (σ_E) between the reconstructed density profiles using reflectometry channel 1 and the Lithium beam density profiles (orange), for multiple values of n_{e0} , in UC and UC+LC regimes of discharge #33291.

It is important to note that the Lithium beam diagnostic has several radially separated (1 cm) channels to measure the line emission profile, which is then used to reconstruct the plasma electron density profile. Improved Li-beam density profile reconstruction algorithms may provide spatial resolutions of 5 mm [128, 129]. This differs from a reflectometry measurement which, instead, measures the radial distance of a plasma layer with a certain electron density. In an ideal initialization, the reflectometry measurements are able to provide sub-cm density profile resolutions.

The mismatch between both profiles σ_E is calculated as two standard deviations of the radial error between the average Lithium beam profiles and the average reflectometry profiles. To calculate this mean error between the profiles, the broader Li-beam profiles are clipped and interpolated to the density range of the reflectometry profiles. It can be observed that the optimized residual density that minimizes the mismatch for the UC regime is $1 \times 10^{17} \text{ m}^{-3}$, while the higher $4 \times 10^{17} \text{ m}^{-3}$ residual density provides

the best results for the UC+LC regime. The first fringe estimation algorithms tend to have an offset in the UC+LC regime, which can be compensated by using a higher residual density.

The mismatch results presented here should be considered as qualitative as they compare a diagnostic measuring the density in front of a static position, Li-beam, and another measuring the radial distances of different density layers, reflectometer. Currently, there is no automatic estimation of the residual density during the density profile reconstruction of a discharge. For the study of the ICRF power coupling, the measurement of the distance between the ICRF cutoff layer and the antenna is affected by the residual density estimation, typically reducing this distance measurement. This offset remains approximately constant during the discharge and still allows the relative comparison of density profiles between intervals with and without ICRF heating. In order to understand and improve the residual density estimation at the first X-mode cutoff reflection, simulations using full wave codes and different density profile conditions must be studied further. Currently, the diagnostic operator must choose the residual density, typically between $0.5 \times 10^{17} \text{ m}^{-3}$ and $2 \times 10^{17} \text{ m}^{-3}$, which remains constant for the whole reconstruction.

4.6 Density profile reconstruction

4.6.1 Validation of the reconstruction data

The success of the density profile reconstruction is greatly dependent on the group delay used as input of the processing algorithm. This delay measurement is mainly affected by the estimation of the first fringe, the residual density and the determination of the main reflection component from the spectrogram data. Automatically processing a complete discharge, with several thousand profiles, may result in a few wrong reconstructions due to noisy data. A reconstructed density profile that is not physically viable should be discarded.

For this purpose, a set of three validation tests were designed. A reconstructed electron density profile must pass these tests to prove its validity and be stored in the official shotfile database. Only validated profiles are stored. These validation tests are:

1. Estimated first reflection position must be in front of the reflectometry antenna.
2. Plasma propagation group delay measurement must always be positive.
3. Propagation delay in vacuum for each radial position of the reconstructed profile must be lower than the corresponding measured group delay.

If the density profile or the input delay data fails any of these tests, then the measurement is either reprocessed with other parameters, or discarded.

Position of first reflection

The position of the first reflection is determined from the magnetic field profile and the estimated local electron cyclotron frequency. By assuming that the first plasma reflection occurs at some residual den-

sity, then the radial position of this reflection occurs nearer to the wall. However, there can be no plasma behind the wall as the first reflection must occur in front of the reflectometry antenna. The f_{ce} at the estimated first reflection position, considering a non-zero residual density, must be higher than the f_{ce} at the wall. An underestimation of the first fringe frequency combined with a high residual density contribute to failing this validation. Figure 4.34 shows the first plasma position assuming different residual density values. We see that the highest n_{e0} places the plasma behind the wall, rendering this estimation invalid.

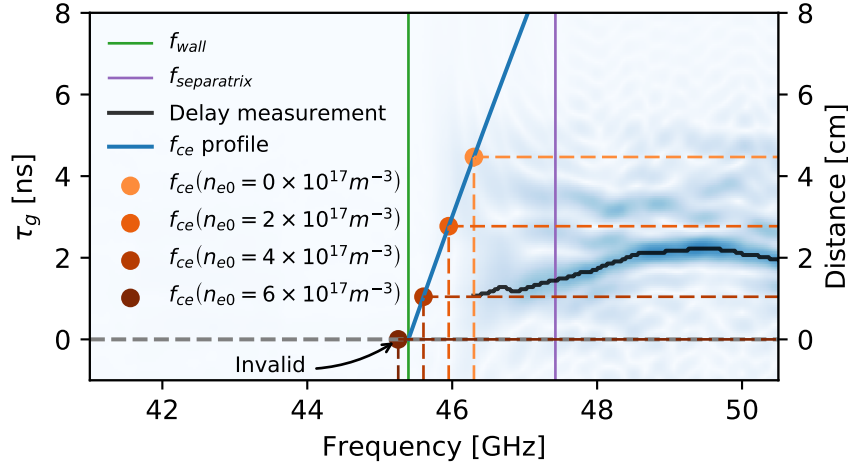


Figure 4.34: Validation test of first plasma position estimation.

Positive plasma propagation delay

Since the calibration procedure sets the reference to the mouth of the reflectometry antenna, all the reflection delay measurements must have a positive value. For density profile reconstruction, the delay due to vacuum propagation must be subtracted from the group delay measurement. This sets the reference for the group delay measurement at the first plasma reflection layer, which should always have a positive value.

An over estimation of the first fringe frequency results in a higher vacuum propagation delay, which is subtracted from the group delay measurement. Multiple reflections or plasma turbulence effects, due to ICRF operation for example, may result in spectrogram modulation features that then translate to negative group delay values. This is specially problematic in H-mode plasmas, which typically already have a low delay measurements due to the steep density gradient right in front of the reflectometry antenna.

Figure 4.35 shows a group delay measurement, whose vacuum delay was corrected using different first fringe frequency estimations. The highest FF estimation of 43.4 GHz results in a delay signal with negative values, making it invalid.

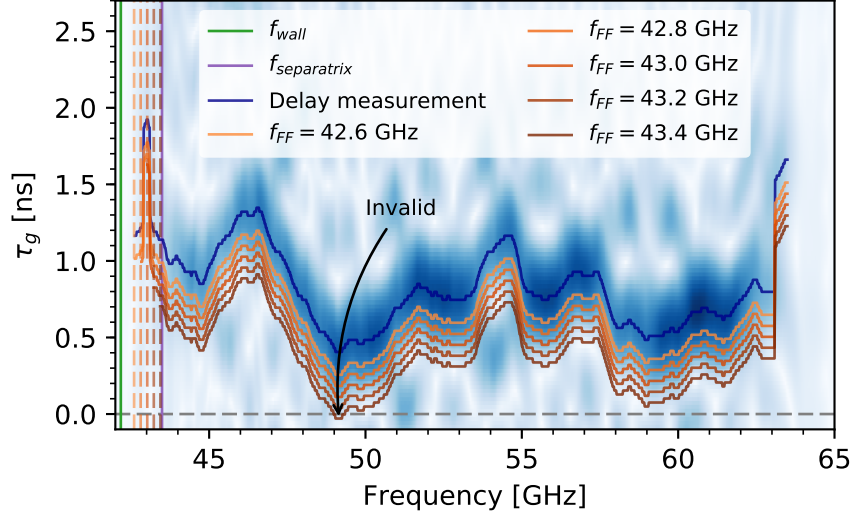


Figure 4.35: Validation test of positive plasma propagation delay.

Comparing reconstructed profile with round trip delay assuming vacuum propagation

Assume that, instead of propagating in plasma, each probing wave propagates through vacuum up to a mirror. The radial position of this mirror depends on the probing wave frequency and is equal to the radial position of the reconstructed density profile. The round trip delay of these waves propagating in vacuum *must always be lower* than the corresponding reflectometry delay measurement, used as input to invert the density profile. Delay measurements with a positive value, such that they pass the previous tests, may still fail this test if the first plasma position is wrongly determined.

Figure 4.36 illustrates how some group delay measurements, that passed the previous tests, may be invalid. The represented delay measurement is the direct reflectometry group delay (τ_g), without compensating for vacuum distance. The remaining delays correspond to the round trip delay assuming propagation in vacuum (τ_{vac}) of probing waves propagating from the wall up to the radial positions of the density profile, given by

$$\tau_{vac}(n) = 2 \frac{r(n)}{c}. \quad (4.22)$$

The condition for validity is

$$\tau_{vac} < \tau_g \quad (4.23)$$

Only the three lower FF estimations shown in the figure provide valid group delays.

Overestimation of the first fringe frequency results in a reconstructed density profile that may not be valid, despite passing the *positive plasma propagation delay* validation test. Increasing the residual density, on the other hand, may compensate this effect by lowering the estimated vacuum distance.

Summary on data validation procedures

These tests provide a validation of the reconstructed density profiles based on their physical feasibility. The *position of first reflection* validation provides an upper limit to the residual density estimate. On the

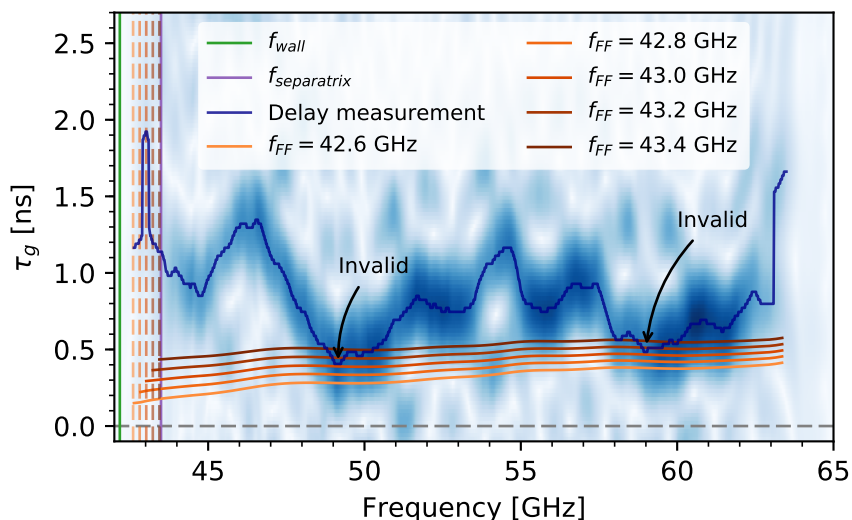


Figure 4.36: Validation test of reconstructed density profile location compared with the round trip delay assuming propagation in vacuum.

other hand, the *plasma propagation delay* test is capable of verifying an overestimation of the first fringe frequency, before reconstructing the density profile. This is specially useful to invalidate reflectometry measurements contaminated with multiple reflections, which result in frequency modulation features in the spectrogram data, and noisy delay measurements.

An iterative procedure to optimize FF frequency and residual density estimates may be implemented. This process would require reconstructing a density profile, validating the reconstruction, providing a new estimate for both residual density and first fringe, and repeat the procedure until the test is passed. Due to the long processing time required for this iterative procedure, and low quality of some reflectometry measurements, invalid reflectometry sweeps are discarded without further attempt at optimization.

4.6.2 Processing the density profiles

The default diagnostic operation mode acquires all three channels 1, 4 and 8, with a 100 μ s interval between sweeps. Faster acquisition modes are possible, with a minimum sweep interval of 25 μ s, to accommodate the settling time of the VCO. The internal memory of the acquisition system limits the acquisition to around 89 thousand profiles per each of the three channels. In the default operation mode, this covers around 8.9 seconds of discharge. A faster acquisition mode can be set to use only channel pairs 1-4 (top and mid plane) or 8-4 (bottom and mid plane), doubling the acquired number of profiles to nearly 178 thousand. All the acquired measurements must be validated and processed automatically. Only the density profiles whose reconstruction has been validated are uploaded to the databases to be accessible by the ASDEX Upgrade community.

Automatic distributed processing of shotfile data

Processing a single channel usually takes up to 3 hours on a single core. However, since each channel is independent, multiple channels and multiple discharges are processed simultaneously on separate cores. To achieve this a queueing system was implemented to manage processing jobs, distributed over multiple computers, using the *RQ* Python library [130]. A centralized server receives the processing job orders from the diagnostic operator, and assigns each job to a connected worker daemon. Up to 210 worker daemons are used to process raw data simultaneously across the 14 shared computation clusters, depending on the available resources. This queueing implementation keeps track of failed and completed jobs, and automatically starts new jobs after the previous one has completed.

Quality control of reconstructed profile data

During the processing of a complete discharge, validated and discarded sweeps are used to calculate an overall quality of the processing procedure. Processing quality is measured as the number of validated profiles over the total acquisitions, and typically ranges between 80-95%. This metric is used by the diagnostic operator to verify processing quality of a discharge and to detect failures that require further tuning of processing parameters.

Official shotfile database

ASDEX Upgrade uses a centralized database to store diagnostic data since the early 1990s. The diagnostic data related to a single discharge is typically called a shotfile. Level-0 shotfiles are typically reserved for acquired raw data, while level-N shotfiles contain processed data derived from level-0 up to level-N-1 shotfiles.

Our validated reflectometry diagnostic data is also made available through the official database: i) reflectometer settings and acquired raw data are stored in a level-0 shotfile; ii) reconstructed and validated density profile data is stored in a level-1 shotfile.

4.7 Summary

This chapter detailed the commissioning of the implemented reflectometry system. First, we described the in-vessel reflection features that appear in the raw reflectometry signal with and without plasma, and detailed the calibration procedure to remove the waveguide dispersion from the measurement.

Two first fringe estimation algorithms were developed. The *ampfilt* algorithm uses the amplitude and spectral signature of the raw signal to determine the start of the plasma reflection. The second algorithm uses neural network model to look for the same signature by interpreting the raw signal spectrogram similarly to a human diagnostician. It was shown that under high core electron density conditions, the reflectometry measurements may be contaminated with the X-mode lower cutoff reflection, which increases difficulty in determining the start of the upper cutoff region.

The density profile is reconstructed using the group delay of the plasma reflection. This delay signal can be obtained from the raw signal phase. However, using the delay spectrogram provides more reliable results as multiple reflections can be distinguished. Several spectrogram techniques were analysed to improve data extraction: window aliasing, padding and persistence. It was determined that a non-zero residual density must be considered to improve density profile accuracy.

Validation tests are used to filter out impossible reconstructions, which are not stored in the official shotfile database. Density profile reconstruction and quality control are performed automatically using a distributed queueing system on the ASDEX Upgrade computation facilities.

Most of the commissioning results presented in this chapter correspond to measurements acquired using channel 1. However, the methodology used for density profile reconstruction is identical to reflectometry channels 4 and 8. New reflectometry channels may be easily added in the future. Their commissioning follows the same structure described in this chapter.

Chapter 5

Experimental results

Most discharges were acquired during the commissioning phase of the reflectometry diagnostic. In this chapter, measured density profiles are validated against other diagnostic data. Results obtained in different plasma regimes are presented. By having multiple channels at different locations, this diagnostic is capable of measuring poloidal variations of plasma events, also presented. The diagnostic results used in ICRF operation studies are discussed.

5.1 Validation of diagnostic commissioning

5.1.1 Comparison electron density profiles with other diagnostics

ASDEX Upgrade is a well diagnosed machine with several electron density profile diagnostics. The Lithium-beam [129] and the broadband O-mode reflectometer [131] are two diagnostics that measure the edge density profiles. In addition to measuring the plasma edge at the low field side (LFS), the O-mode reflectometer has antennas on the high field side (HFS), providing simultaneous LFS and HFS measurements. The density profile results of the new multichannel X-mode reflectometer are compared in this section with the measurements from these standard diagnostics.

The analysis of the density profile data of different diagnostics must take into account the i) measurement principle, ii) the measured range iii) and the location of the diagnostics. The Li-beam diagnostic provides density profile measurements with a radial sensitivity of 5 mm. The O-mode reflectometer probes the radial position of density layers starting at approximately $0.4 \times 10^{19} \text{ m}^{-3}$, requiring the artificial initialization of density profiles below this value. The Thomson scattering diagnostic measures plasma densities at ten 2.5 cm long scattering volumes, separated by 6 cm, at the edge [132, 133]. Despite being presented here, the data from the Thomson scattering diagnostic is not used for comparison. Furthermore, each of these diagnostics, including the three channels of the implemented X-mode reflectometer, look at the plasma from different poloidal and toroidal locations inside the vessel. In order to compare the diagnostic measurements, the density profiles must be projected onto the common magnetic flux lines poloidal coordinates ρ_{pol} , assuming symmetry along the magnetic field lines. The lines of sight of the Li-beam, the O-mode reflectometer (LFS), the Thomson scattering and the three channels

of the X-mode reflectometer (Ant 1, 4 and 8) are projected in the poloidal cross section in Figure 5.1.

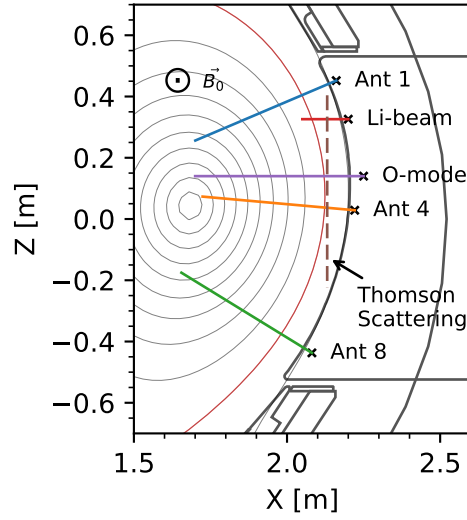


Figure 5.1: Poloidal lines of sight of the different density profile diagnostics on ASDEX Upgrade.

During discharge intervals with a stable plasma, with no ELM activity or ICRF operation, the density profiles measured by diagnostics at the different poloidal locations should overlap. Figure 5.2 shows the edge density profiles of the Li-beam, the O-mode reflectometry and the three new reflectometry antenna channels embedded in the ICRF antenna, during the L-mode discharge #33523 with only ohmic heating around 3.94 s. The magnetic field is -1.9 T and the interferometer diagnostic provides an average integrated density measurement at the edge of $1.5 \times 10^{19} \text{ m}^{-3}$, and $2.9 \times 10^{19} \text{ m}^{-3}$ at the core, which corroborate the observed density profiles.

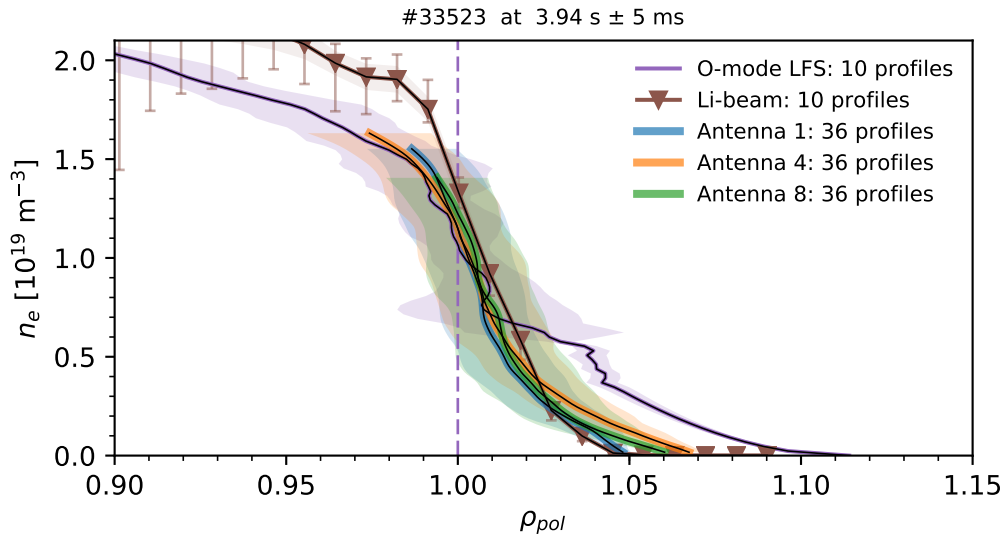


Figure 5.2: Comparing X-mode reflectometry density profiles with Li-beam and O-mode reflectometry in L-mode discharge #33523 with $B_T = -1.9 \text{ T}$.

The represented density profiles are obtained by averaging the multiple profile measurements within

a 10 ms interval, while the shaded regions represent the $\pm 2\sigma$ standard deviation within this interval. The number of profile measurements of each diagnostic in this interval is given in their legend. Reflectometry measurements do not have a direct estimate for the uncertainty, whereas the uncertainty for the Li-beam diagnostic does, as represented by the vertical error bars. For this reason, we qualitatively interpret the error using the deviation ($\pm 2\sigma$) of the reflectometry density profile measurement from the mean profile.

The measured density profiles differ between the antennas, due to the different local magnetic fields that affect the X-mode reflectometry signal. It can be seen that profiles measured from antenna 4, the one influenced by the lowest magnetic field, go up to $1.6 \times 10^{19} \text{ m}^{-3}$, whereas the ones from antenna 8, further inside the vessel and influenced by higher magnetic field, only reaches $1.4 \times 10^{19} \text{ m}^{-3}$.

The X-mode density profiles overlap well with the Li-beam profile at the edge. Both of these diagnostics provide more reliable edge density profile data than the O-mode reflectometer, which requires an artificial initialization up to approximately $0.4 \times 10^{19} \text{ m}^{-3}$. This artificial group delay initialization results in the density profile curve up between $\rho=1.05$ and 1.12. As the density increases, the density profiles overlap within their variation interval. This result provides a good validation of the implemented X-mode measurement and density profile reconstruction methods for L-mode plasmas.

The density profiles in Figure 5.3 were measured in an H-mode plasma with 1.3 MW ECRH and 4.9 MW NBI heating power, within an interval with no ELM activity, or ICRF operation. This high density plasma has an average edge density of $5.3 \times 10^{19} \text{ m}^{-3}$, and a core density of $7.9 \times 10^{19} \text{ m}^{-3}$. The strong magnetic field (-2.5 T) limits the maximum measured density of the X-mode reflectometry diagnostic to approximately $0.6 \times 10^{19} \text{ m}^{-3}$. The steep density gradients at the plasma edge, common to H-mode plasmas, are visible in all measurements, which overlap within the confidence interval.

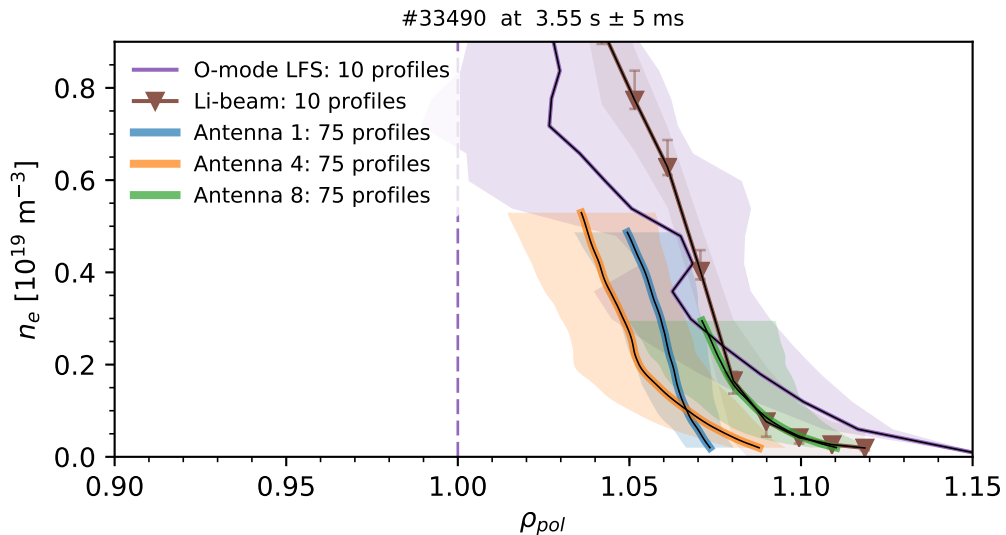


Figure 5.3: Comparing measured density profiles with Li-beam and O-mode reflectometry in H-mode discharge #33490 with $B_T = -2.5 \text{ T}$.

5.1.2 Radial and poloidal sensitivity to plasma displacement

This new diagnostic has three observation points at different poloidal locations, capable of probing the plasma simultaneously. This allows the approximate measurement of plasma shape and movement evolution during a discharge. In discharge #34830, a vertical displacement of a circular plasma was performed. The positions and shape of the circular plasma at times 2 s, 2.4 s and 2.6 s are shown in Figure 5.4. The plus markers determine the magnetic axis and the dashed lines correspond to the separatrix.

The plasma starts near the center of the vessel, as indicated by the magnetic axis aligned with the mid plane antenna 4. At this time, the outer plasma edge closely follows the curvature of the wall. Then, between 2 s and 2.6 s, the plasma is scanned vertically, squeezing the upper plasma edge against the wall limiter, near antenna 1.

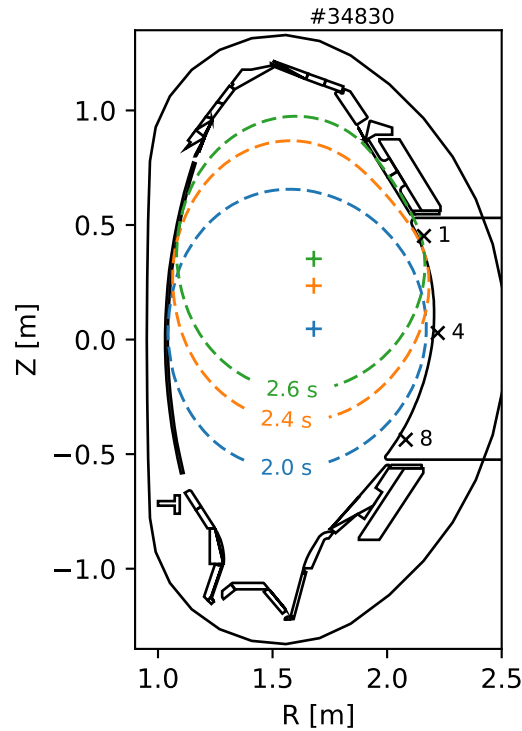


Figure 5.4: Vertical displacement of a circular plasma in discharge #33830.

The probed regions of the plasma depend on the local magnetic field and the plasma edge densities. As the plasma moves, so do the probed regions inside the vessel. These probed regions are shown in Figure 5.5 (left). The probed regions closely follow the edge plasma shape and the separatrix position, as the plasma is scanned upwards.

The corresponding reflectometry upper cutoff group delay measurements for each antenna are shown in Figure 5.5 (right). The plasma is closest to antenna 4 during most of the discharge. This can be observed by the lower measured group delay. Between 2.25 s and 2.5 s, the group delay measured with antenna 8 increases (darker regions) as the plasma moves upwards and distances itself from the bottom antenna 8. Between 2.5 s and 2.7 s, the cutoff conditions along the line of sight of antenna

8 occur outside the probing band of the diagnostic.

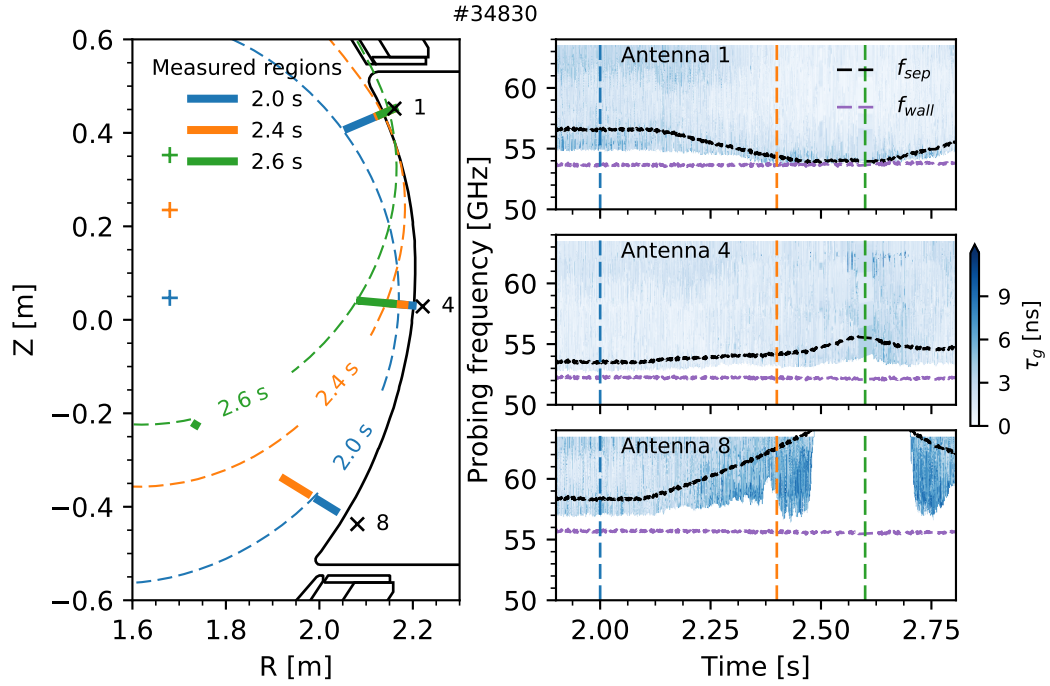


Figure 5.5: Probed plasma regions of the vessel for each plasma shape (left) and group delay measurements (right) of #34830 at each antenna.

The reconstructed density profiles show the evolution of the plasma shape during the discharge, seen in Figure 5.6. The plasma edge is closest to the mid plane antenna 4 at around 2 s. At this time, all channels accurately measure the edge plasma density profiles. Then, as the plasma moves upwards, it distances itself from the bottom antenna 8, and mid plane antenna 4, and becomes closer to top antenna 1. The density profile measurements start at the first fringe location r_0 and may measure beyond the separatrix r_{sep} , depending on the plasma conditions in front of each antenna.

The reconstructed density profiles are represented in a three dimensional view in Figure 5.7, to facilitate their interpretation. The gradual vertical displacement of the plasma can be observed by the radial measurements of each reflectometry channel. As the plasma moves away from the mid plane wall, the density gradient decreases in channel 4. The opposite effect occurs as the plasma is squeezed against the top antenna 1, where the density gradients become very steep.

These results show the good poloidal and radial sensitivity of the diagnostic to the plasma shape. Such sensitivity is useful for studying, for example, the formation of convective cells during ICRF operation, since poloidal differences between the mid plane and the top or bottom layers regions of the plasma can be measured.

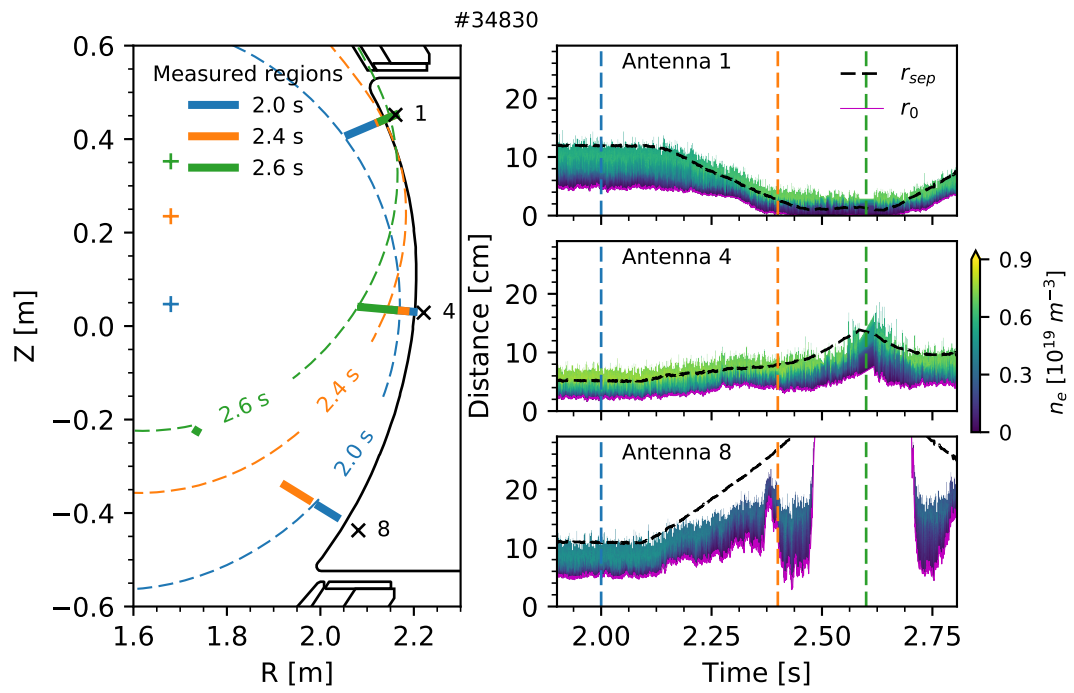


Figure 5.6: Probed regions in the cross section and measured density profile evolution during discharge #34830 (right).

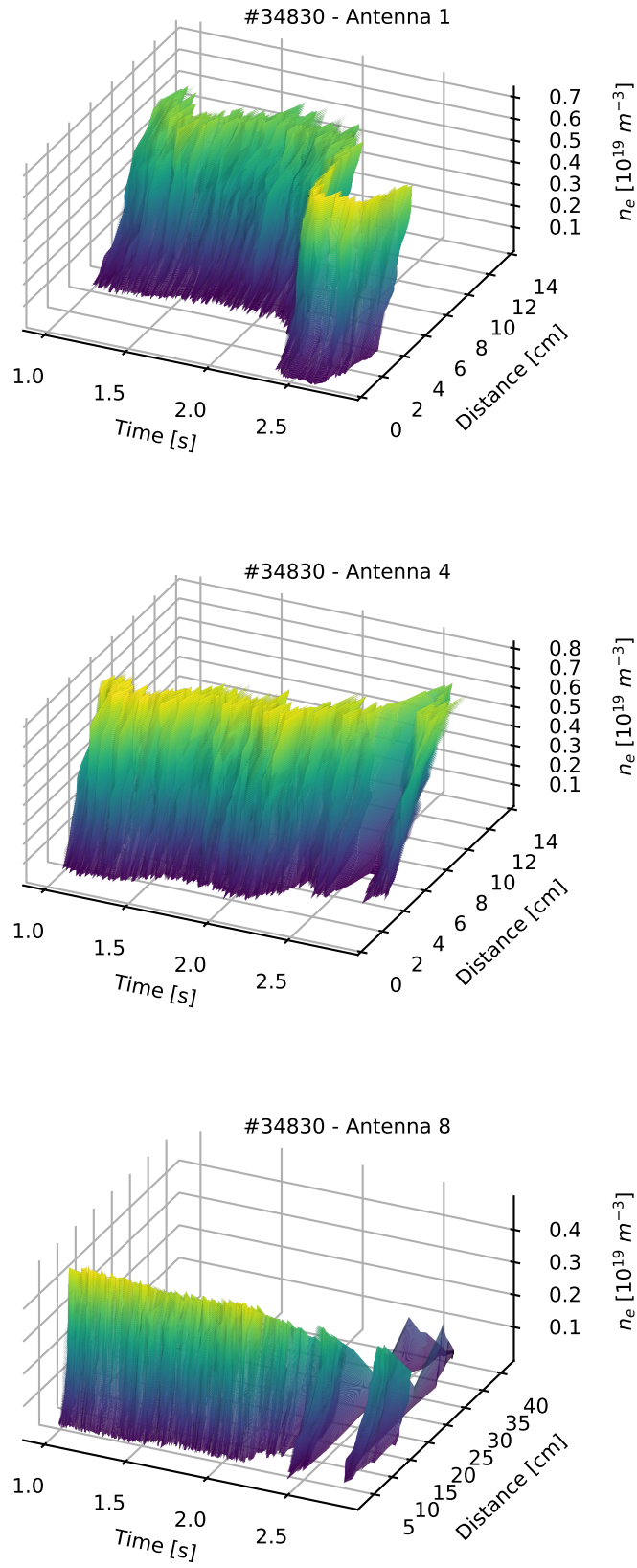


Figure 5.7: Three dimensional view of the reconstructed density profiles of channels 1, 4 and 8 for a vertical scan of a circular plasma in discharge #33830.

5.1.3 Measuring density profiles deep into the plasma

The typical fusion plasma electron profile has a mostly flat density region at the core. In a fusion plasma with an increasing magnetic field profile, this flat density region can be probed using the X-mode upper cutoff region. As the probing frequency increases, the cutoff reflection occurs for a higher magnetic field for the same density, meaning further inside the plasma.

However, the maximum measured density using our X-mode reflectometer is limited by the reduced useful probing bandwidth (up to 64 GHz). The measurement range is maximized for discharges with low magnetic fields and low core densities, and this reflectometry diagnostic is capable of measuring profiles deep into the plasma. Figure 5.8 shows the reconstructed density profiles in front of each channel in discharge #33918 with $B_T = -1.8$ T and core $n_e = 2 \times 10^{19} \text{ m}^{-3}$.

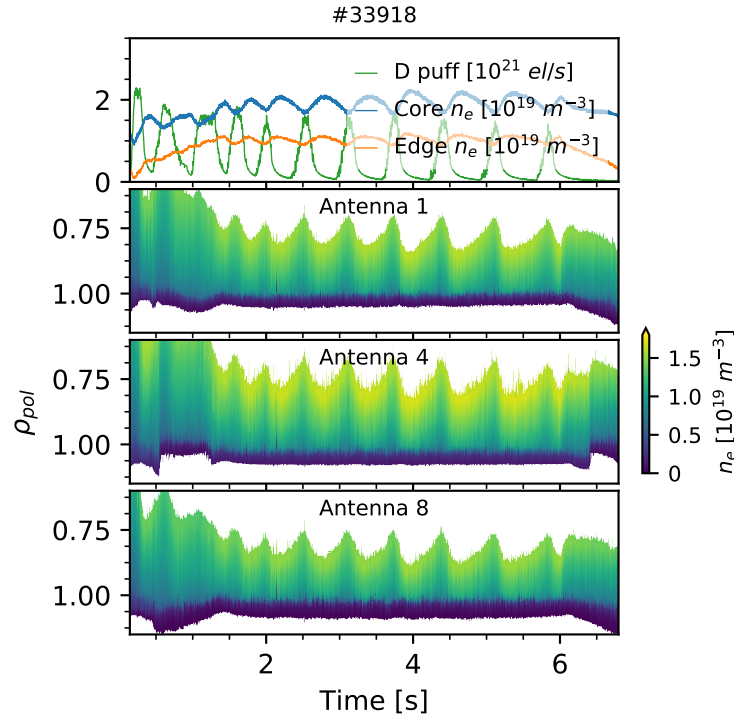


Figure 5.8: Density profile measurements in a discharge with low density and low magnetic field. The effects of gas puffing on the density profiles can be observed.

While the low magnetic field results in a first fringe frequency lower than the probing range, the reconstruction was artificially initialized, assuming a higher residual density, allowing a qualitative analysis of the density profile evolution. Density fluctuations, seen in the core region of the profiles, are coincident with the D gas puffing. The gas puffing effects are easily observed in the three dimensional density profile reconstruction in front of the mid plane antenna 4 in Figure 5.9.

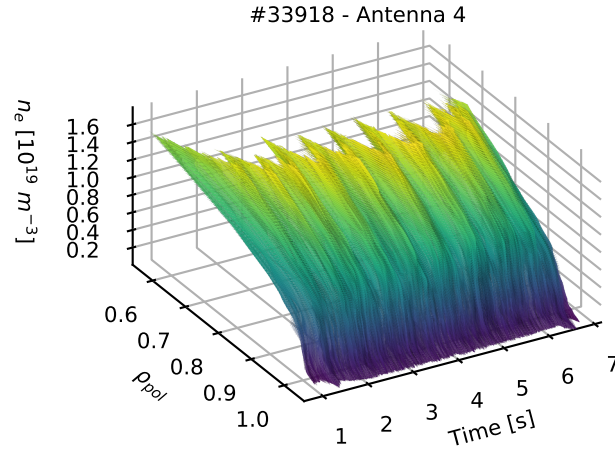


Figure 5.9: 3D reconstruction of density profiles plasma measured with antenna 4 in a discharge with low magnetic field and low core density.

5.2 Observing typical plasma phenomena

The diagnostic was also validated by observing typical plasma phenomena such as the L-H transition and edge plasma instabilities.

5.2.1 L-H transition

The good confinement of plasmas in a tokamak is dependent on the plasma pressure and current and the imposed magnetic fields. By increasing the plasma heating power, a transport barrier is formed at the edge of the plasma which suppresses plasma turbulence and improves the confinement [134]. A pedestal appears in the plasma density profiles, which results in steeper gradients in a narrow edge plasma region. This high confinement scenario is called the H-mode. The transition from low confinement mode (L-mode) to H-mode occurs when the plasma is heated strongly above a certain threshold. The measured density profiles during the L-H transition are observed in Figure 5.10, using the new reflectometer and compared with the density profiles from the Lithium-beam diagnostic.

The average density profiles, and confidence intervals, are calculated within four time intervals along this transition and represented in the right plots, respectively to each antenna measurement in magnetic flux coordinates. In the first interval (blue) the plasma is in L-mode with a more relaxed density profile at the edge. Then, as the average pulse-width modulated (PWM) NBI heating power increases (orange region) the L-H transition is triggered (vertical dashed line), approximately at 1.6 s.

The electron density at the plasma core increases concurrently with the NBI and ECRH heating power (green and red regions). The H_α and ELMs signals indicate the increased ELM activity associated with H-mode plasmas. During this transition, the density profiles move outwards at the edge. This displacement is observed in all the measured reflectometry density profiles, which are consistent with the Lithium-beam measurements. The large displacement in the H-mode region (red region) is consistent

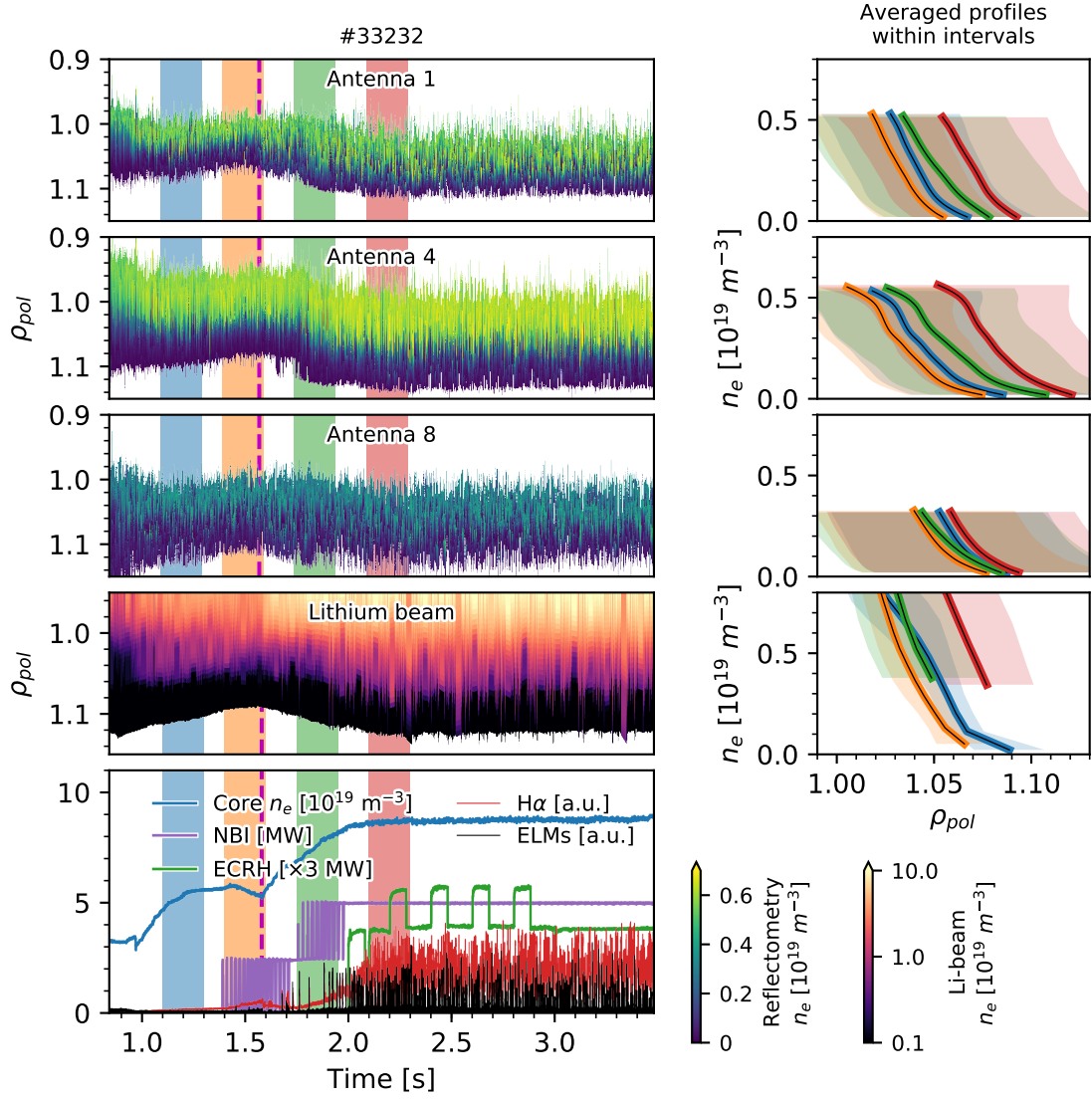


Figure 5.10: Density profile evolution during L-H transition of discharge #33232 measured using the three reflectometry channels and compared with the Lithium-beam density profiles.

between the Lithium-beam measurements and the reflectometry antennas 1 and 4, which are located near the top of the vessel. The antenna 8, closer to the divertor in the lower region of the vessel, does not show such a large displacement, indicating a different shape of the SOL plasma. Due to the limited measurement range of the diagnostic during typical 2.5 T discharges ($<10^{19} \text{ m}^{-3}$), neither the transport barrier or the pedestal top are observed.

5.2.2 Edge localized modes

The steep temperature and density gradients in H-mode plasmas result in edge localized mode (ELM) instabilities. ELMs are short time instabilities in the plasma edge that result in a release of plasma energy and particles towards the wall and divertor. This particle expulsion from the plasma results in a temporary increase of the electron density at the edge. ELM events result in increased heat loads at

the wall and in the divertor regions, which may deteriorate the plasma facing components. Observing, understanding and mitigating ELMs is critical for the long-term exploration of a nuclear fusion reactor.

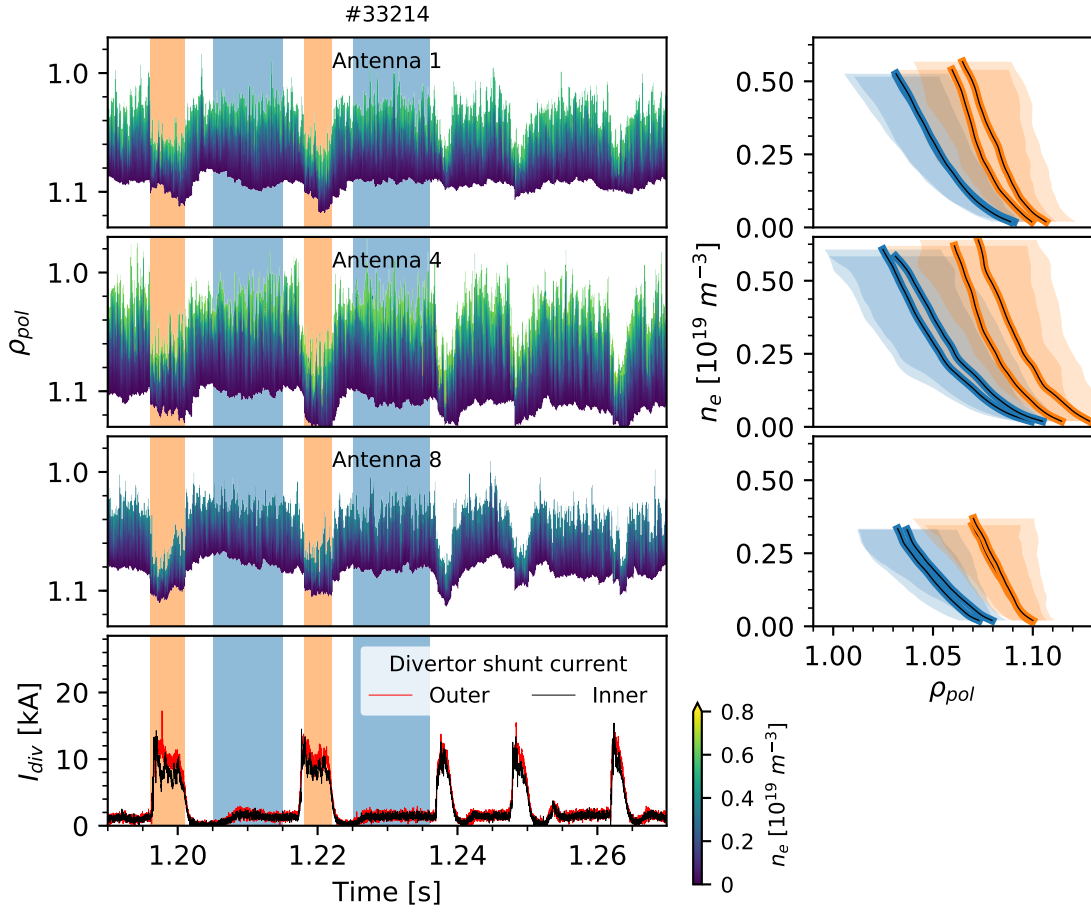


Figure 5.11: Effect of ELM events on the density profiles.

ELMs are observed in Figure 5.11, which shows the plasma density profile evolution in front of the three reflectometry antennas for the H-mode discharge #33214, shortly after the L-H transition. Several ELMs occur during this time interval, with increasing frequency, as indicated by the inner and outer divertor current peaks. The average profiles in regions with and without ELM activity are represented in the plots to the right, where the increase of electron density at the edge during ELMs is clearly visible. The poloidal structure of ELM bursts may be studied using this multichannel diagnostic. The fine structure of the plasma density profiles during ELM transients, including the small ones after 1.23 s, may also be observed. This is possible due to the typical high temporal resolution ($<100 \mu\text{s}$) of the reflectometry diagnostic.

The density profile evolution during one of these ELM events can be observed in the 3D plots in Figure 5.12. Particle release during ELMs appears to be anisotropic. There is stronger release in the top and mid plane regions of the vessel, as indicated by the higher edge density profile in antennas 1 and 4 than in the bottom antenna 8.

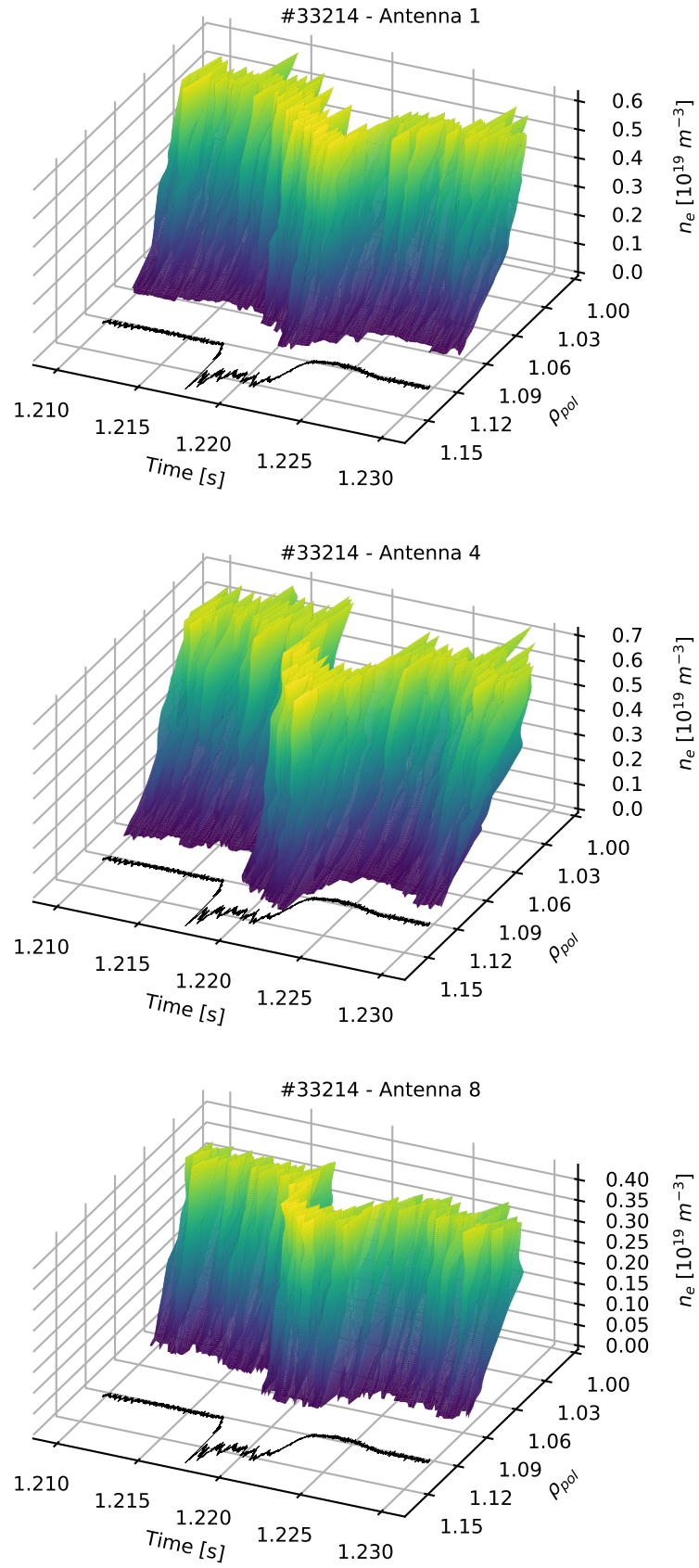


Figure 5.12: 3D visualization of density profile evolution observed in the three reflectometry antennas during an ELM in discharge (divertor shunt current indicated by the solid black line) #33214 with 100 μs time resolution.

5.3 ICRF operation studies

ICRF waves are one of the standard heating methods of plasmas. ICRF power is transferred to the plasma centre using a fast wave. The fast wave is evanescent below a density threshold (in the $1 \times 10^{18} \text{ m}^{-3}$ range) and decays rapidly in the plasma scrape off layer, before reaching the propagative region of higher density.

Optimal power transfer requires the correct coupling of the ICRF power to the plasma load. The load impedance depends on the thickness of this evanescent layer [135, 136] and may vary throughout the discharge, due to density variations, L-H transition or ELMs.

Improving ICRF power coupling requires: i) tweaking generator matching to the different plasma loads before each discharge; ii) compensating load mismatch during the discharge, using gas puffing of varying plasma position [35].

In addition, RF rectification of the plasma potential at the edge is a well known occurrence during ICRF operation [28, 29, 30]. Electrons, being more mobile than the plasma ions, are accelerated towards the wall. To preserve quasineutrality, the plasma develops a negative DC potential at the wall edge. This electrical field has two effects, observed during ICRF operation:

- Ions are accelerated towards the wall, sputtering the wall material, which then contaminates the plasma with impurities, and may lead to a disruption of the plasma.
- The plasma electrons suffer $E \times B$ drifts in this sheath region, forming convective cells, that displace plasma density upwards and generating hot spots. This convective transport changes the shape of the plasma electron density profile, which may alter the coupling of ICRF power to the plasma, reducing heating efficiency. In addition, convective cells may also influence the transport of wall impurities to the plasma core.

Mitigating tungsten impurity release typically requires tailoring discharge parameters, such as gas puffing and plasma position [137, 138], coating the ICRF antennas with low-Z materials, or using broader ICRF limiters [139]. The W impurity source, located at the antenna limiters, has a minimum when the RF currents between the central and outer straps of the ICRF antenna cancel each other. The new 3-strap antenna was designed to reduce the release of tungsten impurities, when compared to the 2-strap ICRF antennas, by optimizing RF currents balance at the straps. This impurity reduction has successfully been achieved with the new antennas installed on ASDEX Upgrade [140].

The multichannel reflectometry system was embedded in the new antenna design to study localized phenomena, such as convective cells and plasma coupling. In this section, we present relevant preliminary results of the local edge density profile diagnostic, used to analyse these ICRF operation effects.

5.3.1 ICRF power coupling to the plasma

The new embedded reflectometer has the advantage of measuring the local electron density profiles in front of the ICRF antenna. This facilitates experiment setup and allows more accurate results than using

remote magnetically connected diagnostics to study ICRF power coupling, as was previously done.

One of the strategies to improve power coupling is to decrease the width of the evanescent layer by increasing the density in the SOL layers through localized gas puffing. Coupling depends on the thickness of the evanescent region d_e between the ICRF antenna and the cutoff density layer of around 10^{18} m^{-3} . Power coupling is given by

$$P_{coupled} \propto \frac{V_{max}^2 R_c}{2Z_c^2}, \quad (5.1)$$

where V_{max} is the anti-node voltage in the transmission line, R_c is the coupling resistance and Z_c is the characteristic impedance of the transmission line. The coupling resistance R_c can be approximated by

$$R_c \propto R_0 e^{-\alpha \cdot d_e}, \quad (5.2)$$

where α is the tunneling factor [141]. Increasing the density at the SOL edge reduces width of the evanescent region and improves power coupling.

ASDEX Upgrade has different gas injection valves, including the lower divertor (DIV), outer top (TOPCO2), and mid plane (MID) regions of the vessel. The valve locations are represented in Figure 5.13 (left). The SOL density in front of the ICRF antennas can be tailored by gas puffing through different valves. Extensive 3D simulations have been performed to understand the gas puffing effects on ICRF power coupling [135, 142, 143]. These results showed that the outer mid plane gas puffing increases the local density in front of the ICRF antennas most efficiently, when compared with the lower divertor gas puffing.

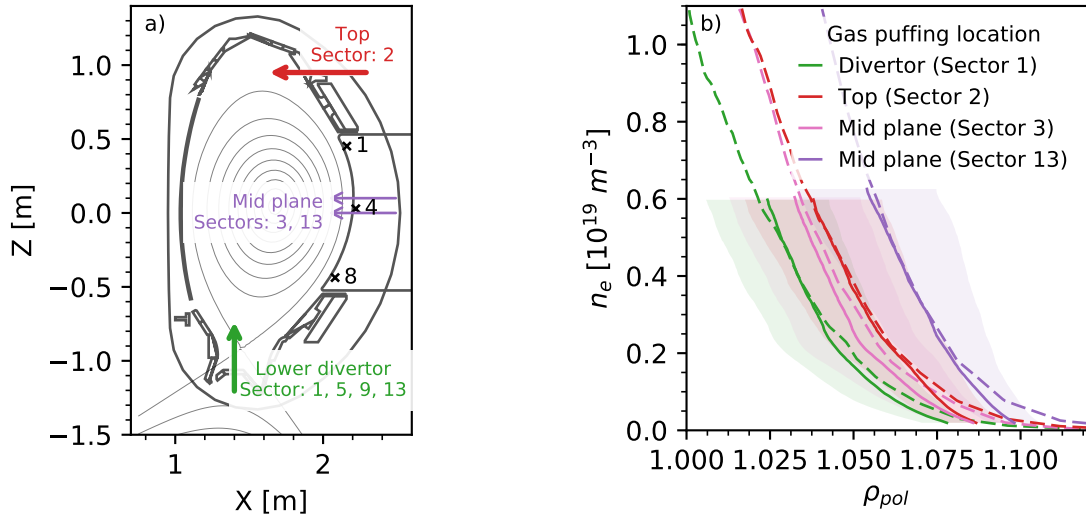


Figure 5.13: a) Cross section view of the top, middle and lower divertor gas valve locations and embedded reflectometry channels. b) Simulated density profiles (dashed lines) at the mid height plane of the ICRF antenna #4 in sector 12 and experimental density profiles (solid lines) measured with channel 4 of embedded reflectometer, for different gas puffing locations.

The influence of the different gas injection locations on ICRF coupling, studied in simulations, was replicated experimentally for L-mode discharges on ASDEX Upgrade [144]. The embedded reflectome-

ter was used to provide the local edge density profile measurements in the mid plane in front of the ICRF antenna, and used to validate the simulation results. These results are shown in Figure 5.13 (right). A good agreement between the experimental (solid lines) and simulated (dashed lines) density profiles, in each gas puffing case, is observed for densities in the range $0.2\text{--}0.6 \times 10^{19} \text{ m}^{-3}$. The discrepancy at the far edge is the result of the reflectometer measuring density profiles at a distance in front of the microwave antennas, while simulations start at the wall.

ICRF power coupling is improved the most for the mid plane gas puffing, as the evanescent region thickness in front of the antenna is reduced. The density values measured during the gas puffing using the mid plane gas valve in sector 13 are much larger than those measured during puffing with the mid plane gas valve in sector 3. This is because the ICRF antenna #4, and embedded reflectometer, in sector 12 are toroidally closer to the gas valve in sector 13 (0.86 m) than to the gas valve in sector 3 (6 m), and the injected gas is diluted in the plasma as it propagates around the torus. Further discussion on the power coupling in the different gas puffing configurations is described in [144].

5.3.2 Poloidal convective cells induced by ICRF heating

In addition to providing local density measurements, the multichannel topology of the new embedded reflectometer enables the simultaneous observation of poloidal differences of plasma events, such as convective cells that form during ICRF operation.

Convective transport of plasma density during ICRF operation has been modelled on ASDEX Upgrade using 3D simulation codes [145]. Convective cells are formed due to $\mathbf{E} \times \mathbf{B}$ drifts in the small RF rectified sheath between the separatrix and the ICRF antenna, as exemplified in Figure 5.14, exaggerated for size. This transport drives particle fluxes towards the wall, increasing the heat load and enhancing plasma-wall interactions [146].

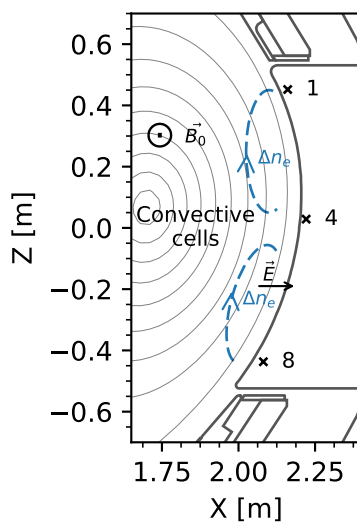


Figure 5.14: Poloidal convective cells associated with ICRF operation. The size of the convective cells is exaggerated.

The simulations in Figure 5.15 show the plasma density profiles in front of ICRF antenna #2 (equal and opposite to ICRF antenna #4 inside the vessel) during an ohmic heating (OH) phase and with ICRF heating (RF). The density differences between OH and RF (right) illustrate convective transport moving in a gyro motion upwards and towards the mid plane. Simulations suggest that the RF convection is much more significant at the top and bottom than at the middle of the ICRF radiating surface. Also, different antenna designs (2-strap or 3-strap) and antenna feeding configurations, such as the phasing and power ratio between the straps, result in different sheath potentials and RF convections [41].

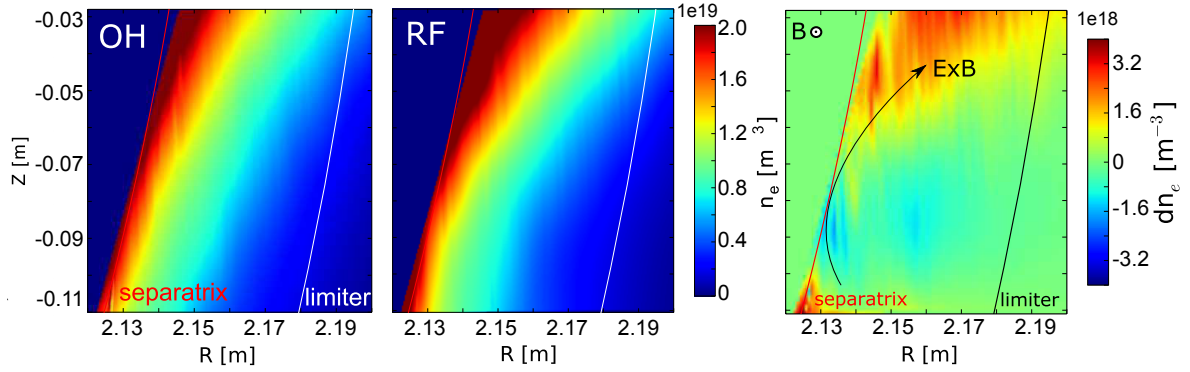


Figure 5.15: Simulation of plasma density profiles during ohmic heating (OH, left) and ICRF operation (RF, middle) on ASDEX Upgrade. The density differences between OH and RF phases shows the resulting convective transport (right). Figures reproduced with permission from [30].

Density perturbations in the SOL on ASDEX Upgrade propagate several meters along the magnetic field lines. Previously, studying the formation of these convective cells experimentally relied on generating different q_{95} safety factors, altering the plasma current to magnetically connect remote diagnostics, such as reflectometry, Li-beam, or retarding field analyzer diagnostics, to the different poloidal locations of the ICRF antenna. Now, direct measurement of the local plasma layers in front of the ICRF antenna is possible using the embedded multichannel reflectometer. These experimental measurements in front of the ICRF antenna #4 are shown in Figure 5.16. ICRF heating is performed using pairs of antennas: 1-3 and 2-4. It can be seen that the SOL density is perturbed when ICRF operation begins at around 3 s.

The average density profiles in the OH phase (blue region) and RF phase (orange region) show enhanced particle transport from the mid plane to the top part of the ICRF radiating surface. This is corroborated by the respective density profile shifts Δn_e in front of the reflectometry antennas 4 and 1. The edge density profile in front of the bottom antenna 8 indicates a small particle transport away from the wall at the lowest density plasma layers. The results presented in this section are more thoroughly studied in the works [41] and [27].

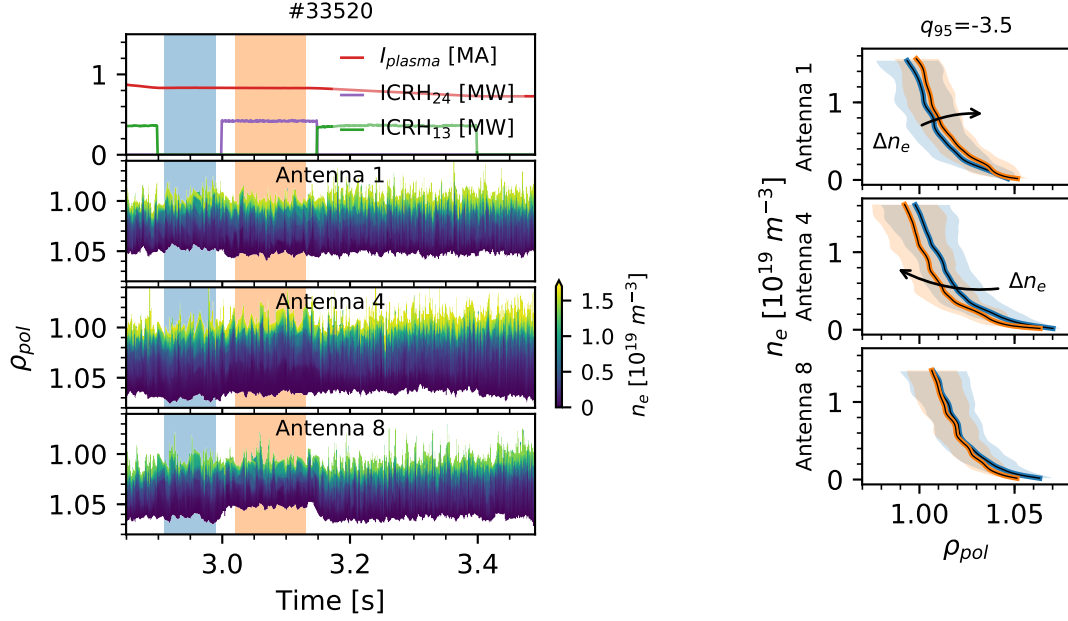


Figure 5.16: ICRF induced convective cells affecting localized density profile measurements during discharge #33520 with non-optimized power ratio between antenna straps.

5.4 Summary

The new edge density profile reflectometer was validated against profiles from other diagnostics on ASDEX Upgrade. The three reflectometry channel measurements were compared with the density profiles of the standard O-mode reflectometry and Lithium-beam diagnostics. Results showed good agreement between the profiles, within their confidence interval, in L-mode and H-mode discharges, during intervals with no significant plasma perturbations such as ELMs or ICRH activity.

The radial and poloidal sensitivity of the diagnostic was evaluated with a circular plasma discharge where the plasma was displaced vertically. The density profiles, measured along the line of sight of each reflectometry antenna, closely followed the expected plasma position, as indicated by the magnetic equilibrium. The width of the probed region depends on the magnetic field and the distance along the line of sight between the plasma and the antenna. The diagnostic offers higher density profile quality for measurements closer to the reflectometry antennas.

It was demonstrated that typical discharge phenomena on ASDEX Upgrade may also be evaluated using the reflectometry diagnostic. The measured edge density profiles steepened as the heating power increased and the plasma underwent the L-H transition. The typical outwards particle transport of ELM instabilities was also observed in the edge density profiles. The high temporal resolution of the diagnostic permits resolving the fine profile structure during fast ELM transients. Despite being specified for edge density profiles, density profiles deep into the plasma were also reconstructed in a discharge with low magnetic field and low core electron density, showing sensitivity to the gas injection into the main chamber.

The reflectometry measurements were used to aid in the ICRF operation studies, fulfilling the pur-

pose of the implementation of this new diagnostic. The experimental density profiles were used to corroborate simulations that determine the optimum gas puffing configuration for ICRF power coupling, which depends on the correct tailoring of edge density. The advantageous multichannel topology was used to evaluate convective transport of plasma particles during ICRF operation.

Chapter 6

Conclusions

This thesis work consisted in the implementation and commissioning of the new X-mode multichannel reflectometry diagnostic for edge electron density profile measurements. The new density profile reflectometer has been successfully installed on ASDEX Upgrade. The main purpose of this diagnostic is to improve ICRF operation studies by directly measuring the plasma layers in front of the ICRF antenna. Up until now, the scrape off layer plasma perturbations due to ICRF operation could only be remotely probed by remote magnetically-connected diagnostics, reducing measurement reliability and requiring complex experimental setups. Now, three embedded poloidally distributed reflectometry channels provide simultaneous edge density profile measurements at the bottom, middle and top regions of the ICRF radiating surface, under most operational conditions of ASDEX Upgrade.

Ten reflectometry antenna pairs, or channels, were embedded at different toroidal and poloidal locations of the ICRF antenna design. Their bistatic configuration, with dedicated transmitting and receiving waveguides, reduces spurious reflections and cross talk between channels. In this work, only three channels were instrumented with microwave reflectometry hardware, despite seven being accessible through the vacuum port. However, the modular system architecture allows more reflectometry channels to be easily integrated in the future. The diagnostic system was installed inside the torus hall, with the microwave hardware attached to the waveguides close to the vessel. The diagnostic is remotely operated from the control room.

The reflectometry system has an heterodyne quadrature detection architecture, which allows for both high detection sensitivity and a direct measurement of the signal phase and amplitude. Coherency is maintained by using a single measure source and a sophisticated frequency translator topology for the probing and reference signals of all channels.

The plasma is probed in the extended 40-68 GHz U-band, measuring densities up to $2 \times 10^{19} \text{ m}^{-3}$, depending on the magnetic field of the experiment. A good linearity of the swept probing frequency ramp is obtained by calibrating the dynamic tuning response of the microwave oscillator. Calibrations were also performed in-vessel to compensate the waveguide dispersion of each channel.

The main issue with X-mode reflectometry is the accurate determination of the start of the upper cut-off region, used to reconstruct density profiles. Much work was invested in developing robust estimation

algorithms to determine the first fringe reflection in all operation conditions. During the commissioning phase of the diagnostic, we observed that the typical high core plasma density of the typical ASDEX Upgrade discharge results in an X-mode lower cutoff reflection appearing inside our probing region, which complicates estimation. The *ampfilt* algorithm uses both amplitude and spectral information, which is required to overcome noisy signals and provide reliable results, even with lower cutoff reflection. A second approach was developed using a neural network model to determine the FF from X-mode group delay spectrograms, mimicking human pattern recognition. This model was trained using a comprehensive experimental dataset. Kalman filters applied to the FF estimations improve the uncertainty of the vacuum distance measurement to less than 1 cm.

The non-zero residual density at the first reflection affects the estimated vacuum distance, required to initialize the X-mode density profile reconstruction. The initialization parameters were optimized to reduce the density profile mismatch in stable plasma situations, when compared with the Lithium-beam diagnostic.

A distributed data processing pipeline that automatically reconstructs density profiles in the available computation servers was developed. Each reconstructed profile is validated to discard those that are not physically possible from being uploaded to the official shotfile database.

The experimental density profile measurements were validated against other existing diagnostics on ASDEX Upgrade. The high radial and poloidal sensitivity of the diagnostic has been demonstrated by tracking a vertical displacement of a circular plasma. The temporal and spatial resolutions of the diagnostic, and typical plasma phenomena such as the L-H transition and ELM events, have been observed.

Finally, the diagnostic has been used in ICRF operation studies. It has provided local density profile measurements that corroborate the simulation predictions of the ICRF power coupling, using optimized gas puffing conditions. In addition, the diagnostic observed the existence of convective transport in front of the ICRF antenna during its operation. Both of these results take advantage of the multichannel topology and its sensitivity to local plasma perturbations.

Future Work

ICRF operation studies could benefit of higher poloidal resolution, which can be achieved by instrumenting more of the available reflectometry channels. Upgrading the number of channels implies replicating the microwave hardware and performing the in-vessel calibrations of the new channel waveguides. The modular structure of the processing software and diagnostic control system allows a quick implementation of additional channels. However, adding more channels may introduce crosstalk issues, which must be accounted for during the commissioning phase. Currently, there is no observed crosstalk between the installed channels, mostly attributed to the distance between them. This issue may appear in channels close to each other with a wide launching and receiving beams, such as the middle channels 2 to 7. Fortunately, any undesired detected crosstalk signals are expected to be attenuated, when compared to the main reflecting beam, and with a higher beat group delay, making them distinguishable from the main reflection.

The neural network model for first fringe estimation, while capable of providing very precise results, is not currently used in production. The open source tools TensorFlow and Keras to handle the creation, training and usage of the neural networks are constantly evolving, often breaking backwards compatibility with the computation environments used for processing the density profiles. In order to provide a robust solution for the density profile reconstruction, the reconstruction codes and neural network models should be stored in a containerized environment, which can be run on any scientific computation cluster independently of the installed software packages. A possible suggestion for this is using the recently released Singularity container system, developed to bring reproducible scientific computation environments to High Performance Computing centers [147].

A deep study into the dependencies of the first plasma reflection should be performed using full wave finite difference time domain (FDTD) simulation codes. It is thought that the low reflection signal amplitude, probing beam scattering at the edge and gradient of the edge density profile may influence the determination of the first fringe reflection. Using the conclusions from the simulations, the accuracy of the density profile reconstructions may be improved by adapting the residual density estimation to the experimental plasma conditions, which may vary throughout the discharge.

The multichannel topology may provide interesting insights for filamentary and edge turbulence studies. However, this diagnostic is not currently capable of measuring plasma fluctuations: the microwave oscillator driver is not optimized for static frequency generation and the acquisition system is AC coupled, filtering fluctuations below 10 kHz. Hardware changes are required to implement this functionality and may be considered in future diagnostic upgrades.

Additional hardware upgrades could include an online dynamic frequency calibration for the microwave sources, which could resolve any deviation of the dynamic response of the microwave sources from the calibration. An absolute frequency measurement module using a markers topology, similar to the one used in other reflectometry diagnostics [56], could correct temperature drifts that may occur in the microwave sources during an operation day.

Chapter 7

Scientific Contributions

Publications

- **D. E. Aguiam**, A. Silva, L. Guimaraes, P. J. Carvalho, G. D. Conway, B. Goncalves, L. Meneses, J.-M. Noterdaeme, J. M. Santos, A. A. Tuccillo, and O. Tudisco, "Estimation of X-mode reflectometry first fringe frequency using neural networks", *IEEE Transactions on Plasma Science*, 2018
- **D. E. Aguiam**, A. Silva, V. Bobkov, P. J. Carvalho, P. F. Carvalho, R. Cavazzana, G. D. Conway, O. D'Arcangelo, L. Fattorini, H. Faugel, A. Fernandes, H. Fünfgelder, B. Goncalves, L. Guimaraes, G. De Masi, L. Meneses, J. M. Noterdaeme, R. C. Pereira, G. Rocchi, J. M. Santos, A. A. Tuccillo, and O. Tudisco, "X-mode raw data analysis of the new AUG ICRF antenna edge density profile reflectometer", *Fusion Engineering and Design*, 2017
- **D. E. Aguiam**, A. Silva, V. Bobkov, P. J. Carvalho, P. F. Carvalho, R. Cavazzana, G. D. Conway, O. D'Arcangelo, L. Fattorini, H. Faugel, A. Fernandes, H. Fünfgelder, B. Gonçalves, L. Guimaraes, G. De Masi, L. Meneses, J. M. Noterdaeme, R. C. Pereira, G. Rocchi, J. M. Santos, A. A. Tuccillo, and O. Tudisco, "Implementation of the new multichannel X-mode edge density profile reflectometer for the ICRF antenna on ASDEX Upgrade", *Review of Scientific Instruments* 87, 2016
- **D. E. Aguiam**, B. B. De Carvalho, and M. L. da Silva, "Feasibility study of a control system based on PLC and EPICS for the ESTHER combustion gas injection", 2015 3rd Experiment@ International Conference (exp.at'15), 2015
- **D. E. Aguiam**, L. S. Rosado, P. M. Ramos, and M. Piedade, "Heterodyning based portable instrument for eddy currents non-destructive testing", *Measurement: Journal of the International Measurement Confederation*, 2015
- **D. E. Aguiam**, L. S. Rosado, P. M. Ramos, and M. Piedade, "Portable instrument for eddy currents Non-Destructive Testing based on heterodyning techniques", *Proceedings of 2014 IEEE International Instrumentation and Measurement Technology Conference (I2MTC)*, 2014

Conference participation

- Talk: D.E. Aguiam, *et al*, "Estimation of X-mode reflectometry first fringe frequency using neural networks", 27th IEEE Symposium On Fusion Engineering (SOF2017), June 4-8 2017, Shanghai, China
- Poster: D.E. Aguiam, *et al*, "X-mode raw data analysis of the new AUG ICRF antenna edge density profile reflectometer", 29th Symposium on Fusion Technology (SOFT2016), September 5-9 2016, Prague, Czech Republic
- Poster: D.E. Aguiam, *et al*, "Implementation of the new multichannel X-mode edge density profile reflectometer for the ICRF antenna on ASDEX Upgrade", 21st Topical Conference on High Temperature Plasma Diagnostics (HTPD2016), June 5-9 2016, Madison, Wisconsin
- Poster: D.E. Aguiam, "Multichannel reflectometer for measuring plasma electron density profiles in front of the ICRH antenna on ASDEX Upgrade", FuseNet PhD Event 2015, November 15-18 2015, Prague, Czech Republic
- Poster: F. da Silva, *et al*, "Refmulf: 2D fullwave FDTD full polarization maxwell code", 42nd European Physical Society Conference on Plasma Physics, June 22-26 2015, Lisbon, Portugal
- Talk: D.E. Aguiam, *et al*, "Feasibility study of a control system based on PLC and EPICS for the ESTHER combustion gas injection", 3rd Experiment@ International Conference (exp.at'15), June 2-4 2015, Ponta Delgada, Portugal

Co-authored publications

- V. Nikolaeva, L. Guimaraes, P. Manz, D. Carralero, M. E. Manso, U. Stroth, C. Silva, G. D. Conway, E. Seliunin, J. Vicente, D. Brida, **D. Aguiam**, J. Santos, and A. Silva, "Characterization of edge turbulence in different states of divertor detachment using reflectometry in the ASDEX Upgrade tokamak", Plasma Physics and Controlled Fusion, 2018
- W. Zhang, W. Tierens, J.-M. Noterdaeme, V. Bobkov, **D. Aguiam**, D. Coster, H. Fuenfgelder, J. Jacquot, R. Ochoukov, A. Silva, L. Colas, and A. Křivská, "Radio frequency heating induced edge plasma convection: self-consistent simulations and experiments on ASDEX Upgrade", Nuclear Fusion 57, 2017
- A. Kallenbach, *et al*, "Overview of ASDEX Upgrade results", Nuclear Fusion 57, 2017
- H. Meyer, *et al*, "Overview of progress in European medium sized tokamaks towards an integrated plasma-edge/wall solution", Nuclear Fusion 57, 2017
- W. Zhang, V. Bobkov, J.-M. Noterdaeme, W. Tierens, R. Bilato, D. Carralero, D. Coster, J. Jacquot, P. Jacquet, T. Lunt, R. A. Pitts, V. Rohde, G. Siegl, H. Fuenfgelder, **D. Aguiam**, A. Silva, L. Colas,

and S. Ceccuzzi, "Effects of outer top gas injection on ICRF coupling in ASDEX Upgrade: towards modelling of ITER gas injection", Plasma Physics and Controlled Fusion 59, 2017

- H. Fuenfgelder, **D. Aguiam**, O. D'Arcangelo, V. Bobkov, S. Ceccuzzi, Y. Chen, H. Faugel, J. Jacquot, R. Maggiora, A. Mancini, D. Milanesio, J. M. Noterdaeme, R. Ochoukov, G. Rocchi, A. Silva, A. Tuccillo, O. Tudisco, T. Vierle, Y. Wang, Q. Yang, and I. Zammuto, "A double success story: The international cooperation to build the new ICRF antennas on ASDEX Upgrade and the results obtained", Fusion Engineering and Design, 2017
- W. Zhang, V. Bobkov, J.-M. Noterdaeme, W. Tierens, **D. Aguiam**, R. Bilato, D. Coster, L. Colas, K. Crombé, H. Fuenfgelder, H. Faugel, Y. Feng, J. Jacquot, P. Jacquet, A. Kallenbach, A. Kostic, T. Lunt, R. Maggiora, R. Ochoukov, A. Silva, G. Suárez, A. A. Tuccilo, O. Tudisco, M. Usoltceva, D. Van Eester, Y. Wang, and Q. Yang, "Recent progress on improving ICRF coupling and reducing RF-specific impurities in ASDEX Upgrade", EPJ Web of Conferences 157, 2017
- W. Zhang, D. Coster, Y. Feng, T. Lunt, **D. Aguiam**, R. Bilato, V. Bobkov, J. Jacquot, P. Jacquet, E. Lerche, J.-M. Noterdaeme, and W. Tierens, "Plasma edge modelling with ICRF coupling", EPJ Web of Conferences 157, 2017
- V. Bobkov, **D. Aguiam**, M. Baruzzo, D. Borodin, I. Borodkina, S. Brezinsek, I. Coffey, L. Colas, A. Czarnecka, E. Delabie, P. Dumortier, F. Durodie, R. Dux, H. Faugel, H. Fünfgelder, C. Giroud, M. Goniche, J. Hobirk, A. Herrmann, J. Jacquot, P. Jacquet, A. Kallenbach, A. Krivska, C. C. Klepper, E. Lerche, S. Menmuir, D. Milanesio, R. Maggiora, I. Monakhov, F. Nave, R. Neu, J. M. Noterdaeme, R. Ochoukov, T. Pütterich, M. Reinke, A. Tuccilo, O. Tudisco, D. Van Eester, Y. Wang, Q. Yang, and W. Zhang, "Progress in reducing ICRF-specific impurity release in ASDEX upgrade and JET", Nuclear Materials and Energy, 2016
- V. Bobkov, **D. Aguiam**, R. Bilato, S. Brezinsek, L. Colas, H. Faugel, H. Fünfgelder, A. Herrmann, J. Jacquot, A. Kallenbach, D. Milanesio, R. Maggiora, R. Neu, J.-M. Noterdaeme, R. Ochoukov, S. Potzel, T. Pütterich, A. Silva, W. Tierens, A. Tuccilo, O. Tudisco, Y. Wang, Q. Yang, and W. Zhang, "Making ICRF power compatible with a high-Z wall in ASDEX Upgrade", Plasma Physics and Controlled Fusion 59, 2016

Conferences

- W. Zhang, *et al*, "Measurements and simulations of ICRF-sheath-induced plasma convection in front of the 3-strap antennas in ASDEX Upgrade", 58th Annual Meeting of the APS Division of Plasma Physics (APS 2016), October 31 – November 4 2016, San Jose, California
- J.M. Noterdaeme, *et al*, "Ion Cyclotron Range of Frequency Power Challenges and Solutions", 26th IAEA Fusion Energy Conference, October 17-22 2016, Kyoto, Japan
- V. Bobkov, *et al*, "ICRF heating in ASDEX Upgrade with W wall", International Conference and School on Plasma Physics and Controlled Fusion, September 12-15 2016, Kharkov, Ukraine

-
- J. Vicente, *et al*, "Relationship between divertor collisionality and filament activity measured with reflectometry at ASDEX Upgrade", 43rd European Physical Society Conference on Plasma Physics, July 4-8 2016, Leuven, Belgium
 - F. da Silva, *et al*, "Refmulf: 2D fullwave FDTD full polarization maxwell code", 42nd European Physical Society Conference on Plasma Physics, 2015

Bibliography

- [1] REN21. RENEWABLES 2017 GLOBAL STATUS REPORT. Technical report, Renewable Energy Policy Network for the 21st Century, Paris, jan 2017.
- [2] BP. BP Statistical Review of World Energy 2017. 2017. URL <http://www.bp.com/content/dam/bp/en/corporate/pdf/energy-economics/statistical-review-2017/bp-statistical-review-of-world-energy-2017-full-report.pdf>.
- [3] W. M. Jones. Half-Life of Tritium. *Physical Review*, **100**, oct 1955.
- [4] M. Zucchetti, L. Di Pace, L. El-Guebaly, J. H. Han, B. N. Kolbasov, V. Massaut, Y. Someya, K. Tobita, and M. Desecures. Recent advances in fusion radioactive material studies. *Fusion Engineering and Design*, **88**, 2013.
- [5] F. H. Chen. *Introduction to Plasma Physics and Controlled Fusion*. 1984.
- [6] T. Johnson. Inertial confinement fusion: Review and perspective. *Proceedings of the IEEE*, **72**, 1984.
- [7] JET - Joint European Torus. URL <https://www.euro-fusion.org/jet/>.
- [8] ITER - International Thermonuclear Experimental Reactor. URL <https://www.iter.org/>.
- [9] B. J. Green, I. I. T. Teams, and Partici. ITER: burning plasma physics experiment. *Plasma Physics and Controlled Fusion*, **45**, may 2003.
- [10] G. Federici, C. Bachmann, W. Biel, L. Boccaccini, F. Cismondi, S. Ciattaglia, M. Coleman, C. Day, E. Diegele, T. Franke, M. Grattarola, H. Hurzlmeier, A. Ibarra, A. Loving, F. Maviglia, B. Meszaros, C. Morlock, M. Rieth, M. Shannon, N. Taylor, M. Q. Tran, J. H. You, R. Wenninger, and L. Zani. Overview of the design approach and prioritization of R&D activities towards an EU DEMO. *Fusion Engineering and Design*, **109-111**, 2015.
- [11] F. Romanelli. EFDA, Fusion Electricity: A roadmap to the realisation of fusion energy. 2012.
- [12] M. Keilhacker, A. Gibson, C. Gormezano, P. Lomas, P. Thomas, M. Watkins, P. Andrew, B. Balet, D. Borba, C. Challis, I. Coffey, G. Cottrell, H. D. Esch, N. Deliyanakis, A. Fasoli, C. Gowers, H. Guo, G. Huysmans, T. Jones, W. Kerner, R. König, M. Loughlin, A. Maas, F. Marcus, M. Nave, F. Rimini, G. Sadler, S. Sharapov, G. Sips, P. Smeulders, F. Söldner, A. Taroni, B. Tubbing, M. von

- Hellermann, D. Ward, and J. Team. High fusion performance from deuterium-tritium plasmas in JET. *Nuclear Fusion*, **39**, feb 1999.
- [13] J. Team and P. Thomas. Alpha particle studies during JET DT experiments. *Nuclear Fusion*, **39**, nov 1999.
- [14] G. Kelley, O. Morgan, L. Stewart, W. Stirling, and H. Forsen. Neutral-beam-injection heating of toroidal plasmas for fusion research. *Nuclear Fusion*, **12**, mar 1972.
- [15] R. Koch. Plasma Heating by Neutral Beam Injection. *Transactions of Fusion Science and Technology*, **49**, 2006.
- [16] J. Busnardo-Neto, J. Dawson, T. Kamimura, and A. T. Lin. Ion-Cyclotron Resonance Heating of Plasmas and Associated Longitudinal Cooling. *Physical Review Letters*, **36**, jan 1976.
- [17] J. Ongena, A. Messiaen, Y. Kazako, R. Koch, R. Ragona, V. Bobkov, K. Crombé, F. Durodié, M. Goniche, A. Krivska, E. Lerche, F. Louche, A. Lyssoivan, M. Vervier, D. V. Eester, M. V. Schoor, T. Wauters, J. Wright, and S. Wukitch. Recent advances in physics and technology of Ion Cyclotron Resonance Heating in view of future fusion reactors. *IAEA conference proceedings*, 2016.
- [18] G. Hoang, A. Bécoulet, J. Jacquinet, J. Artaud, Y. Bae, B. Beaumont, J. Belo, G. Berger-By, J. P. Bizarro, P. Bonoli, M. Cho, J. Decker, L. Delpech, A. Ekedahl, J. Garcia, G. Giruzzi, M. Goniche, C. Gormezano, D. Guilhem, J. Hillairet, F. Imbeaux, F. Kazarian, C. Kessel, S. Kim, J. Kwak, J. Jeong, J. Lister, X. Litaudon, R. Magne, S. Milora, F. Mirizzi, W. Namkung, J. Noterdaeme, S. Park, R. Parker, Y. Peysson, D. Rasmussen, P. Sharma, M. Schneider, E. Synakowski, A. Tanga, A. Tuccillo, and Y. Wan. A lower hybrid current drive system for ITER. *Nuclear Fusion*, **49**, jul 2009.
- [19] V. Erckmann and U. Gasparino. Electron Cyclotron Current Drive in toroidal fusion plasmas. *Plasma Phys. Control. Fusion*, **36**, 1994.
- [20] ASDEX Upgrade. URL <https://www.ipp.mpg.de/16195/asdex>.
- [21] A. Kallenbach, U. Team, and M. S. T. Team. Overview of ASDEX Upgrade results. *Nuclear Fusion*, **57**, oct 2017.
- [22] R. Neu, M. Balden, V. Bobkov, R. Dux, O. Gruber, A. Herrmann, A. Kallenbach, M. Kaufmann, C. F. Maggi, H. Maier, H. W. Müller, T. Pütterich, R. Pugno, V. Rohde, A. C. C. Sips, J. Stober, W. Sutrop, C. Angioni, C. V. Atanasiu, W. Becker, K. Behler, K. Behringer, A. Bergmann, T. Bertinelli, R. Bilato, A. Bottino, M. Brambilla, F. Braun, A. Buhler, A. Chankin, G. Conway, D. P. Coster, P. de Mariné, S. Dietrich, K. Dimova, R. Drube, T. Eich, K. Engelhardt, H.-U. Fahrbach, U. Fantz, L. Fattorini, J. Fink, R. Fischer, A. Flaws, P. Franzen, J. C. Fuchs, K. Gál, M. García Muñoz, M. Gemisic-Adamov, L. Giannone, S. Gori, S. da Graca, H. Greuner, A. Gude, S. Günter, G. Haas, J. Harhausen, B. Heinemann, N. Hicks, J. Hobirk, D. Holtum, C. Hopf, L. Horton, M. Huart, V. Igochine, S. Kálvin, O. Kardaun, M. Kick, G. Kocsis, H. Kollotzek, C. Konz, K. Krieger, T. Kurki-Suonio, B. Kurzan, K. Lackner, P. T. Lang, P. Lauber, M. Laux, J. Likonen, L. Liu, A. Lohs, K. Mank,

- A. Manini, M.-E. Manso, M. Maraschek, P. Martin, Y. Martin, M. Mayer, P. McCarthy, K. McCormick, H. Meister, F. Meo, P. Merkel, R. Merkel, V. Mertens, F. Merz, H. Meyer, M. Mlynec, F. Monaco, H. Murmann, G. Neu, J. Neuhauser, B. Nold, J.-M. Noterdaeme, G. Pautasso, G. Pereverzev, E. Poli, M. Püschel, G. Raupp, M. Reich, B. Reiter, T. Ribeiro, R. Riedl, J. Roth, M. Rott, F. Rytter, W. Sandmann, J. Santos, K. Sassenberg, A. Scarabosio, G. Schall, J. Schirmer, A. Schmid, W. Schneider, G. Schramm, R. Schrittwieser, W. Schustereder, J. Schweinzer, S. Schweizer, B. Scott, U. Seidel, F. Serra, M. Sertoli, A. Sigalov, A. Silva, E. Speth, A. Stäbler, K.-H. Steuer, E. Strumberger, G. Tardini, C. Tichmann, W. Treutterer, C. Tröster, L. Urso, E. Vainonen-Ahlgren, P. Varela, L. Vermare, D. Wagner, M. Wischmeier, E. Wolfrum, E. Würsching, D. Yadikin, Q. Yu, D. Zasche, T. Zehetbauer, M. Zilker, and H. Zohm. Plasma wall interaction and its implication in an all tungsten divertor tokamak. *Plasma Physics and Controlled Fusion*, **49**, dec 2007.
- [23] a. V. Krasilnikov, D. Van Eester, E. Lerche, J. Ongena, V. N. Amosov, T. Biewer, G. Bonheure, K. Crombe, G. Ericsson, B. Esposito, L. Giacomelli, C. Hellesen, a. Hjalmarsson, S. Jachmich, J. Kallne, Y. a. Kaschuck, V. Kiptily, H. Leggate, J. Mailloux, D. Marocco, M.-L. Mayoral, S. Popovichev, M. Riva, M. Santala, M. Stamp, V. Vdovin, and a. Walden. Fundamental ion cyclotron resonance heating of JET deuterium plasmas. *Plasma Physics and Controlled Fusion*, **51**, 2009.
- [24] S. J. Wukitch, B. Lipschultz, E. Marmar, Y. Lin, a. Parisot, M. Reinke, J. Rice, and J. Terry. RF plasma edge interactions and their impact on ICRF antenna performance in Alcator C-Mod. *Journal of Nuclear Materials*, **363-365**, 2007.
- [25] T. H. Stix and R. W. Palladino. Ion Cyclotron Resonance. *Proc. 2d Intern. Conf. Geneva*, **31**, 1958.
- [26] A. Messiaen and R. Weynants. ICRH antenna coupling physics and optimum plasma edge density profile. Application to ITER. *Plasma Physics and Controlled Fusion*, **53**, aug 2011.
- [27] W. Zhang. *Plasma Edge Modeling with ICRF Coupling*. PhD thesis, Universiteit Gent, 2017.
- [28] L. Colas, S. Heuraux, S. Brémond, and G. Bosia. RF current distribution and topology of RF sheath potentials in front of ICRF antennae. *Nuclear Fusion*, **45**, 2005.
- [29] M. Becoulet, L. Colas, S. Pecoul, J. Gunn, P. Ghendrih, A. Becoulet, and S. Heuraux. Edge plasma density convection during ion cyclotron resonance heating on Tore Supra. *Physics of Plasmas*, **9**, 2002.
- [30] W. Zhang, Y. Feng, J.-M. Noterdaeme, V. Bobkov, L. Colas, D. Coster, T. Lunt, R. Bilato, J. Jacquot, R. Ochoukov, D. Van Eester, A. Křivská, P. Jacquet, and L. Guimaraes. Modelling of the ICRF induced ExB convection in the scrape-off-layer of ASDEX Upgrade. *Plasma Physics and Controlled Fusion*, **58**, 2016.
- [31] D. A. D'Ippolito and J. R. Myra. A radio-frequency sheath boundary condition and its effect on slow wave propagation. *Physics of Plasmas*, **13**, 2006.

- [32] K. Theilhaber. Theory of the JET ICRH antenna. *Nuclear Fusion*, **24**, nov 1984.
- [33] P. Dumortier and A. M. Messiaen. ICRH Antenna design and matching. *Fusion Science and Technology*, **61**, 2012.
- [34] H. Faugel, P. Angene, W. Becker, F. Braun, V. V. Bobkov, B. Eckert, F. Fischer, D. a. Hartmann, G. Heilmaier, J. Kneidl, J. M. Noterdaeme, G. Siegl, and E. Würsching. The ASDEX upgrade ICRF system: Operational experience and developments. *Fusion Engineering and Design*, **74**, 2005.
- [35] J. M. Noterdaeme, V. V. Bobkov, S. Brémond, a. Parisot, I. Monakhov, B. Beaumont, P. Lamalle, F. Durodié, and M. Nightingale. Matching to ELMY plasmas in the ICRF domain. *Fusion Engineering and Design*, **74**, 2005.
- [36] D. M. Hangan, V. Bobkov, F. Braun, R. D'Inca, H. Faugel, and J. M. Noterdaeme. Analysis of dynamic matching networks for the ICRF system at ASDEX Upgrade. *Fusion Engineering and Design*, **86**, 2011.
- [37] A. Messiaen, R. Koch, R. R. Weynants, P. Dumortier, F. Louche, R. Maggiora, and D. Milanesio. Performance of the ITER ICRH system as expected from TOPICA and ANTITER II modelling. *Nuclear Fusion*, **50**, 2010.
- [38] J. Zhang, X. Zhang, Y. Cheng, C. Qin, Y. Zhao, Y. Mao, S. Yuan, L. Wang, S. Ju, G. Chen, B. Wan, X. Gong, J. Qian, T. Zhang, J. Li, Y. Song, Y. Yang, Z. Chen, J. Wang, Y. Lin, G. Taylor, S. Wukitch, J. Noterdaeme, J. Hosea, R. Kumazawa, T. Seki, K. Saito, and H. Kasahara. Experimental analysis of the ICRF waves coupling in EAST. *Nuclear Fusion*, **57**, jun 2017.
- [39] V. Bobkov, M. Balden, F. Braun, R. Dux, A. Herrmann, H. Faugel, H. Fünfgelder, L. Giannone, A. Kallenbach, M. Kocan, H. Maier, H. Müller, R. Neu, J.-. Noterdaeme, Y. Podoba, K. Polozhiy, T. Pütterich, V. Rohde, G. Siegl, F. Zeus, H. Zohm, and A. U. Team. ICRF Operation with Improved Antennas in a Full W-wall ASDEX Upgrade, Status and Developments. *Proceedings of 24th IAEA Fusion Energy Conference, IAEA-CN-19*, 2012.
- [40] V. Bobkov, M. Balden, R. Bilato, F. Braun, R. Dux, A. Herrmann, H. Faugel, H. Fünfgelder, L. Giannone, A. Kallenbach, H. Maier, H. Müller, R. Neu, J.-M. Noterdaeme, T. Pütterich, V. Rohde, N. Tsujii, F. Zeus, and H. Zohm. ICRF operation with improved antennas in ASDEX Upgrade with W wall. *Nuclear Fusion*, **53**, sep 2013.
- [41] W. Zhang, W. Tierens, J.-M. Noterdaeme, V. Bobkov, D. Aguiam, D. Coster, H. Fuenfgelder, J. Jacquot, R. Ochoukov, A. Silva, L. Colas, and A. Křivská. Radio frequency heating induced edge plasma convection: self-consistent simulations and experiments on ASDEX Upgrade. *Nuclear Fusion*, **57**, nov 2017.
- [42] V. Bobkov, F. Braun, R. Dux, a. Herrmann, L. Giannone, a. Kallenbach, a. Krivska, H. Müller, R. Neu, J.-M. Noterdaeme, T. Pütterich, V. Rohde, J. Schweinzer, a. Sips, and I. Zammuto. Assessment of compatibility of ICRF antenna operation with full W wall in ASDEX Upgrade. *Nuclear Fusion*, **50**, 2010.

- [43] V. Bobkov, M. Balden, R. Bilato, F. Braun, R. Dux, a. Herrmann, H. Faugel, H. Fünfgelder, L. Giannone, a. Kallenbach, H. Maier, H. Müller, R. Neu, J.-M. Noterdaeme, T. Pütterich, V. Rohde, N. Tsujii, F. Zeus, and H. Zohm. ICRF operation with improved antennas in ASDEX Upgrade with W wall. *Nuclear Fusion*, **53**, 2013.
- [44] V. Bobkov, F. Braun, R. Dux, A. Herrmann, H. Faugel, H. Fünfgelder, A. Kallenbach, R. Neu, J.-M. Noterdaeme, R. Ochoukov, T. Pütterich, A. Tuccillo, O. Tudisco, Y. Wang, and Q. Yang. First results with 3-strap ICRF antennas in ASDEX Upgrade. *Nuclear Fusion*, **56**, 2016.
- [45] M. Willensdorfer, E. Wolfrum, R. Fischer, J. Schweinzer, M. Sertoli, B. Sieglin, G. Veres, and F. Aumayr. Improved chopping of a lithium beam for plasma edge diagnostic at ASDEX Upgrade. *Review of Scientific Instruments*, **83**, 2012.
- [46] A. Silva, L. Cupido, M. Manso, F. Serra, I. Nunes, J. Santos, P. Varela, S. Vergamota, L. Meneses, V. Grossman, F. Silva, C. Loureiro, F. Nunes, B. Kurzan, and W. Suttrop. Microwave reflectometry diagnostic for density profile and fluctuation measurements on ASDEX Upgrade. *Review of Scientific Instruments*, **70**, 1999.
- [47] H. W. Müller, V. Bobkov, V. Rohde, M. Maraschek, J. Neuhauser, A. Schmid, M. Tsalas, and A. U. Team. Plasma Flow in the Scrape-off Layer of ASDEX Upgrade. *Proceedings of 32nd EPS Conference on Plasma Physics, Tarragona*, **29C**, 2005.
- [48] H. Fuenfgelder, D. Aguiam, O. D’Arcangelo, V. Bobkov, S. Ceccuzzi, Y. Chen, H. Faugel, J. Jacquot, R. Maggiora, A. Mancini, D. Milanesio, J. M. Noterdaeme, R. Ochoukov, G. Rocchi, A. Silva, A. Tuccillo, O. Tudisco, T. Vierle, Y. Wang, Q. Yang, and I. Zammuto. A double success story: The international cooperation to build the new ICRF antennas on ASDEX Upgrade and the results obtained. *Fusion Engineering and Design*, **123**, apr 2017.
- [49] A. I. Anisimov, N. I. Vinogradov, V. E. Golant, and B. P. Konstantinov. Method of investigating electron spatial distribution in a plasma. *Soviet Physics - Technical Physics*, **5**, 1961.
- [50] G. Conway. Microwave reflectometry for fusion plasma diagnosis. *Nuclear Fusion*, **46**, 2006.
- [51] D. R. Nicholson. *Introduction to plasma theory*. John Wiley & Sons, Inc, 1983.
- [52] P. I.M and I. M. Podgornyi. *Topics in Plasma Diagnostics*. Springer US, Boston, MA, 1971.
- [53] H. Koskinen. *Physics of Space Storms*. Springer Berlin Heidelberg, Berlin, Heidelberg, 2011. URL <http://link.springer.com/10.1007/978-3-642-00319-6>.
- [54] D. M. Pozar. *Microwave Engineering, 4th Edition*. 2012.
- [55] V. L. Ginzburg. The propagation of electromagnetic waves in plasmas. *International Series of Monographs in Electromagnetic Waves, Oxford: Pergamon, 1970, 2nd rev. and enl. ed.*, **1**, 1970.
- [56] A. Silva. *The ASDEX Upgrade broadband microwave reflectometry system*. PhD thesis, Instituto Superior Técnico, Universidade Técnica de Lisboa, 2006.

- [57] E. Westerhof. Wave propagation through an electron cyclotron resonance layer. *Plasma Physics and Controlled Fusion*, **39**, jun 1997.
- [58] E. Westerhof. Electron Cyclotron Heating and Current Drive. *Fusion Technology*, **33**, mar 1998.
- [59] P. Varela and M. Manso. Density profile measurements with X-mode lower cut-off reflectometry in ASDEX Upgrade. *Review of Scientific Instruments*, **83**, 2012.
- [60] E. Mazzucato. Microwave reflectometry for magnetically confined plasmas. *Review of Scientific Instruments*, **69**, jun 1998.
- [61] M. Hirsch, E. Holzhauer, J. Baldzuhn, and B. Kurzan. Doppler reflectometry for the investigation of propagating density perturbations. *Review of Scientific Instruments*, **72**, 2001.
- [62] K. Peek. *Estimation and compensation of frequency sweep nonlinearity in FMCW radar*. PhD thesis, University of Twente, 2011.
- [63] J. Santos. *Fast reconstruction of reflectometry density profiles on ASDEX Upgrade for plasma position feedback purposes*. PhD thesis, Instituto Superior Técnico, Universidade Técnica de Lisboa, 2008.
- [64] A. Silva, M. E. Manso, L. Cupido, M. Albrecht, F. Serra, P. Varela, J. Santos, S. Vergamota, F. Eusébio, J. Fernandes, T. Grossmann, A. Kallenbach, B. Kurzan, C. Loureiro, L. Meneses, I. Nunes, F. Silva, and W. Suttrop. Ultrafast broadband frequency modulation of a continuous wave reflectometry system to measure density profiles on ASDEX upgrade. *Review of Scientific Instruments*, **67**, 1996.
- [65] F. Clairet, S. Heuraux, C. Bottereau, D. Molina, L. Ducobu, F. Leroux, and A. Barbuti. Fast sweeping reflectometry upgrade on Tore Supra. *Review of Scientific Instruments*, **81**, 2010.
- [66] F. Clairet, C. Bottereau, A. Medvedeva, D. Molina, G. D. Conway, A. Silva, and U. Stroth. $1 \mu s$ broadband frequency sweeping reflectometry for plasma density and fluctuation profile measurements. *Review of Scientific Instruments*, **88**, nov 2017.
- [67] F. Simonet. Measurement of electron density profile by microwave reflectometry on tokamaks. *Review of Scientific Instruments*, **56**, may 1985.
- [68] P. Varela, M. E. Manso, A. Silva, J. Fernandes, and F. Silva. Initialization of plasma density profiles from reflectometry. *Review of Scientific Instruments*, **66**, oct 1995.
- [69] C. Laviron, A. J. H. Donné, M. E. Manso, and J. Sanchez. Reflectometry techniques for density profile measurements on fusion plasmas. *Plasma Physics and Controlled Fusion*, **38**, jul 1996.
- [70] C. A. J. Hugenholtz and S. H. Heijnen. Pulse radar technique for reflectometry on thermonuclear plasmas. *Review of Scientific Instruments*, **62**, apr 1991.
- [71] A. Donné, S. Heijnen, and C. Hugenholtz. Pulsed radar reflectometry and prospects for fluctuation measurements. *Fusion Engineering and Design*, **34-35**, mar 1997.

- [72] C. a. J. Hugenholtz, A. J. H. Donné, B. S. Q. Elzendoorn, J. C. van Gorkom, W. Kooijman, H. a. van der Laan, M. J. van de Pol, a. J. Putter, H. J. F. van Ramele, D. Smit, P. C. de Vries, F. Wijnoltz, W. Pysik, G. Waidmann, and G. P. Ermak. Fast pulsed radar reflectometry for the Textor Tokamak. *Review of Scientific Instruments*, **70**, jan 1999.
- [73] E. A. Azizov, A. V. Babarykin, A. V. Voronin, V. K. Gusev, A. Y. Malyshev, V. K. Markov, A. A. Petrov, V. G. Petrov, Y. V. Petrov, V. V. Rozhdestvenskii, and N. V. Sakharov. First results obtained with a sweeping pulsed radar reflectometer in the Globus-M tokamak. *Plasma Physics Reports*, **30**, may 2004.
- [74] V. F. Shevchenko and M. J. Walsh. First results from the small tight aspect ratio tokamak multifrequency pulse radar reflectometer. *Review of Scientific Instruments*, **68**, may 1997.
- [75] T. Tokuzawa, K. Kawahata, K. Tanaka, and t. L. E. Group. Electron density profile measurement using Ka -band microwave impulse radar reflectometer on LHD. *Nuclear Fusion*, **46**, sep 2006.
- [76] Y. Yokota, A. Mase, K. Uchino, Y. Kogi, T. Tokuzawa, K. Kawahata, Y. Nagayama, and H. Hojo. Reconstruction method of X-mode ultrashort-pulse reflectometry in LHD. *Journal of Physics: Conference Series*, **227**, may 2010.
- [77] M. Zerbini, P. Amadeo, and P. Buratti. Experimental results of amplitude modulation reflectometry on the FTU tokamak. *Review of Scientific Instruments*, **68**, jan 1997.
- [78] D. Pinsonneault, B. Quirion, J. L. Lachambre, and C. Legros. Edge density profile measurements in TdeV using amplitude modulation reflectometry. *Review of Scientific Instruments*, **68**, 1997.
- [79] E. de la Luna, G. Hanson, J. Sanchez, J. B. Wilgen, V. A. Zhuravlev, M. Ono, and R. Kaita. Edge density profile measurements by amplitude modulation reflectometry on PBX-M tokamak. *Plasma Physics and Controlled Fusion*, **37**, sep 1995.
- [80] M. Hirsch, H. Hartfuss, T. Geist, and E. de la Luna. Amplitude modulated heterodyne reflectometer for density profile and density fluctuation profile measurements at W7-AS. *Review of Scientific Instruments*, **67**, may 1996.
- [81] G. R. Hanson, J. B. Wilgen, T. S. Bigelow, I. Collazo, A. C. England, M. Murakami, D. A. Rasmussen, C. E. Thomas, J. R. Wilson, and H. K. Park. Microwave reflectometry for edge density profile measurements on TFTR. *Plasma Physics and Controlled Fusion*, **36**, dec 1994.
- [82] G. R. Hanson, J. B. Wilgen, T. S. Bigelow, I. Collazo, and C. E. Thomas. A swept two-frequency microwave reflectometer for edge density profile measurements on TFTR. *Review of Scientific Instruments*, **63**, oct 1992.
- [83] G. R. Hanson, J. B. Wilgen, T. S. Bigelow, I. Collazo, A. C. England, M. Murakami, D. A. Rasmussen, and J. R. Wilson. Differential-phase reflectometry for edge profile measurements on Tokamak fusion test reactor. *Review of Scientific Instruments*, **66**, jan 1995.

- [84] K. Nagata, H. Idei, M. Sakaguchi, K. Dono, Y. Wataya, S. Kawasaki, H. Zushi, K. Hanada, K. Nakamura, M. Sakamoto, M. Hasegawa, Y. Higashizono, Y. Takase, T. Maekawa, O. Mitarai, Y. Kishimoto, H. Nakashima, and A. Higashijima. Differential-phase reflectometry using phased-array antenna system in QUEST. In *35th International Conference on Infrared, Millimeter, and Terahertz Waves*, **1**, 1–2. IEEE, sep 2010.
- [85] H. Idei, K. Nagata, K. Mishra, M. K. Yamamoto, T. Itado, R. Akimoto, K. Hanada, and H. Zushi. Adaptive array technique for differential-phase reflectometry in QUEST. *Review of Scientific Instruments*, **85**, nov 2014.
- [86] G. R. Hanson, J. B. Wilgen, C. Lau, Y. Lin, G. M. Wallace, and S. J. Wukitch. Scrape-off layer reflectometer for Alcator C-Mod. *Review of Scientific Instruments*, **79**, oct 2008.
- [87] C. Lau, G. Hanson, J. Wilgen, Y. Lin, and S. Wukitch. Scrape-off layer reflectometer for Alcator C-Mod. *Review of Scientific Instruments*, **81**, oct 2010.
- [88] J. S. Belrose. Reginald Aubrey Fessenden and the birth of wireless telephony. *IEEE Antennas and Propagation Magazine*, **44**, 2002.
- [89] J. L. Doane, E. Mazzucato, and G. L. Schmidt. Plasma density measurements using FM-CW millimeter wave radar techniques. *Review of Scientific Instruments*, **52**, 1981.
- [90] B. Boashash and S. Member. Estimating and Interpreting The Instantaneous Frequency of a Signal-Part 1 : Fundamentals. **80**, 1992.
- [91] E. J. Doyle, T. Lehecka, N. C. Luhmann, and W. A. Peebles. X-mode broadband reflectometric density profile measurements on DIII-D. *Review of Scientific Instruments*, **61**, 1990.
- [92] A. Silva, L. Cupido, M. Manso, F. Serra, F. X. Söldner, and P. Varela. Fast sweep multiple broadband reflectometer for ASDEX Upgrade. In *Proc. 17th Symp. on Fusion Technology (Rome, Italy)*, 747–750, 1992.
- [93] A. Silva, L. Cupido, M. E. Manso, P. Varela, F. M. Serra, and U. Team ASDEX. Continuous phase derivative evaluation for density profile measurements from FM broadband reflectometry. In *Proc. 22nd EPS Conf. on Controlled Fusion and Plasma Physics (Bournemouth, UK, 1995)*, **19**, 413–416, 1995.
- [94] K. W. Kim, E. J. Doyle, W. A. Peebles, A. Ejiri, N. C. Luhmann, and C. L. Rettig. Advances in reflectometric density profile measurements on the DIII-D tokamaka). *Review of Scientific Instruments*, **66**, 1995.
- [95] O. Tudisco, A. Silva, S. Ceccuzzi, O. D’Arcangelo, G. Rocchi, H. Fuenfgelder, V. Bobkov, R. Cavazzana, G. D. Conway, J. Friesen, B. Gonçalves, A. Mancini, L. Meneses, J. M. Noterdaeme, G. Siegl, A. Simonetto, N. Tsujii, A. A. Tuccillo, T. Vierle, I. Zammuto, ASDEX Upgrade Team, and FTU Team. A multichannel reflectometer for edge density profile measurements at the ICRF antenna in ASDEX Upgrade. In *AIP Conference Proceedings*, **1580**, 566–569, 2014.

- [96] D. E. Aguiam, A. Silva, V. Bobkov, P. J. Carvalho, P. F. Carvalho, R. Cavazzana, G. D. Conway, O. D'Arcangelo, L. Fattorini, H. Faugel, A. Fernandes, H. Fünfgelder, B. Gonçalves, L. Guimarães, G. De Masi, L. Meneses, J. M. Noterdaeme, R. C. Pereira, G. Rocchi, J. M. Santos, A. A. Tuccillo, and O. Tudisco. Implementation of the new multichannel X-mode edge density profile reflectometer for the ICRF antenna on ASDEX Upgrade. *Review of Scientific Instruments*, **87**, nov 2016.
- [97] W. L. Stutzman and G. A. Thiele. *Antenna theory and design*. J. Wiley, 1998.
- [98] EIA RS-261-B "Rectangular Waveguides (WR3 to WR2300)". Technical report, 1979.
- [99] Sivers Ima. URL <https://www.siversima.com/>.
- [100] LC Technologies. URL <http://www.cupidotech.com/>.
- [101] L. Meneses, L. Cupido, and M. E. Manso. New frequency translation technique for FM-CW reflectometry. *Review of Scientific Instruments*, **81**, oct 2010.
- [102] Wenzel Associates, Inc. URL <http://www.wenzel.com/>.
- [103] Millitech. URL <http://www.millitech.com/>.
- [104] CernexWave. URL <http://www.cernexwave.com/>.
- [105] R. C. Pereira, A. M. Fernandes, A. C. Neto, J. Sousa, A. J. Batista, B. B. Carvalho, C. M. B. A. Correia, and C. A. F. Varandas. ATCA fast data acquisition and processing system for JET gamma-ray cameras upgrade diagnostic. *IEEE Transactions on Nuclear Science*, **57**, 2010.
- [106] G. Raupp, R. Cole, K. Behler, M. Fitzek, P. Heimann, A. Lohs, K. Lüddecke, G. Neu, J. Schacht, W. Treutterer, D. Zasche, T. Zehetbauer, and M. Zilker. A "Universal Time" system for ASDEX upgrade. *Fusion Engineering and Design*, **66-68**, 2003.
- [107] D. Aguiam, A. Silva, V. Bobkov, P. Carvalho, P. Carvalho, R. Cavazzana, G. Conway, O. D'Arcangelo, L. Fattorini, H. Faugel, A. Fernandes, H. Fünfgelder, B. Goncalves, L. Guimarães, G. De Masi, L. Meneses, J. Noterdaeme, R. Pereira, G. Rocchi, J. Santos, A. Tuccillo, and O. Tudisco. X-mode raw data analysis of the new AUG ICRF antenna edge density profile reflectometer. *Fusion Engineering and Design*, **87**, apr 2017.
- [108] D. E. Aguiam, A. Silva, L. Guimarães, P. J. Carvalho, G. D. Conway, B. Goncalves, L. Meneses, J.-M. Noterdaeme, J. M. Santos, A. A. Tuccillo, and O. Tudisco. Estimation of X-Mode Reflectometry First Fringe Frequency Using Neural Networks. *IEEE Transactions on Plasma Science*, **46**, may 2018.
- [109] A. F. Harvey. *Microwave engineering*. Academic Press Inc. (London) Ltd., 2 edition, 1963.
- [110] K. W. Kim, E. J. Doyle, W. A. Peebles, A. Ejiri, N. C. Luhmann, and C. L. Rettig. Advances in reflectometric density profile measurements on the DIII-D tokamak. *Review of Scientific Instruments*, **66**, 1995.

- [111] F. Clairet, C. Bottereau, J. M. Chareau, M. Paume, and R. Sabot. Edge density profile measurements by X-mode reflectometry on Tore Supra. *Plasma Physics and Controlled Fusion*, **43**, 2001.
- [112] H. Qu, T. Zhang, S. Zhang, F. Wen, Y. Wang, D. Kong, X. Han, Y. Yang, Y. Gao, C. Huang, J. Cai, and X. Gao. Q-Band X-Mode Reflectometry and Density Profile Reconstruction. *Plasma Science and Technology*, **17**, 2015.
- [113] P. J. Carvalho, L. Meneses, J. Santos, B. Gonçalves, and J. Contributors. A hybrid X-mode reflectometry first fringe detection algorithm for JET. *1st EPS conference on Plasma Diagnostics (ECPD2015)*, 2015.
- [114] C. Lau, G. Hanson, Y. Lin, J. Wilgen, S. Wukitch, B. Labombard, and G. Wallace. First results of the SOL reflectometer on Alcator C-Mod. *Review of Scientific Instruments*, **83**, 2012.
- [115] G. Wang, L. Zeng, E. J. Doyle, T. L. Rhodes, and W. A. Peebles. Improved reflectometer electron density profile measurements on DIII-D. *Review of Scientific Instruments*, **74**, 2003.
- [116] R. E. Kalman. A New Approach to Linear Filtering and Prediction Problems. *Journal of Basic Engineering*, **82**, 1960.
- [117] F. Chollet. *Deep Learning with Python*, **1**. Manning Publications Co., Shelter Island, NY, 2017.
- [118] Y. LeCun, Y. Bengio, and G. Hinton. Deep learning. *Nature*, **521**, may 2015.
- [119] A. Agarwal, P. Barham, E. Brevdo, Z. Chen, C. Citro, G. S. Corrado, A. Davis, J. Dean, M. Devin, S. Ghemawat, I. Goodfellow, A. Harp, G. Irving, M. Isard, Y. Jia, R. Jozefowicz, L. Kaiser, M. Kudlur, J. Levenberg, D. Man, R. Monga, S. Moore, D. Murray, C. Olah, M. Schuster, J. Shlens, B. Steiner, I. Sutskever, K. Talwar, P. Tucker, V. Vanhoucke, V. Vasudevan, F. Vi, O. Vinyals, P. Warden, M. Wattenberg, M. Wicke, Y. Yu, and X. Zheng. TensorFlow: Large-Scale Machine Learning on Heterogeneous Systems. *White Paper*, 2015.
- [120] F. Chollet. Keras: Deep Learning library for Theano and TensorFlow. *GitHub Repository*, 2015.
- [121] F. A. Matos, D. R. Ferreira, and P. J. Carvalho. Deep learning for plasma tomography using the bolometer system at JET. *Fusion Engineering and Design*, **114**, 2017.
- [122] O. Barana, A. Murari, I. Coffey, and JET-EFDA Contributors. Artificial Neural Networks for Real-time Diagnostic of High-Z Impurities in Reactor-relevant Plasmas. In *2007 IEEE International Symposium on Intelligent Signal Processing*, 1–5. IEEE, 2007.
- [123] J. Santos, F. Nunes, M. Manso, and I. Nunes. Neural network evaluation of reflectometry density profiles for control purposes. *Review of Scientific Instruments*, **70**, 1999.
- [124] J. Hernandez, A. Vannucci, T. Tajima, Z. Lin, W. Horton, and S. McCool. Neural network prediction of some classes of tokamak disruptions. *Nuclear Fusion*, **36**, 1996.

- [125] C. Windsor, G. Pautasso, C. Tichmann, R. Buttery, T. Hender, J. E. Contributors, and t. A. U. Team. A cross-tokamak neural network disruption predictor for the JET and ASDEX Upgrade tokamaks. *Nuclear Fusion*, **45**, 2005.
- [126] D. P. Kingma and J. Ba. Adam: A Method for Stochastic Optimization. dec 2014.
- [127] P. Varela, M. Manso, A. Silva, t. C. Team, and t. A. U. Team. Review of data processing techniques for density profile evaluation from broadband FM-CW reflectometry on ASDEX Upgrade. *Nuclear Fusion*, **46**, 2006.
- [128] K. McCormick, S. Fiedler, G. Kocsis, J. Schweinzer, and S. Zoletnik. Edge density measurements with a fast Li beam probe in tokamak and stellarator experiments. *Fusion Engineering and Design*, **34-35**, 1997.
- [129] R. Fischer, E. Wolfrum, and J. Schweinzer. Probabilistic lithium beam data analysis. *Plasma Physics and Controlled Fusion*, **50**, 2008.
- [130] V. Driessen. RQ (Redis Queue) Python library. URL <https://github.com/nvie/rq>.
- [131] A. Silva, L. Cupido, M. E. Manso, F. Serra, I. Nunes, J. Santos, P. Varela, S. Vergamota, L. Menezes, V. Grossman, F. Silva, C. Loureiro, F. Nunes, B. Kurzan, and W. Suttrop. Microwave reflectometry diagnostic for density profile and fluctuation measurements on ASDEX Upgrade. *Review of Scientific Instruments*, **70**, 1999.
- [132] H. Murmann, S. Götsch, H. Röhr, H. Salzmann, and K. H. Steuer. The Thomson scattering systems of the ASDEX upgrade tokamak. *Review of Scientific Instruments*, **63**, 1992.
- [133] B. Kurzan and H. D. Murmann. Edge and core Thomson scattering systems and their calibration on the ASDEX Upgrade tokamak. *Review of Scientific Instruments*, **82**, 2011.
- [134] F. Wagner, G. Becker, K. Behringer, D. Campbell, A. Eberhagen, W. Engelhardt, G. Fussmann, O. Gehre, J. Gernhardt, G. v. Gierke, G. Haas, M. Huang, F. Karger, M. Keilhacker, O. Klüber, M. Kornherr, K. Lackner, G. Lisitano, G. G. Lister, H. M. Mayer, D. Meisel, E. R. Müller, H. Murmann, H. Niedermeyer, W. Poschenrieder, H. Rapp, H. Röhr, F. Schneider, G. Siller, E. Speth, A. Stäbler, K. H. Steuer, G. Venus, O. Vollmer, and Z. Yü. Regime of Improved Confinement and High Beta in Neutral-Beam-Heated Divertor Discharges of the ASDEX Tokamak. *Physical Review Letters*, **49**, nov 1982.
- [135] W. Zhang, V. Bobkov, T. Lunt, J.-M. Noterdaeme, D. Coster, R. Bilato, P. Jacquet, D. Brida, Y. Feng, E. Wolfrum, and L. Guimaraes. 3D simulations of gas puff effects on edge density and ICRF coupling in ASDEX Upgrade. *Nuclear Fusion*, **56**, mar 2016.
- [136] R. Bilato, M. Brambilla, D. Hartmann, and A. Parisot. Influence of an evanescence layer in front of the antenna on the coupling efficiency of ion cyclotron waves. *Nuclear Fusion*, **45**, feb 2005.

- [137] E. Lerche, M. Goniche, P. Jacquet, D. Van Eester, V. Bobkov, L. Colas, A. Czarnecka, S. Brezinsek, M. Brix, K. Crombe, M. Graham, M. Groth, I. Monakhov, T. Mathurin, G. Matthews, L. Meneses, C. Noble, V. Petržilka, F. Rimini, and A. Shaw. Impact of localized gas injection on ICRF coupling and SOL parameters in JET-ILW H-mode plasmas. *Journal of Nuclear Materials*, **463**, 2015.
- [138] V. Bobkov, F. Braun, R. Dux, a. Herrmann, L. Giannone, a. Kallenbach, a. Krivska, H. Müller, R. Neu, J.-M. Noterdaeme, T. Pütterich, V. Rohde, J. Schweinzer, a. Sips, and I. Zammuto. Assessment of compatibility of ICRF antenna operation with full W wall in ASDEX Upgrade. *Nuclear Fusion*, **50**, 2010.
- [139] V. Bobkov, M. Balden, R. Bilato, F. Braun, R. Dux, A. Herrmann, H. Faugel, H. Fünfgelder, L. Giannone, A. Kallenbach, H. Maier, H. Müller, R. Neu, J.-M. Noterdaeme, T. Pütterich, V. Rohde, N. Tsujii, F. Zeus, and H. Zohm. ICRF operation with improved antennas in ASDEX Upgrade with W wall. *Nuclear Fusion*, **53**, 2013.
- [140] V. Bobkov, D. Aguiam, M. Baruzzo, D. Borodin, I. Borodkina, S. Brezinsek, I. Coffey, L. Colas, A. Czarnecka, E. Delabie, P. Dumortier, F. Durodie, R. Dux, H. Faugel, H. Fünfgelder, C. Giroud, M. Goniche, J. Hobirk, A. Herrmann, J. Jacquot, P. Jacquet, A. Kallenbach, A. Krivska, C. C. Klepper, E. Lerche, S. Menmuir, D. Milanese, R. Maggiora, I. Monakhov, F. Nave, R. Neu, J. M. Noterdaeme, R. Ochoukov, T. Pütterich, M. Reinke, A. Tuccilo, O. Tudisco, D. Van Eester, Y. Wang, Q. Yang, and W. Zhang. Progress in reducing ICRF-specific impurity release in ASDEX upgrade and JET. *Nuclear Materials and Energy*, **12**, 2016.
- [141] W. Zhang, V. Bobkov, T. Lunt, J.-M. Noterdaeme, D. Coster, R. Bilato, P. Jacquet, D. Brida, Y. Feng, E. Wolfrum, and L. Guimaraes. 3D simulations of gas puff effects on edge density and ICRF coupling in ASDEX Upgrade. *Nuclear Fusion*, **56**, mar 2016.
- [142] W. Zhang, V. Bobkov, J.-M. Noterdaeme, W. Tierens, D. Aguiam, R. Bilato, D. Coster, L. Colas, K. Crombé, H. Fuenfgelder, H. Faugel, Y. Feng, J. Jacquot, P. Jacquet, A. Kallenbach, A. Kostic, T. Lunt, R. Maggiora, R. Ochoukov, A. Silva, G. Suárez, A. A. Tuccilo, O. Tudisco, M. Usoltceva, D. Van Eester, Y. Wang, and Q. Yang. Recent progress on improving ICRF coupling and reducing RF-specific impurities in ASDEX Upgrade. *EPJ Web of Conferences*, **157**, 2017.
- [143] W. Zhang, D. Coster, Y. Feng, T. Lunt, D. Aguiam, R. Bilato, V. Bobkov, J. Jacquot, P. Jacquet, E. Lerche, J.-M. Noterdaeme, and W. Tierens. Plasma edge modelling with ICRF coupling. *EPJ Web of Conferences*, **157**, oct 2017.
- [144] W. Zhang, V. Bobkov, J.-m. Noterdaeme, W. Tierens, R. Bilato, D. Carralero, D. Coster, J. Jacquot, P. Jacquet, T. Lunt, R. A. Pitts, V. Rohde, G. Siegl, H. Fuenfgelder, D. Aguiam, A. Silva, L. Colas, and S. Ceccuzzi. Effects of outer top gas injection on ICRF coupling in ASDEX Upgrade: towards modelling of ITER gas injection. *Plasma Physics and Controlled Fusion*, **59**, jul 2017.
- [145] W. Zhang, Y. Feng, J.-M. Noterdaeme, V. Bobkov, L. Colas, D. Coster, T. Lunt, R. Bilato, J. Jacquot, R. Ochoukov, D. Van Eester, A. Křivská, P. Jacquet, and L. Guimaraes. Modelling of the ICRF in-

- duced $E \times B$ convection in the scrape-off-layer of ASDEX Upgrade. *Plasma Physics and Controlled Fusion*, **58**, sep 2016.
- [146] M. Martin, W. Gekelman, B. Van Compernelle, P. Pribyl, and T. Carter. Experimental Observation of Convective Cell Formation due to a Fast Wave Antenna in the Large Plasma Device. *Physical Review Letters*, **119**, 2017.
- [147] G. M. Kurtzer, V. Sochat, and M. W. Bauer. Singularity: Scientific containers for mobility of compute. *PLOS ONE*, **12**, may 2017.
- [148] A. Kay and T. Green. Analog Engineer 's Pocket Reference. 2014.

Appendix A

Quadrature phase uncertainty

The group delay measurement of a swept frequency density profile reflectometry system is dependent on the frequency sweep rate df/dt and the beat frequency measurement f_b

$$\Delta\tau = \frac{1}{\Delta f_b} \left(\frac{df}{dt} \right)^{-1}. \quad (\text{A.1})$$

In a quadrature detection system, the beat frequency measurement is determined by the sampling frequency f_s and the phase estimation

$$\Delta f_b = \frac{\Delta\varphi}{2\pi} f_s. \quad (\text{A.2})$$

The phase estimation, however, has an uncertainty, σ_φ , that depends on the signal to noise ratio (S/N) of the analog quadrature plasma reflection signals, and the propagated uncertainties of the analog to digital converters (ADC), σ_{ADC} , and the phase calculation.

A quadrature detection system acquires two signals that correspond to the in-phase and quadrature components of the measurement. These analog signals typically have the form

$$I_a(t) = A(t)\sin(\varphi(t)) \pm \sigma_a \quad (\text{A.3})$$

and

$$Q_a(t) = A(t)\cos(\varphi(t)) \pm \sigma_a, \quad (\text{A.4})$$

where σ_a is the uncertainty of the input analog signal.

The signal to noise ratio of the input reflectometry signal determines the relative uncertainty of the analog signal σ_a , approximated by

$$\sigma_a \approx \frac{1}{S/N}. \quad (\text{A.5})$$

The S/N is the signal to noise ratio of the detection mechanism, which depends on a variety of factors, the attenuation of the reflection signal through the plasma, plasma turbulence, linearity of the frequency sweep, the time overlap between the reference and reflected waves and the quadrature detection mechanism.

The amplitude of the original signal can be extracted by calculating

$$A(t) = \sqrt{I_a^2(t) + Q_a^2(t)}. \quad (\text{A.6})$$

And the phase measurement is given by

$$\varphi(t) = \tan^{-1} \left(\frac{Q_a(t)}{I_a(t)} \right). \quad (\text{A.7})$$

Here we describe the uncertainty propagation of the quadrature phase measurement, as illustrated in Figure A.1.

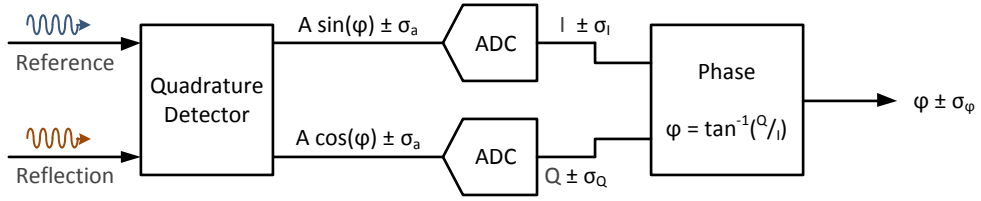


Figure A.1: Diagram of phase measurement in a quadrature detection system.

The analog to digital conversion has the transfer function

$$f(x) = x \pm \sigma_{\text{ADC}}, \quad (\text{A.8})$$

where the relative uncertainty of the ADC, σ_{ADC} , corresponds to its S/N [148]

$$\sigma_{\text{ADC}} = \frac{1}{S/N_{\text{ADC}}} = \frac{1}{2^{N-1}\sqrt{6}}. \quad (\text{A.9})$$

The digitized I_d and Q_d have a combined relative uncertainty

$$I_d = I_a \pm (\sigma_a + \sigma_{\text{ADC}}) = I_a \pm \sigma_I, \quad (\text{A.10})$$

$$Q_d = Q_a \pm (\sigma_a + \sigma_{\text{ADC}}) = Q_a \pm \sigma_Q, \quad (\text{A.11})$$

where

$$\sigma_I = \sigma_Q = \sigma_a + \sigma_{\text{ADC}} = \sigma_{IQ}. \quad (\text{A.12})$$

The current uncertainty of the digital codes is

$$\sigma_{IQ} = \frac{1}{S/N} + \frac{1}{2^{N-1}\sqrt{6}} = \frac{S/N + 2^{N-1}\sqrt{6}}{2^{N-1}\sqrt{6}S/N} \quad (\text{A.13})$$

The phase calculation has a two step uncertainty propagation. The Q/I division calculated as

$$f_1(I, Q) = \frac{Q}{I}, \quad (\text{A.14})$$

with relative uncertainty

$$\sigma_{f_1} = \left| \frac{Q}{I} \right| \sqrt{\sigma_I^2 + \sigma_Q^2}. \quad (\text{A.15})$$

The inverse tangent function

$$f_2(x) = \tan^{-1}(x), \quad (\text{A.16})$$

has a relative uncertainty

$$\sigma_{f_2} = \frac{\sigma_x}{1 + x^2}. \quad (\text{A.17})$$

Combining both we obtain the phase uncertainty as a function of σ_I and σ_Q

$$\sigma_\varphi = \frac{\left| \frac{Q}{I} \right| \sqrt{\sigma_I^2 + \sigma_Q^2}}{1 + \left(\frac{Q}{I} \right)^2}. \quad (\text{A.18})$$

Since $\sigma_I = \sigma_Q$, the uncertainty becomes

$$\sigma_\varphi = \frac{\left| \frac{Q}{I} \right| \sigma_{IQ} \sqrt{2}}{1 + \left(\frac{Q}{I} \right)^2}. \quad (\text{A.19})$$

The worst uncertainty, majoring σ_φ , occurs when $Q/I \rightarrow 0$ in equation (A.19). As I and Q are digital codes, this minimum occurs when

$$\frac{Q}{I} = \frac{\text{LSB}}{\text{FSR}} = \frac{\text{FSR}/2^N}{\text{FSR}} = \frac{1}{2^N}, \quad (\text{A.20})$$

where LSB is the value of the least significant bit, FSR is the full scale range of the ADC, and N is the number of bits of the ADC.

Replacing in (A.19) results in

$$\sigma_\varphi = \frac{1}{2^N} \frac{\sigma_{IQ} \sqrt{2}}{1 + \left(\frac{1}{2^N} \right)^2} = \frac{\sigma_{IQ} \sqrt{2}}{2^N + \frac{1}{2^N}} \approx \frac{\sigma_{IQ} \sqrt{2}}{2^N}. \quad (\text{A.21})$$

And replacing σ_{IQ} we obtain

$$\sigma_\varphi \approx \sqrt{2} \frac{S/N + 2^{N-1} \sqrt{6}}{2^{2N-1} \sqrt{6} S/N} = \frac{\sqrt{2}}{2^{2N-1} \sqrt{6}} + \frac{\sqrt{2}}{2^N S/N}. \quad (\text{A.22})$$

Since

$$\frac{\sqrt{2}}{2^{2N-1} \sqrt{6}} \ll \frac{\sqrt{2}}{2^N S/N}, \quad (\text{A.23})$$

then the relative phase uncertainty is approximated by

$$\sigma_\varphi \approx \frac{\sqrt{2}}{2^N S/N}, \quad (\text{A.24})$$

where N is the number of bits and S/N is the signal to noise ratio of the detection mechanism.

Funding Institutions

Fundação para a Ciência e a Tecnologia



This work was supported in part by the Fundação para a Ciência e a Tecnologia through the Project under Grant UID/FIS/50010/2013 and the Ph.D. Scholarship under Grant FCT-SFRH/BD/52414/2013.

This work was developed as part of the Advanced Program in Plasma Science and Engineering .

Fusion-DC



This work was also developed as part of the FUSION-DC Erasmus Mundus Joint Doctorate Program.

EUROfusion



This work has been carried out within the framework of the EUROfusion Consortium and has received funding from the Euratom research and training programme 2014-2018 under grant agreement No 633053. The views and opinions expressed herein do not necessarily reflect those of the European Commission.
